

**COST-EFFECTIVE PREPREG MANUFACTURING
FOR HIGH-VOLUME APPLICATIONS**

by
Alex Reichanadter

A Dissertation

*Submitted to the Faculty of Purdue University
In Partial Fulfillment of the Requirements for the degree of*

Doctor of Philosophy



Davidson School of Chemical Engineering
West Lafayette, Indiana
December 2021

THE PURDUE UNIVERSITY GRADUATE SCHOOL
STATEMENT OF COMMITTEE APPROVAL

Dr. Jan-Anders E. Mansson, Chair

School of Materials Engineering, Davidson School of Chemical Engineering, and School of
Aeronautics and Astronautics

Dr. R. Byron Pipes

Davidson School of Chemical Engineering, School of Materials Engineering, and School of
Aeronautics and Astronautics

Dr. James Caruthers

Davidson School of Chemical Engineering

Dr. Joshua Dustin

The Boeing Company

Approved by:

Dr. John A. Morgan

*Dedicated to my Parents, Lydia and Larry Reichenadter,
as well as my Brother, Adam Reichenadter.*

ACKNOWLEDGMENTS

The resins provided by Dow Chemical Company were much appreciated for cure kinetics study. I would also like to acknowledge the financial support by the Department of Energy's effort within the Institute for Advanced Composites Manufacturing Innovation (IACMI) and the Composite Manufacturing and Simulation Center (CMSC).

The carbon fiber compaction study wouldn't have been possible without DowAksa providing the A-42 fiber. Additionally, the lab spaces in the Composite Manufacturing and Simulation Center (CMSC) at Purdue University were utilized in this study. The experimental work performed by Ryan Bing was greatly appreciated. We would like to thank David Welsh of Hexagon/MSD for providing technical support for MSC Cradle.

Dr. Joshua Dustin for always making time to hear the issues I was facing in the lab. He was always a source of positivity and support when tests did not go as expected.

Dr. Jim Caruthers has been influential on the content and overall philosophical approach towards the PhD process. Additionally, he was a pleasure to have in the classroom as he was the catalyst which transitioned me from a "book smart" student to an independent researcher.

Dr. R. Byron Pipes has been a wealth of composites knowledge. Since joining Purdue University, he has sat with me on a number of lunches in the cafeteria and has never failed to share an original tale of how he made his way to being the Director of the Composites Manufacturing and Simulation Center. These stories have been inspirational to continue down the path of PhD.

Finally, I would not be here, if not for the vision of my thesis advisor and Head of the Manufacturing Design Laboratory (MDLab), Prof. Jan-Anders Mansson. His passion for composites originally attracted me to work for MDLab. His enthusiasm for researching composites and bringing them into the sports and automotive world was refreshing. Furthermore, he is an incredible advisor that knows how to motivate me, while looking out for my well-being.

I would like to thank my research group for reflecting on my ideas/approaches for this study and how they were able to push me through mental blocks along the way. They have been incredibly supportive in their efforts to review my work. In particular, I would like to extend a thanks to Justin Miller and Robin Glebes for listening to my work and life issues and always being able to provide encouraging words. Additionally, Morgan Chamberlain has been instrumental in studying the multi-phase resins.

TABLE OF CONTENTS

LIST OF TABLES	9
LIST OF FIGURES	11
ABSTRACT	17
1. PREPREGGING ESSENTIALS FOR HIGH PERFORMANCE COMPOSITES	19
1.1 Fundamentals of Infiltration Processes Through Porous Media	20
1.1.1 Multi-phase Resins	22
1.1.2 Particle Filtration in Porous Media and Aligned Fiber Beds	25
1.1.3 Cost Effective Prepreg Solutions - Irregularly Shaped Carbon Fiber	28
1.2 Considerations for Different Thermoset Prepregging Methods	29
1.2.1 Prepreg Processing: Resin Bath Method	33
1.2.2 Prepreg Processing: Hot-Melt Thermoset Prepregging	34
1.3 Thermoplastic Prepregging Methods	35
1.3.1 Prepreg Processing: Hot-Melt Thermoplastic Prepregging	36
1.3.2 Prepreg Processing: Solution Processing	38
1.3.3 Prepreg Processing: Fiber Co-Mingling	39
1.3.4 Prepreg Processing: Powder Deposition	40
1.3.4.1 Dry Powder Deposition	41
1.3.4.2 Wet Powder Deposition (Slurry)	42
1.4 Research Objectives	43
1.5 References	45
2. COMPACTION AND PERMEABILITY OF ALIGNED, KIDNEY-BEAN SHAPED CARBON FIBER BEDS	58
2.1 Introduction	58
2.2 Carbon Fiber Compaction Background	59
2.3 Carbon Fiber Permeability Background	60
2.4 Experimental Methods and Permeability Simulation Conditions	62
2.4.1 Material for tensioned compaction experiments	62
2.4.2 Tensioned Fiber Bed Compaction Method	63
2.4.3 Representative Kidney-Bean Fiber Unit Cells	65

2.4.4	Flow Simulation and Boundary Conditions	66
2.5	Results and Discussion	69
2.5.1	Kidney-Bean shaped carbon fiber compaction.....	69
2.5.2	Permeability Simulation of Kidney-Bean Shaped Fibers	74
2.5.3	Modeling Permeability in Kidney-Bean Shaped Fibers	80
2.6	Conclusions.....	84
2.7	References.....	86
3.	RHEO-KINETIC CHARACTERIZATION OF A RAPID CURE EPOXY RESIN FOR PREPREG MANUFACTURING.....	90
3.1	Considerations for Low-Cost and High-Production Volume Thermoset Prepreg.....	90
3.2	Material and Methods for Epoxy Characterization and Prepreg Modeling.....	92
3.2.1	Material.....	92
3.2.2	Differential Scanning Calorimeter (DSC) Test Method.....	93
3.2.3	Rheological Characterization and Dynamic Mechanical Analysis Test Method	93
3.2.4	Prepreg Manufacturing Layout for Modeling Resin and Particle Infiltration	94
3.2.4.1	Prepreg Layout: S-Wrap Configuration	97
3.2.4.2	Prepreg Layout: Nip-Roller Configuration.....	99
3.3	Cure Kinetics and Chemorheology Characterization	100
3.3.1	Curing Behavior and Kinetics	100
3.3.2	Curing Kinetics Analysis	101
3.3.3	Chemorheology Model	108
3.3.4	Rheological Analysis	109
3.4	Hot-Melt Prepregging Modeling.....	111
3.4.1	Hot-Melt Prepregging: S-Wrap Configuration.....	112
3.4.2	Hot-Melt Prepregging: Nip-Roller Configuration	113
3.5	Conclusions.....	116
3.6	References.....	117
4.	MANUFACTURING AND CHARACTERIZING UNIDIRECTIONAL, THERMOPLASTIC PREPREG TAPE.....	122
4.1	Introduction and Background	122
4.2	Materials, Manufacturing, and Methods.....	124

4.2.1	Materials	124
4.2.2	Prepreg Manufacturing	124
4.2.3	Specimen Preparation for Mechanical Testing.....	129
4.2.4	Digital Image Correlation (DIC) Strain Measurement	133
4.2.5	Tensile Testing Methodology	133
4.2.6	Shear Testing Methodology.....	134
4.2.7	Compression Testing Methodology.....	135
4.2.8	Flexure Testing Methodology.....	136
4.2.9	Rheological Testing Methodology	138
4.2.10	Coefficient of Thermal Expansion Testing Methodology.....	139
4.3	Results & Discussion	139
4.3.1	Rheological Characterization.....	139
4.3.2	Tensile Samples	142
4.3.3	Shear Samples.....	146
4.3.4	Compression Samples.....	147
4.3.5	Flexure Samples.....	151
4.3.6	Thermoelastic Characterization	153
4.4	Conclusions.....	154
4.5	References.....	156
	APPENDIX A: PREPREG AND LAMINATE PROCESS CONDITIONS	158
	APPENDIX B: MECHANICAL TESTING SAMPLE DIMENSIONS	161
5.	EXPERIMENTAL OBSERVATIONS OF MULTI-PHASE THERMOPLASTIC RESINS IN PREPREG MANUFACTURING.....	165
5.1	Introduction and Background	165
5.2	Materials, Manufacturing Conditions, and Methods	166
5.2.1	Materials	166
5.2.2	Viscosity Measurements.....	167
5.2.3	Manufacturing Conditions	168
5.2.4	Prepreg Line Modeling Methods	169
5.2.5	Microscopy Methods	171
5.3	Results and Discussion	171

5.3.1	Viscosity Measurements	171
5.3.2	Experimental Observations on Prepreg Quality	172
5.3.3	Modeling Prepreg Infiltration	182
5.4	Conclusions	187
5.5	References	188
APPENDIX C: RHEOLOGICAL DATA		190
6.	CONCLUSIONS	193
6.1	Compaction Behavior of Kidney-Bean Shaped Carbon Fiber.....	194
6.2	Simulated Permeability of Kidney-Bean Shaped Carbon Fiber	195
6.3	Characterization of a Rapid Cure Epoxy Resin with Internal Mold-Release	197
6.4	Manufacturing Effects on Resin and Particle Infiltration in Multi-Phase Thermoplastic Prepreg Tape	199
6.5	Summary	202

LIST OF TABLES

Table 2.1: Parameters used for Equations (2.1) and (2.22) to model the kidney-bean shaped fibers and compare to circular fibers.....	71
Table 2.2: Constants (C) for Equation (2.23) with various unit cell orientations and packing arrangements for KB-fibers.	84
Table 3.1: Summarizing process parameters for the S wrap and Nip roll process.	95
Table 3.2: Cure kinetic physical constants and modeling parameters for the rapid cure epoxy resin systems.....	105
Table 3.3: Summary of glass transition temperatures with one standard deviation for the rapid cure epoxy resin systems.	106
Table 3.4: Heat of reaction for the rapid cure epoxy resin systems under various dynamic scan rates, reported error is one standard deviation.	106
Table 3.5: Rheological physical constants and modeling parameters for the rapid cure epoxy resin systems.....	111
Table 4.1: PA-6/Kevlar [®] prepreg manufacturing conditions.....	127
Table 4.2: Pressing conditions for PA-6/Kevlar [®] prepreg.....	130
Table 4.3: Fiber volume fraction from manufactured plates from prepreg ID 28 showing consistent fiber content throughout the plate and across plates.	132
Table 4.4: Arrhenius parameters for the zero and infinite shear viscosities of the PA-6 resin. .	140
Table 4.5: Tensile modulus and strength results from plates 23 and 26 for the 0° samples. The sample nomenclature is described in Figure 4.6.	144
Table 4.6: Tensile modulus and strength results from plates 24 and 25 for the 90° samples. The sample nomenclature is described in Figure 4.6.	146
Table 4.7: Shear modulus and strength results from plate 31. The sample nomenclature is described in Figure 4.6.	147
Table 4.8: Compression modulus and strength results from plates 23, 24, 25, and 26 for the 0° samples.....	149
Table 4.9: Compression modulus and strength results from plates 23, 24, 25, and 26 for the 90° samples. The sample nomenclature is described in Figure 4.6.....	150
Table 4.10: Flexural modulus and strength results from plates 23 and 26 for the 0° samples. The sample nomenclature is described in Figure 4.6.....	152
Table 4.11: Flexural modulus and strength results from plates 24 and 25 for the 90° samples. The sample nomenclature is described in Figure 4.6.....	153

Table 4.12: Coefficient of thermal expansion along the fiber direction for samples from plates 24, 25, and 26. The sample nomenclature is described in Figure 4.6.	154
Table 4.13: Coefficient of thermal expansion transverse to the fiber direction for samples from plates 24, 25, and 26. The sample nomenclature is described in Figure 4.6.....	154
Table 4.14: Summary of material properties from characterization tests for PA-6/Kevlar® prepreg.	155
Table 5.1: Total web tensions as measured at the creel.	169
Table 5.2: Rheological parameters to Carreau-Yasuda model for neat PA-66, RT PA-66, and GB PA-66 resins.	172
Table 5.3: Typical fiber bundle thicknesses that were able to be saturated with the PA-66 resins. Bolded values indicated samples that had poor overall fiber bed saturation.	180
Table 5.4: Fiber-bed fiber volume fractions for the fiber beds shown in Figure 5.9, Figure 5.11, and Figure 5.13.	186
Table 5.5: Fiber bed thicknesses for the fiber beds shown in Figure 5.9, Figure 5.11, and Figure 5.13 and were model inputs for Darcy’s law.	186

LIST OF FIGURES

Figure 1.1: Description of resin flowing transversely through an aligned fiber bed.	20
Figure 1.2: Toughening mechanisms in thermoplastic-modified epoxy: 1) crack pinning, 2) particle bridging, 3) crack path deflection, 4) particle yielding, 5) particle-yielding-induced shear banding, and 6) microcracking. Adapted from [53].	24
Figure 1.3: Types of particle retention sites in porous, isotropic media. Modified from Herzig et al [65].	26
Figure 1.4: Effect DMSO concentration has on PAN fiber cross-sectional shape [79].	29
Figure 1.5: Typical viscosity profile for a thermosetting polymer, demonstrating the dwell in viscosity before gelation where viscosity rapidly rose.	32
Figure 1.6: Time-temperature-transformation principles diagram for thermosetting polymers [5].	33
Figure 1.7: Example of the resin bath prepreg tape production process with the vertically oriented furnace. Adapted from [95].	34
Figure 1.8: Hot-melt prepreg line layout for thermoplastic resin. Where dashed lines represent the option to switch to an S-wrap configuration.	35
Figure 1.9: Schematic of the double belt press impregnation unit. Adapted from [115].	38
Figure 1.10: Solution processing prepreg manufacturing diagram.	39
Figure 1.11: Representative commingled yarn cross-section and assumed consolidation mechanism. Adapted from [122].	40
Figure 1.12: Examples of a) good fiber wetting and b) poor fiber wetting from [129].	41
Figure 1.13: Dry powder deposition diagram for thermoplastic prepreg tape production.	42
Figure 1.14: Wet powder deposition diagram for prepreg tape production.	43
Figure 1.15: Thesis layout and main chapter emphasizes.	45
Figure 2.1: Representative micrograph of A-42 carbon fibers showing kidney-bean shaped cross-section with an equivalent ellipse overlaid where the major (D_{maj}) and minor (D_{min}) axis of the ellipse were identified.	62
Figure 2.2: Examples of square packed unit cells with their maximum packing fraction for a) circular fiber, b) kidney-bean shaped fibers with consistent in-plane fiber alignment, c) elliptically shaped fiber with consistent in-plane fiber alignment.	63
Figure 2.3: Experimental setup for fiber bed compaction where θ represents the fiber wrap angle and m represents the mass attached to the fiber tow.	63

Figure 2.4: Front view of the notched pin showing the fiber bed profile (in gray) occupied by the tow above the surface.....	64
Figure 2.5: Representative micrograph of A-42 carbon fibers showing kidney-bean shaped cross-section with the following dimensions in μm were used to construct the representative fiber: $A = 2.40$, $B = 2.88$, $C = 1.68$, $D = R5.02$, and $\theta = 45.7^\circ$	65
Figure 2.6: Examples of fiber packing unit cells with their maximum packing fraction for a) hexagonal pack – 1 KB-fiber, b) hexagonal pack – 2 KB-fiber, c) square pack KB-fiber, d) hexagonal pack circular fiber, e) square pack circular fiber.	66
Figure 2.7: Example of meshed fiber array for KB-fiber with a hexagonal pack – 2 at 0.75 fiber volume fraction.	67
Figure 2.8: Example of element count sensitivity on pressure and permeability.	67
Figure 2.9: Kidney-bean shaped fiber compaction data compared to circular fibers. The kidney-bean shaped fibers were fitted to Equations (2.1) and (2.22) with the model parameters shown in Table 2.1. Error bars represented replicate error of the compacted tows.	69
Figure 2.10: A-42 fiber compaction data for samples consisting of multiple fiber tows, demonstrating the experimental setup was not sensitive to tow count.	72
Figure 2.11: Reduced fiber tension vs the fiber volume fraction for various compaction pressures.	72
Figure 2.12: Example of pressure drop across fiber bed from permeability simulations.	74
Figure 2.13: Permeabilities from the flow simulation for kidney-bean and circular fibers with different unit cell orientations for a) hexagonal pack – 1 KB-fibers, b) hexagonal pack – 2 KB-fibers, c) square pack KB-fibers, d) hexagonal pack circular fibers, and e) square pack circular fibers with f) comparing permeabilities for all fiber packing arrangements. Where d) and e) were compared to the theoretical permeability value in Equations (2.2) and (2.3).	75
Figure 2.14: Normalized infiltration times for various KB-fiber packing arrangements and orientations relative to hexagonally packed circular fibers at the same fiber volume fractions. This shows the kidney-bean shaped fibers will have a substantially longer infiltration time at high fiber volume fractions relative to circular fibers with hexagonal packing.	77
Figure 2.15: Tortuosity with different fluid flow directions for a) hexagonally pack – 1 KB-fibers, b) hexagonally pack – 2 KB-fibers, c) square pack KB-fibers, d) hexagonally pack circular fibers, and e) square pack circular fibers with f) comparing tortuosities for all fiber packing arrangements.	79
Figure 2.16: Permeability of KB-fibers compared to Equation (2.4) for a) Hexagonal Pack – 1, c) Hexagonal Pack – 2, and e) Square Pack. Permeability of KB-fibers compared to Equation (2.23) for b) Hexagonal Pack – 1, d) Hexagonal Pack – 2, and f) Square Pack.	81
Figure 2.17: Shape factor with different fluid flow directions for a) hexagonally pack – 1 KB-fibers, b) hexagonally pack – 2 KB-fibers, c) square pack KB-fibers, d) hexagonally pack circular fibers, and e) square pack circular fibers with f) comparing shape factors for all fiber packing arrangements.	82

Figure 2.18: Kozeny constants with different fluid flow directions for a) hexagonally pack – 1 KB-fibers, b) hexagonally pack – 2 KB-fibers, c) square pack KB-fibers, d) hexagonally pack circular fibers, and e) square pack circular fibers with f) comparing Kozeny constants for all fiber packing arrangements.	83
Figure 2.19: Upper and lower bound permeability across all KB-fiber unit cells compared to circular fibers with hexagonal packing.	85
Figure 3.1: Particle size distribution for the rapid cure epoxy resins.	92
Figure 3.2: a) Simplified S-wrap impregnation process where tension over rollers are the driving force for impregnation. b) The simplified nip-roll impregnation process where the displacement between the rollers is the driving force for impregnation.	94
Figure 3.3: Hexagonally pack unit cell for a circular (left) and elliptic (right) fiber beds where constriction points between neighboring fibers are considered pores [33].	95
Figure 3.4: Average pore size as a function of fiber volume fraction for various fiber sizes.	96
Figure 3.5: Simplified S-wrap impregnation process where tension over rollers are the driving force for impregnation.	97
Figure 3.6: Representation of inner tangents between two circles (left) and wrap angle of fibers around roller (right). Adapted from [35].	98
Figure 3.7: Hot-melt prepreg line layout in a nip-roller configuration.	100
Figure 3.8: Differential scanning calorimetry isothermal cure curves for a) RCE and b) RCE+IMR resins.	102
Figure 3.9: Isothermal analysis of the 1 st reaction step to determine the A_1 and E_1 for the rapid cure epoxy resin systems.	102
Figure 3.10: Linearization of the auto-catalytic kinetics to determine K_2 and m from the intercept and slope within Region II and identify the reaction and diffusion dominated regions.	104
Figure 3.11: Isothermal analysis to determine the A_2 and E_2 for the rapid cure epoxy resin systems.	104
Figure 3.12: a) RCE and RCE+IMR b) resins isothermal cure $[X]$ comparison to autocatalytic kinetics with WLF diffusion model [-].	105
Figure 3.13: Comparison between the rapid cure epoxy resin with an additional 2.5wt% internal mold-release at 110°C.	107
Figure 3.14: Time to reach $\alpha = 0.5$ for various temperatures showing the 2 nd reaction is delayed but unhindered by the presence of internal mold-release.	108
Figure 3.15: Arrhenius viscosity analysis for the rapid cure epoxy resin systems, where the best fit line only considers 100°C – 120°C RCE data and 110°C – 130°C RCE+IMR data.	109
Figure 3.16: Isothermal viscosity behavior $[X]$ compared with rheological model [-] for the RCE resin (a) and RCE+IMR (b).	110

Figure 3.17: Dynamic mechanical analysis of the a) RCE and b) RCE+IMR resins at 3, 5, and 10°C/min from 50°C – 200°C.....	111
Figure 3.18: Impregnation and cure through an S-Wrap hot-melt process for a rapid cure epoxy resin.....	113
Figure 3.19: Simplified nip-roller impregnation progress between point I (initial contact with roller) and II (end of contact with roller) of the nip-rollers.	115
Figure 4.1: Overview image of the prepreg tape line's 48 position creel (left) and fixed bar fiber spreading unit (right).....	125
Figure 4.2: Overview image of the prepreg tape line's extruder, melt pump, and impregnation die.	126
Figure 4.3: PA-6/Kevlar® prepreg exiting the impregnation die.	126
Figure 4.4: Estimated fiber volume fraction compared to measured fiber volume fraction for different pump to puller ratios. Assuming 26 yarns of Kevlar® were used.	128
Figure 4.5: Example from prepreg ID 16 showing the fiber volume fraction varying at different locations along the prepreg width. The spacing between prepreg strips is a result of the mounting epoxy, not because there is a resin rich layer at the prepreg surface.	129
Figure 4.6: Waterjet cutting profile for unidirectional samples (left) and + 45° samples (right). File naming convention: XX = plate number, YY = fiber orientation (0° or 90°), ZZ = fiber orientation (90° or 0°), T = tensile test, C = compression test, F = 3pt bending test, and S = shear test.....	131
Figure 4.7: Plate 26 after being waterjetted, showing the naming convention used for unidirectional samples.....	132
Figure 4.8: Compression test setup using the standard modified D695 test fixture. Samples are from a failed 0° sample (left) and 90° (right).	136
Figure 4.9: Flexure sample test setup using 3-point bending test fixture with a 33.9mm span..	137
Figure 4.10: PA-6 resin dynamic viscosity vs frequency for temperatures 250 to 290°C. For clarity, the Cross Model (Equation (4.15)) fit is shown for 1Hz and 50Hz, demonstrating the model fit.	141
Figure 4.11: Viscosity vs shear rate as modeled with (4.15) for temperatures ranging from 240°C – 300°C.	141
Figure 4.12: Failed 0° tensile samples from plates 23 and 26. The sample nomenclature is described in Figure 4.6.	142
Figure 4.13: Stress vs strain curve for 0° samples from plates 23 and 26. The sample nomenclature is described in Figure 4.6.	143
Figure 4.14: Rules of mixing for tensile Young's modulus in the fiber direction for Kevlar® 29 and 49 fibers compared to the experimentally measured values for PA-6/Kevlar® prepreg.....	144
Figure 4.15: Failed 90° tensile samples from plates 24 and 25. The sample nomenclature is described in Figure 4.6.....	145

Figure 4.16: Tensile stress vs strain curve for 90° samples from plates 24 and 25. The sample nomenclature is described in Figure 4.6.	146
Figure 4.17: Shear stress vs strain for samples from plate 31 with layup $\pm 45_2S$. The sample nomenclature is described in Figure 4.6.	147
Figure 4.18: Compressive stress vs strain curves for unidirectional 0° samples. The sample nomenclature is described in Figure 4.6.	148
Figure 4.19: Typical failure examples for compression 0° samples (left) in buckling and 90° samples (right) in shear.	149
Figure 4.20: Compressive stress vs strain curves for unidirectional 90° samples. The sample nomenclature is described in Figure 4.6.	150
Figure 4.21: 3-point bending load vs displacement curve for 0° samples from plates 23 and 26. The sample nomenclature is described in Figure 4.6.	151
Figure 4.22: 3-point bending load vs displacement curve for 90° samples from plates 24 and 25. The sample nomenclature is described in Figure 4.6.	152
Figure 4.23: Thermal strain vs temperature curves from plates 24, 25, and 26 for strains in the 0° and 90° directions. The sample nomenclature is described in Figure 4.6.	154
Figure 5.1: Thermoplastic extrusion hot-melt impregnation line layout, where the process moved from left to right.	168
Figure 5.2: Representation of wrap angle of fibers around the die ridge.	170
Figure 5.3: Carreau model description of the viscosity for PA-66 resins. Model parameters were reported in Table 5.2.	172
Figure 5.4: Examples of the a) neat PA-66, b) RT PA-66, and c) GB PA-66 preregs.	173
Figure 5.5: Optical microscopy of neat PA-66 prepreg showing the variability in prepreg thickness and local fiber volume fraction for tension a) level 1 (min), b) level 2, c) level 3, and d) level 4 (max) as described in Table 5.1. Each piece of prepreg was cut into 4 sections.	175
Figure 5.6: Optical microscopy of RT PA-66 prepreg showing the variability in prepreg thickness and local fiber volume fraction for tension a) level 1 (min), b) level 2, c) level 3, and d) level 4 (max) as described in Table 5.1. Each piece of prepreg was cut into 4 sections.	177
Figure 5.7: Optical microscopy of GB PA-66 prepreg showing the variability in prepreg thickness and local fiber volume fraction for tension a) level 1 (min), b) level 2, c) level 3, and d) level 4 (max) as described in Table 5.1. Each piece of prepreg was cut into 4 sections.	179
Figure 5.8: Average pore size for hexagonally packed fibers as a function of fiber volume fraction for various fiber diameters.	181
Figure 5.9: Optical microscopy of neat PA-66/Kevlar® prepreg for tension settings of: a) 2975g, b) 4700g, c) 6200g, and d) 7825g showing the resin was able to consistently saturate the fiber bed at each fiber tension.	182

Figure 5.10: Modeled infiltration profiles with neat PA-66 resin for the fiber beds shown in Figure 5.9. Fiber bed values used in modeling are reported in Table 5.4 and Table 5.5. Tension levels were reported in Table 5.1.	183
Figure 5.11: Optical microscopy of rubber toughened PA-66/Kevlar [®] prepreg for tension settings of: a) 3100g, b) 4600g, c) 6200g, and d) 7675g showing the resin was able to saturate the fiber bed when the fiber bed was suitably thin at each fiber tension.	183
Figure 5.12: Modeled infiltration profiles with RT PA-66 resin for the fiber beds shown in Figure 5.11. Fiber bed values used in modeling are reported in Table 5.4 and Table 5.5. Tension levels were reported in Table 5.1.	184
Figure 5.13: Optical microscopy of GB PA-66/Kevlar [®] prepreg for tension settings of: a) 3200g, b) 4625g, c) 6235g, and d) 7950g showing the resin was only able to saturate the lowest tension while the other tensions were partially saturated.	185
Figure 5.14: Modeled infiltration profiles with GB PA-66 resin for the fiber beds shown in Figure 5.13. Fiber bed values used in modeling are reported in Table 5.4 and Table 5.5. Tension levels were reported in Table 5.1.	185
Figure 5.15: Modeled infiltration profiles for neat, rubber toughened, and glass bead filled PA-66 prepreps at tension level 1.....	186
Figure 6.1: Kidney-bean shaped fiber compaction data compared to circular fibers. The kidney-bean shaped fibers were fitted to Equations (2.1) and (2.22) with the model parameters shown in Table 2.1. Error bars represented replicate error of the compacted tows.	195
Figure 6.2: Examples of fiber packing unit cells with their maximum packing fraction for a) hexagonal pack – 1 KB-fiber, b) hexagonal pack – 2 KB-fiber, c) square pack KB-fiber, d) hexagonal pack circular fiber, e) square pack circular fiber.	196
Figure 6.3: Upper and lower bound permeability across all KB-fiber unit cells compared to circular fibers with hexagonal packing.	197
Figure 6.4: a) RCE and RCE+IMR b) resins isothermal cure [X] comparison to autocatalytic kinetics with WLF diffusion model [-].	198
Figure 6.5: Thermoplastic extrusion hot-melt impregnation line layout, where the process moved from left to right.	199
Figure 6.6: Average pore size for hexagonally packed fibers as a function of fiber volume fraction for various fiber diameters.	200
Figure 6.7: Modeled infiltration profiles for neat, rubber toughened, and glass bead filled PA-66 prepreps at tension level 1.....	201

ABSTRACT

In this doctoral thesis work, the impacts of alternative constituent material's impact on low-cost prepreg manufacturing for high volume applications will be considered. Unidirectional prepreps offer the potential for significant increase of specific-properties and thereby weight savings. Hence the automotive industry is seeking to utilize composite components in their design, in order to meet new fuel economy ratings and global emissions targets imposed by governments. New resin formulations to achieve 3-minute cycle times or low-cost carbon fiber manufacturing have been created to address the needs of the automotive and other cost-sensitive industries, however these innovations have led to challenges in the composites manufacturing process. Quality control issues may include variations in resin saturation of the fiber bed, consolidation, porosity, and fiber volume fraction. These quality issues arise in the part forming step or from the initial resin infiltration during prepregging.

Some low-cost carbon fiber has a kidney-bean shaped cross-section which has implications on the compaction and permeability of the fiber bed. The kidney-bean shaped fibers were shown in this work to follow a different compaction trend compared to circular fibers. Furthermore, these fibers required an order of magnitude larger force to compact than circular fibers to achieve similar fiber volume fraction, which had implications on the infiltration and consolidation step. A shape correction factor based on the fiber cross-sectional aspect ratio was proposed to extend the existing compaction model to fibers with irregular cross-sectional shapes. Additionally, permeability simulations were performed on the kidney-bean shaped carbon fiber in various fiber packing unit cells. Since the kidney-bean shaped fiber had some degree of asymmetry, there are two valid hexagonal packing arrangements. At a minimum, the hexagonal packed unit cell orientation caused a 17% reduction in permeability for the same unit cell and fiber volume fraction between the $\pm 90^\circ$ and 0° orientations. In the most extreme case, a 47% reduction in the permeability was observed between the $\pm 90^\circ$ and 0° orientations. Depending on the fiber orientation, comparable permeabilities to circular fibers were attained or up to a 74% reduction in permeability. This means a selection of low-cost carbon fiber could cause the infiltration time to be up to 3.86 longer than for a traditional carbon fiber.

The low-cost carbon fiber was paired with a rapid cure epoxy resin which contained internal mold-release to further improve part cycle times to 3-minutes and reduce part costs. The

effect of polar and non-polar internal mold-release was studied for its potential influence on cure kinetics. The polar internal mold-release caused a 20 second delay in the 3-minute part cycle, which increased the cycle time by 10% and would therefore influence part production schedules. This prepreg system was reported to have prepreg quality issues related to solids filtering during infiltration. A hot-melt prepregging process was modeled for S-wrap and nip-roller configurations. The S-wrap process was found to better suited for prepregging multi-phase resins since lower pressures were used. Additionally, a general rule was established when working with multi-phase resins was established, particle diameters should not exceed fiber radii.

The general design principles from the thermoset hot-melt prepregging were used to develop a thermoplastic prepreg tape line. Thermoplastic composites lend themselves to efficient manufacturing processes such as hybrid overmolding which is suitable for the automotive industry. polyamide-66/Kevlar[®] prepreg tapes were manufactured at various line tensions. Neat, rubber toughened, and glass bead filled polyamide-66 based resins were considered. The neat polyamide-66 resin provided a baseline and was able to consistently saturate the fiber bed up to 400 μ m regardless of manufacturing conditions. The addition of rubber particles did reduce the infiltration distances from the base resin by 20% with significant a significant 50% reduction when the fiber volume fraction reached 0.70. While the addition of glass particles significantly reduced the infiltration distances by up to 70% across all manufacturing conditions. The reduction in flow distance resulted in poor infiltration in thicker fiber beds.

1. PREPREGGING ESSENTIALS FOR HIGH PERFORMANCE COMPOSITES

Composite materials are attractive to industries where specific-mechanical performance (strength, stiffness) is important. Complex, structural composite parts are often constructed from pre-impregnated composite (prepreg) tape which is an intermediate material-form. The aerospace industry has long been the most notable for incorporating composite materials in their products and led the development of advanced composite materials [1]. Since the 1960's, the aerospace industry has replaced metal parts with an equivalent composite analog in an effort to decrease weight while maintaining or increasing specific-performance (strength, stiffness, or energy absorption to weight ratio) [1]. As such, the resins used were designed for longer cure cycles, to ensure dimensional stability and consistent material properties [1–3]. Furthermore, an aerospace part design will remain in service for decades because of the lengthy design and certification process [2]. Until recently, the aerospace industry was the primary user of composite material. However, new use-cases and industries are embracing lightweight composite material, which do not directly conform to previous norms.

Most prominently, the automotive industry is seeking to utilize composite components in their design, in order to meet new fuel economy ratings and global emissions targets imposed by governments [4]. Composites produced from unidirectional prepreg are appealing to the automotive industry as they are suited for structural applications where significant weight savings can be attained. Yet for composites to be considered by the automotive industry, newly tailored composite materials and material-forms need to be capable of high-volume production and low-cost through improved cycle times, process automation, material flexibility, resin formulations, moldability, and fiber manufacturing [3]. The changes in resin formulation or low-cost fiber manufacturing may create challenges in the composites manufacturing process and cause part quality variations. Quality control issues may include variations in resin saturation of the fiber bed, consolidation, porosity, and fiber volume fraction. These quality issues arise in the part forming step or from the initial resin infiltration during prepregging [5]. During prepregging, the resin content and fiber bed saturation are established from the infiltration process where the thermoplastic/thermoset resin flows into the fiber bed.

1.1 Fundamentals of Infiltration Processes Through Porous Media

The prepregging process involved the flow of resin through a fiber bed. An example of the transverse flow is shown in Figure 1.1. The flow front velocity of the resin during fiber bed impregnation was captured by Darcy's Law. This related the permeability (K), bed thickness (L), viscosity (η), fiber volume fraction (V_f), applied mechanical pressure (ΔP), and capillary pressure (P_c) to the superficial velocity ($\frac{dX}{dt}$) of the flow front at which material moves through a porous medium. The differential form of Darcy's law is shown in Equation (1.1) [6]. This simplified model is applicable when the flow regime has a Reynolds number < 1 , which are typical conditions during the prepregging process.

$$\frac{dX}{dt} = \frac{K(\Delta P + P_c)}{\eta X(1 - V_f)} \quad (1.1)$$

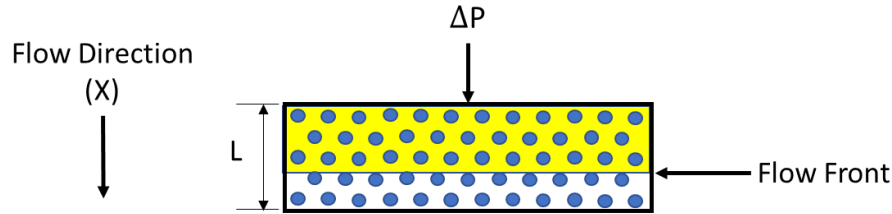


Figure 1.1: Description of resin flowing transversely through an aligned fiber bed.

The fiber volume fraction and pressure have an inverse relationship which was described by Gutowski for circular fibers, where individual fibers were considered beams in bending. The model is shown in Equation (1.9), where A is a constant representing the effective fiber bed stiffness, V_o is the initial fiber volume fraction at 0 pressure, and V_a is the maximum available fiber volume fraction.

$$P = A \frac{\sqrt{\frac{V_f}{V_o}} - 1}{\left(\sqrt{\frac{V_a}{V_f}} - 1 \right)^4} \quad (1.2)$$

For aligned fiber beds, the permeability is inversely related to the applied pressure, as studied extensively by Gutowski, Advani, Dave, and Gebart [7–10]. Several models for fiber bed

transverse permeability dependence on fiber packing have been proposed and are shown in Equations (1.3), (1.4), and (1.5). The Carman-Kozeny model (Equation (1.3)) was popularized since the fiber radius (r) and an empirical Kozeny constant (k) were needed to model the permeability, but the model did not account for the no-flow condition when the fiber bed was at maximum packing.

$$K = \frac{r^2 (1 - V_f)^3}{k V_f^2} \quad (1.3)$$

$$K = \frac{r^2 \left(\sqrt{\frac{V_{a'}}{V_f}} - 1 \right)^3}{4k \frac{V_{a'}}{V_f} + 1} \quad (1.4)$$

$$K = r^2 C \left(\sqrt{\frac{V_{fmax}}{V_f}} - 1 \right)^{\frac{5}{2}} \quad (1.5)$$

Gutowski expanded on permeability model shown in Equation (1.4) by considering the fiber's waviness and redefined the hydraulic diameter as the arch height $\left(2r \left(\sqrt{\frac{V_{a'}}{V_f}} - 1 \right) \right)$ of the fibers where $V_{a'}$ was the maximum available fiber volume fraction to describe the transverse permeability. This provided an appropriate permeability fit for AS-4 carbon fibers with a fiber volume fraction of 0.68 – 0.72 [7]; however, Gutowski did not extend this to a wider range of fiber volume fractions. Gebart proposed a model where the pressure drop was assumed to be caused by the narrow spacing between adjacent fibers was much smaller than the fiber radius. He compared the results of this with finite element analysis for square and hexagonally packed fiber arrays which showed the analytical model (Equation (1.5)) provided an appropriate fit from $V_f = 0.35 - 0.65$. This was true even at low fiber volume fractions where the fiber spacing was comparable to the fiber radius [10]. Additionally, the model accounted for the maximum fiber volume fraction and required an empirically fitted constant, C . All of these permeability models were derived and studied with circular fibers.

The goal of impregnation is to saturate the fiber bed with polymer matrix while minimizing porosity. Composite mechanical properties are inversely related to void fraction [11]. Thus, minimum void content in the final composite part is desired (aerospace rule of thumb is below 1

vol%). Unfortunately, void formation occurs during the impregnation of the fiber bed due to incomplete impregnation or poor wetting of the fibers [12]. Grunenfelder et al. [13,14] showed void content in the final laminate part is highly dependent on the quality of prepreg used. Additionally, they looked at composites processing under vacuum and showed that periodic breaks in the resin film layer allow for better air evacuation and thus lower porosity. Their approach was applicable to processes under vacuum, but would not be suitable for standard compression molding. Barrera-Betanzos, Gabrion, Advani, and Gangloff Jr observed pressure and temperature have little effect on removing voids from a composite part. Instead, the resin saturation of the prepreg greatly influences void removal [15–18]. Prior to impregnation, fiber bed thickness is controlled by spreading fiber tows. Production lines are designed to take advantage of unique properties of the matrix material (viscosity, physical state at room temperature, etc.) to minimize processing time.

Examples of processes exploiting different aspects of Darcy's Law include: wet/dry powder deposition, solution processing, solvent dipping, resin bath, fiber co-mingling, and hot-melt impregnation [19–23]. Research groups choose a manufacturing approach for the ease, simplicity, relevance to industry, application for the material system, or low equipment cost. Of these approaches, powder deposition and fiber co-mingling focus on reducing the distance that the matrix must flow. Solution processing, solvent dipping, and resin baths rely on the resin having a sufficiently low viscosity for resin infiltration. The prepreg manufacturing processes relevant to thermoset resins are discussed in Section 1.2 and processes relevant for thermoplastic resins are discussed in Section 1.3.

1.1.1 Multi-phase Resins

Occasionally, a second phase has been introduced to resins for improved reaction speeds, thermal stability, or fracture toughness. For increased reaction speeds, a heterogeneous catalyst has been introduced to some thermosetting resins [23,24]. As such, the catalyst needed to be well dispersed throughout the resin to promote uniform reaction rates and provide comparable cross-link densities throughout the resin. Inconsistent catalyst dispersal led to variation in mechanical properties (glass transition temperature, modulus, strength) throughout the cured specimen [25]. When properly dispersed, the mechanical properties of the catalyzed and uncatalyzed systems were comparable [26]. Additionally, catalysts often contain expensive metals, such as Titanium [27]; therefore, efficient dispersal of the catalyst was necessary to maintain cost savings.

In addition to improved cure times, resin manufacturers have added internal mold-release (IMR) to reduce mold preparation times. The IMR was used for thermosetting resins and was mixed into the resin prior to prepregging. The desired goal of the internal mold-release was to provide consistent release properties suitable for high volume production [28,29]. The mechanism for mold-release was dictated by the type of mold-release used, metallic salt or wax. The IMR either becomes insoluble and migrates to the part surface or metallic salts migrate to the part surface and form a fatty mono-layer [28–33]. Adding IMR to epoxy resins has been shown to produce similar tensile and flexure properties compared to the neat resin [28,29]. However, some researchers have noted the glass transition temperatures decreased with the addition of certain IMR's [29,30,34], which implied the formation of the molecular network was impacted by these IMR's. Furthermore, Karbhari [29,30] noted minor retardation in peak reaction rates and decrease in total heat of reaction with increased IMR content in epoxy backbone vinyl esters but did not comment on any viscosity changes from the IMR. Since IMR's have been noted to reduce reaction rates, the type of mold-release should be carefully selected and the cure kinetics measured of the resulting resin.

In general, addition of a hard, solid filler improved polymer modulus and dimensional stability of molded parts, but reduced resin toughness [35]. Common solid filler included glass bead, BaSO₄ [36], CaCO₃ [37], silica [38], clay [39], and talc [40]. For mechanical properties, decreased particle diameter improved modulus when the diameter was below 10nm, otherwise particle diameter had little effect on the modulus [41]. For example, nanoclay [39] or nanotalc [40] had been shown to improve the dimensional stability of molded parts. Nanoclay was preferred over nanotalc because of a modest improvement in flexural strength and tensile modulus of 12% and 27%, respectively. Additionally, nanotalc (20-150nm diameter) and fine talc (1.5μm diameter) provided comparable dimensional stability, but the finer particles provided improved flexural modulus for the same talc loading. While modulus was improved, the resins with talc or clay demonstrated poor tensile toughness.

To improve fracture toughness, particles such as polyamide [42–44], rubber [45], polyethersulfone [46–49], polyetherimide [50–52], or polyphenylene oxide [53,54] were added to thermoset or thermoplastic resins. In addition to crack tip blunting, rubber particles have been shown to improve the impact performance of polyamide [55,56], which has important implications for energy absorption during a high speed impact (eg. automobile crash, sports equipment). A

common rubber additive for polyamide was styrene–ethylene–butylene–styrene (SEBS) [55,56]. The primary energy absorption mechanism for relatively ductile particles was plastic deformation as the crack front moved through the matrix. Other energy absorption mechanisms identified by Pearson et al. [53] were crack pinning and patch deflection which caused the crack path to elongate and resulted in additional fracture energy being absorbed by the matrix, but these mechanisms were primarily for hard particles. An example schematic of the toughening mechanisms for particle reinforced epoxy is shown in Figure 1.2.

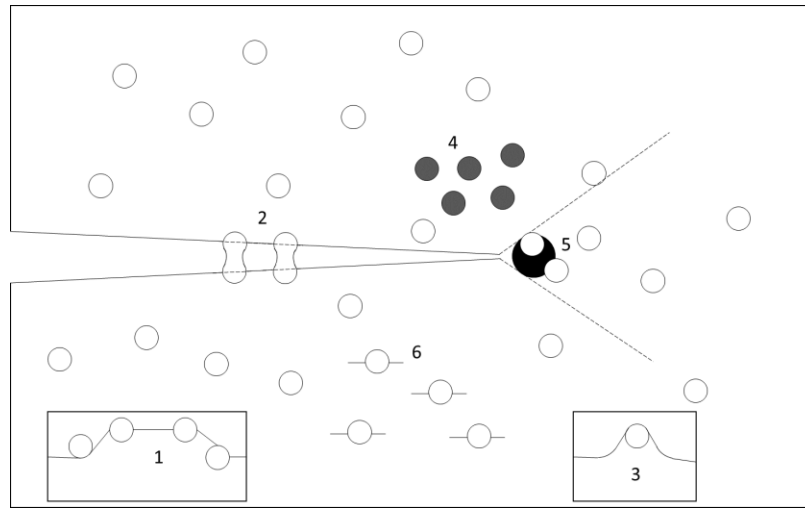


Figure 1.2: Toughening mechanisms in thermoplastic-modified epoxy: 1) crack pinning, 2) particle bridging, 3) crack path deflection, 4) particle yielding, 5) particle-yielding-induced shear banding, and 6) microcracking. Adapted from [53].

In composite laminates, adding a ductile particle at the ply interfaces improved interlaminar fracture properties [50,57–59]. Takeda et al. [59] demonstrated a rubber particle rich interlayer between lamina plies could prevent transverse cracking from spreading through the laminate. The most common way these particles were introduced into the laminate were by preparing a separate resin film layer with the rubber particles and applying this between layers of prepreg [50,58,60,61]. This process of preparing a film between the plies was known as interleaving [62–64]. Typically, the rubber toughened layer was 15 – 30 μm thick with particle diameters from 50nm – 3 μm [45,55]. Placement of the layer ensured the rubber particles remained in the inter-ply regions. While other Liu et al. blended the rubber particles into the resin before infiltrating the fiber bed and noted that the rubber particles were filtered by the fiber bed [57]. The filtration of the rubber particles at the

fiber surface were viewed as an in-situ method for creating a particle rich layer in the inter-ply region. Since the resin was rubber toughened prior to impregnation, the particles have the opportunity to penetrate the fiber bed. Additionally, the study did not vary pressure nor quantify the particles that penetrated the fiber bed. Instead, the particles were assumed to reside in the inter-ply region as well. Since impregnation pressure has been known to change the fiber volume fraction and thus the inter-fiber spacing, the processing conditions during resin impregnation should be investigated for particle penetration into the fiber bed. Furthermore, there may be prepregging conditions paired with suitable particle sizes where particles infiltrate the fiber bed rather than deposit on the fiber surface.

1.1.2 Particle Filtration in Porous Media and Aligned Fiber Beds

Particle retention in porous materials can be broken down into retention sites and retention mechanisms. These mechanisms and sites were in isotropic, porous media were summarized by Herzig et al. [65]. In general, porous materials particle retention sites included: surface, cavern, crevice, and constriction types, which are shown in Figure 1.3. Particle retention at these sites occurred through various retention mechanisms. For surface sites, hydrodynamic effects, direct interception, and diffusion were possible mechanisms for particle retention. Hydrodynamic effects were present when non-spherical particles were flowing through a nonuniform shear field, which caused transverse movement of the particle towards surface sites [65,66]. Direct interception occurred when particle streamlines approached filter medium with half of the particle diameter. While diffusion was present van der Waals forces dominated, when the Peclet number (Pe) $\gg 1$. Where Pe was a ratio of advective transport rate (L , characteristic length and u , velocity) to diffusive rate (D_B) as shown in Equation (1.6) [67]. Additionally, the diffusive rate was inversely related to the fluid viscosity.

$$Pe = \frac{L u}{D_B} \quad (1.6)$$

Cavern sites retained particles primarily through inertial impaction and sedimentation. Inertial impaction occurred when the particle density was greater than the fluid density and the particle centrifugal force caused the particle to leave the streamline. Likewise, sedimentation was

a result of the particles leaving the streamline because of gravitational forces [65,66,68]. Crevice sites strained particles when particle diameters were smaller than the pore size or gap available between walls of the porous material [65,66,69]. Constriction sites captured particles that initially penetrated the porous material, but were trapped when the surrounding material shrank, typically from applied pressure [65,66]. These sites differ from crevice sites since a reversal of flow will not release these entrapped particles whereas a crevice site entrapped particle would be released. In general, particles

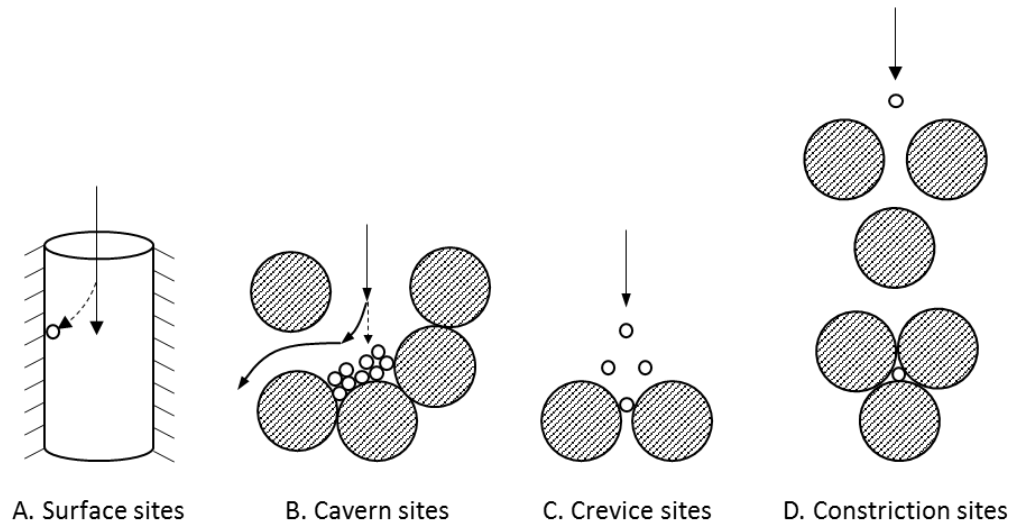


Figure 1.3: Types of particle retention sites in porous, isotropic media. Modified from Herzig et al [65].

From these different retention sites, the most relevant filtration site in aligned fiber beds for most composites manufacturing was straining and constriction. Because flow velocity is very small, resin viscosity is relatively high, the Peclet number will be large. Thus, particle retention at surface and cavern sites are unlikely. Additionally, fibers do not have internal porous cavities for particles to diffuse into. Straining occurred when the local inter-fiber spacing is smaller than the particle's diameter which was attempting to flow through the fiber bed. During sieving, particles accumulated on the porous media surface when the particle diameter was larger than the porous openings. The layer of accumulated particles on the fiber surface grew and formed a cake layer [69,70]. Cake layer formation was an inefficient filtration method, because as the cake layer grew, the resistance to flow also increased. The deposition rate of particles before cake layer formation

was described by the following kinetic equation (Equation (1.7)), where A was the filtration constant, σ was the amount of particles deposited in the pores, and σ_{max} was the maximum particle retention in the pores before cake formation [71].

$$\frac{d\sigma}{dt} = A(\sigma_{max} - \sigma) \quad (1.7)$$

Aligned fiber beds can be considered porous materials, since the inter-fiber spacing represent pores and act as a sieve preventing particles from flowing completely through. Furthermore, the applied mechanical pressure during prepregging to flow molten matrix material through the fiber bed is known to compact the fiber bed [7], increasing the fiber volume fraction while reducing the inter-fiber spacing. Since the inter-fiber spacing affects the permeability and porosity of the fiber bed, the ability for particles to penetrate the fiber bed will be reduced at higher pressures since the crevice site sizes will be reduced. Therefore, the reduction in inter-fiber spacing impacts what sized particles are capable of flowing through aligned fiber beds. Work by Steggall-Murphy et al. [71] considered a suspension of thermoplastic particles (average particle diameter = 20 μ m) flowing through a woven fabric preform. The fluid was evaporated, and the fabric was saturated with epoxy to preserve the particle positions before polishing. The addition of epoxy resin was assumed to not disturb the particle locations, however this was not verified. Steggall-murphy et al. found reasonable agreement with their experimental findings to Equation (1.7) with an A value of 0.021 [71].

For instance, Chohra et al modeled aluminum oxide particles with an average diameter of 40 μ m through an E-glass woven preform via vacuum assisted resin transfer molding. Their purpose was to see how particles will infiltrate a fabric preform, since the tows created overlapping regions with macropores for the particles to infiltrate further into the fiber bed. Since the particles were significantly larger than the inter-fiber spacing, the fiber tows were treated as a sieve preventing particles from infiltrating and therefore formed a cake layer. They described the cake layer formation and resistance to flow using the Ruth equation (Equation (1.8)), where ρ was the density of the particle, α was the average resistance of the cake, m was the ratio of wet to dry cake mass, and $v_f(t)$ was the cumulative cake volume. By including the cake layer formation and resistance to flow, the concentration gradient throughout the woven fabric was modeled.

$$R_c = \frac{\rho \alpha c v_f(t)}{2A(1-mc)} \quad (1.8)$$

While many studies have been conducted on the benefits of polymer filled composites on mechanical properties [50,57–61], they have not investigated the manufacturing conditions on solid particles infiltrating the fiber bed.

1.1.3 Cost Effective Prepreg Solutions - Irregularly Shaped Carbon Fiber

Carbon is predominantly produced from polyacrylonitrile (PAN) fibers with a minor amount being produced from pitch. Typically, carbon fiber cross-sections have a circular shape, however this was not always true. In the 1990's, researchers purposely produce ribbon and “C” shaped carbon fiber to address thermal management issues in composites [72–74]. Where mesophase pitch was melt spun and drawn through a ribbon shaped capillary die. The resulting carbon fiber resembled an ellipse with aspect ratios ranging from 3:1 to 5:1. Additionally, the “C” shaped carbon fiber provided increased surface free energy, which provided better matrix/fiber bonding. The irregularly shaped fibers from mesopitch provided improved conductivity and matrix/fiber bonding, however the technology was not commercially adopted.

In contrast, the cross-sectional shape of carbon fiber produced from PAN fibers was formed during the PAN precursor fabrication [75,76]. The preferred shape of PAN based carbon fiber was circular as this provided the high tensile strength and modulus that carbon fiber was well know for. However, PAN based carbon can have an irregularly shaped cross-section often referred to as a kidney-bean. The fiber shape was formed in the PAN precursor coagulation bath where the polymer solute diffusion and solvent out-diffusion dictated the fiber shape. The diffusion rates for solute and solvent were related to the coagulation bath solvent type, temperature, pH, and solvent concentration. Commonly used solvents were water, dimethyl formamide (DMF) [77], Dimethyl acetamide (DMAc) [76], and dimethylsulfoxide (DMSO) [78]. Depending on the solvent type, bath temperature, pH, and solvent concentration were varied to balance the solute-solvent diffusive flux. In general, bath temperatures ranged from 10 – 70°C, but they were typically between 30 – 60°C. Additionally, the DMF solutions typically contained 72.5 – 87.5wt% solvent while DMSO solutions ranged from 43 – 73wt% solvent. The effect of solvent concentration on PAN fiber shape and morphology is shown in Figure 1.4. The desired solvent concentration varied with pH and temperature. A pH around 6.0 produced circular fibers with decreasing pH producing kidney-bean

shaped fibers [76]. For high strength carbon fiber, low temperatures were preferred, but lower temperatures reduced the diffusion rate and extended the required coagulation time, therefore slowing production speeds.

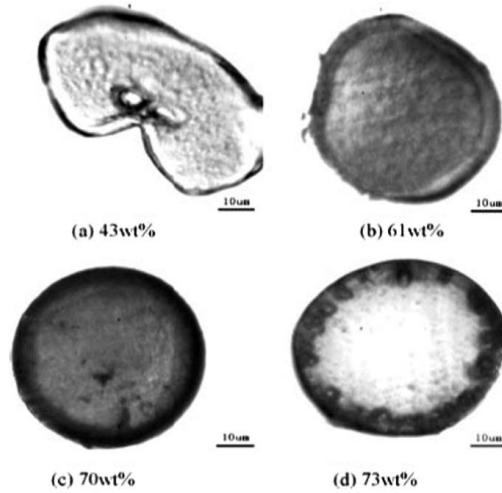


Figure 1.4: Effect DMSO concentration has on PAN fiber cross-sectional shape [79].

The reduced manufacturing speeds increase the manufacturing costs for PAN based carbon fiber [76,80–82]. Additionally, half of the costs for carbon fiber were attributed to the PAN precursor. Hence, manufacturers have endeavored to reduce the coagulation time and increase the production rate of PAN fiber by altering the solvent type, bath temperature, pH, and solvent concentration. As a result, the push for low-cost carbon fiber with comparable mechanical properties to traditional carbon fiber has incentivized manufacturers to produce carbon fiber from lower grade PAN resulting in kidney-bean shaped fiber. With the commercial availability of kidney-bean shaped fibers, the compaction behavior and permeability of these fiber beds must be investigated and compared to circular fibers to inform subsequent composites manufacturing.

1.2 Considerations for Different Thermoset Prepregging Methods

When working with thermosetting resins, such as epoxies, polyesters, polyurethanes, etc., the degree of cure (α) and chemorheology of the resin throughout the process needs to be monitored. As such, cure kinetic models have been used to describe the degree of cure. The most common were n^{th} order and autocatalytic kinetics, shown in Equations (1.9) and (1.10),

respectively. The choice in kinetics model was dictated by the chemistry of the thermosetting resin. The powers m and n represent the reaction order and typically range between 0.5 – 3.0. Both models had a reaction rate constant (k) which was a function of temperature, shown in Equation (1.11). Additionally, the autocatalytic model was sometimes simplified to the form shown in Equation (1.12). The simplification was only valid when the activation energy for the 1st and 2nd step reactions were nearly identical; however, this was not always the case. As such, the autocatalytic form in Equation (1.10) was preferred. Differential scanning calorimetry was the most common method to define the kinetic parameters (Arrhenius frequency factor, A_i and activation energy E_i) and reaction order n and m via isothermal experiments according to ASTM E2070 [83].

$$\frac{d\alpha}{dt} = k(1 - \alpha)^n \quad (1.9)$$

$$\frac{d\alpha}{dt} = (k_1 + k_2\alpha^m)(1 - \alpha)^n \quad (1.10)$$

$$k = A_i e^{-\frac{E}{RT}} \quad (1.11)$$

$$\frac{d\alpha}{dt} = k\alpha^m(1 - \alpha)^n \quad (1.12)$$

The glass transition temperature (T_g) was a measure of the long-range chain mobility and can be used as a measure for the diffusivity of the polymer matrix. The T_g was defined as the observed change in the volume vs temperature slope. Which can be observed through the change in heat capacity, therefore differential scanning calorimetry can be used to determine the T_g . The T_g may also be determined from the change in the storage modulus curve using dynamic mechanical analysis. The T_g can be defined at the onset temperature, midpoint, or endpoint, where the onset was the lowest and endpoint was the highest value [84,85]. For reacting systems (thermosets), an initial glass transition temperature (T_{go}) and final glass transition temperature ($T_{g\infty}$) were needed to describe the polymer system via the DiBenedetto equation (Equation (1.13)) [86]. From this information, the degree of cure advancement can be estimated for the system to determine if the matrix material still has the desired processing window for subsequent process steps.

$$T_g(\alpha) = \frac{T_{go}}{\frac{T_{go}}{T_{g\infty}}\alpha + 1 - \alpha} \quad (1.13)$$

Thermosetting resin viscosities have been known to strongly depend on their degree of cure and sharply rise when near the gelation point (α_{gel}). Gelation was commonly defined as the point where the loss modulus was smaller than the storage modulus, essentially meaning the point at which flow was no longer possible. These resins typically exhibit a minimum dwell viscosity, as shown in Figure 1.5 before gelation occurred and the viscosity rapidly rose. Several models have been proposed to capture the viscosity rise during cure, the Castro-Macosko [87] expression and modified William-Landel-Ferry [88] equation were two examples, shown in Equations (1.14) and (1.15), respectively. Equation (1.14) related the degree of cure with the degree of cure at gelation (α_{gel}) and empirical constants (B and C). In contrast, Equation (1.15) used the time-temperature-superposition principle and related the curing temperature to the glass transition temperature during the curing process. Three fitted constants (c_1 , c_2 , and c_3) were required for this model. These models required the viscosity of the uncured resin (η_o) which was given with Equation (1.16), where η_∞ was the viscosity at infinite temperature, E_η was the activation energy, and R was the ideal gas constant. Both models have been shown to describe the chemorheology of thermosetting resins and the viscosity measurements for thermosetting resins were most commonly performed with a parallel plate rheometer [87–91].

$$\eta = \eta_o \left(\frac{\alpha}{\alpha - \alpha_{gel}} \right)^{B+C\alpha} \quad (1.14)$$

$$\eta = \eta_o + c_3 e^{\frac{-c_1(T-T_g(\alpha))}{c_2+T-T_g(\alpha)}} \quad (1.15)$$

$$\eta_o = \eta_\infty e^{\frac{E_\eta}{RT}} \quad (1.16)$$

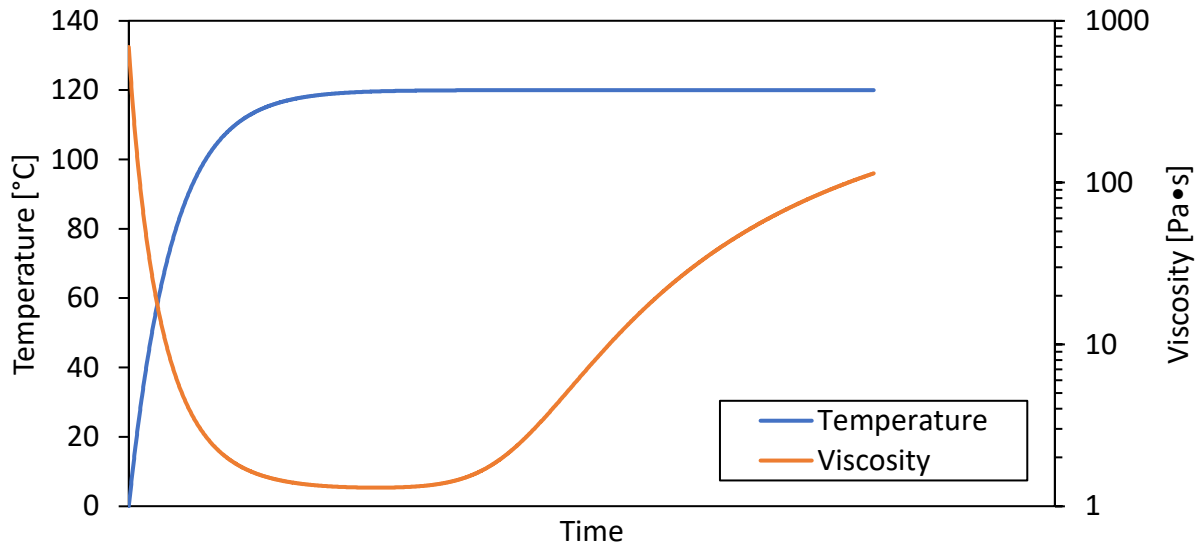


Figure 1.5: Typical viscosity profile for a thermosetting polymer, demonstrating the dwell in viscosity before gelation where viscosity rapidly rose.

Since most thermosetting resins are a liquid at room temperature, the prepregging process for thermosets must advance the reaction enough during manufacturing to prevent the resin from flowing away from the fibers during layup. Typically, the resin is cured enough, such that the glass transition temperature is near room temperature. The process of purposefully advancing the reaction like this is commonly referred to as B-staging and is common practice in industry. When B-staging, it is important to not gel or come close to gelling the resin. Once gelation occurs, the resin can no longer flow, which limits the usefulness of the prepreg for molding parts. Thus, the prepregging process for thermosets has two purposes: saturate the fiber bed with resin and B-stage the resin. It is sometimes helpful to construct a time-temperature-transformation diagram for thermoset resins, as shown in Figure 1.6. Of importance to note is the gelation line, which once crossed, no longer allows the resin to flow. Additionally, this can be helpful to identify how long the resin needs to remain at the processing temperature for adequate T_g development [5].

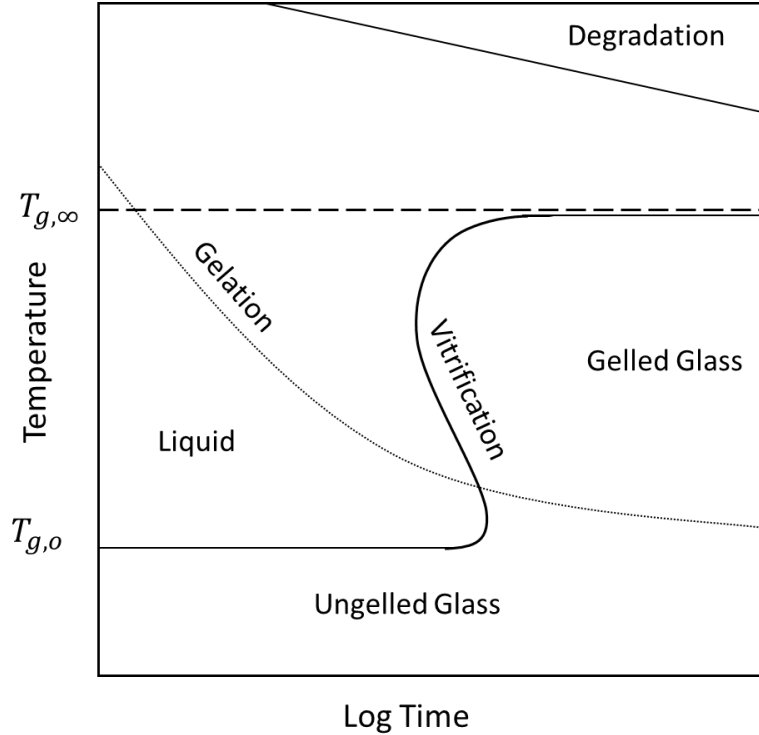


Figure 1.6: Time-temperature-transformation principles diagram for thermosetting polymers [5].

1.2.1 Prepreg Processing: Resin Bath Method

The resin bath prepregging process dragged tensioned fibers through a resin bath along pins to drive the resin into the fiber bed. The general layout for the process is shown in Figure 1.7, where the furnace was used to B-stage the resin [92]. These furnaces were either convection oven or heated die. The length, temperature and processing speed were in careful balance to provide appropriate resin infiltration and cure progression. The driving force for resin infiltration was the tension of the fibers. Section 1.2.2.1 detailed the pressure generation from the tension and Section 1.3.1 reviewed the rise in tension caused by dragging the fibers over static pins.

The process was typically modeled with Darcy's law (Equation (1.1)), cure kinetics (Equation (1.9)), chemorheology ((1.14)), and the heat transfer equation (Equation (1.17)), where T was temperature, ρ was density, C_p was the heat capacity, k was thermal conductivity, H_r was heat of reaction, and m_m was mass of matrix [93]. The process was well suited for resins that had sufficiently low viscosity ($\sim \text{Pa}\cdot\text{s}$) and did not quickly react at prepregging temperatures since the resin may remain in the bath for an extended period of time. Drawbacks of this process included resin waste from the bath and cleaning the bath with solvents between production [92,94].

$$\frac{\rho C_p V \delta T}{\delta x} - \frac{\delta}{\delta x} \left(k_x \frac{\delta T}{\delta x} \right) - \frac{\delta}{\delta y} \left(k_y \frac{\delta T}{\delta y} \right) - H_r \rho m_m \frac{\delta \alpha}{\delta t} = 0 \quad (1.17)$$

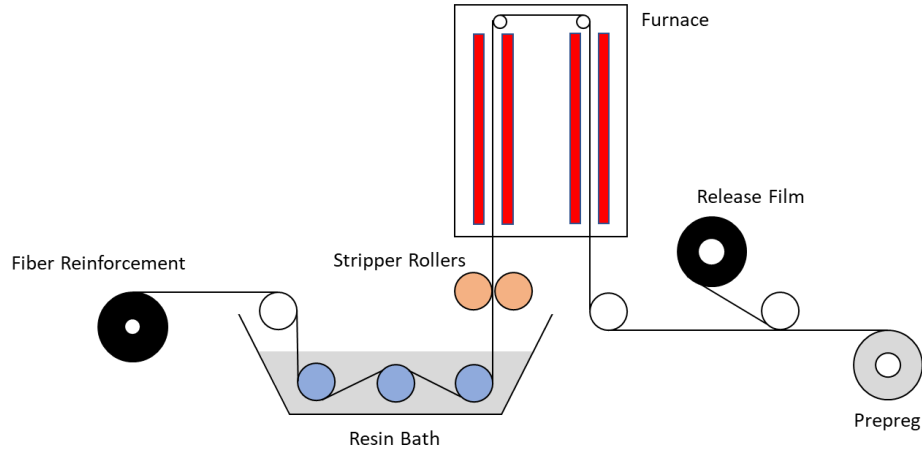


Figure 1.7: Example of the resin bath prepreg tape production process with the vertically oriented furnace. Adapted from [95].

Typically, thermosetting resins have a suitably low viscosity for infiltration of the fiber bed, lower viscosities have been required when working with some fabrics as the applied mechanical pressure can distort the fiber orientation. Therefore, reducing a material's viscosity by dissolving the matrix in a solvent was attempted. The process was often referred to as solvent dipping. The solvent dip process was similar to the resin bath method. The solvents were removed in-line, typically with a furnace to evaporate them. The furnace from the resin bath would either need to be elongated or speeds reduced to ensure the solvent was removed. Unfortunately, the solvents used posed environmental concerns or reduced matrix performance [63,92,96–98]. Thus, the practice is not common today.

1.2.2 Prepreg Processing: Hot-Melt Thermoset Prepregging

The hot-melt processes are attractive for their higher throughput and simplicity, but are restricted to processing only low viscosity resins [92,99–101]. For the thermoset hot-melt prepreg process, a resin film was placed on the top and bottom of the fibers, then sent through a series of compaction rollers, as shown in Figure 1.8 to drive the resin into the fiber bed. The temperature of the process was carefully controlled to allow for sufficiently low resin viscosity and B-staging to occur [92,99–101]. These rollers can be arranged in a S-wrap or nip-roller configuration. In the S-

wrap configuration, fiber tension, tape width, and wrap angle around the roller determined the pressure driving the resin film into the fiber bed. In contrast, the nip-roller configuration generated pressure through the displacement caused by the distance between the rollers. After infiltration, the prepreg tape must be cooled, typically via a chilled table to quench the reaction.

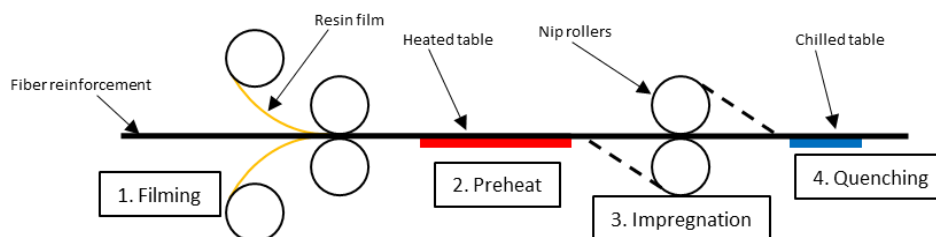


Figure 1.8: Hot-melt prepreg line layout for thermoplastic resin. Where dashed lines represent the option to switch to an S-wrap configuration.

The resin films can be prepared beforehand and typically placed on backing paper. An example of the hot-melt prepreg process is shown in Figure 1.8, where the resin was filmed in a separate step from the hot-melt process [95]. The benefit of the hot-melt process was the resin was not wasted like in the resin bath process, since there was no leftover resin. The prepared resin films need to be refrigerated and have a shelf life of approximately 8 weeks. Since the resin film storage can become expensive and risk expiring, some manufacturers will opt to produce the resin in-line with the prepreg process.

A pilot hot-melt prepreg line at Scale-Up Research Facility (SURF) in the Corktown district of Detroit, MI was used to trial prepreg production of a rapid cure epoxy resin with kidney-bean shaped fibers. The facility was supported by the Institute for Advanced Composites Manufacturing Innovation (IACMI). The hot-melt prepreg line used a Litzler brand line to produce novel prepreg materials.

1.3 Thermoplastic Prepregging Methods

Thermoplastics have a much higher viscosity ($\sim 100 \text{ Pa}\cdot\text{s}$) compared to thermosets ($\sim 1 \text{ Pa}\cdot\text{s}$). Additionally, the dynamic viscosity of thermoplastic resins typically exhibited shear thinning behavior. Resins such as polyamide-6 (PA-6) [102], polyethylene (PE) [103], polypropylene (PP) [103–105], and poly-ether-ether-ketone (PEEK) [106] were a few notable

examples. To describe these shear thinning fluids, there were two common models, the Cross model [107] and the Carreau model [108], which are shown in Equations (4.15) and (1.19), respectively. Both models considered the zero shear ($\eta_{0,shear}$) and infinite shear ($\eta_{\infty,shear}$) viscosities, power-law index (n), time constant (λ), and strain rate (γ). Equation (1.19) was sometimes simplified to the form shown in Equation (1.20) for thermoplastics since the infinite shear rate viscosity was negligible compared to the zero shear viscosity.

$$\eta_D(T, \gamma) = \frac{\eta_{0,shear} - \eta_{\infty,shear}}{1 + (\lambda\gamma)^n} + \eta_{\infty,shear} \quad (1.18)$$

$$\eta_D(T, \gamma) = (\eta_{0,shear} - \eta_{\infty,shear})(1 + (\lambda\gamma)^2)^{\frac{n-1}{2}} + \eta_{\infty,shear} \quad (1.19)$$

$$\eta_D(T, \gamma) = \eta_{0,shear}(1 + (\lambda\gamma)^2)^{\frac{n-1}{2}} \quad (1.20)$$

Because of the much larger viscosity, several prepregging routes have been developed for thermoplastics, which included hot-melt, fiber co-mingling, solution processing, emulsion processing, and powder processing [19–21]. Hot-melt (Section 1.3.1) utilized an impregnation and worked well for thermoplastics with relatively lower viscosity (certain PE, PP, and PA). The fiber co-mingling (Section 1.3.2) and powder deposition (Section 1.3.4) attempted to reduce the flow distance required for impregnation. The emulsion (Section 1.3.4.2) processing suspended resin particles in a fluid to deposit into the fiber bed. Solution (Section 1.3.2) processing used solvents to dissolve and reduce the viscosity of the thermoplastic resin.

1.3.1 Prepreg Processing: Hot-Melt Thermoplastic Prepregging

In hot-melt prepregging, the thermoplastic resin typically infiltrated the fiber bed via an impregnation die, which was fed from an extruder. These dies allowed for a large range of thermoplastic resins to be used, such as PE, PP, and PA [99]. The main limitation for a hot-melt impregnation die was the resin viscosity and thermal stability [109]. Therefore, resins with a high viscosity, such as PEEK or resins susceptible to degradation, like polyphenylene sulfide (PPS) were typically impregnated with other methods [106]. The driving force for impregnation with the die was similar to the S-wrap hot-melt configuration, except the tension increased as the fibers traveled through the die, since the fibers were dragged over fixed bars or ridges.

The impregnation die typically had a wave plate design where the fibers would be dragged along the ridges of the die. Rollers were impractical because of the temperatures and exposure to resin. The entrapped resin between the fiber and die body would be driven into the fibers by the fiber tension and wrap angle. The prepreg thickness was determined by the exit geometry of the die. Some dies were equipped with lip screws to adjust the exit thickness of the die. Typical prepreg thicknesses ranged between 0.127 – 1 mm for unidirectional prepreg [92,94].

Since the ridges were static, the tension increased proportional to the drag force the resin imparted on the moving fibers. The tension (T) across the ridge can be described by the fluid drag forces used to describe the drag force in Stokes flow (Reynolds number $\ll 1$), shown in Equation (1.21). Where η was the fluid viscosity, θ was the wrap angle (in radians) around the ridge, V was the fiber speed, and h_o was the initial resin film thickness [22,110,111].

$$T(\theta) = T_o + \frac{\eta \theta V r w}{h_o} \quad (1.21)$$

A variation of the hot-melt process using a double belt press was used for PPS [112], PA [113] and PP [114] resin films. The belts drove the resin into the fibers via a heated press where the distance between the belts were fixed or decreased [113]. Belt gaps were reported up to 2.5mm [112,113]. The double-belt press would replace the impregnation die with the rest of the hot-melt process unchanged. A schematic of the double-belt press impregnation unit is shown in Figure 1.9. The pressure generated in this process was similar to a nip-roller, where the physical gap between the belts caused a compressive force and drove resin into the fibers.

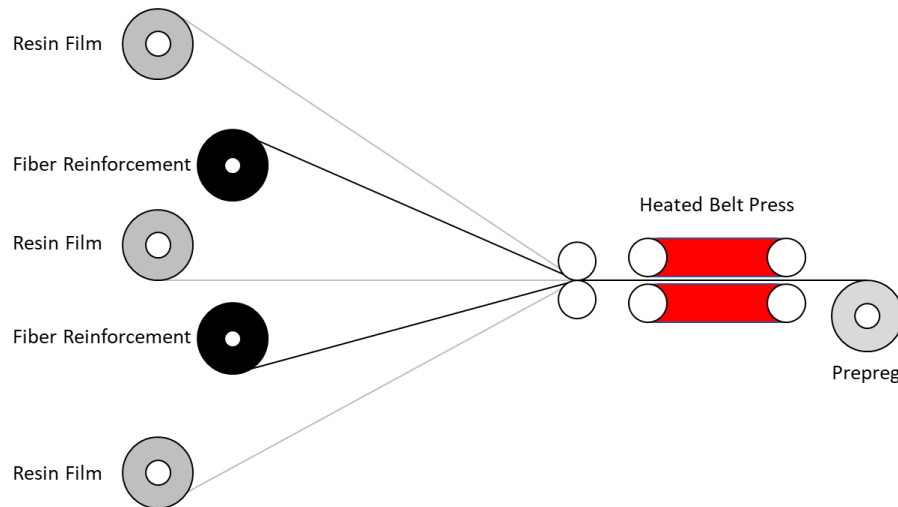


Figure 1.9: Schematic of the double belt press impregnation unit. Adapted from [115].

1.3.2 Prepreg Processing: Solution Processing

Thermoplastic resin viscosities can be lowered through dissolving them in select solvents and go through the resin bath impregnation route described in Section 1.2.1. The process must be amended with a dryer unit, as shown in Figure 1.10, to remove as much solvent as possible. A common solvent used to dissolve polyetherimide (PEI) [116,117], polyethersulfone (PES) [21,109], polyimide [109], polyamide [118], and polyester [119] was 1-methyl-2-pyrrolidinone (NMP). The resin concentration in NMP solution ranged from 15 – 50 wt%. The researchers all noted some combination of the following issues: insufficient solvent removal, reduced T_g , altered crystallinity, and environmental concerns related to the solvent. When the solvent was removed, some voids formed in the prepreg which persisted through consolidation. Goodman et al. noted the solvent removal took 6 hours at 275°C to be “fully dried”. In actuality, complete removal of the solvent was impossible and the glass transition temperature was reduced.

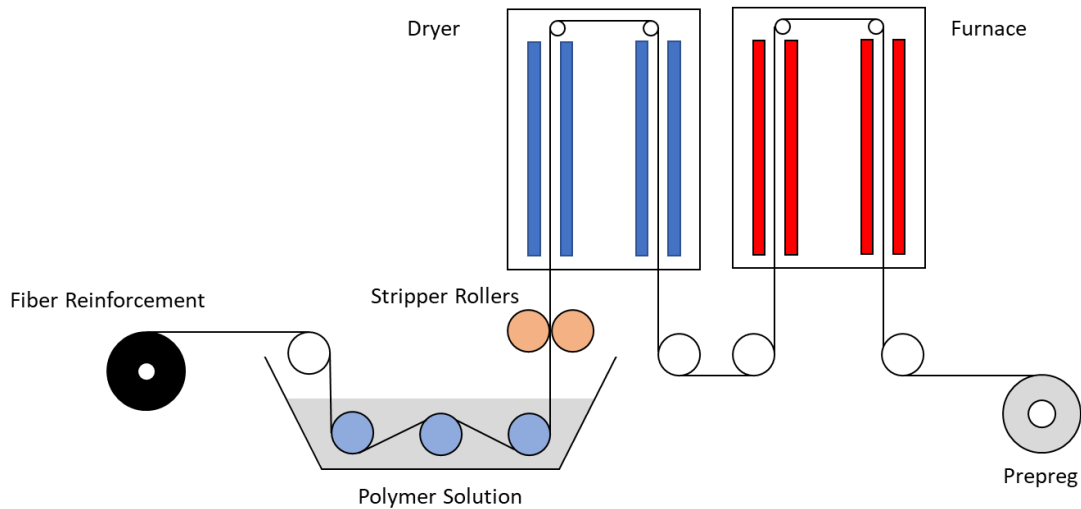


Figure 1.10: Solution processing prepreg manufacturing diagram.

Solution processing was initially used because of the ability to reduce the viscosity of thermoplastic polymers with exceptionally high viscosities. Unfortunately, when using this process, the properties of the polymer were diminished. While, this process negatively impacts the performance of the resin and environmental impacts, this process line is still available through Litzler Co.

1.3.3 Prepreg Processing: Fiber Co-Mingling

Since thermoplastics were capable of being spun into fibers, these plastic fibers were mixed with reinforcing fibers to reduce the flow distance [23,120–125]. The thermoplastic filament surrounds individual yarns of reinforcing fiber. The co-mingled fibers were heated and the resin flowed into the yarns. An example of the microstructure from co-mingled fibers to consolidation is shown in Figure 1.11 [122]. Common thermoplastic filaments used were PP [23,121,124,125], PEEK [120], PA [122], and poly-lactic acid (PLA) [123]. For this process, efficient spreading of the reinforcing fibers and the thermoplastic filaments was the critical for intimate co-mingling of the fibers [125]. Compressed air was commonly used to spread the fibers. Additionally, it was noted that smaller thermoplastic filament and reinforcing fiber bundles allowed for better fiber co-mingling. After co-mingling, the fibers were sent through a double-belt press to saturate the fiber bed. The main drawback of fiber co-mingling was the cost. Since the thermoplastic must be spun into fibers and then sent through an impregnation process.

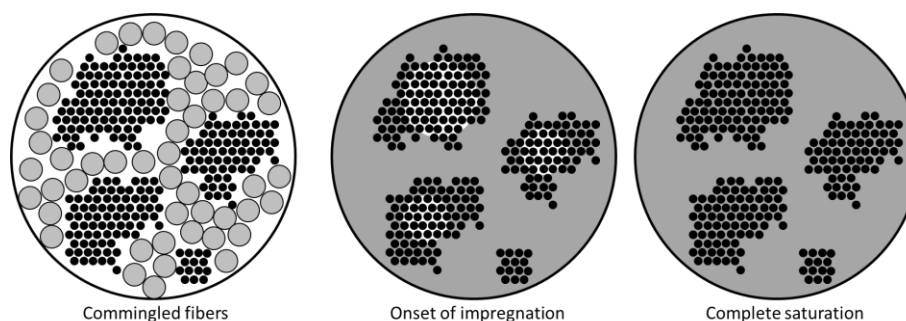


Figure 1.11: Representative commingled yarn cross-section and assumed consolidation mechanism. Adapted from [122].

Void content up to 7.4 vol% was reported with glass fiber co-mingled with polypropylene, however slower processing speeds reduced the void content to 2.2 vol% [23]. The high void content may have been caused by large filament diameters or heavy yarns and the authors did not comment what size filament and yarn were used. While void content in PEEK/carbon fiber and PA-12/carbon fiber was reported below 1 vol% after consolidation [120,122]. PEEK fibers with a 20 μ m filament size and 3k carbon fiber tows were co-mingled with carbon fiber to produce plies with an areal weight 145 – 213 g/m². The small filament and carbon fiber count was noted to have some fiber alignment issues [22,120,126]. In general, fiber co-mingling was reserved for high viscosity resins like PEEK where hot-melt impregnation was not feasible.

1.3.4 Prepreg Processing: Powder Deposition

Similarly to fiber co-mingling, powder deposition also sought to reduce resin flow distances by depositing thermoplastic powder into the fiber bed. The powder has been introduced to the fiber bed either as a dry or wet powder. For dry powder processes, a fluidized bed was commonly used and sometimes the powder would be electrostatically charged to promote particle capture within the fiber bed. For wet powder processes, a slurry is formed with the thermoplastic resin. The slurry remained in suspension via mixing and a recirculation pump. Typically, these process required the particle diameters to be less than 30 μ m [127]. Additionally, thermoplastics with lower T_g 's either required cryogenic grinding or the use of reactor powders to achieve desired particle diameters [22,111,128–130]. The necessity for small resin particle diameters increased the cost of the resin for this process.

Additionally, the correct sizing of the fiber became increasingly important for effective consolidation and minimum void content. Fiber sizing is a surface treatment of the fiber to promote bonding since thermoplastic resin does not chemically bond to the fibers. The sizing needed to be selected for the specific thermoplastic resin used (PP vs PA), since the chemistry of the resin dictated what intermolecular forces were present for secondary bonding. These chemistries also effected the fiber wetting which was crucial for consolidation [20,22,111,129,131]. An example of good and bad poor fiber wetting is shown in Figure 1.12. Poor fiber wetting led to increased porosity.

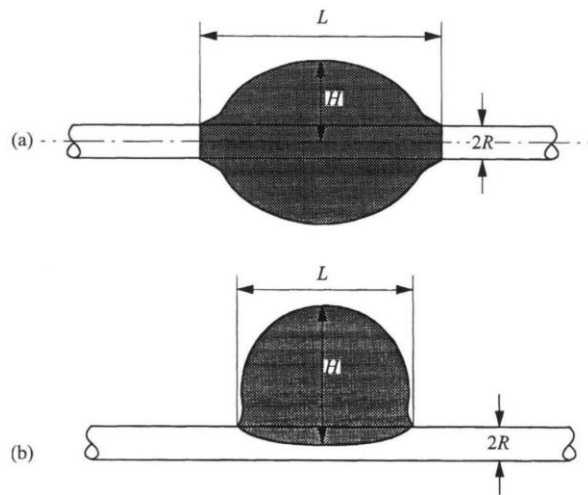


Figure 1.12: Examples of a) good fiber wetting and b) poor fiber wetting from [129].

1.3.4.1 Dry Powder Deposition

Dry thermoplastic powders were retained by the fiber bed either by mechanical entrapment or electrostatic forces. The general process layout for dry powder deposition is shown in Figure 1.13, where the fibers were spread either by fixed bar spreaders or compressed gas blown through the fiber bed. The fibers would pass through a fluidized bed of thermoplastic particles which could penetrate the fiber bed and be retained through a sieving process. From there, the particle laden fiber bed would go through a heated consolidation chamber and resulting tape rolled up [19,20,132–135]. Alternatively, the bed of fluidized particles can be attached to an electrostatic spray nozzle and the particles are sprayed onto the fiber bed [19,71,127,136–140]. For this process, the fibers must pass over a grounding roller, or else the fibers will develop a potentially hazardous static charge. The voltage used to statically charge the powder must at least be 30kV [140].

Additionally, particle retention was improved up to 50kV after which there was no benefit of additional voltage for resin retention [139–142]. The static charge on the particles improved adherence to the fiber bed and allowed for larger particles to be used, up to 200 μ m in diameter.

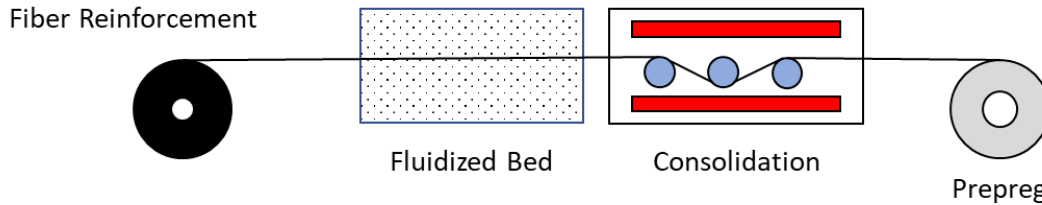


Figure 1.13: Dry powder deposition diagram for thermoplastic prepreg tape production.

1.3.4.2 Wet Powder Deposition (Slurry)

Wet powder deposition is a combination of the solution processing method in Section 1.3.2 and dry powder deposition. A suspension or slurry of the thermoplastic powder with water was formed. Water was the preferred solvent of choice because of its low viscosity, health impacts, and cost [19]. An emulsifying agent was typically added to the solvent to improve settling times. An overview of the wet powder deposition process is shown in Figure 1.14, where fibers were dragged over pins through a polymer slurry to drive the polymer suspension into the fiber bed [19,106,120,128,130,143–147]. The suspension was recirculated through a mixing tank with a peristaltic pump. A set of stripper rollers was used to remove the excess solvent from the fiber surface. The solvent was removed in a dryer where the temperature was above the T_g of the resin, but below the melting temperature. These processing conditions were important to allow the solvent to evaporate and not become trapped by molten polymer. The polymer was sent through an oven to melt and consolidate the resin. The process of heating and melting the polymer was also referred to as densifying.

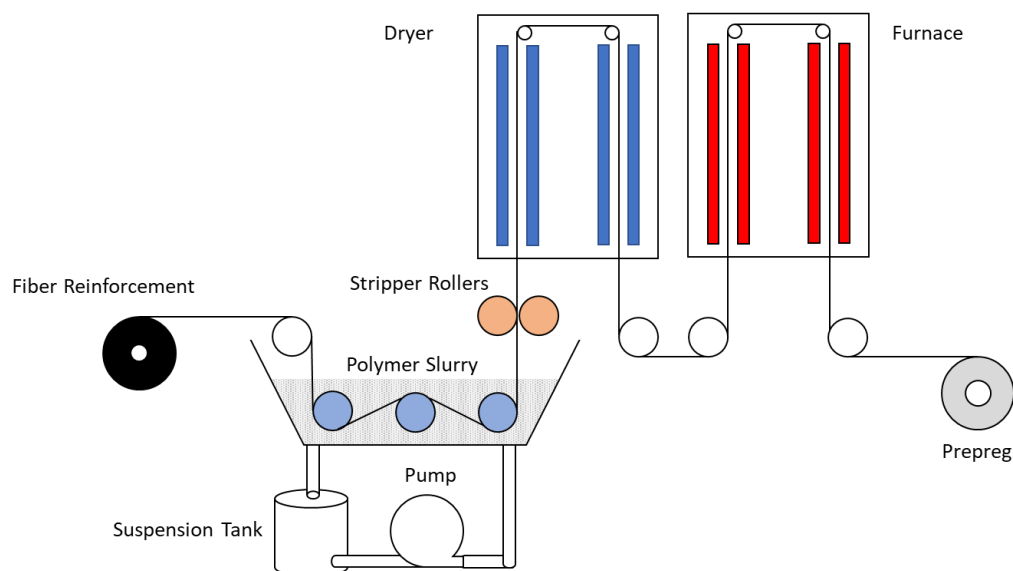


Figure 1.14: Wet powder deposition diagram for prepreg tape production.

Unlike solution processing, the solvent was generally able to be removed before consolidation. While the solvent was removed, the dispersant used would remain and potentially impact the mechanical properties of the resin. For instance, in PE 1wt% of dispersant did not influence the mechanical properties while 3wt% led to a decrease in specific strength [146]. The suspended polymer concentrations ranged from 5 – 10wt%. This process does provide benefits over the solution process since the solvent was more easily removed and there was less impact on the mechanical properties. Because of the risk of reduced mechanical properties and additional costs related to the drying and grinding of resin, this was generally not preferred over hot-melt. Today, this process line is available by Litzler Co.

1.4 Research Objectives

In the pursuit of reducing the costs of polymer-composite based parts, epoxy resin formulations have been altered for 2-minute cure times and introduced internal mold-release to reduce mold preparation times. Additionally, carbon fiber manufacturers are working with low-cost process for PAN fibers, resulting in kidney-bean shaped carbon fiber. Also, fillers have been added to resins to improve cure times, resin stiffness, thermal stability, or resin toughness. These changes to material properties solved certain manufacturing or performance deficiencies, but these improvements may have unforeseen consequences. The impact of the internal mold-release on the

cure kinetics was unknown. Likewise, the carbon fiber's kidney-bean shape on compaction and permeability was unknown. Finally, the manufacturing conditions for particle infiltration into fiber beds was unknown.

This work will address four issues regarding different aspects and considerations during composites manufacturing.

1. What is the compaction behavior of kidney-bean shaped carbon fiber?
2. What effect does the packing arrangement and unit cell orientation of kidney-bean shaped fibers have on fiber bed permeability?
3. How does the presence of non-polar and polar internal mold-releases impact the cure kinetics of epoxy resins?
4. During hot-melt prepregging, what effect does fiber tension have on resin and particle infiltration into the fiber bed for hard and ductile particles?

In this doctoral thesis work, aspects of the fiber and matrix are characterized to model thermoset and thermoplastic hot-melt impregnation processes. An experimental study of the compaction behavior of kidney-bean shaped carbon fiber and simulation of the fiber's permeability was conducted. The results of those studies are presented in Chapter 2. A rapid cure epoxy resin with internal mold-release was characterized for its cure kinetic and chemorheological behavior. The characterized material was modeled through a hot-melt impregnation process. The results of this work are presented in Chapter 3. A thermoplastic hot-melt prepreg line was designed and built to produce 75mm wide prepreg tape and study manufacturing effects on particle infiltration. A validation study of the line and resulting prepreg characterization is presented in Chapter 4. The particle infiltration study of rubber and glass bead filled resins is presented in Chapter 5. Final conclusions of this PhD work are presented in Chapter 6. The layout and flow of the thesis is shown in Figure 1.15.

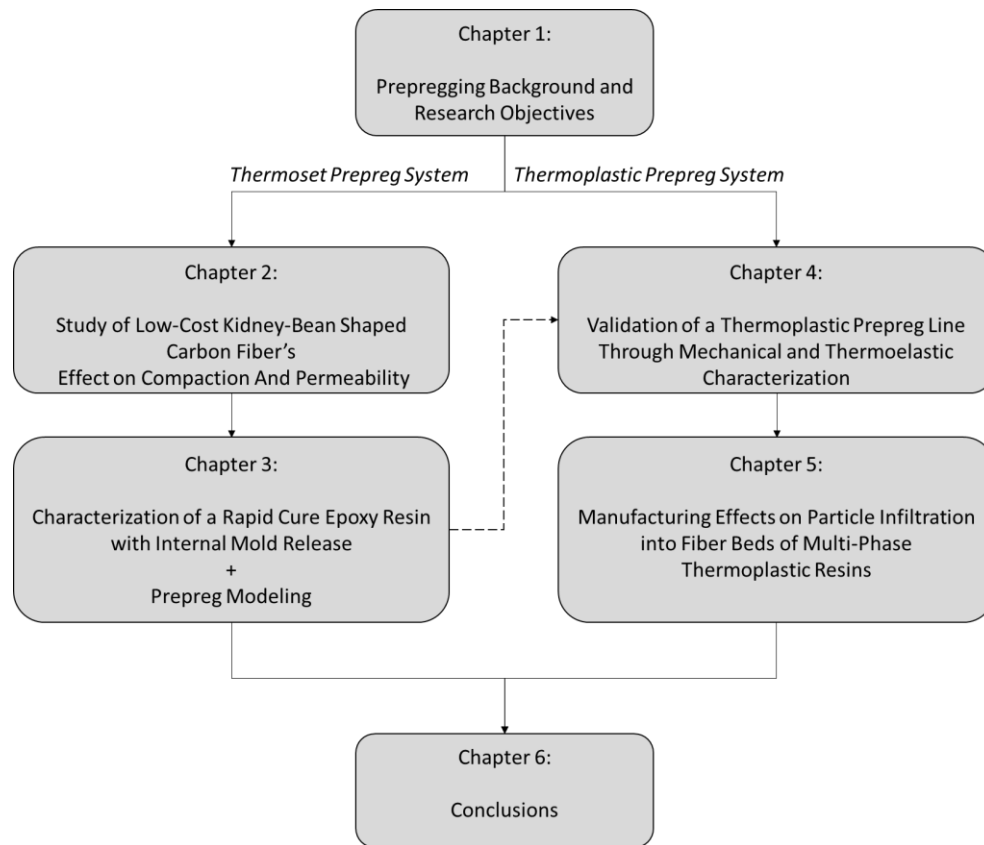


Figure 1.15: Thesis layout and main chapter emphases.

1.5 References

- [1] Edwards T. Composite Materials Revolutionise Aerospace Engineering. *Ingenia* 2008;24–8.
- [2] Barbosa GF, Carvalho J. Analytical model for aircraft design based on Design for Excellence (DFX) concepts and use of composite material oriented to automated processes. *Int J Adv Manuf Technol* 2013;69:2333–42. <https://doi.org/10.1007/s00170-013-5211-7>.
- [3] Martensson P, Zenkert D, Akernö M. Effects of manufacturing constraints on the cost and weight efficiency of integral and differential automotive composite structures. *Compos Struct* 2015;134:572–8. <https://doi.org/10.1016/j.compstruct.2015.08.115>.
- [4] Code of Federal Regulations (CFR) 2015, Title 40 - Protection of Environment, Parts 1 to 1899. Office of the Federal Register OFR; 2015.
- [5] Manson J-AE, Wakeman MD, Bernet N. Composite Processing and Manufacturing—An Overview. *Compr Compos Mater* 2000;577–607. <https://doi.org/10.1016/b0-08-042993-9/00167-4>.

- [6] Lam RC, Kardos JL. The permeability and compressibility of aligned and cross-ply carbon-fiber beds during processing of composites. *Polym Eng Sci* 1991;31:1064–70. <https://doi.org/10.1002/pen.760311411>.
- [7] Gutowski TG, Cai Z, Bauer S, Boucher D, Kingery J, Wineman S. Consolidation Experiments For Laminate Composites. *J Compos Mater* 1987;21:650–69. <https://doi.org/10.1177/002199838702100705>.
- [8] Sadiq TAK, Advani SG, Parnas RS. Experimental Investigation Of Transverse Flow-Through Aligned Cylinders. *Int J Multiph Flow* 1995;21:755–74. [https://doi.org/10.1016/0301-9322\(95\)00026-t](https://doi.org/10.1016/0301-9322(95)00026-t).
- [9] Dave R, Kardos JL, Dudukovic MP. A Model For Resin Flow During Composite Processing .1. General Mathematical Development. *Polym Compos* 1987;8:29–38. <https://doi.org/10.1002/pc.750080106>.
- [10] Gebart BR. Permeability of unidirectional reinforcements for RTM. *J Compos Mater* 1992;26:1100–33. <https://doi.org/10.1177/002199839202600802>.
- [11] Liu L, Zhang BM, Wang DF, Wu ZJ. Effects of cure cycles on void content and mechanical properties of composite laminates. *Compos Struct* 2006;73:303–9. <https://doi.org/10.1016/j.compstruct.2005.02.001>.
- [12] Patel N, Rohatgi V, Lee LJ. Micro Scale Flow Behavior And Void Formation Mechanism During Impregnation Through A Unidirectional Stitched Fiberglass Mat. *Polym Eng Sci* 1995;35:837–51. <https://doi.org/10.1002/pen.760351006>.
- [13] Grunenfelder LK, Dills A, Centea T, Nutt S. Effect of prepreg format on defect control in out-of-autoclave processing. *Compos Part a-Applied Sci Manuf* 2017;93:88–99. <https://doi.org/10.1016/j.compositesa.2016.10.027>.
- [14] Grunenfelder LK, Centea T, Hubert P, Nutt SR. Effect of room-temperature out-time on tow impregnation in an out-of-autoclave prepreg. *Compos Part a-Applied Sci Manuf* 2013;45:119–26. <https://doi.org/10.1016/j.compositesa.2012.10.001>.
- [15] Betanzos FB, Gimeno-Fabra M, Segal J, Grant D, Ahmed I. Cyclic pressure on compression-moulded bioresorbable phosphate glass fibre reinforced composites. *Mater Des* 2016;100:141–50. <https://doi.org/10.1016/j.matdes.2016.03.108>.
- [16] Gabrion X, Placet V, Trivaudey F, Boubakar L. About the thermomechanical behaviour of a carbon fibre reinforced high-temperature thermoplastic composite. *Compos Part B Eng* 2016. <https://doi.org/10.1016/j.compositesb.2016.03.068>.
- [17] Gangloff JJ, Cender TA, Eskizeybek V, Simacek P, Advani SG. Entrapment and venting of bubbles during vacuum bag prepreg processing. *J Compos Mater* 2017;51:2757–68. <https://doi.org/10.1177/0021998316676325>.

- [18] Gangloff JJ, Hwang WR, Advani SG. The investigation of bubble mobility in channel flow with wavy porous media walls. *Int J Multiph Flow* 2015;70:1–14. <https://doi.org/10.1016/j.ijmultiphaseflow.2014.11.005>.
- [19] Ramani K, Woolard DE, Duvall MS. An electrostatic powder spray process for manufacturing thermoplastic composites. *Polym Compos* 1995;16:459–69. <https://doi.org/10.1002/pc.750160604>.
- [20] Iyer SR, Drzal LT. Manufacture of Thermoplastic Composites. *J Thermoplast Compos Mater* 1990;3:325–55.
- [21] Goodman KE, Loos AC. Thermoplastic Prepreg Manufacture. *J Thermoplast Compos Mater* 1990;3:34–40. <https://doi.org/10.1177/089270579000300104>.
- [22] Connor M, Toll S, Manson JAE, Gibson AG. A Model For The Consolidation Of Aligned Thermoplastic Powder Impregnated Composites. *J Thermoplast Compos Mater* 1995;8:138–62.
- [23] Liu D, Ding JP, Fan XY, Lin XY, Zhu YD. Non-isothermal forming of glass fiber/polypropylene commingled yarn fabric composites. *Mater Des* 2014;57:608–15. <https://doi.org/10.1016/j.matdes.2014.01.027>.
- [24] Li M, Gu YZ, Zhang ZG, Sun ZJ. A simple method for the measurement of compaction and corresponding transverse permeability of composite prepregs. *Polym Compos* 2007;28:61–70. <https://doi.org/10.1002/pc.20255>.
- [25] Schichtel JJ, Chattopadhyay A. Modeling thermoset polymers using an improved molecular dynamics crosslinking methodology. *Comput Mater Sci* 2020;174:109469. <https://doi.org/10.1016/j.commatsci.2019.109469>.
- [26] Simon SL, Gillham JK. Cure kinetics of a thermosetting liquid dicyanate ester monomer high-tg polycyanurate material. *J Appl Polym Sci* 1993;47:461–85. <https://doi.org/10.1002/app.1993.070470308>.
- [27] Slot TK, Natu V, Ramos-Fernandez E V, Sepúlveda-Escribano A, Barsoum M, Rothenberg G, et al. Enhancing catalytic epoxide ring-opening selectivity using surface-modified Ti₃C₂T_x MXenes. *2D Mater* 2021;8:035003. <https://doi.org/10.1088/2053-1583/abe951>.
- [28] Mishra R, Behera BK, Rajpurohit AN, Behera P, Petru M, Muller M. Effect of internal mold release agent on flexural and inter laminar shear properties of carbon and glass fabric reinforced thermoset composites. *Polym Adv Technol* 2021;32:282–93. <https://doi.org/10.1002/pat.5084>.
- [29] Karbhari VM, Chhabra G. Effect of resin system parameters on resin transfer molding of vinyl ester based composites—a statistically designed study. *Polym Plast Technol Eng* 1995;34:599–620. <https://doi.org/10.1080/03602559508012207>.

- [30] Karbhari VM. Effect of internal mold release agent on the cure and property variation in resin transfer molding composites. *J Mater Sci Lett* 1998;17:2061–2. <https://doi.org/10.1023/A:1006663612780>.
- [31] Serré C, Vayer M, Erre R. Behavior of internal mold release agent during BMC thermosets composites cure and aging. *J Mater Sci Lett* 2001;20:1989–91. <https://doi.org/10.1023/A:1013107407505>.
- [32] Bjeković R, Piotrowicz K. Epoxy resin and release agents part I: Influence of external and internal release agents on the adhesive properties of epoxy resin. *J Appl Eng Sci* 2015;13:45–50. <https://doi.org/10.5937/jaes13-7210>.
- [33] Briscoe BJ, Khan MB, Richardson SM. Rotary injection reaction injection molding (RI-RIM). Part II: Interfacial segregation of release systems. *Polym Eng Sci* 1990;30:175–86. <https://doi.org/10.1002/pen.760300307>.
- [34] Briscoe BJ, Khan MB, Richardson SM. Rotary injection reaction injection molding (RI-RIM). Part I: Basic design features. *Polym Eng Sci* 1990;30:162–74. <https://doi.org/10.1002/pen.760300306>.
- [35] Fu SY, Feng XQ, Lauke B, Mai YW. Effects of particle size, particle/matrix interface adhesion and particle loading on mechanical properties of particulate-polymer composites. *Compos Part B Eng* 2008;39:933–61. <https://doi.org/10.1016/j.compositesb.2008.01.002>.
- [36] Wang K, Wu J, Ye L, Zeng H. Mechanical properties and toughening mechanisms of polypropylene/barium sulfate composites. *Compos Part A Appl Sci Manuf* 2003;34:1199–205. <https://doi.org/10.1016/j.compositesa.2003.07.004>.
- [37] Pukanszky B, VÖRÖS G. Mechanism of interfacial interactions in particulate filled composites. *Compos Interfaces* 1993;1:411–27. <https://doi.org/10.1163/156855493x00266>.
- [38] Nakamura Y, Yamaguchi M, Okubo M, Matsumoto T. Effects of particle size on mechanical and impact properties of epoxy resin filled with spherical silica. *J Appl Polym Sci* 1992;45:1281–9. <https://doi.org/10.1002/app.1992.070450716>.
- [39] DePolo WS, Baird DG. Particulate reinforced PC/PBT composites. II. Effect of nano-clay particles on dimensional stability and structure-property relationships. *Polym Compos* 2009;30:200–13. <https://doi.org/10.1002/pc.20552>.
- [40] DePolo WS, Baird DG. Particulate reinforced PC/PBT composites. I. Effect of particle size (nanotalc versus fine talc particles) on dimensional stability and properties. *Polym Compos* 2009;30:188–99. <https://doi.org/10.1002/pc.20554>.
- [41] Ji XL, Jing JK, Jiang W, Jiang BZ. Tensile modulus of polymer nanocomposites. *Polym Eng Sci* 2002;42:983–93. <https://doi.org/10.1002/pen.11007>.
- [42] Cardwell BJ, Yee AF. Toughening of epoxies through thermoplastic crack bridging. *J Mater Sci* 1998;33:5473–84. <https://doi.org/10.1023/A:1004427123388>.

- [43] Kim S, Kim J, Lim SH, Jo WH, Choe CR. Effects of mixing temperatures on the morphology and toughness of epoxy/polyamide blends. *J Appl Polym Sci* 1999;72:1055–63. [https://doi.org/10.1002/\(SICI\)1097-4628\(19990523\)72:8<1055::AID-APP10>3.0.CO;2-8](https://doi.org/10.1002/(SICI)1097-4628(19990523)72:8<1055::AID-APP10>3.0.CO;2-8).
- [44] Kim JK, Robertson RE. Toughening of thermoset polymers by rigid crystalline particles. *J Mater Sci* 1992;27:161–74. <https://doi.org/10.1007/bf00553852>.
- [45] Young RJ, Maxwell DL, Kinloch AJ. The deformation of hybrid-particulate composites. *J Mater Sci* 1986;21:380–8. <https://doi.org/10.1007/BF01145498>.
- [46] Hedrick JL, Yilgor I, Jurek M, Hedrick JC, Wilkes GL, McGrath JE. Chemical modification of matrix resin networks with engineering thermoplastics: 1. Synthesis, morphology, physical behaviour and toughening mechanisms of poly(arylene ether sulphone) modified epoxy networks. *Polymer (Guildf)* 1991;32:2020–32. [https://doi.org/10.1016/0032-3861\(91\)90168-I](https://doi.org/10.1016/0032-3861(91)90168-I).
- [47] Raghava RS. Role of matrix-particle interface adhesion on fracture toughness of dual phase epoxy-polyethersulfone blend. *J Polym Sci Part B Polym Phys* 1987;25:1017–31. <https://doi.org/10.1002/polb.1987.090250504>.
- [48] Mackinnon AJ, Jenkins SD, Mcgrail PT, Pethrick RA. Cure and physical properties of thermoplastic modified epoxy resins based on polyethersulfone. *J Appl Polym Sci* 1995;58:2345–55. <https://doi.org/10.1002/app.1995.070581302>.
- [49] Blanco I, Cicala G, Lo Faro C, Recca A. Improvement of thermomechanical properties of a DGEBS/DDS system blended with a novel thermoplastic copolymer by realization of a semi-IPN network. *J Appl Polym Sci* 2003;88:3021–5. <https://doi.org/10.1002/app.12007>.
- [50] Naffakh M, Dumon M, Gérard JF. Study of a reactive epoxy-amine resin enabling in situ dissolution of thermoplastic films during resin transfer moulding for toughening composites. *Compos Sci Technol* 2006;66:1376–84. <https://doi.org/10.1016/j.compscitech.2005.09.007>.
- [51] Chen MC, Hourston DJ, Schafer FU, Huckerby TN. Miscibility and fracture behaviour of epoxy resin-nitrated polyetherimide blends. *Polymer (Guildf)* 1995;36:3287–93. [https://doi.org/10.1016/0032-3861\(95\)99427-V](https://doi.org/10.1016/0032-3861(95)99427-V).
- [52] Cho JB, Hwang JW, Cho K, An JH, Park CE. Effects of morphology on toughening of tetrafunctional epoxy resins with poly(ether imide). *Polymer (Guildf)* 1993;34:4832–6. [https://doi.org/10.1016/0032-3861\(93\)90005-U](https://doi.org/10.1016/0032-3861(93)90005-U).
- [53] Pearson RA, Yee AF. Toughening mechanisms in thermoplastic-modified epoxies: 1. Modification using poly(phenylene oxide). *Polymer (Guildf)* 1993;34:3658–70. [https://doi.org/10.1016/0032-3861\(93\)90051-B](https://doi.org/10.1016/0032-3861(93)90051-B).
- [54] Wu SJ, Lin TK, Shyu SS. Cure behavior, morphology, and mechanical properties of the melt blends of epoxy with polyphenylene oxide. *J Appl Polym Sci* 2000;75:26–34. [https://doi.org/10.1002/\(SICI\)1097-4628\(20000103\)75:1<26::AID-APP4>3.0.CO;2-3](https://doi.org/10.1002/(SICI)1097-4628(20000103)75:1<26::AID-APP4>3.0.CO;2-3).

- [55] Wu H, Krifa M, Koo JH. Rubber (SEBS-g-MA) Toughened Flame-Retardant Polyamide 6: Microstructure, Combustion, Extension, and Izod Impact Behavior. *Polym - Plast Technol Eng* 2018;57:727–39. <https://doi.org/10.1080/03602559.2017.1344856>.
- [56] Wu G, Zhang K, Takagi K, Sano H, Yui H. Rubber-toughened polyamide-6 with a low thermal expansion coefficient: Effect of preferential distribution of rubber and inorganic filler. *Polym Int* 2016;65:102–8. <https://doi.org/10.1002/pi.5036>.
- [57] Liu D, Li G, Li B, Luan Y, Ling H, Yang X. In-situ toughened CFRP composites by shear-calender orientation and fiber-bundle filtration of PA microparticles at prepreg interlayer. *Compos Part A Appl Sci Manuf* 2016. <https://doi.org/10.1016/j.compositesa.2016.01.015>.
- [58] Groleau MR, Shi YB, Yee AF, Bertram JL, Sue HJ, Yang PC. Mode II fracture of composites interlayered with nylon particles. *Compos Sci Technol* 1996;56:1223–40. [https://doi.org/10.1016/S0266-3538\(96\)00080-2](https://doi.org/10.1016/S0266-3538(96)00080-2).
- [59] Takeda N, Ogihara S. Micromechanical characterization of local deformation in interlaminar-toughened CFRP laminates. *Compos Part A Appl Sci Manuf* 1998;29:1545–52. [https://doi.org/10.1016/S1359-835X\(98\)00067-0](https://doi.org/10.1016/S1359-835X(98)00067-0).
- [60] Caprino G, Iaccarino P, Lamboglia A. The effect of shear on the rigidity in three-point bending of unidirectional CFRP laminates made of T800H/3900-2. *Compos Struct* 2009;88:360–6. <https://doi.org/10.1016/j.compstruct.2008.04.014>.
- [61] Hojo M, Matsuda S, Tanaka M, Ochiai S, Murakami A. Mode I delamination fatigue properties of interlayer-toughened CF/epoxy laminates. *Compos Sci Technol* 2006;66:665–75. <https://doi.org/10.1016/j.compscitech.2005.07.038>.
- [62] Khan SU, Kim JK. Improved interlaminar shear properties of multiscale carbon fiber composites with bucky paper interleaves made from carbon nanofibers. *Carbon N Y* 2012. <https://doi.org/10.1016/j.carbon.2012.07.011>.
- [63] Ma L, Wu L, Cheng X, Zhuo D, Weng Z, Wang R. Improving the interlaminar properties of polymer composites using a situ accumulation method to construct the multi-scale reinforcement of carbon nanofibers/carbon fibers. *Compos Part A Appl Sci Manuf* 2015. <https://doi.org/10.1016/j.compositesa.2015.01.023>.
- [64] Jackson A, Dutton S, Gunnion AJ, Kelly D. Effect of manufacture and laminate design on energy absorption of open carbonfibre/ epoxy sections. *ICCM Int Conf Compos Mater* 2009.
- [65] Herzig JP, Leclerc DM, Legoff P. Flow of suspensions through porous media - application to deep filtration. *Ind Eng Chem* 1970;62:8-. <https://doi.org/10.1021/ie50725a003>.
- [66] Jegatheesan V, Vigneswaran S. Deep bed filtration: Mathematical models and observations. *Crit Rev Environ Sci Technol* 2005;35:515–69. <https://doi.org/10.1080/10643380500326432>.

- [67] Ebach EA, White RR. Mixing of fluids flowing through beds of packed solids. *AIChE J* 1958;4:161–9. <https://doi.org/10.1002/aic.690040209>.
- [68] Di Carlo D, Irimia D, Tompkins RG, Toner M. Continuous inertial focusing, ordering, and separation of particles in microchannels. *Proc Natl Acad Sci U S A* 2007;104:18892–7. <https://doi.org/10.1073/pnas.0704958104>.
- [69] Steggall-murphy C, Simacek P, Advani SG. A Model for Particle Deposition During Impregnation of Fibrous Pourous Media 2011;14:383–94.
- [70] Martinez-Carvajal GD, Oxarango L, Adrien J, Molle P, Forquet N. Assessment of X-ray Computed Tomography to characterize filtering media from Vertical Flow Treatment Wetlands at the pore scale. *Sci Total Environ* 2019;658:178–88. <https://doi.org/10.1016/j.scitotenv.2018.12.119>.
- [71] Steggall-Murphy C, Simacek P, Advani SG, Yarlagadda S, Walsh S. A model for thermoplastic melt impregnation of fiber bundles during consolidation of powder-impregnated continuous fiber composites. *Compos Part A Appl Sci Manuf* 2010;41:93–100. <https://doi.org/10.1016/j.compositesa.2009.09.026>.
- [72] Edie DD, Fain CC, Robinson KE, Harper AM, Rogers DK. Ribbon-shape carbon fibers for thermal management. *Carbon N Y* 1993;31:941–9. [https://doi.org/10.1016/0008-6223\(93\)90196-H](https://doi.org/10.1016/0008-6223(93)90196-H).
- [73] Emig G, Popovska N, Edie DD, Rhee BS. Surface free energy of carbon fibers with circular and non-circular cross sections coated with silicon carbide. *Carbon N Y* 1995;33:779–82. [https://doi.org/10.1016/0008-6223\(95\)00008-2](https://doi.org/10.1016/0008-6223(95)00008-2).
- [74] Robinson KE, Edie DD. Microstructure and texture of pitch-based ribbon fibers for thermal management. *Carbon N Y* 1996;34:13–36. [https://doi.org/10.1016/0008-6223\(95\)00129-8](https://doi.org/10.1016/0008-6223(95)00129-8).
- [75] Ogale A, Zhang M, Jin J. Sustainable polymers and polymer science: Dedicated to the life and work of Richard P. Wool. *J Appl Polym Sci* 2016;133. <https://doi.org/10.1002/app.44212>.
- [76] Khayyam H, Jazar RN, Nunna S, Golkarnarenji G, Badii K, Fakhrhoseini SM, et al. PAN precursor fabrication, applications and thermal stabilization process in carbon fiber production: Experimental and mathematical modelling. *Prog Mater Sci* 2020;107:100575. <https://doi.org/10.1016/j.pmatsci.2019.100575>.
- [77] Mikołajczyk T, Krucińska I, Kamecka-Jędrzejczak K. Correlation Between Copolymer Characteristics, Conditions of Fiber Formation, and Mechanical Properties of PAN Carbon Fiber Precursor: Part III: Effect of Fiber Formation Conditions on Mechanical Properties. *Text Res J* 1989;59:665–70. <https://doi.org/10.1177/004051758905901106>.
- [78] Yang Z, Peng H, Wang W, Liu T. Crystallization behavior of poly(ϵ -caprolactone)/layered double hydroxide nanocomposites. *J Appl Polym Sci* 2010;116:2658–67. <https://doi.org/10.1002/app>.

- [79] Peng GQ, Zhang XH, Wen YF, Yang YG, Liu L. Effect of coagulation bath DMSO concentration on the structure and properties of polyacrylonitrile (PAN) nascent fibers during wet-spinning. *J Macromol Sci Part B Phys* 2008;47:1130–41. <https://doi.org/10.1080/00222340802403214>.
- [80] Baker DA, Rials TG. Recent advances in low-cost carbon fiber manufacture from lignin. *J Appl Polym Sci* 2013;130:713–28. <https://doi.org/10.1002/app.39273>.
- [81] Nunna S, Maghe M, Rana R, Varley RJ, Knorr DB, Sands JM, et al. Time dependent structure and property evolution in fibres during continuous carbon fibre manufacturing. *Materials (Basel)* 2019;12. <https://doi.org/10.3390/ma12071069>.
- [82] Gill AS, Visotsky D, Mears L, Summers JD. Cost Estimation Model for Polyacrylonitrile-Based Carbon Fiber Manufacturing Process. *J Manuf Sci Eng Trans ASME* 2017;139:1–8. <https://doi.org/10.1115/1.4034713>.
- [83] E2070-13 Standard Test Methods for Kinetic Parameters by Differential Scanning Calorimetry Using Isothermal Methods. West Conshohocken: ASTM International; 2018. <https://doi.org/https://doi.org/10.1520/E2070-13R18>.
- [84] Ramis X, Salla JM. Time-temperature transformation (TTT) cure diagram of an unsaturated polyester resin. *J Polym Sci Part B Polym Phys* 1997;35:371–88. [https://doi.org/10.1002/\(SICI\)1099-0488\(19970130\)35:2<371::AID-POLB13>3.3.CO;2-6](https://doi.org/10.1002/(SICI)1099-0488(19970130)35:2<371::AID-POLB13>3.3.CO;2-6).
- [85] Wisanrakkit G, Gillham JK. The Glass-Transition Temperature (T_g) As An Index Of Chemical Conversion For A High-T_g Amine Epoxy System - Chemical And Diffusion-Controlled Reaction-Kinetics. *J Appl Polym Sci* 1990;41:2885–929. <https://doi.org/10.1002/app.1990.070411129>.
- [86] Dibenedetto AT. Prediction Of The Glass-Transition Temperature Of Polymers - A Model Based On The Principle Of Corresponding States. *J Polym Sci Part B-Polymer Phys* 1987;25:1949–69. <https://doi.org/10.1002/polb.1987.090250914>.
- [87] Castro JM, Macosko CW. Studies of mold filling and curing in the reaction injection molding process. *AIChE J* 1982;28:250–60. <https://doi.org/10.1002/aic.690280213>.
- [88] Enns JB, Gillham JK. Time Temperature Transformation (TTT) Cure Diagram - Modeling the Cure Behavior of Thermosets. *J Appl Polym Sci* 1983;28:2567–91. <https://doi.org/10.1002/app.1983.070280810>.
- [89] Kenny JM, Apicella A, Nicolais L. A model for the thermal and chemorheological behavior of thermosets .1. Processing of epoxy-based composites. *Polym Eng Sci* 1989;29:973–83. <https://doi.org/10.1002/pen.760291502>.
- [90] Tcharkhtchi A, Nony F, Khelladi S, Fitoussi J, Farzaneh S. Epoxy/amine reactive systems for composites materials and their thermomechanical properties. vol. 1. Elsevier Ltd.; 2015. <https://doi.org/10.1016/B978-1-78242-307-2.00013-0>.

- [91] Roller MB. Rheology of curing thermosets - a review. *Polym Eng Sci* 1986;26:432–40. <https://doi.org/10.1002/pen.760260610>.
- [92] Irfan MS, Shotton-Gale N, Paget MA, Machavaram VR, Leek C, Wootton S, et al. A modified pultrusion process. *J Compos Mater* 2017;51:1925–41. <https://doi.org/10.1177/0021998316666653>.
- [93] Suratno BR, Ye L, Mai YW. Simulation of temperature and curing profiles in pultruded composite rods. *Compos Sci Technol* 1998;58:191–7. [https://doi.org/10.1016/s0266-3538\(97\)00132-2](https://doi.org/10.1016/s0266-3538(97)00132-2).
- [94] Pandita S, Irfan M, Machavaram V, Shotton-Gale N, Mahendran R, Wait C, et al. Clean wet-filament winding – Part 1: design concept and simulations. *J Compos Mater* 2013;47:379–90. <https://doi.org/10.1177/0021998312440474>.
- [95] Cherif C. Textile materials for lightweight constructions: Technologies - methods - materials – properties. 2016. <https://doi.org/10.1007/978-3-662-46341-3>.
- [96] Molyneux M, Murray P, P. Murray B. Prepreg, tape and fabric technology for advanced composites. *Composites* 1983;14:87–91. [https://doi.org/10.1016/S0010-4361\(83\)80003-2](https://doi.org/10.1016/S0010-4361(83)80003-2).
- [97] Putnam JW, Seferis JC, Pelton T, Wilhelm M. Perceptions of Prepreg Tack for Manufacturability in Relation to Experimental Measures. *Sci Eng Compos Mater* 1995;4:143–54. <https://doi.org/10.1515/SECM.1995.4.3.143>.
- [98] Chmielewski C, Jayaraman K, Petty CA. Processing effects in production of composite prepreg by hot-melt impregnation. *Polym Compos* 1993;14:257–64. <https://doi.org/10.1002/pc.750140311>.
- [99] Babeau A, Comas-Cardona S, Binetruy C, Orange G. Modeling of heat transfer and unsaturated flow in woven fiber reinforcements during direct injection-pultrusion process of thermoplastic composites. *Compos Part a-Applied Sci Manuf* 2015;77:310–8. <https://doi.org/10.1016/j.compositesa.2015.04.017>.
- [100] Borges SG, Ferreira CA, Andrade JM, Prevedello ALA. The influence of bath temperature on the properties of pultruded glass fiber reinforced rods. *J Reinf Plast Compos* 2015;34:1221–30. <https://doi.org/10.1177/0731684415587411>.
- [101] Simacek P, Advani SG. Simulating tape resin infiltration during thermoset pultrusion process. *Compos Part a-Applied Sci Manuf* 2015;72:115–26. <https://doi.org/10.1016/j.compositesa.2015.01.020>.
- [102] Ngo SI, Lim Y Il, Hahn MH, Jung J, Bang YH. Multi-scale computational fluid dynamics of impregnation die for thermoplastic carbon fiber prepreg production. *Comput Chem Eng* 2017. <https://doi.org/10.1016/j.compchemeng.2017.03.007>.

- [103] Wilkes GL. An overview of the basic rheological behavior of polymer fluids with an emphasis on polymer melts. *J Chem Educ* 1981;58:880–92. <https://doi.org/10.1021/ed058p880>.
- [104] Koubaa S, Burtin C, Le Corre S. Investigation of capillary impregnation for permeability prediction of fibrous reinforcements. *J Compos Mater* 2016;50:1417–29. <https://doi.org/10.1177/0021998315593797>.
- [105] Wakeman MD, Cain TA, Rudd CD, Brooks R, Long AC. Compression moulding of glass and polypropylene composites for optimised macro- and micro-mechanical properties II. Glass-mat-reinforced thermoplastics. *Compos Sci Technol* 1999;59:709–26. [https://doi.org/10.1016/S0266-3538\(98\)00124-9](https://doi.org/10.1016/S0266-3538(98)00124-9).
- [106] Yu TH, Davis RM. The Effect of Processing Conditions on the Properties of Carbon Fiber-LaRC TPI Composites Made by Suspension Prepregging. *J Thermoplast Compos Mater* 1993;6:62–90. <https://doi.org/10.1177/089270579300600106>.
- [107] Xie J, Jin YC. Parameter determination for the cross rheology equation and its application to modeling non-Newtonian flows using the WC-MPS method. *Eng Appl Comput Fluid Mech* 2016;10:111–29. <https://doi.org/10.1080/19942060.2015.1104267>.
- [108] Astrom BT, Pipes RB, Advani SG. On flow through aligned fiber beds and its application to composites processing. *J Compos Mater* 1992;26:1351–73. <https://doi.org/10.1177/002199839202600907>.
- [109] Hartness T. Thermoplastic Powder Technology for Advanced Composite Systems. *J Thermoplast Compos Mater* 1988;1:210–20. <https://doi.org/10.1177/089270578800100301>.
- [110] Stokes GG. On the Effect of the Internal Friction of Fluids on the Motion of Pendulums. *Math Phys Pap* 2010;1–10. <https://doi.org/10.1017/cbo9780511702266.002>.
- [111] Connor M, Toll S, Manson J-AE. On surface energy effects in composite and impregnation consolidation 1995;6:289–95.
- [112] Liu D, Zhu YD, Ding JP, Lin XY, Fan XY. Experimental investigation of carbon fiber reinforced poly(phenylene sulfide) composites prepared using a double-belt press. *Compos Part B-Engineering* 2015;77:363–70. <https://doi.org/10.1016/j.compositesb.2015.03.062>.
- [113] Wang X, Mayer C, Neitzel M. Some issues on impregnation in manufacturing of thermoplastic composites by using a double belt press. *Polym Compos* 1997;18:701–10. <https://doi.org/10.1002/pc.10323>.
- [114] Fang X, Shen CY, Dai G. Comparative Investigation of Molded Thickness and Surface Density on the Structures and Mechanical Properties of Lightweight Reinforced Thermoplastic Composites. *Fibers Polym* 2017;18:303–12. <https://doi.org/10.1007/s12221-017-6067-5>.

- [115] Wang R-M, Zheng S-R, Zheng Y-P. Fabrication of the half-finished products for polymer composites. *Polym Matrix Compos Technol* 2011;213–548. <https://doi.org/10.1533/9780857092229.2.213>.
- [116] Vaidya UK, Chawla KK. Processing of fibre reinforced thermoplastic composites n.d. <https://doi.org/10.1179/174328008X325223>.
- [117] Nelson KM, Manson JAE, Seferis JC. Compression Thermal Analysis of the Consolidation Process for Thermoplastic Matrix Composites. *J Thermoplast Compos Mater* 1990;3:216–32. <https://doi.org/10.1177/089270579000300304>.
- [118] Hou TH, Bryant RG. Processing and properties of IM7 / LARC TM -SCI composite * 1996;8:169–84.
- [119] Xu AC, Bao LM, Nishida M, Yamanaka A. Molding of PBO fabric reinforced thermoplastic composite to achieve high fiber volume fraction. *Polym Compos* 2013;34:953–8. <https://doi.org/10.1002/pc.22501>.
- [120] De Almeida O, Feuillerat L, Nouri V, Choquet K. Influence of composite preform fabrication on the integrity of poly-aryl-ether-ketone matrices. *J Appl Polym Sci* 2021:1–15. <https://doi.org/10.1002/app.50719>.
- [121] Bernhardsson J, Shishoo R. Effect of Processing Parameters on Consolidation Quality of GF/PP Commingled Yarn Based Composites. *J Thermoplast Compos Mater* 2000;13:292–313.
- [122] Bernet N, Wakeman MD, Bourban PE, Manson JA. An integrated cost and consolidation model for commingled yarn based composites. *Compos - Part A Appl Sci Manuf* 2002;33:495–506. [https://doi.org/10.1016/S1359-835X\(01\)00140-3](https://doi.org/10.1016/S1359-835X(01)00140-3).
- [123] Linganisio LZ, Bezerra R, Bhat S, John M, Braeuning R, Anandjiwala RD. Pultrusion of flax/poly(lactic acid) commingled yarns and nonwoven fabrics. *J Thermoplast Compos Mater* 2014;27:1553–72. <https://doi.org/10.1177/0892705713486137>.
- [124] Risicato J V, Kelly F, Soulat D, Legrand X, Trumper W, Cochrane C, et al. A Complex Shaped Reinforced Thermoplastic Composite Part Made of Commingled Yarns With Integrated Sensor. *Appl Compos Mater* 2015;22:81–98. <https://doi.org/10.1007/s10443-014-9400-9>.
- [125] Kravaev P, Stolyarov O, Seide G, Gries T. Influence of process parameters on filament distribution and blending quality in commingled yarns used for thermoplastic composites. *J Thermoplast Compos Mater* 2014;27:350–63.
- [126] Batch GL, Cumiskey S, Macosko CW. Compaction of fiber reinforcements. *Polym Compos* 2002;23:307–18. <https://doi.org/10.1002/pc.10433>.

- [127] Woolard DE, Ramani K. Electric field modeling for electrostatic powder coating of a continuous fiber bundle. *J Electrostat* 1995;35:373–87. [https://doi.org/10.1016/0304-3886\(95\)00029-A](https://doi.org/10.1016/0304-3886(95)00029-A).
- [128] Texier A, Davis RM, Lyon KR, Gungor A, McGrath JE, Marand H, et al. Fabrication of PEEK/carbon fibre composites by aqueous suspension prepregging. *Polymer (Guildf)* 1993;34:896–906. [https://doi.org/10.1016/0032-3861\(93\)90378-N](https://doi.org/10.1016/0032-3861(93)90378-N).
- [129] Connor M, Harding PH, Månson JAE, Berg JC. Influence of the fiber surface properties on the mechanical strength of unidirectional fiber composites. *J Adhes Sci Technol* 1995;9:983–1004. <https://doi.org/10.1163/156856195X00833>.
- [130] Zhang R, Fallon JJ, Joseph RM, Thomas JA, Hassan MS, Choudhury SR, et al. Preparation of Submicrometer High-Performance Poly(ether imide) Particles for Fabricating Carbon Fiber Reinforced Polymer Composites. *Ind Eng Chem Res* 2018;57:15346–56. <https://doi.org/10.1021/acs.iecr.8b02930>.
- [131] Connor M, Bidaux JE, Månson JAE. A criterion for optimum adhesion applied to fibre reinforced composites. *J Mater Sci* 1997;32:5059–67. <https://doi.org/10.1023/A:1018657131178>.
- [132] Nunes JP, Silva JF, Marques AT, Crainic N, Cabral-Fonseca S. Production of powder-coated towpregs and composites. *J Thermoplast Compos Mater* 2003;16:231–48. <https://doi.org/10.1177/0892705703016003003>.
- [133] Nunes JP, Silva JF, Silva L, Novo PJ, Marques AT. Equipment to Produce Continuously Powder Coated Thermoplastic Matrix Prepregs (Towpregs), 2002.
- [134] Baucom R, Snoha J, Marchello J. United States Patent 5057338, 1991.
- [135] Iyer S, Drzal L, Jayaraman K. United States Patent 5102690, 1992.
- [136] Muzzy JD, Varughese B. United States Patent 5,171,630, 1992.
- [137] Baucom RM, Marchello JM. NASA Technical Memorandum 110386 1996.
- [138] Goud V, Singh D, Ramasamy A, Das A, Kalyanasundaram D. Investigation of the mechanical performance of carbon/polypropylene 2D and 3D woven composites manufactured through multi-step impregnation processes. *Compos Part A Appl Sci Manuf* 2020;130:105733. <https://doi.org/10.1016/j.compositesa.2019.105733>.
- [139] Goud V, Ramasamy A, Das A, Kalyanasundaram D. Box-Behnken technique based multi-parametric optimization of electrostatic spray coating in the manufacturing of thermoplastic composites. *Mater Manuf Process* 2019;34:1638–45. <https://doi.org/10.1080/10426914.2019.1666991>.

- [140] Goud V, Alagirusamy R, Das A, Kalyanasundaram D. Dry Electrostatic Spray Coated Towpregs for Thermoplastic Composites. *Fibers Polym* 2018;19:364–74. <https://doi.org/10.1007/s12221-018-7470-7>.
- [141] Jaber AA, Obaid AA, Advani SG, Gillespie JW. Prediction of equilibrium spacing between charged polymer particles in contact with a carbon fiber. *J Electrostat* 2021;111:103577. <https://doi.org/10.1016/j.elstat.2021.103577>.
- [142] Peart J. Powder electrostatics: Theory, techniques and applications. *KONA Powder Part J* 2001;19:34–45. <https://doi.org/10.14356/kona.2001009>.
- [143] O'Connor J. United States Patent 4,680,224, 1987.
- [144] Taylor G. United States Patent 4,292,105, 1981.
- [145] McGregor OPL, Somashekar AA, Bhattacharyya D, McGregor OPL, Duhovic M. Pre-impregnated natural fibre-thermoplastic composite tape manufacture using a novel process. *Compos Part A Appl Sci Manuf* 2017;101:59–71. <https://doi.org/10.1016/j.compositesa.2017.05.025>.
- [146] Tang L, Li L, Yi X, Pan Z. Aqueous powder slurry manufacture of continuous fiber reinforced polyethylene composite. *Polym Compos* 1997;18:223–31. <https://doi.org/10.1002/pc.10276>.
- [147] Kingsley KCH, Shamsuddin SR, Matthew L, Bismarck A. Unidirectional carbon fibre reinforced poly (vinylidene fluoride): Impact of atmospheric plasma on composite performance. *Compos Part A Appl Sci Manuf* 2011;42:453–61. <https://doi.org/10.1016/j.compositesa.2011.01.001>.

2. COMPACTION AND PERMEABILITY OF ALIGNED, KIDNEY-BEAN SHAPED CARBON FIBER BEDS

Portions of this chapter have been submitted to the Journal of Composite Materials.

In this chapter, a low-cost kidney-bean shaped carbon fiber intended for automotive prepreg was considered. The effect of the kidney-bean shaped cross section was investigated for its compaction behavior and permeability properties compared to circular fibers with equivalent cross-sectional area. The compaction behavior was experimentally quantified. The permeabilities were simulated for various packing arrangements and orientations to establish an upper and lower bound for the permeability. These properties were used in Chapter 3 to model a hot-melt impregnation process for low-cost prepreg intended for automotive applications.

2.1 Introduction

Carbon fiber composites are well known for exceptional specific stiffness and strength [1]. However, product cost sensitive industries, such as automotive, struggle to justify using carbon fiber over a lower cost glass fiber alternative [2]. These higher costs of carbon fiber were often inculcated on the carbonization process with long dwell times at high temperatures, but the majority of cost comes from the polyacrylonitrile (PAN) precursor fabrication [3–6]. Since alternative precursor materials to PAN fiber have not yet been widely commercially adopted, manufacturers have endeavored to modify solvent concentrations, pH, solvent type, and temperature to increase processing speeds and reduce manufacturing cost. However, changing the PAN fiber processing conditions to make inexpensive PAN fiber causes an asymmetric solvent-solute diffusive flux to occur. The imbalanced diffusion rates causes the fiber cross-section to appear kidney-bean shaped [4,7,8]. This cross-sectional shape persists through the carbonization step and expresses itself in the final carbon fiber shape. The push for low cost carbon fiber with comparable mechanical properties to traditional carbon fiber has incentivized manufacturers to produce carbon fiber from lower grade PAN resulting in kidney-bean shaped fiber. Existing relationships for fiber bed compaction and permeability considered circular fibers, therefore these relationships should be revisited for kidney-bean shaped fibers.

2.2 Carbon Fiber Compaction Background

The fiber compaction model derived by Gutowski and Cai [13,14] expressed the non-linear deformation behavior of well aligned AS4 carbon fiber (circular cross-section) beds during consolidation. Their model assumed well aligned fibers, a square packed unit cell consisting of circular fibers, and that fibers acted as bending beams with multiple contact points. The approximated pressures from their model showed good agreement with their data and has been widely adopted by the scientific community [15–20]. The model described by Gutowski and Cai [13,14] in Equation (2.1) only required three parameters: uncompact fiber volume fraction (V_o), maximum packed fiber volume fraction (V_a), and effective fiber bed stiffness (A). However, their studies on fiber bed compaction were limited to fibers with a circular cross section.

$$P = A \frac{\sqrt{\frac{V_f}{V_o}} - 1}{\left(\sqrt{\frac{V_a}{V_f}} - 1 \right)^4} \quad (2.1)$$

Now that kidney-bean fibers are commercially available, the consequences of this fiber shape should be investigated for their influence on the composites manufacturing process. All composite preform manufacturing goes through an infiltration step where resin flows transversely through the fiber bed. Resin infiltration through the fiber bed is described by Darcy's Law which relates the flow front velocity to viscosity, pressure, permeability, and the fiber bed thickness [9–12]. The pressure pumps the resin into the fiber bed, which compacts and reduces the permeability. Because of this link between pressure and permeability, Gutowski and Cai proposed a model to relate the fiber bed fiber volume fraction to compaction pressure [13–15]. Therefore, a compaction study investigating kidney-bean shaped fiber was warranted to determine the applicability of the Gutowski model for kidney-bean shaped fibers.

Gutowski's original work only measured fiber volume fractions above 0.5 because of the limited pressure sensitivity [13]. Follow-up work by Kastanis et al. [15] demonstrated continuous carbon fiber tow compaction behavior can be measured using an approach they called laser light sectioning. Where the cross-sectional area of the tow was measured using a laser scanner. With their approach, fiber volume fractions down to 0.30 were measured. In the present study, the laser light section equipment was replaced with a camera attached to a microscope for the fiber volume

fraction measurement. Additionally, the effect of the novel kidney-bean shape on fiber bed compaction was investigated. The pressure vs fiber volume fraction compaction data was compared to the well-known relationship that Gutowski developed for circular fibers. The compaction behavior of the kidney-bean fibers was not correctly estimated by the Gutowski model and a shape correction factor related to the fiber's cross-sectional aspect ratio was proposed.

2.3 Carbon Fiber Permeability Background

With the commercial availability of kidney-bean shaped carbon fibers, implications of the fiber shape should be investigated for its impact on subsequent composites manufacturing processes. Importantly, all polymer composites must at one stage undergo a resin infiltration process. During this process, the resin flows through the fiber bed, where the superficial velocity can be described by Darcy's Law with the viscosity, pressure, permeability, and fiber bed thickness [9–12,20]. The composites manufacturing time is dictated by the resin velocity, which is dependent on the fiber bed permeability. The fiber bed permeability varies by orders of magnitude across by varying fiber volume fraction (V_f), packing arrangements, fiber shape, and fiber radius (r) [11]. The packing arrangement (e.g. hexagonal or square) of circular fibers has also been shown to influence the fiber bed permeability [11,24]. The fiber shape and orientation have also been shown to influence permeability [13,25,26]. While these studies expanded permeability trends to various packing arrangements, orientations, and shapes, they have not considered a kidney-bean shaped fiber's effect on permeability.

Existing permeability models were derived and validated with circular fibers, such as Gebart's model [11] or the Carman-Kozeny equation [27]. Both of these models have been widely used in the literature to model resin infiltration processes [16,24,26,28–34]. Gebart's model was derived using Darcy's Law to describe the pressure drop a fluid would experience as it passed between adjacent fibers. This model assumed most of the flow resistance transverse to the fibers occurred in the narrow gap formed between neighboring fibers. The resulting permeability model for hexagonal and square packed circular fibers are shown in Equations (2.2) and (2.3), respectively [11]. For circular fibers, Gebart identified theoretical constants for hexagonal and square packing. His model accounted for the maximum packing fraction ($V_{f\max}$) for the fiber unit cell and appropriately predicted the permeability near maximum packing. Equation (2.3) for square

packed fibers tended to slightly overpredict the permeability at low fiber volume fractions (below 0.35) but Equation (2.2) provided an appropriate fit for hexagonal packed fibers [26].

$$K_{hex\ pack} = \frac{16 r^2}{9\pi \sqrt{6}} \left(\sqrt{\frac{V_{f\ max}}{V_f}} - 1 \right)^{\frac{5}{2}} \quad (2.2)$$

$$K_{square\ pack} = \frac{16 r^2}{9\pi \sqrt{2}} \left(\sqrt{\frac{V_{f\ max}}{V_f}} - 1 \right)^{\frac{5}{2}} \quad (2.3)$$

In contrast, the Carman-Kozeny equation shown in Equation (2.4) was derived using a capillary model [27]. The Carman-Kozeny model is commonly used to define the transverse permeability of fiber beds. However, the tortuosity (K_o) and shape factor (K_1) constants that define the Kozeny constant (k) (Equation (2.5)) are not constant and vary with fiber volume fraction [12,24,26,29,32,34–36]. This is partially caused by the hydraulic diameter defined in the original work which did not account for the no-flow condition at maximum fiber packing. As a result, the Carman-Kozeny equation was normally used to describe the transverse permeability for a narrow fiber volume fraction range, typically 0.3 – 0.6 [32,34]. Modifications to the Carman-Kozeny equation have been proposed to account for no-flow at maximum packing [13,16,24,28–30,33,34,36].

$$K = \frac{r^2 (1-V_f)^3}{k V_f^2} \quad (2.4)$$

$$k = K_o K_1^2 \quad (2.5)$$

In this study, numerical flow simulations were performed on a representative kidney-bean shaped fiber in various unit cell packing arrangements and unit cell orientations to determine the fiber bed transverse permeability. The computational fluid dynamics simulation was validated with circular fibers packed in hexagonal and square arrays and compared to literature values. The flow simulations considered two hexagonal and one square packing arrangement for the kidney-bean shaped fiber. Additionally, the effect unit cell orientation had on permeability was investigated with the following unit cell orientations: 0° , $+90^\circ$, and -90° . These various packing conditions were used to establish an upper and lower bound for permeability and compare infiltration times

to circular fibers. The resulting permeabilities were fitted to the Carman-Kozeny equation and the Gebart model.

2.4 Experimental Methods and Permeability Simulation Conditions

2.4.1 Material for tensioned compaction experiments

A 24k DowAksa A-42 carbon fiber, further referred to as A-42, was used for the fiber bed compaction experiments. This fiber was known to have a kidney-bean shaped cross-section, shown in Figure 2.1. In order to generalize the fiber bed microstructure, the kidney-bean shape was approximated as an ellipse using FIJI fit ellipse algorithm[37] to determine the aspect ratio of the kidney-bean fiber. Representative square packed unit cells for circular, kidney-bean, and elliptically shaped fibers are shown in Figure 3.3. The maximum packing fraction for consistently oriented kidney-bean fibers was calculated to be 0.843 compared to 0.785 for circular and elliptically shaped fibers in the unit cell configuration described in Figure 3.3. The maximum hexagonal pack was 0.923 for kidney-bean and 0.901 for circular fibers.

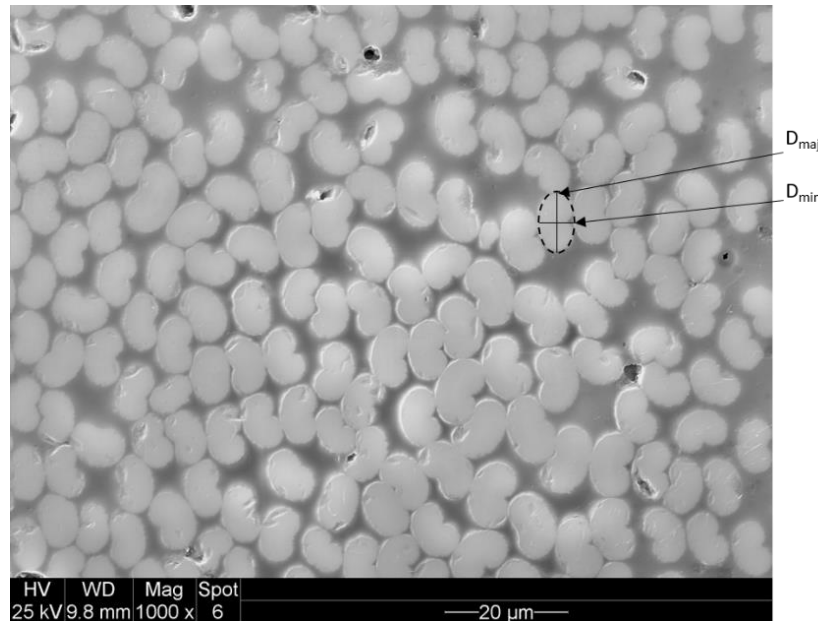


Figure 2.1: Representative micrograph of A-42 carbon fibers showing kidney-bean shaped cross-section with an equivalent ellipse overlaid where the major (D_{maj}) and minor (D_{min}) axis of the ellipse were identified.

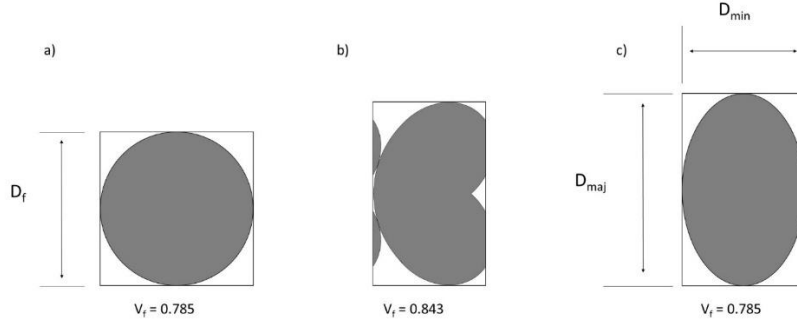


Figure 2.2: Examples of square packed unit cells with their maximum packing fraction for a) circular fiber, b) kidney-bean shaped fibers with consistent in-plane fiber alignment, c) elliptically shaped fiber with consistent in-plane fiber alignment.

2.4.2 Tensioned Fiber Bed Compaction Method

The experimental setup for fiber bed compaction is shown in Figure 2.3, where the dry, untwisted carbon fiber tows were attached at a fixed position and draped over a notched pin (4.68mm wide, 7.15mm in diameter) with a mass (m) attached to the end of the tow, shown in Figure 2.4. The compaction force (F) was calculated from the force balance on the pin, Equation (2.6). The horizontal (F_x) and vertical (F_y) components of the compaction force were calculated from the wrap angle (θ) and tow tension (T) with Equations (2.7) and (2.8), respectively.

$$F = \sqrt{F_x^2 + F_y^2} \quad (2.6)$$

$$F_x = -T \sin(\theta) \quad (2.7)$$

$$F_y = T \cos(\theta) - T \quad (2.8)$$

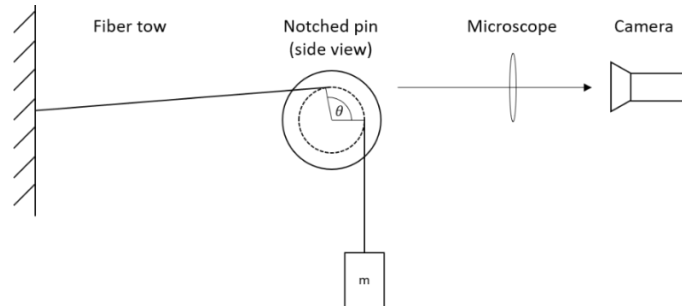


Figure 2.3: Experimental setup for fiber bed compaction where θ represents the fiber wrap angle and m represents the mass attached to the fiber tow.

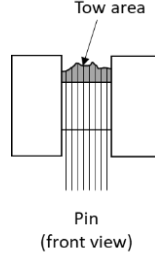


Figure 2.4: Front view of the notched pin showing the fiber bed profile (in gray) occupied by the tow above the surface.

The compaction samples had pre-measured weight (9g to 19.7kg) attached to the end of the sample to control the compaction pressure. The compaction samples consisted of 1, 2, and 4 carbon fiber tows to verify compaction behavior did not scale with individual fiber tension. The loaded sample rested for 1 minute to allow fiber relaxation to occur, before the 3MP Leica camera (mounted on a stereo microscope) captured an image of the compacted fiber bed profile. The method for recording the compacted fiber bed profile was a modification to the laser light sectioning method described by Kastanis et al.[15]. The tows wrapped 95° (θ) around the curved surface to ensure the trailing fibers were not in the image. This process was repeated in triplicate for each weight.

The compaction pressure (P) was calculated from the wrap area (A_{wrap}) and compaction force (F) on the tow, as shown in Equation (2.9). The wrap area was calculated from the pin diameter (d), pin width (w), and wrap angle (θ) in degrees and is shown in Equation (2.10).

$$P = \frac{F}{A_{wrap}} \quad (2.9)$$

$$A_{wrap} = \pi d w \frac{\theta}{360^\circ} \quad (2.10)$$

The fiber volume fraction measurements were measured using the optical microscope to capture the compacted tow profiles. The images of the tow profile were analyzed in ImageJ to determine the area of the compacted tow (A_{tow}). During image post processing, the compacted tow images were compared to the unloaded tow to determine the projected tow area above the notched pin. The compacted tow area was defined by the top profile of the compacted fiber bed and the contact surfaces with the pin, which corresponded to the gray region in Figure 2.4. The total area

of the fiber (A_{fibers}) calculated as average fiber cross-sectional area ($39.2\mu\text{m}^2$) multiplied by the filament count (24,000) and the number of tows (1, 2, or 4). The fiber volume fraction was calculated with Equation (2.11). The reported error represented the replicate error in the fiber volume fraction measurement.

$$V_f = \frac{A_{\text{tow}}}{A_{\text{fibers}}} \quad (2.11)$$

2.4.3 Representative Kidney-Bean Fiber Unit Cells

The representative kidney-bean shaped fiber referred to as “KB-fiber” used in this study was selected from DowAksa A-42 carbon fiber, shown in Figure 2.1. A representative fiber geometry was selected from Figure 3.3. The KB-fiber’s geometry closely matched the perimeter of the A-42 fiber and was scaled to have the same average cross-sectional area, $39.20\mu\text{m}^2$. This fiber area corresponded to an equivalent circular fiber with a diameter of $7.06\mu\text{m}$. The geometry was constructed with a set of intersecting ellipses coincident at their co-vertex. The ellipses were placed at an angle 2θ relative to each other and an arc on the convex side connected the ellipses at their opposite co-vertex. Figure 2.1 shows the dimensions used for the KB-fiber geometry. The representative fiber was used in the flow simulations to determine the permeability of the fiber bed.

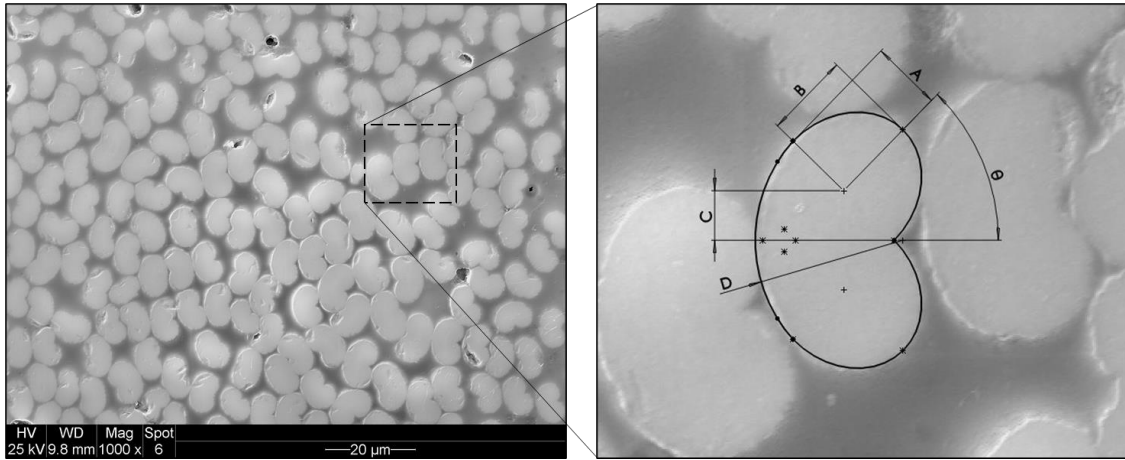


Figure 2.5: Representative micrograph of A-42 carbon fibers showing kidney-bean shaped cross-section with the following dimensions in μm were used to construct the representative fiber: $A = 2.40$, $B = 2.88$, $C = 1.68$, $D = R5.02$, and $\theta = 45.7^\circ$.

The KB-fiber was placed in hexagonally and square packed unit cells and their associated maximum packing fractions are shown in Figure 3.3 compared to circular fibers. The kidney-bean and circular fibers were scaled to have the same fiber cross-sectional area. The KB-fiber was assumed to have a consistent in-plane orientation. Additionally, KB-fiber had two distinct hexagonally packed unit cell geometries because of the fiber's asymmetry. The unit cells transverse permeabilities were used to compare the permeability of the KB-fibers to circular fibers with fiber volume fractions 0.30 – 0.75 and unit cell orientations: 0° , $+90^\circ$, and -90° .

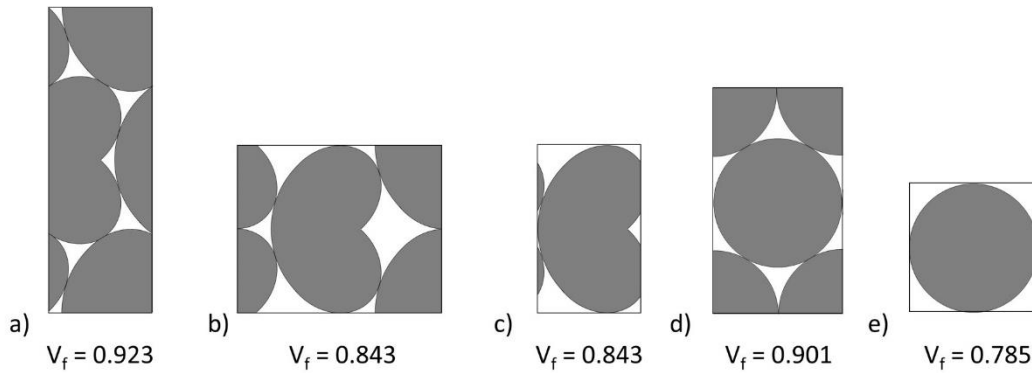


Figure 2.6: Examples of fiber packing unit cells with their maximum packing fraction for a) hexagonal pack – 1 KB-fiber, b) hexagonal pack – 2 KB-fiber, c) square pack KB-fiber, d) hexagonal pack circular fiber, e) square pack circular fiber.

2.4.4 Flow Simulation and Boundary Conditions

The hexagonal and square packed unit cells of kidney-bean and circular fibers were placed in fiber arrays consisting of 32 to 96 unit cells, depending on fiber volume fraction. Approximate fiber array dimensions were $100\mu\text{m} \times 100\mu\text{m} \times 10\mu\text{m}$. The mesh was generated using scFLOW software with an octree parameter of 6,000,000. From there, a surface mesh was generated, prism layers were inserted and converted to a polyhedral mesh. A meshed fiber array example is shown in Figure 2.7. Seven prism layer elements were inserted on the model fiber surfaces to ensure a minimum of 14 elements would define the narrow channel gap at high fiber volume fractions. The mesh was swept along the fiber direction and arrays consisted of 500,000 to 850,000 elements depending on packing density. The high element count ensured the results were not mesh size dependent, as can be seen in Figure 2.8. The fiber array inlet boundary condition was set to a normal velocity of 0.1mm/s and the outlet pressure was specified to be 0 Pa. The array sidewall

boundary conditions were set to free-slip so array edge effects would not influence the pressure drop across the array. The fiber surfaces were modeled with a no-slip boundary condition.

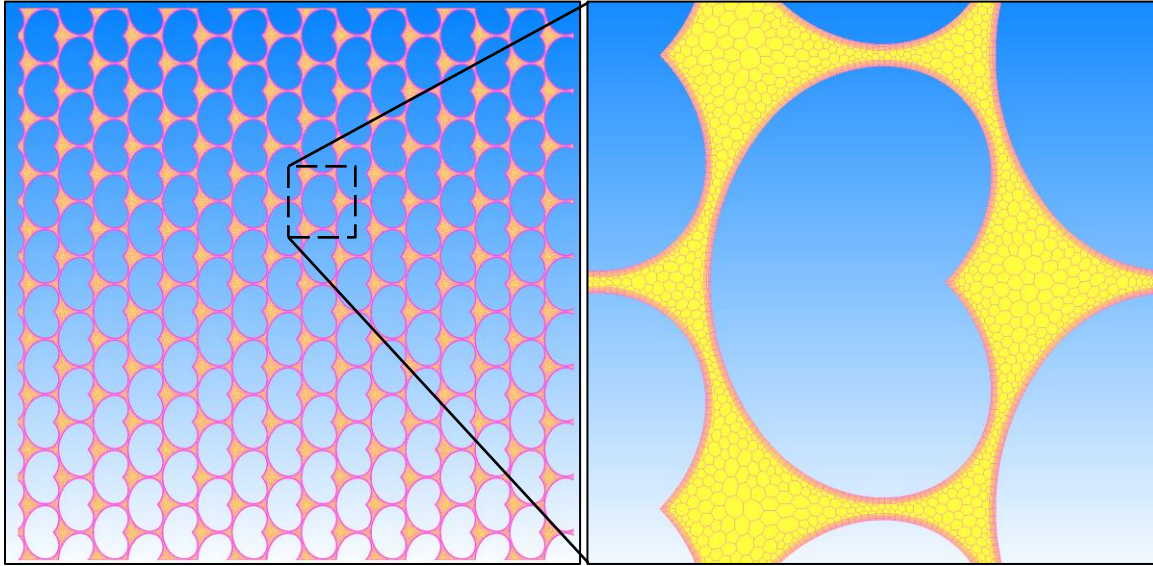


Figure 2.7: Example of meshed fiber array for KB-fiber with a hexagonal pack – 2 at 0.75 fiber volume fraction.

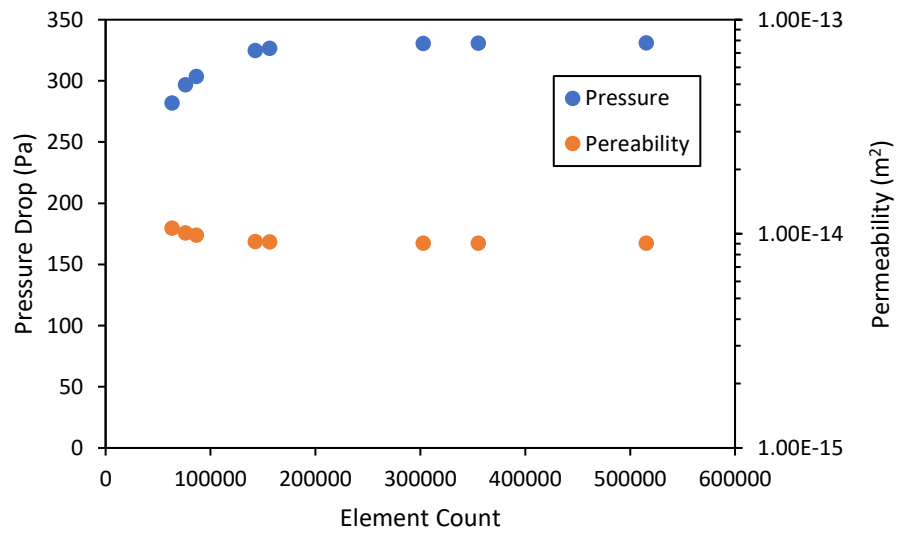


Figure 2.8: Example of element count sensitivity on pressure and permeability.

The computational fluid dynamic flow simulations were performed with water as fluid at steady-state to measure the pressure drop and determine the permeability across the fiber array.

The water was at 20°C with a viscosity of $1.016 \times 10^{-4} \text{ Pa}\cdot\text{s}$. The mass and momentum conservation equations for an isothermal, incompressible fluid at steady state are shown in Equations (2.12) and (2.13). The Navier-Stokes equation was solved using the Semi-Implicit Method for Pressure Linked Equations-Consistent (SIMPLEC) algorithm. A convergence check for steady-state analysis compared the momentum, pressure, and turbulent kinetic energy terms residual for the convergence criterion of 10^{-5} . The KB-fiber array inlet conditions were applied to the top (0°), right ($+90^\circ$), and left (-90°) array surfaces with the outlet conditions applied on the surface parallel to the inlet. The variations in kidney-bean orientation established the effect orientation had on transverse permeability.

$$\frac{\delta_i u_i}{\delta x_i} = 0 \quad (2.12)$$

$$\rho \frac{\delta u_j u_i}{\delta x_j} = -\frac{\delta p}{\delta x_j} + \mu \frac{\delta^2 u_i}{\delta x_j \delta x_j} \quad (2.13)$$

The permeability was calculated from the pressure drop (ΔP) from the flow simulation across the fiber bed, superficial velocity (u), thickness (X), and viscosity (η) using Darcy's law, shown in Equation (2.14) and rearranged for permeability (K) in Equation (2.15). The superficial velocity was calculated from the normal velocity and inlet area fraction. Depending on the fiber volume fraction, the superficial velocity varied between 0.01 – 0.08 mm/s. The tortuosity (K_1), shown in Equation (2.16), for each finite element simulation was determined by taking the streamline length (L_e) that passed through the region of maximum velocity and normalized to the array thickness.

$$u = \frac{K \Delta P}{\eta X (1-V_f)} \quad (2.14)$$

$$K = \frac{u X \eta}{\Delta P} \quad (2.15)$$

$$K_1 = \frac{L_e}{X} \quad (2.16)$$

2.5 Results and Discussion

2.5.1 Kidney-Bean shaped carbon fiber compaction

The measured fiber volume fractions ranged from 0.29 to 0.80 and corresponded with pressures from 0.01 to 10.25 MPa. The compaction data in Figure 2.9 for kidney-bean shaped carbon fiber showed similar final fiber volume fractions compared to the circular carbon fiber compaction data reported by Gutowski et al.[13]. Below $V_f = 0.65$, the pressures for the kidney-bean shaped fibers at comparable fiber volume fractions were often one to two orders of magnitude larger than the circular fiber. For comparison, the circular carbon fiber compaction trend modeled by Equation (2.1) is shown in Figure 2.9. The higher required compaction pressures for comparable fiber volume fractions suggested the fiber's irregular cross-sectional shape influenced the compaction behavior.

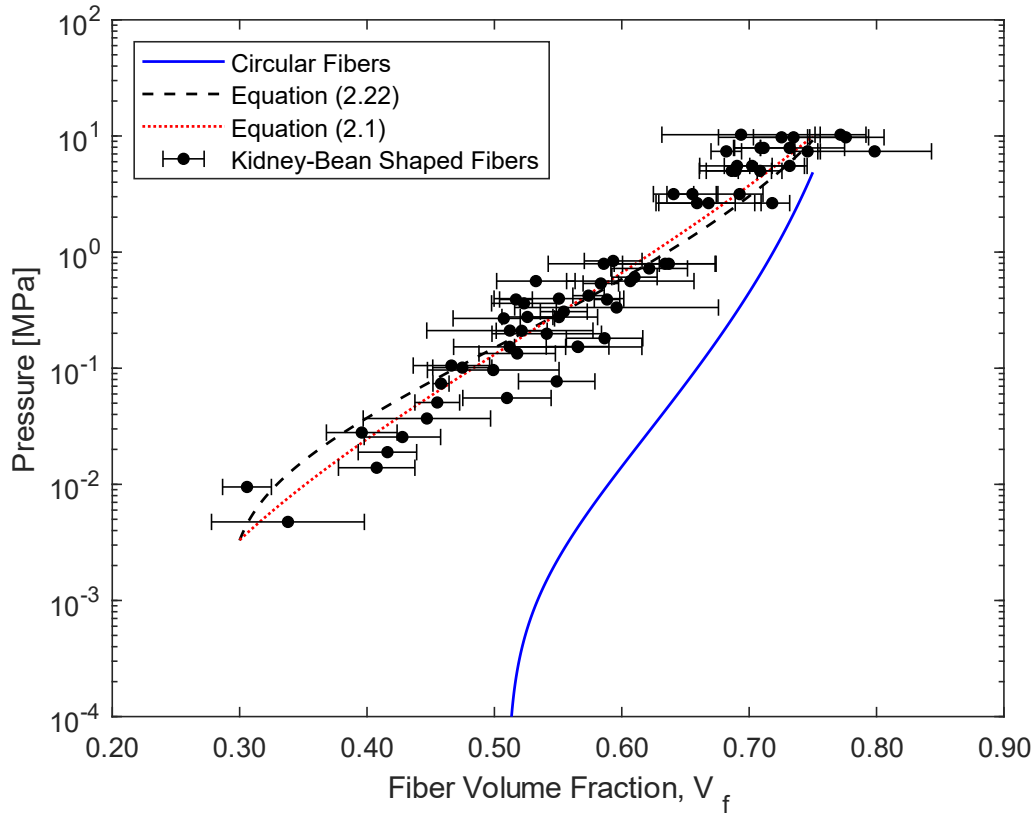


Figure 2.9: Kidney-bean shaped fiber compaction data compared to circular fibers. The kidney-bean shaped fibers were fitted to Equations (2.1) and (2.22) with the model parameters shown in Table 2.1. Error bars represented replicate error of the compacted tows.

The different compaction trends were considered to be caused by the difference in stiffness of the kidney-bean shaped fibers. The modulus of the kidney-bean shaped fiber (240GPa) was similar to the previously studied circular fibers (230GPa) and did not justify the difference in compaction between the different fiber shapes. Next, the difference in second moments of area (I) for the fiber shapes were considered to explain the compaction trends observed. The second moments of area appeared in the A term of Equation (2.1). The general description of A is shown in Equation (2.11), where β is the span length to height ratio, E is the modulus, and D is the fiber diameter.

$$A = \frac{192 EI}{D^4 \beta^4} \quad (2.17)$$

For circular fibers, the out of plane bending behavior was the same regardless of fiber orientation and is shown in Equation (2.18). For an irregularly shaped fiber, the second moment of area was dependent on fiber orientation. Since the fiber orientation varied throughout the tow, both bending axes were considered. The second moments of area for an ellipse were used to define the upper and lower bound of I for the kidney-bean shaped fibers and are shown in Equations (2.19) and (2.20), where D_{maj} was the major ellipse axis and D_{min} was the minor ellipse axis.

$$I_x = I_y = \frac{\pi}{64} D^4 \quad (2.18)$$

$$I_x = \frac{\pi}{64} D_{maj}^3 D_{min} \quad (2.19)$$

$$I_y = \frac{\pi}{64} D_{maj} D_{min}^3 \quad (2.20)$$

The kidney-bean shape observed in Figure 2.1 was generalized to an ellipse shape using FIJI fit ellipse algorithm [37]. A total of 187 kidney-bean shaped fibers were measured and found to have an average cross-sectional area of $39.2 \pm 5.2 \mu m^2$. The resulting ellipse fit was found to have $D_{maj} = 8.8 \pm 0.7 \mu m$ and $D_{min} = 5.6 \pm 0.5 \mu m$. The second moments of area for an ellipse provided an upper and lower bound for the fibers depending on the fiber orientation. This can be related back to the second moment of area for a circular fiber via the fiber in-plane aspect ratio (ϕ) and the expression shown in Equation (2.21).

$$\frac{1}{\phi} I_{circle} \leq I_{ellipse} \leq \phi I_{circle} \quad (2.21)$$

After considering the difference in geometric stiffness of the fibers, the compaction data was fitted to Equation (2.1) as shown in Figure 2.9. In order to not bias the data towards the larger compaction pressures, the log of compaction pressure was fitted to determine V_o , V_a , and A using the sum of squared residuals approach. These parameters are reported in Table 2.1. While the optimized parameters to Equation (2.1) modeled the compaction trends, the resulting V_a parameter had a nonphysical value of 1.011. Expected values of V_a for circular fibers ranged between the maximum square pack (0.785) and hexagonal pack (0.901).

Table 2.1: Parameters used for Equations (2.1) and (2.22) to model the kidney-bean shaped fibers and compare to circular fibers.

ϕ	A [MPa]	V_o	V_a	β	Comments
-	0.000159	0.51	0.829	340	Reported values for circular fiber [13]
-	0.00710	0.199	1.011	20 – 30	Optimized fit for Equation (2.1)
1.57	0.0165	0.289	0.865	100 – 130	Optimized fit for Equation (2.22)

Additionally, the compaction samples consisted of 1, 2, and 4 carbon fiber tows and showed no discernible difference in compaction behavior, shown in Figure 2.10. Increasing the tow count decreased the tension per fiber for a given pressure and allowed more fibers to interact with the notched pin wall. Additionally, the tension was varied for the same compaction pressure and showed no secondary trend with the fiber volume fraction. The reduced fiber tension vs fiber volume fraction is shown in Figure 2.11, where the tension was normalized to the maximum tension for the specified compaction pressure. The fiber volume fraction was independent of tow tension. Since the compaction trends were the unaffected by tow count, this indicated neither the individual fiber tension nor pin side walls influenced the compaction behavior.

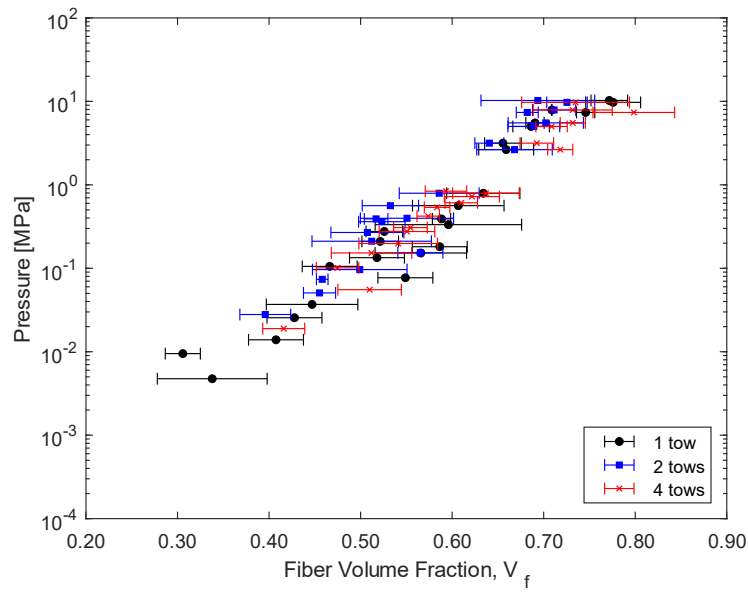


Figure 2.10: A-42 fiber compaction data for samples consisting of multiple fiber tows, demonstrating the experimental setup was not sensitive to tow count.

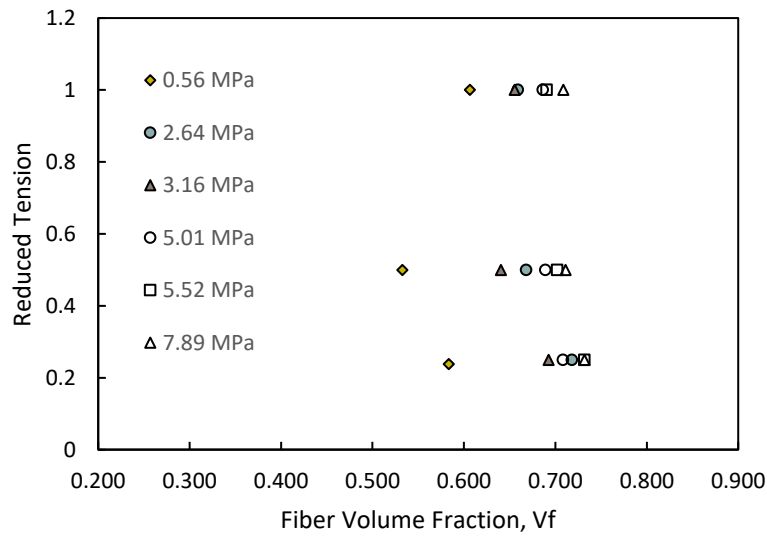


Figure 2.11: Reduced fiber tension vs the fiber volume fraction for various compaction pressures.

The pressure-fiber volume fraction relationship for the kidney-bean shaped fiber appeared to follow a different compaction trend compared to the circular fibers. Even after accounting for the fiber geometry's effect on the bending stiffness, Equation (2.1) with optimized parameters

didn't model the compaction trends with physical values for the model parameters. This indicated the shape of the fiber cross-section influenced the non-linear elastic response of the fiber bed and suggested a shape correction factor was warranted to extend Equation (2.1) to other fiber shapes. Any correction factor applied to Equation (2.1) needed to remain valid for circular fibers and recover the physical meaning of the parameters.

The proposed correction factor was based on the fiber's cross-sectional aspect ratio ($\phi = \frac{D_{maj}}{D_{min}}$). The aspect ratio from the ellipse fitting with ImageJ was found to be 1.57. The proposed modification to the Equation (2.1) utilized the fiber cross-sectional aspect ratio as a shape correction factor, shown in Equation (2.22), to account for fiber cross-sectional shape in the non-linear elastic term of the Gutowski model.

$$P = A \left(\frac{\sqrt{\frac{V_f}{V_o}} - 1}{\left(\sqrt{\frac{V_a}{V_f}} - 1 \right)^4} \right)^{\frac{1}{\phi}} \quad (2.22)$$

The modified Gutowski model was plotted in Figure 2.9 and showed good agreement with the kidney-bean fiber compaction data. The parameters used to model the A-42 fibers in Figure 2.9 with Equation (2.22) are summarized in Table 2.1. The model fit with Equation (2.22) led to reasonable values of $V_a = 0.865$, whereas Equation (2.1) resulted in a $V_a = 1.011$. Equation (2.22) had a $\beta = 100 - 130$, whereas Equation (2.1) had a $\beta = 20 - 30$, depending on the fiber orientation. Cai et al.[14] noted that β typically ranged between 100 - 300 for graphite fibers, which further suggested Equation (2.1) was not effectively describing the compaction of the kidney-bean shaped fibers. The cross-sectional aspect ratio term in Equation (2.22) accounted for the inefficient packing of an irregularly shaped fiber, such as a kidney-bean, while the fundamental compaction behavior originally defined by Gutowski model was preserved. Furthermore, the modified Gutowski model recovered the original equation for circular fibers when $\phi = 1$. The modified Gutowski model assumed the fiber cross-sections were randomly oriented and the non-linear elastic response of the fiber bed was caused by the fiber cross sectional shape. With these assumptions, the Gutowski model can be generalized for various fiber cross-sectional aspect ratios.

2.5.2 Permeability Simulation of Kidney-Bean Shaped Fibers

The unit cells considered in this analysis assumed a consistent in-plane fiber alignment and the permeabilities were determined from the pressure drop across the fiber bed. The pressure drop was uniform across the fiber bed, as see in Figure 2.12. Additionally, the free slip boundary condition at the edges of the fiber arrays did not disturb the pressure gradient along the flow direction.

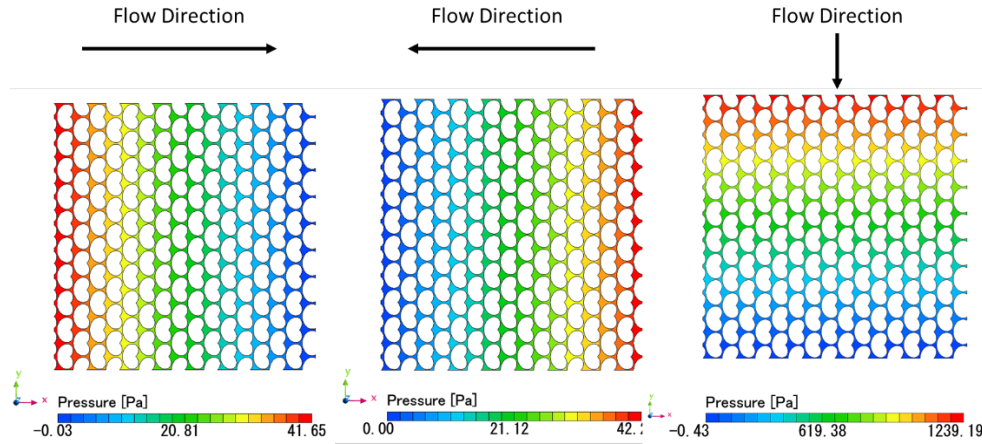


Figure 2.12: Example of pressure drop across fiber bed from permeability simulations.

The permeabilities from the flow simulation are shown in Figure 2.13 demonstrated that the fiber shape, unit cell orientation, and packing arrangement all had a substantial impact on the permeability of the fiber bed compared to circular fibers. The simulated permeabilities for the KB-fibers showed unit cells had an upper and lower bound of transverse permeability based on unit cell orientation. Additionally, the KB-fiber permeability decreased with fiber volume fraction, similarly to circular fibers. The flow simulation was validated by comparing the simulated permeability of circular fibers for a square and hexagonal unit cell to theoretical values described by Gebart [11]. The theoretical equations used for the validation are Equations (2.2) and (2.3) which accurately predicted the permeabilities shown in Figure 2.13-d) and e) for circular fibers.

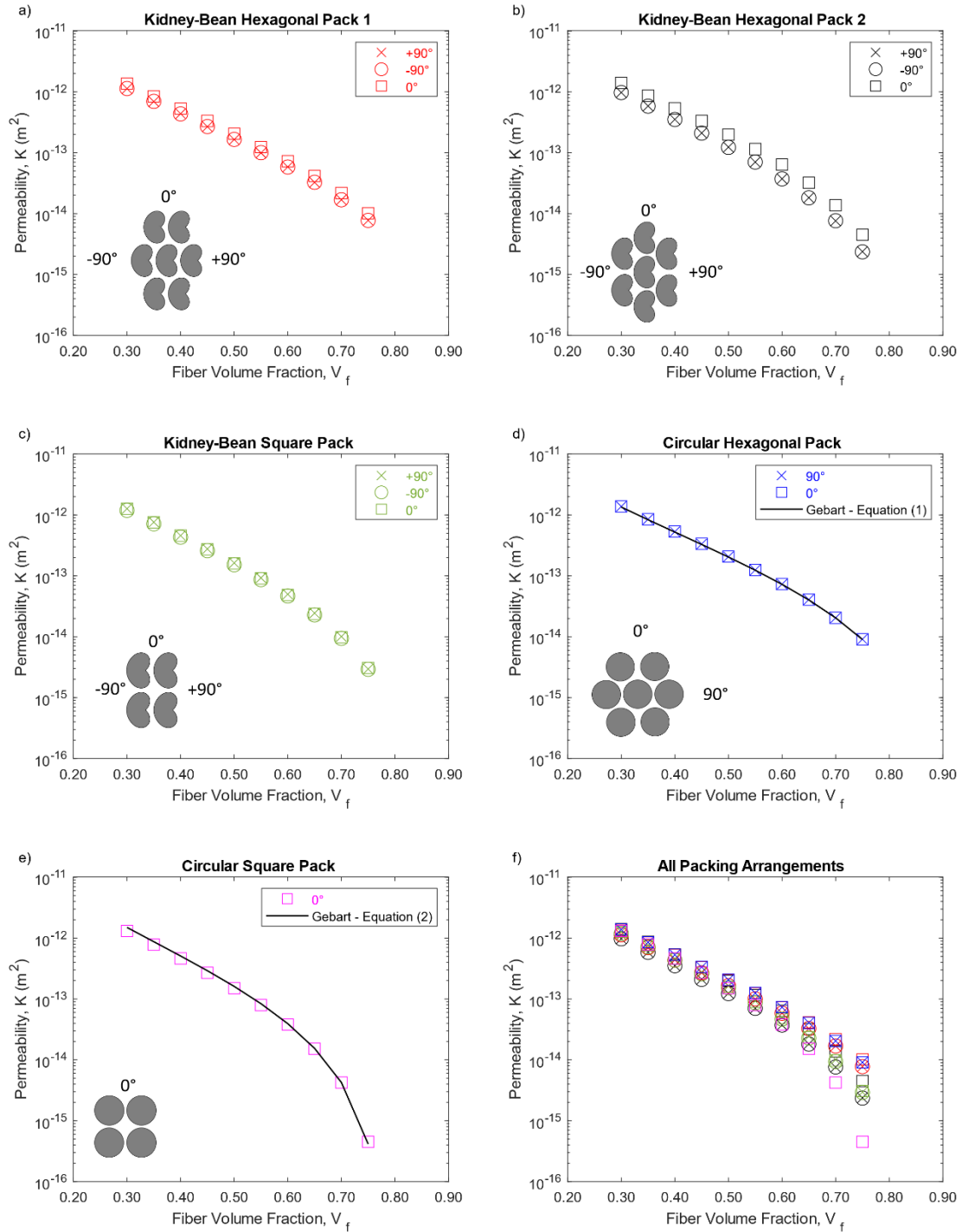


Figure 2.13: Permeabilities from the flow simulation for kidney-bean and circular fibers with different unit cell orientations for a) hexagonal pack – 1 KB-fibers, b) hexagonal pack – 2 KB-fibers, c) square pack KB-fibers, d) hexagonal pack circular fibers, and e) square pack circular fibers with f) comparing permeabilities for all fiber packing arrangements. Where d) and e) were compared to the theoretical permeability value in Equations (2.2) and (2.3).

The permeabilities for KB-fibers in hexagonal pack – 1 and – 2 are shown in Figure 2.13- a) and b), respectively. From these figures, there was a general trend for the $\pm 90^\circ$ unit cell orientations to have a lower permeability than the circular fibers with hexagonal packing. The 0° unit cell orientation for the KB-fibers hexagonal pack – 1 and – 2 had comparable permeabilities to the circular fibers at fiber volume fractions below 0.60. At higher fiber volume fractions, the permeability for the 0° unit cell orientation hexagonal pack – 1 was lower than the circular fibers while the hexagonal pack – 2 was larger. Furthermore, the difference in permeability between 0° and $\pm 90^\circ$ orientations for the hexagonal pack – 1 was mild and ranged from 17% at $V_f = 0.75$ to 24% at $V_f = 0.30$ while the difference for the hexagonal pack – 2 was more pronounced and ranged from 30% at $V_f = 0.75$ to 47% at $V_f = 0.30$. As fiber volume fraction decreased, unit cell orientation had a larger effect on the unit cell permeability, which can be seen from the normalized infiltration times in Figure 2.14.

The difference between circular and KB-fiber permeabilities was highlighted in Figure 2.14 through the infiltration time of fiber beds of equal thickness. The permeabilities determined from the simulations were used to compare infiltration times. The permeabilities determined from the simulations were used to compare infiltration times. The KB-fiber infiltration times were normalized with the infiltration time for a circular hexagonally packed fiber at the same fiber volume fraction. The $\pm 90^\circ$ orientations for KB-fibers with hexagonal packing had a normalized infiltration time 1.22 to 3.86 times longer than the hexagonal packed circular fibers. The difference in infiltration times indicated the cost savings A-42 fibers provided during the carbon fiber production may be lost during subsequent infiltration steps. Additionally, the difference in permeabilities was more pronounced at higher fiber volume fractions and was reduced by 15% at $V_f = 0.30$ and up to 74% at $V_f = 0.75$ compared to circular fibers with hexagonal packing.

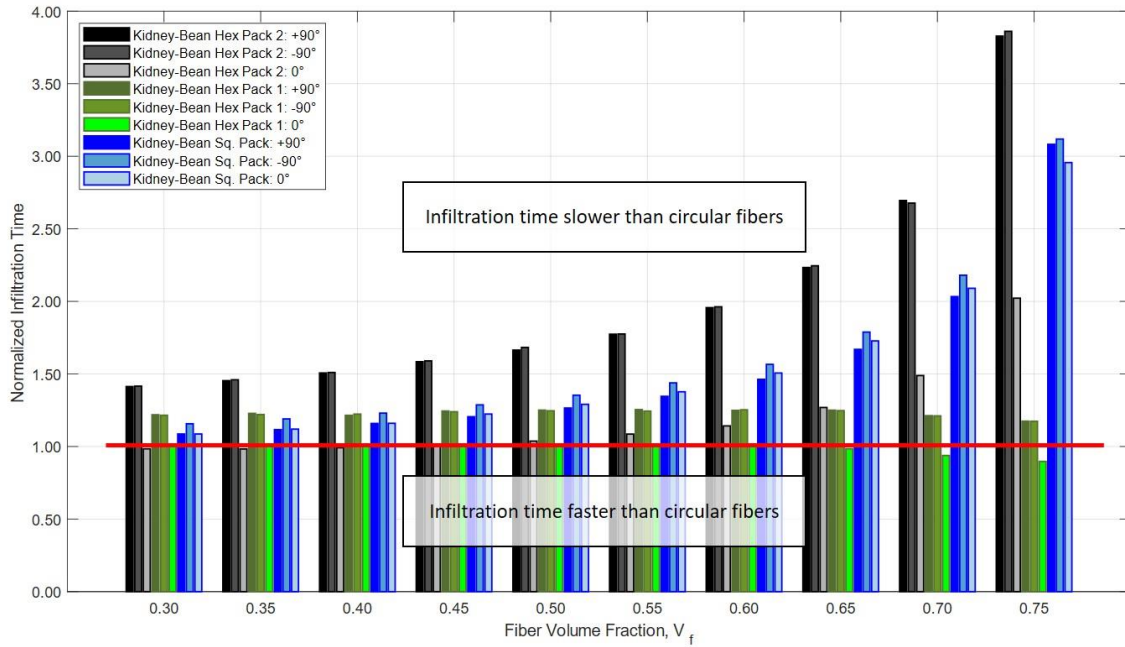


Figure 2.14: Normalized infiltration times for various KB-fiber packing arrangements and orientations relative to hexagonally packed circular fibers at the same fiber volume fractions. This shows the kidney-bean shaped fibers will have a substantially longer infiltration time at high fiber volume fractions relative to circular fibers with hexagonal packing.

The square packed KB-fiber permeability was not sensitive to unit cell orientation as seen in Figure 2.13-c). The normalized infiltration time shown in Figure 2.14 for the square packed KB-fiber unit cell was comparable at low fiber volume fractions to circular fibers, but quickly rose to 3.12 times the infiltration time at high fiber volume fractions. Thus, the square packed KB-fiber packing arrangement will infiltrate similarly to hexagonally packed circular fibers at low fiber volume fractions.

The tortuosity for the KB-fibers was dependent on the packing arrangement, fiber volume fraction, and unit cell orientation, as seen in Figure 2.15. The tortuosity measurements were taken from the streamline that passed through the maximum velocity. The KB-fiber hexagonal pack – 2's $\pm 90^\circ$ orientation's tortuosity was significantly larger compared to the 0° orientation, shown in Figure 2.15b. The difference in tortuosity highlighted the dependence the unit cell orientation had on the hexagonal pack – 2's permeability. Furthermore, the $\pm 90^\circ$ hexagonal pack – 2's tortuosity increased with fiber volume fraction, while the tortuosity in the 0° orientation was not sensitive to fiber volume fraction. The tortuosity for the KB-fiber hexagonal pack – 1 was not significantly

influenced by unit cell orientation, shown in Figure 2.15-a); however, there was a slight increase in tortuosity as the fiber volume fraction increased. Finally, the KB-fiber square packed unit tortuosity did not exhibit a significant dependence on the unit cell orientation nor fiber volume fraction, as seen in Figure 2.15c.

In any composite component, a variety of fiber packing microstructures will be present. This was exceptionally true for kidney-bean shaped carbon fibers, as seen in Figure 2.1. Therefore, the permeabilities for different packing arrangements and unit cell orientations provided a quantified upper and lower bound for kidney-bean shaped fiber permeabilities. When compared across all packing arrangements and unit cell orientations, the upper bound permeability for KB-fibers can be the same as circular fibers. The lower bound for permeability was 74% smaller compared to hexagonal packed circular fibers. Furthermore, these bounds indicated that infiltrating KB-fibers will take appreciably longer than circular fibers and therefore require additional manufacturing considerations when selecting them.

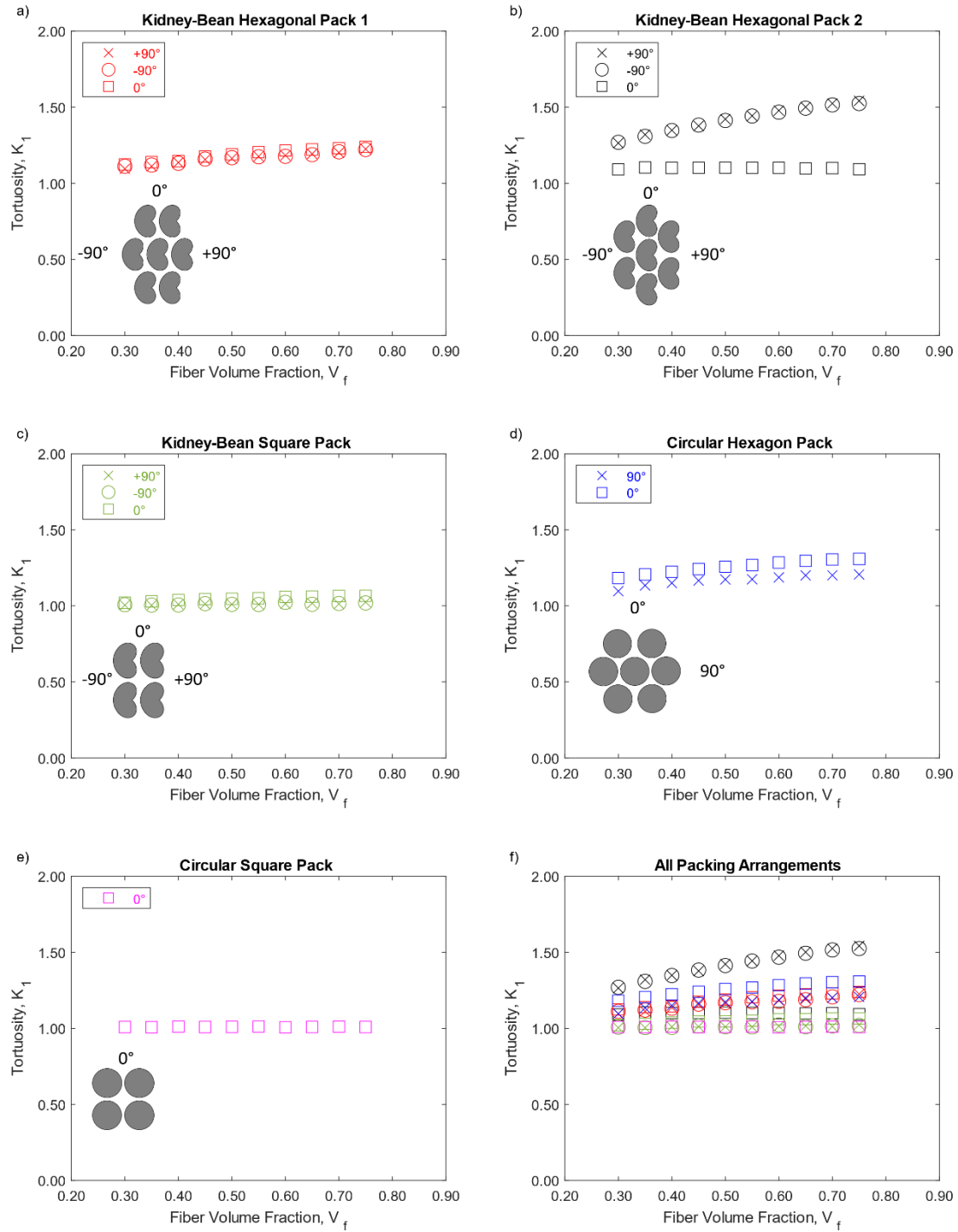


Figure 2.15: Tortuosity with different fluid flow directions for a) hexagonally pack – 1 KB-fibers, b) hexagonally pack – 2 KB-fibers, c) square pack KB-fibers, d) hexagonally pack circular fibers, and e) square pack circular fibers with f) comparing tortuosities for all fiber packing arrangements.

2.5.3 Modeling Permeability in Kidney-Bean Shaped Fibers

The permeabilities determined from the flow simulation were modeled with the Equation (2.4) and Equation (2.23). Both equations were able to model the permeability for the KB-fiber unit cells, shown in Figure 2.16. To fit Equation (2.4) to the KB-fiber's permeability, the tortuosity needed to be measured and the shape factor term be empirically fitted. The tortuosity and shape factor were combined to form the Kozeny constant (k), shown in Equation (2.5). In contrast, Equation (2.23) required the maximum fiber volume fraction ($V_{f \max}$) and only required a single constant (C) to be fitted for each unit cell.

$$K = r^2 C \left(\sqrt{\frac{V_{f \max}}{V_f}} - 1 \right)^{\frac{5}{2}} \quad (2.23)$$

The Carman-Kozeny equation provided an excellent fit, shown in Figure 2.16-a), c), and e) when a unique Kozeny constant was used for each fiber volume fraction, unit cell, and orientation. The shape factor term for the Carman-Kozeny equation was empirically fitted and is shown in Figure 2.17. The shape factors for all fiber packing arrangements displayed a parabolic relationship with fiber volume fraction. The tortuosities measured from the flow simulations shown in Figure 2.15 demonstrated the tortuosity was not constant and increased with fiber volume fraction for both fiber shapes. The Carman-Kozeny constant had been reported in the literature as not being a constant because of the change in tortuosity with fiber volume fraction [12,24,26,29,35,36]. When combined to form the Kozeny constant shown in Figure 2.18, the Kozeny constant appeared to also have a parabolic relationship with fiber volume fraction. This indicated the Kozeny constant was more impacted by the shape factor than the tortuosity as previously believed. The parabolic relationship between shape factor and fiber volume fraction was also observed by Yazdchi [26] for circular, square, and elliptic shaped fibers. The Carman-Kozeny equation did not consider the maximum fiber volume fraction for each cell, hence impacting the shape factor fit. Therefore, the Carman-Kozeny equation required a unique constant to be fitted for each fiber volume fraction, which made the Carman-Kozeny equation a poor method to model the transverse permeability.

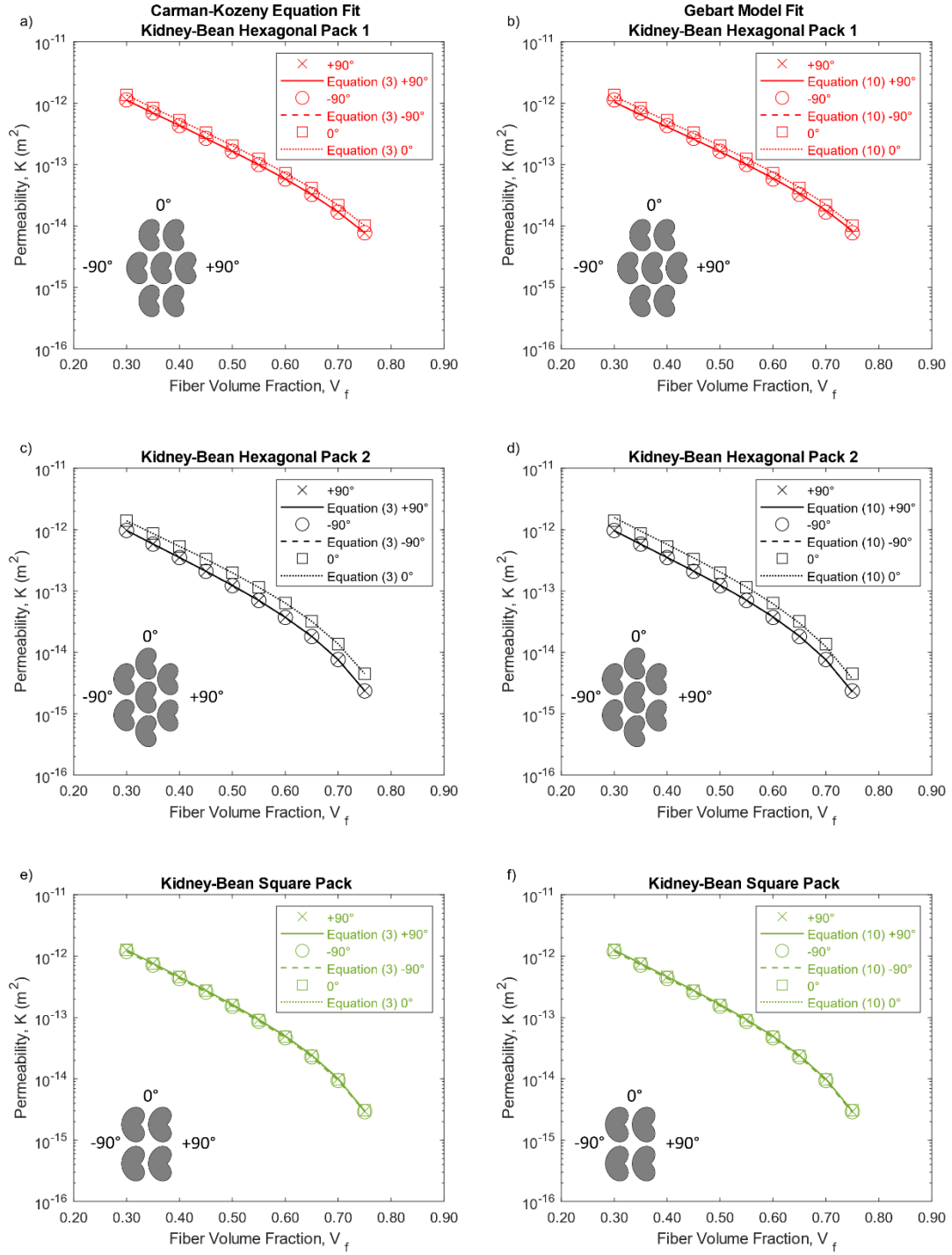


Figure 2.16: Permeability of KB-fibers compared to Equation (2.4) for a) Hexagonal Pack – 1, c) Hexagonal Pack – 2, and e) Square Pack. Permeability of KB-fibers compared to Equation (2.23) for b) Hexagonal Pack – 1, d) Hexagonal Pack – 2, and f) Square Pack.

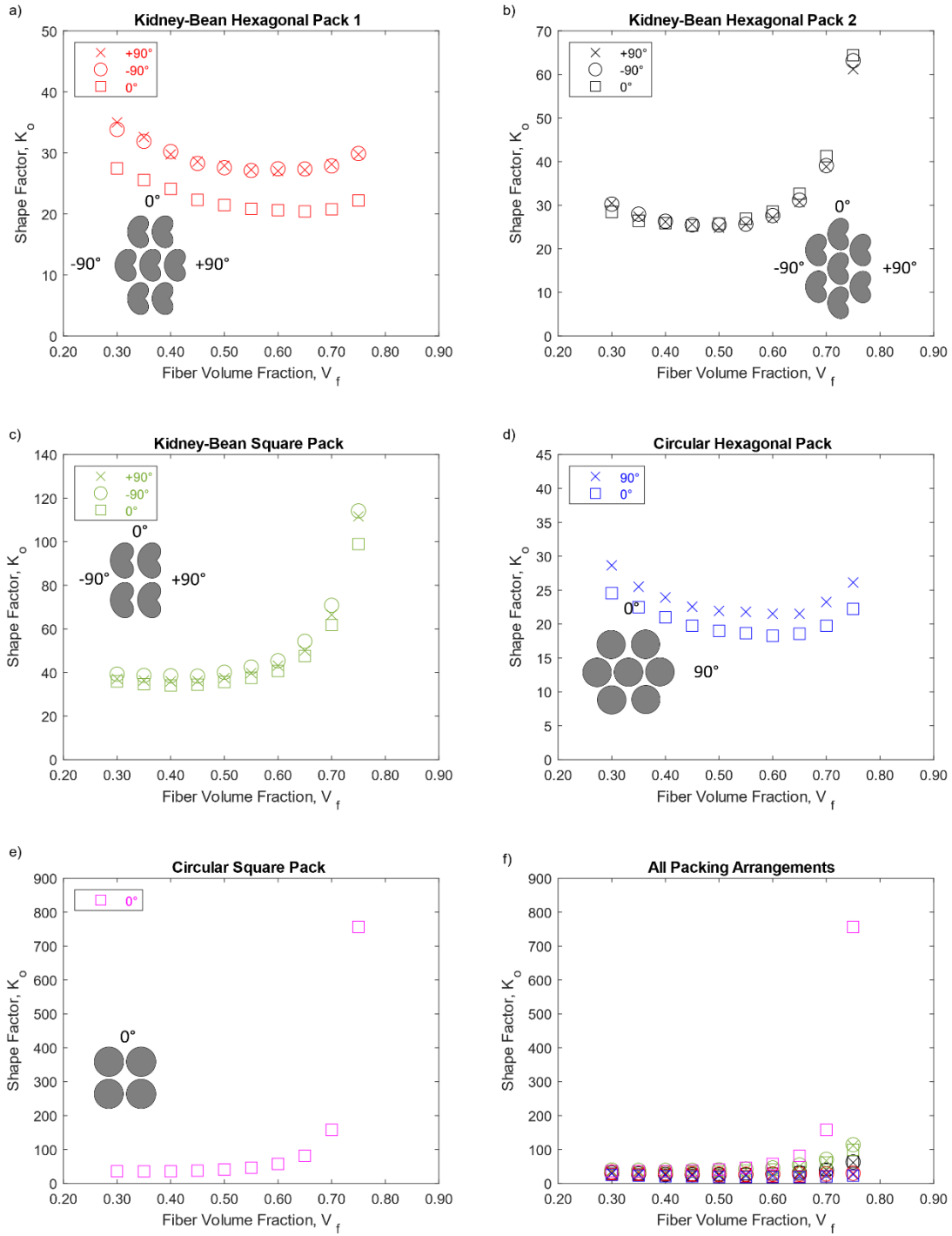


Figure 2.17: Shape factor with different fluid flow directions for a) hexagonally pack – 1 KB-fibers, b) hexagonally pack – 2 KB-fibers, c) square pack KB-fibers, d) hexagonally pack circular fibers, and e) square pack circular fibers with f) comparing shape factors for all fiber packing arrangements.

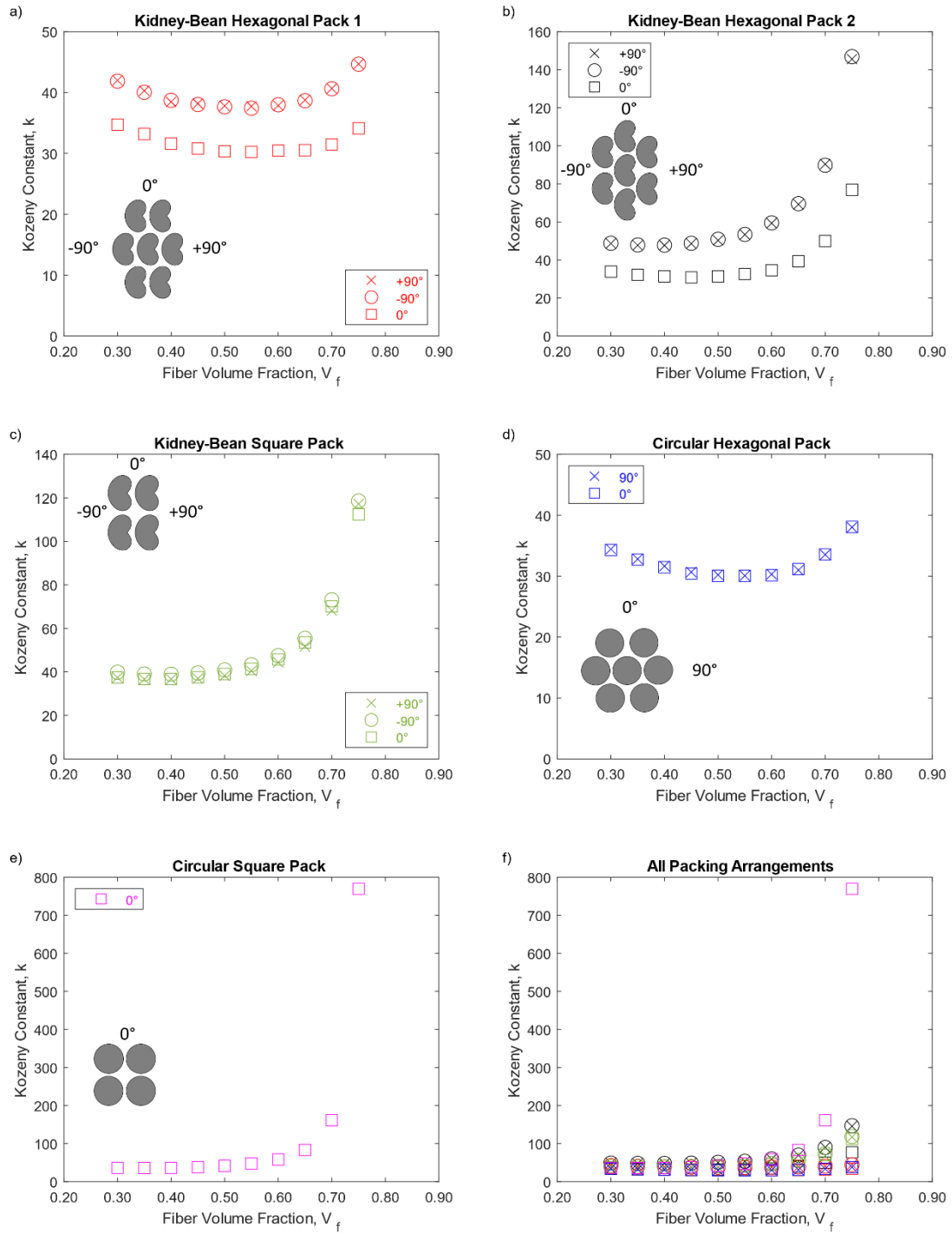


Figure 2.18: Kozeny constants with different fluid flow directions for a) hexagonally pack – 1 KB-fibers, b) hexagonally pack – 2 KB-fibers, c) square pack KB-fibers, d) hexagonally pack circular fibers, and e) square pack circular fibers with f) comparing Kozeny constants for all fiber packing arrangements.

Equation (2.23) accounted for the maximum fiber volume fraction, but was originally derived for circular fibers. Because the work was derived based on the gap between fibers, Equation (2.23) can be extended to different fiber shapes by empirically fitting the constant (C) for each unit cell orientation. The empirically fitted constants for Equation (2.23) are reported in Table 2.2 and the maximum fiber volume fraction for each unit cell is reported in Figure 3.3. These constants provided an excellent fit to Equation (2.23) for each unit cell and orientation, which can be seen in Figure 2.16-b), d), and f). Furthermore, Equation (2.23) provided a more robust fit compared to Equation (2.4) since a single constant was needed for each unit cell orientation. Therefore, Equation (2.23) was a more appropriate model to estimate the transverse permeability of the KB-fibers.

Table 2.2: Constants (C) for Equation (2.23) with various unit cell orientations and packing arrangements for KB-fibers.

Orientation	Hexagonal Pack 1	Hexagonal Pack 2	Square Pack
+90°	0.170	0.206	0.270
-90°	0.171	0.206	0.254
0°	0.213	0.338	0.267

2.6 Conclusions

In this study, the laser light sectioning method was modified to capture kidney-bean shaped carbon fiber tow deformations via stereo microscopy. The compaction data showed the irregular shape of carbon fiber required more pressure to compact, which has implications during infiltration and consolidation efficiency compared to circular carbon fiber. This work demonstrated that the difference in compaction trends was not solely caused by the fiber stiffness, but also a change in the non-linear elastic response of the fiber bed. Furthermore, the compaction data for kidney-bean shaped carbon fiber was not modeled by Equation (2.1) with physically valid V_a values. Therefore, a shape correction factor was proposed for the Gutowski model, shown in Equation (2.22), which provided an excellent fit with the compaction data. The shape correction factor was based on $\frac{1}{\text{Aspect ratio}}$ and applied to the non-linear elastic response. The shape correction factor accounted for the fiber bed's resistance to compaction with a physical constant describing the fiber's irregular shape. The modified Gutowski model accurately predicted the compaction for the kidney-bean

shaped fibers with a cross-sectional aspect ratio of 1.57. Additionally, the proposed extension to the Gutowski model recovered the original solution for circular fibers. Finally, the extension of the Gutowski model to irregularly shaped fibers is important as inexpensive carbon fibers become commonly available.

The kidney-bean shaped carbon fiber's cross-sectional shape was caused by manufacturing conditions during the PAN precursor production. A representative KB-fiber was used to establish different unit cell configurations for this novel carbon fiber shape. Since the KB-fiber had some degree of asymmetry, there were two valid hexagonal packing arrangements. The unit cells were placed in fiber arrays and flow simulations were performed to determine the fiber's transverse permeability. The simulations demonstrated that unit cell orientation affected the permeability. Thus, an upper and lower bound for KB-fiber permeability was established based on unit cell arrangement and orientation, shown in Figure 2.19. At a minimum, the hexagonal packed unit cell orientation caused a 17% reduction in permeability for the same unit cell and fiber volume fraction between the $\pm 90^\circ$ and 0° orientations. In the most extreme case, a 47% reduction in the permeability was observed between the $\pm 90^\circ$ and 0° orientations. Additionally, the permeability's dependence on unit cell orientation increased with fiber volume fraction. The true permeability of KB-fibers will lie somewhere between these bounds, since fiber packing in polymer composites has a variety of local packing arrangements, fiber orientations, and fiber volume fractions.

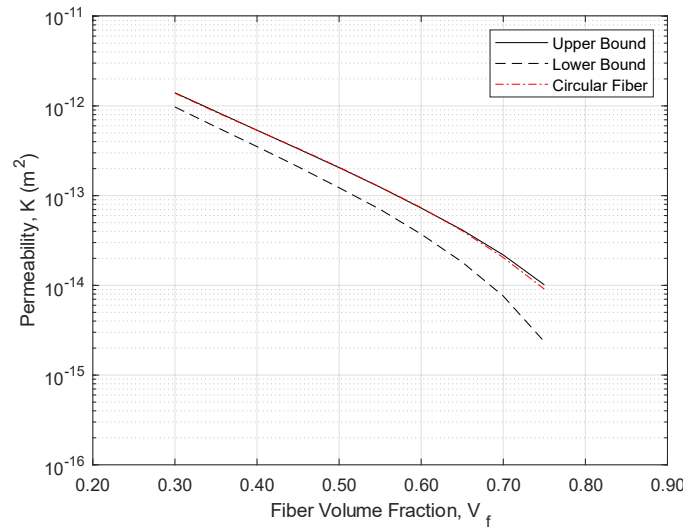


Figure 2.19: Upper and lower bound permeability across all KB-fiber unit cells compared to circular fibers with hexagonal packing.

The permeability for the KB-fiber was consistently lower across all unit cell arrangements and orientations when compared to circular fibers with hexagonal packing. At maximum, a 74% reduction in permeability was observed for the KB-fiber which corresponded to a 3.86 time increase in infiltration compared to traditional carbon fiber. The permeability was also modeled using the Carman-Kozeny equation (Equation (2.4)) and Gebart's model (Equation (2.23)). Equation (2.4) was able to fit the KB-fiber permeability when unique shape factors were fitted for each unit cell arrangement, orientation, and fiber volume fraction. The fitting resulted in the Kozeny constant having a parabolic relationship with fiber volume fraction. In contrast, Equation (2.23) provided an appropriate fit to the KB-fiber permeability vs fiber volume fraction with a unique constant for each unit cell arrangement and orientation. Thus, Equation (2.23) was found to be better suited to describe the transverse permeability for the KB-fiber.

Determining the compaction and permeability behavior of the kidney-bean shaped carbon fiber was critical for modeling an infiltration process. In Chapter 3, these properties were used to describe an infiltration process with a rapid cure epoxy resin.

2.7 References

- [1] Jones RM. Mechanics of Composite Materials. 2nd ed. CRC Press; 1999. <https://doi.org/10.1201/9781498711067>.
- [2] Martensson P, Zenkert D, Akernro M. Effects of manufacturing constraints on the cost and weight efficiency of integral and differential automotive composite structures. *Compos Struct* 2015;134:572–8. <https://doi.org/10.1016/j.compstruct.2015.08.115>.
- [3] Baker DA, Rials TG. Recent advances in low-cost carbon fiber manufacture from lignin. *J Appl Polym Sci* 2013;130:713–28. <https://doi.org/10.1002/app.39273>.
- [4] Khayyam H, Jazar RN, Nunna S, Golkarnarenji G, Badii K, Fakhrhoseini SM, et al. PAN precursor fabrication, applications and thermal stabilization process in carbon fiber production: Experimental and mathematical modelling. *Prog Mater Sci* 2020;107:100575. <https://doi.org/10.1016/j.pmatsci.2019.100575>.
- [5] Nunna S, Maghe M, Rana R, Varley RJ, Knorr DB, Sands JM, et al. Time dependent structure and property evolution in fibres during continuous carbon fibre manufacturing. *Materials (Basel)* 2019;12. <https://doi.org/10.3390/ma12071069>.
- [6] Gill AS, Visotsky D, Mears L, Summers JD. Cost Estimation Model for Polyacrylonitrile-Based Carbon Fiber Manufacturing Process. *J Manuf Sci Eng Trans ASME* 2017;139:1–8. <https://doi.org/10.1115/1.4034713>.

- [7] Ogale A, Zhang M, Jin J. Sustainable polymers and polymer science: Dedicated to the life and work of Richard P. Wool. *J Appl Polym Sci* 2016;133. <https://doi.org/10.1002/app.44212>.
- [8] Dong R, Keuser M, Zeng X, Zhao J, Zhang Y, Wu C, et al. Phase equilibria and charge fractionation in polydisperse polyelectrolyte solutions 2004. <https://doi.org/10.1002/polb>.
- [9] Molyneux M, Murray P, P. Murray B. Prepreg, tape and fabric technology for advanced composites. *Composites* 1983;14:87–91. [https://doi.org/10.1016/S0010-4361\(83\)80003-2](https://doi.org/10.1016/S0010-4361(83)80003-2).
- [10] Dave R, Kardos JL, Dudukovic MP. A Model For Resin Flow During Composite Processing .1. General Mathematical Development. *Polym Compos* 1987;8:29–38. <https://doi.org/10.1002/pc.750080106>.
- [11] Gebart BR. Permeability of unidirectional reinforcements for RTM. *J Compos Mater* 1992;26:1100–33. <https://doi.org/10.1177/002199839202600802>.
- [12] Astrom BT, Pipes RB, Advani SG. On flow through aligned fiber beds and its application to composites processing. *J Compos Mater* 1992;26:1351–73. <https://doi.org/10.1177/002199839202600907>.
- [13] Gutowski TG, Cai Z, Bauer S, Boucher D, Kingery J, Wineman S. Consolidation Experiments For Laminate Composites. *J Compos Mater* 1987;21:650–69. <https://doi.org/10.1177/002199838702100705>.
- [14] Cai Z, Gutowski T. The 3-D Deformation Behavior of a Lubricated Fiber Bundle. *J Compos Mater* 1992;26:1207–37. <https://doi.org/10.1177/002199839202600808>.
- [15] Kastanis D, Steiner H, Fauster E, Schledjewski R. Compaction behavior of continuous carbon fiber tows: an experimental analysis. *Adv Manuf Polym Compos Sci* 2015;1:169–74. <https://doi.org/10.1080/20550340.2015.1114794>.
- [16] Li M, Gu YZ, Zhang ZG, Sun ZJ. A simple method for the measurement of compaction and corresponding transverse permeability of composite prepregs. *Polym Compos* 2007;28:61–70. <https://doi.org/10.1002/pc.20255>.
- [17] Batch GL, Cumiskey S, Macosko CW. Compaction of fiber reinforcements. *Polym Compos* 2002;23:307–18. <https://doi.org/10.1002/pc.10433>.
- [18] Niaki SA, Forghani A, Vaziri R, Poursartip A. A two-phase integrated flow-stress process model for composites with application to highly compressible phases. *Mech Mater* 2017;109:51–66. <https://doi.org/10.1016/j.mechmat.2017.03.016>.
- [19] Luisier A, Bourban PE, Månson JAE. Reaction injection pultrusion of PA12 composites: Process and modelling. *Compos Part A Appl Sci Manuf* 2003;34:583–95. [https://doi.org/10.1016/S1359-835X\(03\)00101-5](https://doi.org/10.1016/S1359-835X(03)00101-5).

- [20] Connor M, Toll S, Manson JAE, Gibson AG. A Model For The Consolidation Of Aligned Thermoplastic Powder Impregnated Composites. *J Thermoplast Compos Mater* 1995;8:138–62.
- [21] Glebes R, Dustin J, Mansson J-A. Technical Cost Modeling Methodology for Novel Manufacturing. *SAMPE 2019 - Charlotte, NC*, vol. 2019- May, SAMPE; 2019. <https://doi.org/10.33599/nasampe/s.19.1490>.
- [22] Bernet N, Wakeman MD, Bourban PE, Månson JA. An integrated cost and consolidation model for commingled yarn based composites. *Compos - Part A Appl Sci Manuf* 2002;33:495–506. [https://doi.org/10.1016/S1359-835X\(01\)00140-3](https://doi.org/10.1016/S1359-835X(01)00140-3).
- [23] Verrey J, Wakeman MD, Michaud V, Månson J-AE. Manufacturing cost comparison of thermoplastic and thermoset RTM for an automotive floor pan. *Compos Part A Appl Sci Manuf* 2006;37:9–22. <https://doi.org/10.1016/j.compositesa.2005.05.048>.
- [24] Shou DH, Ye L, Fan JT. On the longitudinal permeability of aligned fiber arrays. *J Compos Mater* 2015;49:1753–63. <https://doi.org/10.1177/0021998314540192>.
- [25] Cihat Bayta A, Erdem D, Acar H, Cetiner O, Basci H. Experimental investigation of interfacial conditions between fluid and porous layer formed by periodic arrays of circular and non-circular cylinders. *Acta Phys Pol A* 2018;133:1314–23. <https://doi.org/10.12693/APhysPolA.133.1314>.
- [26] Yazdchi K, Srivastava S, Luding S. Microstructural effects on the permeability of periodic fibrous porous media. *Int J Multiph Flow* 2011;37:956–66. <https://doi.org/10.1016/j.ijmultiphaseflow.2011.05.003>.
- [27] Carman PG. Fluid flow through granular beds. *Chem Eng Res Des* 1937;75:S32–48. [https://doi.org/10.1016/s0263-8762\(97\)80003-2](https://doi.org/10.1016/s0263-8762(97)80003-2).
- [28] Nguyen VH, Lagardere M, Park CH, Panier S. Permeability of natural fiber reinforcement for liquid composite molding processes. *J Mater Sci* 2014;49:6449–58. <https://doi.org/10.1007/s10853-014-8374-1>.
- [29] Sadiq TAK, Advani SG, Parnas RS. Experimental Investigation Of Transverse Flow-Through Aligned Cylinders. *Int J Multiph Flow* 1995;21:755–74. [https://doi.org/10.1016/0301-9322\(95\)00026-t](https://doi.org/10.1016/0301-9322(95)00026-t).
- [30] Ganapathi AS, Joshi SC, Chen Z. Flow-compacted deformations coupled with thermo-chemically induced distortions in manufacturing of thick unidirectional carbon fiber reinforced plastics composites. *J Compos Mater* 2016;50:3325–43. <https://doi.org/10.1177/0021998315618455>.
- [31] Simacek P, Advani SG. Simulating tape resin infiltration during thermoset pultrusion process. *Compos Part a-Applied Sci Manuf* 2015;72:115–26. <https://doi.org/10.1016/j.compositesa.2015.01.020>.

- [32] Amico S, Lekakou C. An experimental study of the permeability and capillary pressure in resin-transfer moulding. *Compos Sci Technol* 2001. [https://doi.org/10.1016/S0266-3538\(01\)00104-X](https://doi.org/10.1016/S0266-3538(01)00104-X).
- [33] Seo JW, Lee WL. A model of the resin impregnation in thermoplastic composites. *J Compos Mater* 1991;25:1127–42. <https://doi.org/10.1177/002199839102500903>.
- [34] Westhuizen J, Plessis JP du. Quantification of Unidirectional Fiber Bed Permeability. *J Compos Mater* 1994;28:619–37. <https://doi.org/10.1177/002199839402800703>.
- [35] Lam RC, Kardos JL. The permeability and compressibility of aligned and cross-ply carbon-fiber beds during processing of composites. *Polym Eng Sci* 1991;31:1064–70. <https://doi.org/10.1002/pen.760311411>.
- [36] Chohra M, Advani SG, Gokce A, Yarlagaadda S. Modeling of filtration through multiple layers of dual scale fibrous porous media. *Polym Compos* 2006;27:570–81. <https://doi.org/10.1002/pc.20228>.
- [37] Schindelin J, Arganda-carreras I, Frise E, Kaynig V, Longair M, Pietzsch T, et al. Fiji : an open-source platform for biological-image analysis. *Nat Methods* 2012;9. <https://doi.org/10.1038/nmeth.2019>.

3. RHEO-KINETIC CHARACTERIZATION OF A RAPID CURE EPOXY RESIN FOR PREPREG MANUFACTURING

Portions of this chapter have been published in Polymer Engineering and Science journal published by Wiley, Reichenadter A., Bank D., and Mansson J.-A. E. "A novel rapid cure epoxy resin with internal mold release", Polymer Engineering and Science, vol 61 (6), pp 1819-1828 (2021), <https://doi.org/10.1002/pen.25703>.

This chapter utilized the compaction and permeability properties for kidney-bean shaped carbon fiber determined in Chapter 2 to model a hot-melt prepregging process. The kidney-bean shaped carbon fiber properties were chosen to represent a low-cost prepreg material for automotive applications. The resin chosen to be modeled in the prepregging process was a rapid cure epoxy resin with internal mold-release. The experimental procedures for differential scanning calorimetry and rheology are discussed with the characterized cure kinetic and chemorheology properties presented. These properties were used in the prepregging model to describe the hot-melt prepregging process for a low-cost prepreg intended for automotive applications.

3.1 Considerations for Low-Cost and High-Production Volume Thermoset Prepreg

Composites produced from prepreg are appealing to the automotive industry to meet desired stiffness-to-weight ratios that lead to improvements in fuel efficiency [2], however, composite materials were developed for low volume applications, like in the aerospace industry and military functions [3]. These resins were designed for longer cure cycles, to ensure dimensional stability and consistent material properties [2,4,5]. For adoption into high-production volume markets, innovations in composites processing, carbon fiber manufacturing, and resin chemistries were needed. As seen Chapter 2, DowAksa introduced an inexpensive carbon fiber option to improve the suitable applications carbon fiber composites may be used. To address the cure cycle issue, companies like Dow Chemical Company have formulated new, rapid curing epoxy resins. These resins have targeted part cycle times of 3 minutes [6].

To achieve high reactivity, a heterogeneous catalyst was typically introduced to the thermosetting resins [7,8]. As such, the catalyst needed to be well dispersed throughout the resin to promote uniform reaction rates and provide comparable cross-link densities throughout the resin. A concern when flowing the multi-phase resin through a fiber bed was for the solids to

preferentially filter at the surface and not penetrate the fiber bed. The fiber bed acted as a sieve which had differing pore sizes depending on the fiber volume fraction during processing. In consistent catalyst dispersal led to variation in mechanical properties (glass transition temperature, modulus, strength) throughout the cured specimen [9]. Therefore, when modeling the prepregging process, the average pore size should be considered to quantify the particle filtration.

While rapid cure epoxy resins solve the problems associated with long cycle times, these new resins tighten the window for composites processing. All composites must at one stage go through an impregnation step to infiltrate the fiber bed [10–14]. During impregnation, the reaction progression should be kept to a preset low value, a so call B-staging, to prevent the viscosity from significantly rising and allowing the prepreg to resemble a pseudo solid near room temperature [14–18]. Thus, unique chemistries are needed to ensure flowability at processing temperatures and not progress beyond B-stage. While in the part forming step, curing time ultimately dictates cycle time for the composite part. A typical part forming process for prepreg is compression molding [19]. Additionally, the degree of cure is dependent on time and curing temperature as epoxy resins are often diffusion limited at cooler temperatures [15–17,20]. Thus, rheological and cure kinetic models are needed to establish a connection between thermal history with the resin's viscosity and degree of cure for reliable resin impregnation and curing.

In addition to improved cure times, resin manufacturers have added internal mold-release (IMR) to reduce mold preparation times. The IMR is typically blended in with the thermosetting resin, which produces consistent release properties suitable for high volume production [21,22]. During the cure cycle, the IMR either becomes insoluble and migrates to the part surface or metallic salts migrate to the part surface and form a fatty mono-layer [21–26]. Adding IMR to epoxy resins has been shown to produce similar tensile and flexure properties compared to the neat resin [21,22]. However, some researchers have noted the glass transition temperatures decreased with the addition of certain IMR's [22,23,27], which implied the formation of the molecular network was impacted by these IMR's. Furthermore, Karbhari [22,23] noted minor retardation in peak reaction rates and decrease in total heat of reaction with increased IMR content in epoxy backbone vinyl esters but did not comment on any viscosity changes from the IMR.

Since the final degree of cure significantly impacts the mechanical properties of a composite part, isothermal and dynamic curing tests will be used to characterize the cure behavior of rapid cure epoxy resins with internal mold-release. The resulting data will be fitted to an

appropriate cure kinetic and diffusion model. Additionally, rheological behavior will be characterized since maintaining low viscosity is crucial for impregnation. The rheo-kinetic properties were used to model the impregnation process for a hot-melt impregnation process. Furthermore, a brief comparison is given on the influence of inert internal mold-release on curing kinetics. In the present study, differential scanning calorimetry, rheology, and dynamic mechanical analysis were used to determine rheological and cure kinetic parameters of a rapid cure epoxy resins with internal mold-release.

3.2 Material and Methods for Epoxy Characterization and Prepreg Modeling

3.2.1 Material

The resins used in this study were composed of propane, 2,2-bis[p-(2,3-epoxypropoxy)phenyl] and dicyandiamide curative, internal mold-release, and a urea based accelerant [28]. The rapid epoxy resins are trade named VORAFUSE™ P6300 and M6400 resin by DOW Chemical Company in Midland, MI. While both resins contain inert non-polar wax type internal mold-release, one resin had an additional 2.5wt% polar internal mold-release. The base rapid cure epoxy resin system will be referred to as RCE (P6300) and the resin with an additional 2.5wt% IMR (M6400) as RCE+IMR for simplicity. Both rapid cure epoxy resins contained solids with a particle distribution shown in Figure 3.1.

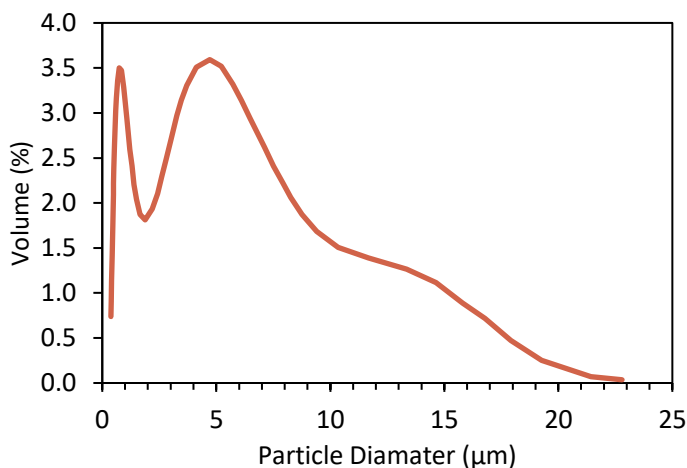


Figure 3.1: Particle size distribution for the rapid cure epoxy resins.

3.2.2 Differential Scanning Calorimeter (DSC) Test Method

The cure kinetic behavior of the resin was evaluated using a TA Instruments Q100 DSC. During testing, samples weighed approximately 10mg, were sealed in a hermetic pan, and kept in a Nitrogen environment with a constant N₂ flow of 50mL/min. The rapid cure epoxy resins exhibited accelerating reaction kinetics, so the ASTM E2070 Test Method B procedure was used for data collection and analysis [29].

Arrhenius parameters were determined from isothermal scans ranging from 110°C to 150°C in 10°C increments. These temperatures were chosen as this would be a representative temperature range that encompasses temperatures for the impregnation and cure cycle processes. Isothermal scans were started at 0°C and heated using the equilibrate function in the TA Instruments software to the isothermal test temperature. Heating scans of 3°C/min, 5°C/min, and 10°C/min were used to determine the initial glass transition temperature (T_{go}), final glass transition temperature ($T_{g\infty}$), and ΔH_{rxn} . These scans ramped from -20°C to 200°C. Cured samples were rescanned from 100°C to 200°C to obtain $T_{g\infty}$. Glass transition temperatures were determined using the midpoint temperature method as described in ASTM D3418 [30] and reported values were extrapolated to the 0°C/min rate.

3.2.3 Rheological Characterization and Dynamic Mechanical Analysis Test Method

The rheological behavior of the rapid cure epoxy resins was determined using a TA Instruments Discovery HR-2. 25mm disposable parallel plates were used with an approximate gap of 1mm. The top plate oscillated at a frequency of 1Hz with an amplitude of 0.1% strain, and torque was applied using non-iterative strain control mode. Samples were tested by ramping at 3°C/min, 5°C/min, and 10°C/min from room temperature to 200°C. The final glass transition temperature was recorded as the maximum of the loss factor after curing. However, the Discovery HR-2 parallel plates were not suitable to measure the initial glass transition temperature since the plates would slip. Isothermal tests were performed between 100°C and 140°C in 10°C increments. The temperature range was lowered by 10°C from the DSC scans since the resin would react too quickly at 150°C. Test procedures follow ASTM D4440 [31] except for the isothermal tests since the rapid cure epoxy resins were too sensitive to small changes in thermal history. Instead, the

samples were loaded into the chamber at room temperature and heated rapidly within the apparatus to the isothermal temperatures.

The TA Instruments Dynamic Mechanical Analyzer Q800 was used to determine the initial glass transition temperature of the rapid cure epoxy resins. The approximate sample dimensions were 56 x 13 x 3 mm. Samples were cooled to -5°C overnight before being loaded into the tension grips following ASTM D7028 [32]. Dynamic temperature scans started at -20°C and heated at 1°C/min to 30°C with strain amplitude and frequency of 1μm and 1Hz, respectively.

3.2.4 Prepreg Manufacturing Layout for Modeling Resin and Particle Infiltration

Two hot-melt impregnation processes were modeled for particle infiltration in a hexagonally packed, elliptic-shaped fiber bed, a force and displacement-controlled process. The force-controlled process, was referred to as the S-wrap process, shown in Figure 3.2a, while the displacement-controlled process, was referred to as the nip-roll process, shown in Figure 3.2b. Both processes considered a fiber bed sandwiched between two resin films with backing paper. The resin material properties were representative of a rapid cure epoxy resin. The S-wrap process used tension in the fiber bed passing over frictionless rollers to drive the resin into the fiber bed. In contrast, the nip-roll process progressively deforms the fiber bed, resulting in a rise in pressure. These two processes were used to compare how inter-fiber spacing evolves during processing and the consequences this has for particle infiltration. Since the focus is on particle infiltration, both processes neglected any heating or cooling steps and only focused on the impregnation process. The parameters used for both impregnation processes are summarized in Table 3.1.

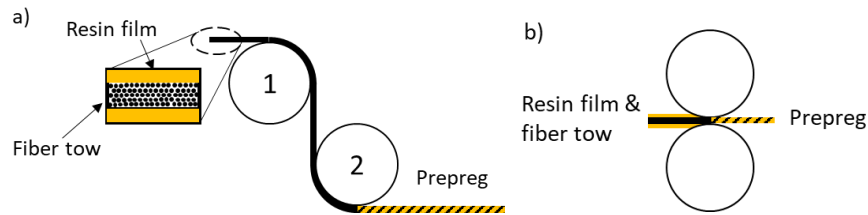


Figure 3.2: a) Simplified S-wrap impregnation process where tension over rollers are the driving force for impregnation. b) The simplified nip-roll impregnation process where the displacement between the rollers is the driving force for impregnation.

Table 3.1: Summarizing process parameters for the S wrap and Nip roll process.

Process:	S wrap	Nip roll
Line speed [m/s]	0.03	0.03
Temperature [°C]	120	120
Prepreg thickness [mm]	0.4	0.4
Tape width [mm]	76.2	76.2
Roller radius [m]	0.047	0.2
Roller gap [mm]	-	0.6
Pulling force [N]	500	-
Paper thickness [mm]	0.1	0.1
Time in process [sec]	0.4	8

To highlight the influence of manufacturing conditions on particle infiltration of the rapid cure epoxy resin, the nip-roller and S-wrap processes were selected as they were excellent examples of a displacement and force-controlled process, respectively. The resin with solid particles flowed into the fiber bed consisting of elliptically shaped fibers. These fibers had the same dimensions as the generalized shape defined for the kidney bean shaped carbon fiber in Chapter 2. The solids in the rapid cure epoxy resin were subjected to sieving from the fiber bed at major and minor pore crevice sites, as shown in Figure 3.3. The process conditions are summarized in Table 3.1. Heat transfer was neglected, and the roller diameters were adjusted to ensure both processes achieved full degree of impregnation ($DoI = 1$) at the end of the process while maintaining the same line speed, 0.03 m/s.

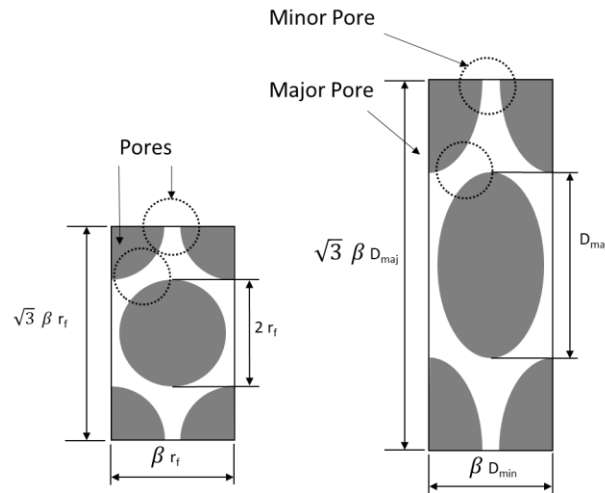


Figure 3.3: Hexagonally pack unit cell for a circular (left) and elliptic (right) fiber beds where constriction points between neighboring fibers are considered pores [33].

The average fiber pore size was geometrically defined using the hex-packed unit cells shown in Figure 3.3 for circular and elliptically shaped fibers. A scaling factor (β) was used to define the unit cell dimensions and average pore sizes for fiber volume fractions ranging from 0.3 to 0.7, shown in Figure 3.4. The average pore sizes were calculated for an elliptically shaped fiber with aspect ratio of 1.57 to represent the kidney bean shaped carbon fibers. Additionally, the average pore sizes for representative circular-fiber diameters (D_f) were calculated from the hex-packed unit cell for carbon ($D_f = 7\mu\text{m}$), Kevlar ($D_f = 12\mu\text{m}$), and glass fibers ($D_f = 25\mu\text{m}$). The average pore size for the fibers are shown in Figure 3.4 where particle diameters smaller than the pore size pass infiltrate the fiber bed while larger particles are filtered out. The elliptically shaped fibers showed two distinct average pore sizes for the major and minor crevice sites, while the circular fiber had one average pore size. Additionally, from Figure 3.4, the fiber diameter had a significant influence on pore size. Therefore, smaller fibers, like carbon fiber, were more susceptible to filtration vs large fibers, such as glass fiber. Furthermore, most prepreg is processed to have a $V_f = 0.5$, which corresponded to an average pore size approximately the size of the fiber radius. This indicated particle diameters should not exceed the fiber radius in order to avoid particle filtration.

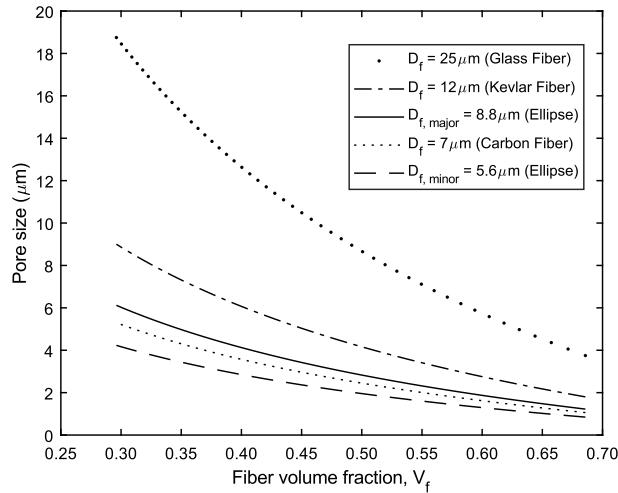


Figure 3.4: Average pore size as a function of fiber volume fraction for various fiber sizes.

3.2.4.1 Prepreg Layout: S-Wrap Configuration

A hot-melt prepregging process in an S-wrap configuration was considered to quantify the resin and particle infiltration into the fiber bed. The fiber bed was considered to be composed of kidney-bean shaped carbon fiber compaction and permeabilities described in Chapter 2. The process layout shown in Figure 3.5 was used to show the pressure, resin infiltration, and degree of cure advancement through an S-wrap configuration. For this example, the tension remained constant throughout the process as the rollers were assumed to be frictionless/driven at the line speed of the process. The pressure (P_i) generated over each roller was calculated from the force balance (Equations (3.1) - (3.4)) around the roller was dependent on the wrap angle. Where F was force on the resin and $F_{x,i}$ and $F_{y,i}$ were the horizontal and vertical forces, respectively [33,34].

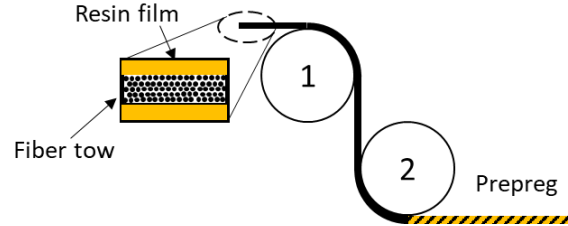


Figure 3.5: Simplified S-wrap impregnation process where tension over rollers are the driving force for impregnation.

$$F_i = \sqrt{F_{x,i}^2 + F_{y,i}^2} \quad (3.1)$$

$$F_{x,i} = T \cos(\theta_{1,i}) + T \cos(\theta_{2,i}) \quad (3.2)$$

$$F_{y,i} = T \sin(\theta_{1,i}) + T \sin(\theta_{2,i}) \quad (3.3)$$

$$P_i = \frac{F_i}{A_{wrap,i}} \quad (3.4)$$

The wrap angle for each roller was divided into two angles ($\theta_{1,i}$ and $\theta_{2,i}$) as shown in Figure 3.6. Since the tape was wrapped around the roller, the resin impregnation was spread over a large contact area ($A_{wrap,i}$) on the roller (Equation (3.5)). As a result, the flow front velocity was slowed down because of the reduction in pressure. This was observed in pressure generated from roller 1

and roller 2 as the wrap angle changed from 90° to 180° , respectively. Since the pressures were lower, the degree of fiber bed compaction was reduced.

$$A_{wrap,i} = \pi d_i w \frac{\theta_{1,i} + \theta_{2,i}}{360^\circ} \quad (3.5)$$

The wrap angle was a function of roller diameter (d_i) and position of adjacent rollers. The wrap angle around the roller by the fiber path can be measured at the process or calculated from the relative roller positions and diameters. The wrap angles were generically described by considering the inner tangents of two circles, as shown in Figure 3.6.

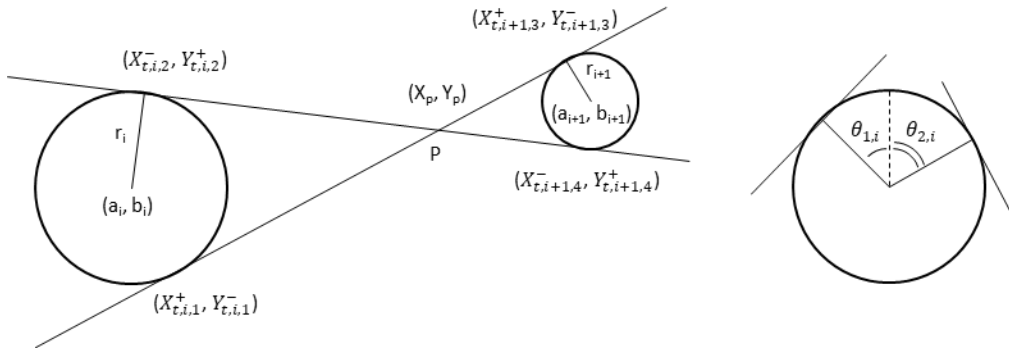


Figure 3.6: Representation of inner tangents between two circles (left) and wrap angle of fibers around roller (right). Adapted from [35].

With the relative position and radius of adjacent rollers, the tangent points where fiber/resin contact was made/lost with the rollers can be determined. The point where the two inner tangents cross will be referred to as point P with coordinates (X_p, Y_p) , which are defined in Equations (3.6) and (3.7), where the values a_i and b_i represent the centers of cylinder I [35].

$$X_p = \frac{a_{i+1}r_i + a_i r_{i+1}}{r_i + r_{i+1}} \quad (3.6)$$

$$Y_p = \frac{b_{i+1}r_i + b_i r_{i+1}}{r_i + r_{i+1}} \quad (3.7)$$

The X and Y tangent points for the i^{th} cylinder are represented in Equations (3.8) and (3.9), respectively. The equations were similar, but the order of the $+/-$ was switched between the two

and corresponded to the 1st/2nd set of tangent points for the i^{th} cylinder. The corresponding 3rd/4th tangent points on the $i + 1$ cylinder are defined in Equations (3.10) and (3.11) [35].

$$X_{t,i,1}^+ = X_{t,i,2}^- = \frac{r_i^2(X_{p,i}-a_i) \pm r_i(Y_{p,i}-b_i) \sqrt{(X_{p,i}-a_i)^2 + (Y_{p,i}-b_i)^2 - r_i^2}}{(X_{p,i}-a_i)^2 + (Y_{p,i}-b_i)^2} + a_i \quad (3.8)$$

$$Y_{t,i,1}^- = Y_{t,i,2}^+ = \frac{r_i^2(Y_{p,i}-b_i) \mp r_i(X_{p,i}-a_i) \sqrt{(X_{p,i}-a_i)^2 + (Y_{p,i}-b_i)^2 - r_i^2}}{(X_{p,i}-a_i)^2 + (Y_{p,i}-b_i)^2} + b_i \quad (3.9)$$

$$X_{t,i+1,3}^+ = X_{t,i+1,4}^- = \frac{r_{i+1}^2(X_{p,i+1}-a_{i+1}) \pm r_{i+1}(Y_{p,i+1}-b_{i+1}) \sqrt{(X_{p,i+1}-a_{i+1})^2 + (Y_{p,i+1}-b_{i+1})^2 - r_{i+1}^2}}{(X_{p,i+1}-a_{i+1})^2 + (Y_{p,i+1}-b_{i+1})^2} + a_{i+1} \quad (3.10)$$

$$Y_{t,i+1,3}^- = Y_{t,i+1,4}^+ = \frac{r_{i+1}^2(Y_{p,i+1}-b_{i+1}) \mp r_{i+1}(X_{p,i+1}-a_{i+1}) \sqrt{(X_{p,i+1}-a_{i+1})^2 + (Y_{p,i+1}-b_{i+1})^2 - r_{i+1}^2}}{(X_{p,i+1}-a_{i+1})^2 + (Y_{p,i+1}-b_{i+1})^2} + b_{i+1} \quad (3.11)$$

From the tangent points, the partial wrap angles described in Figure 3.6 were defined with Equations (3.12) and (3.13). Where two sets of wrap angles were defined depending on the fiber path through the rollers (over-under or under-over).

$$\theta_{1,i} = \tan^{-1} \left(\frac{Y_{t,i,3}^- - Y_{t,i-1,1}^-}{X_{t,i,3}^+ - X_{t,i-1,1}^+} \right) \text{ or } \tan^{-1} \left(\frac{Y_{t,i,4}^+ - Y_{t,i-1,2}^+}{X_{t,i,4}^- - X_{t,i-1,2}^-} \right) \quad (3.12)$$

$$\theta_{2,i} = \tan^{-1} \left(\frac{Y_{t,i+1,4}^+ - Y_{t,i,2}^+}{X_{t,i+1,4}^- - X_{t,i,2}^-} \right) \text{ or } \tan^{-1} \left(\frac{Y_{t,i+1,3}^- - Y_{t,i,1}^-}{X_{t,i+1,3}^+ - X_{t,i,1}^+} \right) \quad (3.13)$$

3.2.4.2 Prepreg Layout: Nip-Roller Configuration

When the hot-melt nip-roller process shown in Figure 3.2 used a nip-roller configuration, the process became displacement-controlled since the driving force for impregnation was generated by the distance between the rollers. The distance between the rollers compacted the fiber bed which induced a pressure dependent on the fiber bed's ability to resist compaction [36]. The pressure from the displacement was related to the fiber volume fraction as defined in Equation (3.27). The resin and backing paper were treated as incompressible. Additionally, the gap between the two rolls served to set the thickness of the final prepreg. As the sandwich structure moved through the rollers, the fiber bed was compacted further, but the resin draining from the film into the fiber bed decreased the degree of compaction since the fiber bed had more space between the rollers.

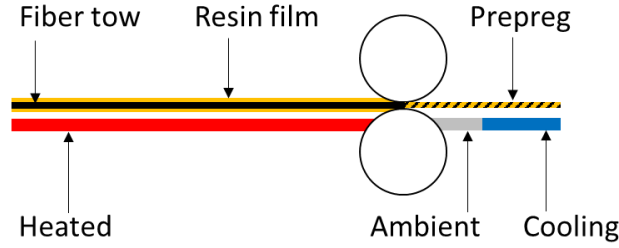


Figure 3.7: Hot-melt prepreg line layout in a nip-roller configuration.

3.3 Cure Kinetics and Chemorheology Characterization

3.3.1 Curing Behavior and Kinetics

Thermosets can follow a variety of kinetic models depending on the chemistry of the reaction, however, most epoxy reactions follow either n^{th} order or autocatalytic cure kinetics [14,18,37–40]. These functional models explicitly define the reaction rate ($\frac{d\alpha}{dt}$) and can be written into two fundamental components, an observed reaction rate constant (k) and a function of degree of cure, $f(\alpha)$, shown in Equation (3.14). The reaction rate is commonly determined from differential scanning calorimetry (DSC) experiments, which is subsequently integrated with respect to time, Equation (3.15) [41]. The reaction rate is defined by the heat flow, q (W/g), and is normalized by the heat of reaction (ΔH_{rxn}) in J/g. This thermal analysis assumes the heat of reaction is not a function of temperature and all reactions present release the same amount of energy for each new bond formation [41]. The rapid cure epoxy resins were assumed to follow autocatalytic kinetics, Equation (3.16), where an n^{th} order reaction produces a reactive intermediate from the 1^{st} step of the reaction which can further react with the reactants in the 2^{nd} step, accelerating the reaction.

$$\frac{d\alpha}{dt} = \frac{q}{\Delta H_{rxn}} = k(T) f(\alpha) \quad (3.14)$$

$$\alpha(t) = \int_0^t \frac{d\alpha}{dt'} dt' \quad (3.15)$$

$$\frac{d\alpha}{dt} = (k_1 + k_2 \alpha^m)(1 - \alpha)^n \quad (3.16)$$

The observed reaction rate constant (k) is known to follow Arrhenius type behavior across a variety of reactions when kinetically limited, Equation (3.17) [41]. However, the reaction will deviate from Arrhenius kinetics once the system has entered the diffusion limited regime which is typically after gelation [42,43]. Thus the observed reaction rate constant (k_i) will be dependent on the Arrhenius reaction rate constant (K_i) and diffusion rate constant (K_d), which is shown in Equation (3.18) [44]. The kinetic parameters, A_i and E_i , are the frequency factor (s^{-1}) and activation energy (J/mol), respectively, where the indices correspond to the 1st and 2nd steps of the reaction. The diffusion rate constant is estimated using the William-Landel-Ferry (WLF) Equation (3.19) [15]. This diffusion model uses the superposition principle to relate the molecular diffusivity of the system to the evolving glass transition temperature. The DiBenedetto equation was used to estimate the glass transition temperature (T_g) of the system, Equation (3.20) [20].

$$K_i = A_i e^{-\frac{E_i}{RT}} \quad (3.17)$$

$$\frac{1}{k_i} = \frac{1}{K_i} + \frac{1}{K_d} \quad (3.18)$$

$$K_d = k_{dr} e^{\frac{c_1(T-T_g(\alpha)-dT)}{c_2+T-T_g(\alpha)-dT}} \quad (3.19)$$

$$T_g(\alpha) = \frac{T_{go}}{\frac{T_{go}}{T_{g\infty}} \alpha + 1 - \alpha} \quad (3.20)$$

3.3.2 Curing Kinetics Analysis

For the initial, n^{th} order reaction, the Arrhenius reaction rate constants were calculated when the degree of cure (α) is near zero, at the beginning of an isothermal DSC experiment. While in this regime, Equation (3.17) simplifies to the result shown in Equation (3.21), which remains valid during the early stages of the experiment ($\alpha \leq 0.03$). The reaction order n was empirically determined and was found to be $n = 1.67$ and 1.54 for RCE and RCE+IMR resins, respectively, which was in the typical range of 1 to 3 for autocatalytic epoxy reactions [37,43]. Isothermal cures using differential scanning calorimetry were iteratively performed over the temperature range $110^\circ\text{C} - 150^\circ\text{C}$ for the RCE and RCE+IMR resins, as shown in Figure 3.8 to determine A_1 and E_1 . The Arrhenius equation was linearized in Equation (3.22) and $\ln(K_1)$ vs $\frac{1}{T}$ was plotted in Figure 3.9 to determine the constants A_1 and E_1 for the rapid cure epoxy resin systems. The addition of

2.5wt% internal mold-release influenced the reaction kinetics and retarded the 1st step of the reaction, which was evident by the increase in E_1 . The internal mold-release likely formed a diffusive barrier, causing the apparent activation energy to increase.

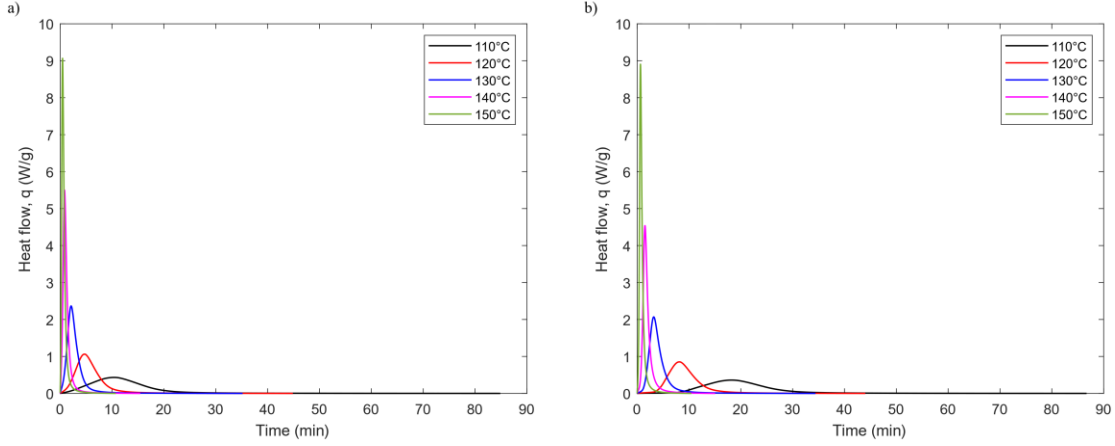


Figure 3.8: Differential scanning calorimetry isothermal cure curves for a) RCE and b) RCE+IMR resins.

$$\frac{d\alpha}{dt} = K_1 \quad (3.21)$$

$$\ln(K_1) = A_1 - \frac{E_1}{RT} \quad (3.22)$$

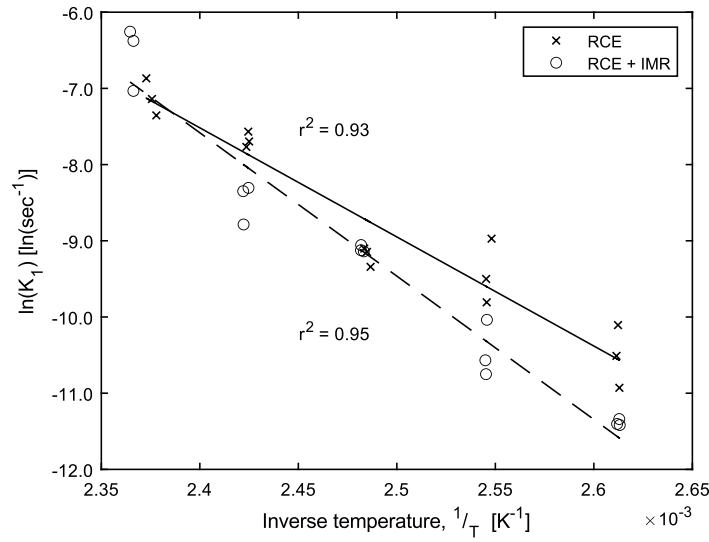


Figure 3.9: Isothermal analysis of the 1st reaction step to determine the A_1 and E_1 for the rapid cure epoxy resin systems.

In Figure 3.10, three distinct reaction regions are shown for the rapid cure epoxy resin systems. Within Region I, $\alpha \leq 0.03$, the 1st reaction step was dominant while the 2nd step of the reaction had not been initiated. The separation between Region I and II in Figure 3.10 was determined by the change in slope of the $\ln\left(\frac{\frac{d\alpha}{dt}}{(1-\alpha)^n} - K_1\right)$ vs $\ln(\alpha)$ curve, which corresponded approximately to $\alpha = 0.03$. Region II ($0.03 \leq \alpha \leq 0.63$) corresponded to the time where the 1st and 2nd steps of the reaction proceeded without hindrance from the IMR nor the molecular diffusion due to cross-linking. Finally, in Region III ($\alpha \geq 0.63$), the reaction became limited by molecular diffusion from the cross-linking. The reaction being diffusion limited after $\alpha = 0.63$ closely aligns with the theoretical degree of cure gelation point of 0.57 as described by Cadento and Enns et al [16,45]. To determine the Arrhenius reaction rate constants for the 2nd step of the reaction, Equation (3.16) was linearized into the form shown in Equation (3.23) and $\ln\left(\frac{\frac{d\alpha}{dt}}{(1-\alpha)^n} - K_1\right)$ vs $\ln(\alpha)$ was plotted to determine A_2 and E_2 . The data range used to determine the 2nd step's reaction rate constants was $0.03 \leq \alpha \leq 0.63$ as they can be isolated in this range. Then A_2 and E_2 were determined from the same analysis used for the 1st step reaction, which is shown in Figure 3.11. The activation energies for the RCE and RCE+IMR resins were statistically the same, which indicated the internal mold-release was no longer hindering the reaction kinetics. The reaction kinetic parameters were reported in Table 3.2.

$$\ln\left(\frac{\frac{d\alpha}{dt}}{(1-\alpha)^n} - K_1\right) = \ln(K_2) + m \ln(\alpha) \quad (3.23)$$

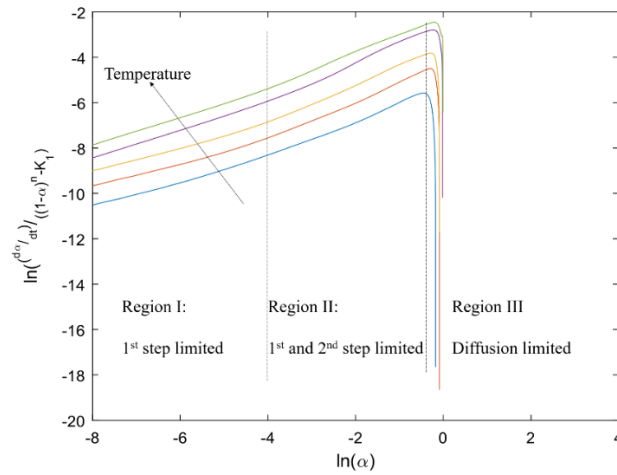


Figure 3.10: Linearization of the auto-catalytic kinetics to determine K_2 and m from the intercept and slope within Region II and identify the reaction and diffusion dominated regions.

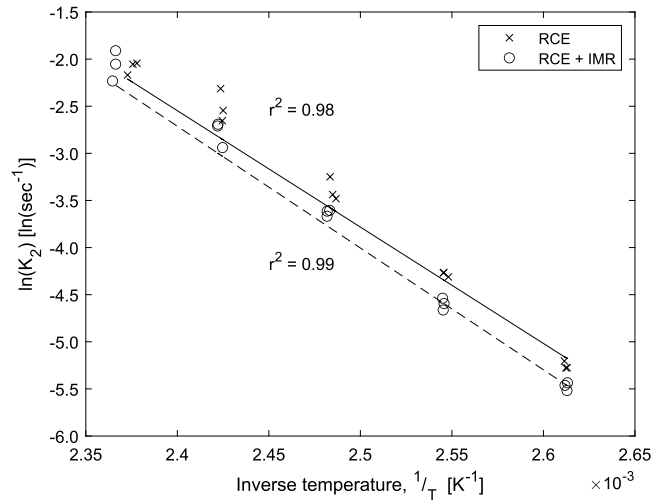


Figure 3.11: Isothermal analysis to determine the A_2 and E_2 for the rapid cure epoxy resin systems.

In Figure 3.12, the isothermal cure kinetics data for the RCE resin systems were modeled using autocatalytic kinetics with William-Landel-Ferry diffusion model, Equations (3.16) and (3.19). The RCE resin was faster to react than the RCE+IMR, however, both resins achieved similar final degrees of cure. This indicated the IMR only delayed the 2nd step reaction and did not significantly influence the cross-link density. The autocatalytic reaction for both resins became diffusion limited at gelation ($\alpha \geq 0.63$). Additionally, the reaction was quenched prematurely

when isothermal cure temperatures were below 150°C. The kinetic parameters for both resins were reported in Table 3.2.

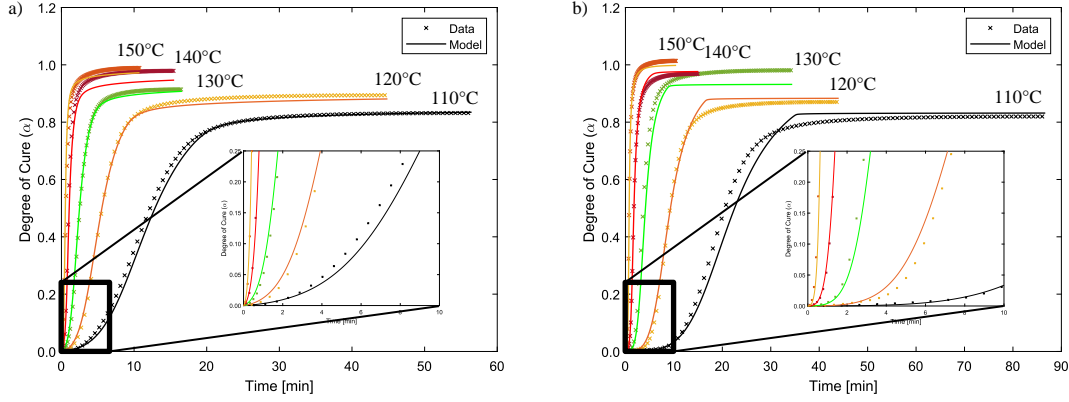


Figure 3.12: a) RCE and RCE+IMR b) resins isothermal cure [X] comparison to autocatalytic kinetics with WLF diffusion model [-].

Table 3.2: Cure kinetic physical constants and modeling parameters for the rapid cure epoxy resin systems.

Kinetic parameter	RCE	RCE+IMR
A_1 [sec ⁻¹]	$46 \times 10^{10} \pm 3 \times 10^{10}$	$24 \times 10^{15} \pm 2 \times 10^{15}$
E_{a1} [kJ/mol]	118 ± 9	165 ± 9
A_2 [sec ⁻¹]	$58 \times 10^{10} \pm 2 \times 10^{10}$	$16 \times 10^{11} \pm 1 \times 10^{11}$
E_{a2} [kJ/mol]	103 ± 4	107 ± 2
n	1.67	1.54
m	0.85	0.81
k_{dr} [sec ⁻¹]	0.84	33.11
c_1 []	12.7	2.2
c_2 [K]	83.4	19.3
dT [K]	13.4	-2.7

Additionally, the glass transition temperatures for the rapid cure epoxy resin systems were reported in Table 3.2 for DSC and DMA experiments. The glass transition temperature determined from DSC measurements used the midpoint technique and extrapolated the 0°C/min T_g from the dynamic scan rates. However, the glass transition temperature from the DSC measurements resulted in a poor fit for the WLF diffusion model. Therefore, the T_g from DMA was used for the

diffusion model as this provided the best fit for the isothermal cure profiles and was recommended by TA Instruments for cured thermosets [46]. The DMA T_g better represented the diffusive state of the system since this was measured at the maxima of the loss tangent rather than at the midpoint of the DSC curve. The glass transition temperatures for both rapid cure epoxy resin systems were similar. Even though the glass transition temperatures determined from DMA and DSC were measured at the same heating rates, the measured T_g should not be directly compared. In addition, the glass transition temperature determined by DMA has a frequency dependence. A lower T_g measured by DSC compared to DMA has been observed by other researchers [46–48]. The DSC T_g was measured at a constant rate, while the DMA T_g was measured at a constant heating rate and frequency.

Additionally, the heat of reaction for the dynamic temperature scans from 3°C/min to 10°C/min are reported in Table 3.4 for each resin system and showed no statistical difference in heat of reaction with ramp rate. This indicates the heat evolved from the reaction is not dependent on the reaction temperature. Furthermore, the heat evolved from the RCE+IMR resin is slightly lower than the RCE resin, however, this decrease is minor.

Table 3.3: Summary of glass transition temperatures with one standard deviation for the rapid cure epoxy resin systems.

	DSC		DMA	
	T_{go} [°C]	$T_{g\infty}$ [°C]	T_{go} [°C]	$T_{g\infty}$ [°C]
RCE	6.2 ± 0.4	140.3 ± 0.5	15.3 ± 1.4	165.5 ± 5.4
RCE+IMR	6.3 ± 0.4	133.4 ± 0.2	17.2 ± 2.7	163.8 ± 2.4

Table 3.4: Heat of reaction for the rapid cure epoxy resin systems under various dynamic scan rates, reported error is one standard deviation.

Heating rate [°C/min]	3	5	10
RCE heat of reaction [J/g]	373 ± 8	377 ± 5	379 ± 9
RCE+IMR heat of reaction [J/g]	366 ± 2	370 ± 6	373 ± 2

Finally, the RCE resin was noted to be quite reactive at 150°C, reaching 94% cure in 2 minutes, which is within the targeted molding time for the automotive industry. While the two resins did exhibit similar curing profiles, the addition of an extra 2.5wt% internal mold-release

appeared to retard the 1st reaction step, which was evident by the cure profiles in Figure 3.13. Additionally, the final degree of cure was similar, at 110°C the $\alpha = 0.82$ and 0.83 for RCE and RCE+IMR, respectively. Additionally, the time to reach $\alpha = 0.80$ for the RCE was 24 minutes while RCE+IMR was 40 minutes. All of this indicated the presence of additional internal mold-release retarded the 1st step of the reaction, while the 2nd step was not hindered. This was observed by the increased E_1 for RCE+IMR and similar values for E_2 . Furthermore, plotting $1/T$ vs $\log(\text{time})$ for $\alpha = 0.5$ showed the 2nd reaction step for both resin systems had the same reactivity, just delayed because of the restricted 1st step of the reaction in the RCE+IMR resin, shown in Figure 3.14. This retardation of the reaction rate had been observed by Karbhabi in vinyl ester resin systems with internal mold-release [23]. During the isothermal cure, the IMR melted and migrated to the sample surface. While this was occurring, it was hypothesized that the IMR created a diffusive barrier for the reactants, which hindered the 1st step of the reaction. Once the IMR had moved to the surface, the reaction was able to proceed unhindered.

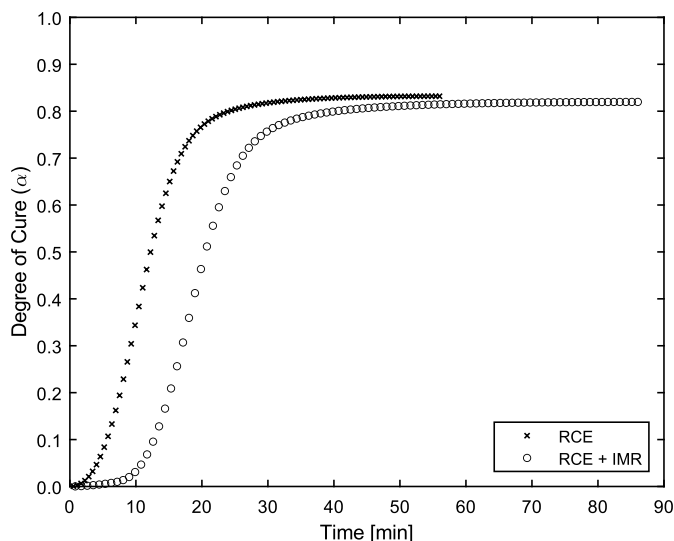


Figure 3.13: Comparison between the rapid cure epoxy resin with an additional 2.5wt% internal mold-release at 110°C.

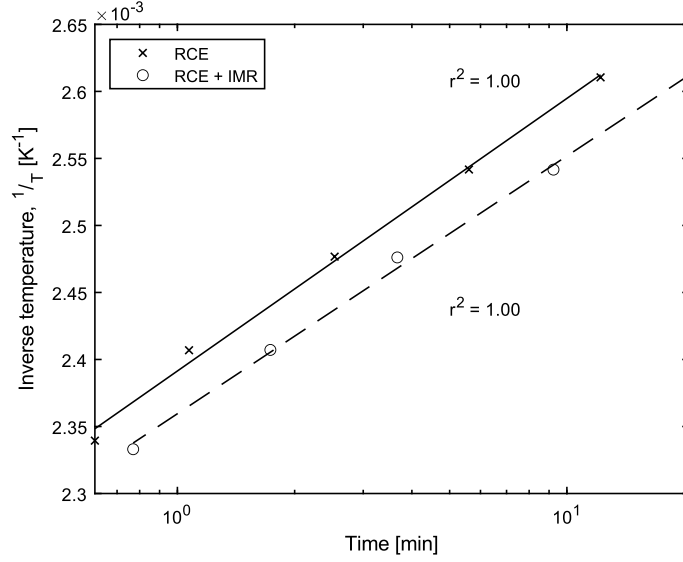


Figure 3.14: Time to reach $\alpha = 0.5$ for various temperatures showing the 2nd reaction is delayed but unhindered by the presence of internal mold-release.

3.3.3 Chemorheology Model

The viscosity of rapid cure epoxy resins while curing was determined using a dynamic mechanical analyzer (DMA). By assuming the Cox-Merz rule, Equation (3.24) can be used to define the dynamic viscosity (η_D) from the loss modulus (G'') and frequency (ω) [49]. This relationship breaks down once the resin has gelled, but at this point, flow is no longer possible. The gelation point is defined when an infinite weight molecular network is formed, which is indicated by $\frac{G''}{G'} = 1$ [45,50].

$$\eta_D = \frac{G''}{\omega} \quad (3.24)$$

For reacting systems like epoxies, the viscosity is a function of the degree of cure as well as the temperature. A modified William-Landel-Ferry model (WLF) is known to capture the viscosity evolution of these systems throughout the curing process [16]. This modification to the typical Arrhenius viscosity is warranted because once a critical cure state is achieved (near gelation) the viscosity becomes highly dependent on the degree of cure [16,39,51]. The modified WLF model is shown in Equation (3.25).

$$\eta_D = \eta_\infty e^{\frac{E_\eta}{RT}} + c_3 e^{\frac{-c_1(T-T_g(\alpha))}{c_2+T-T_g(\alpha)}} \quad (3.25)$$

3.3.4 Rheological Analysis

The uncured viscosity for the rapid cure epoxy resin systems was measured during the dwell of each isothermal experiment, well before gelation. The resins were heated from room temperature rather than preheating the chamber since the cross-linking reaction was too sensitive to small changes in thermal history. To determine the viscosity constants η_∞ (Pa•s) and E_η (J/mol), Equation (3.25) was linearized as shown in Equation (3.26) and plotted in Figure 3.15. This linearization assumed the degree of cure was low, so the 2nd term could be neglected. Due to the resin's high reactivity and limitations of the experiment design and setup, the 130°C and 140°C for RCE and 140°C and 150°C for the RCE+IMR resin were excluded from the Arrhenius viscosity analysis since the viscosity was influenced by the cross-linking reaction before the isothermal dwell temperature could be reached. The RCE+IMR resin was able to experience higher test temperatures because of the IMR hindering the 1st step of the reaction. The additional IMR appeared to slightly raise the viscosity of the resin While the reactivity of the resins was different, the uncured resin's viscosity E_η was the same.

$$\ln \eta_D = \ln \eta_\infty + \frac{E_\eta}{RT} \quad (3.26)$$

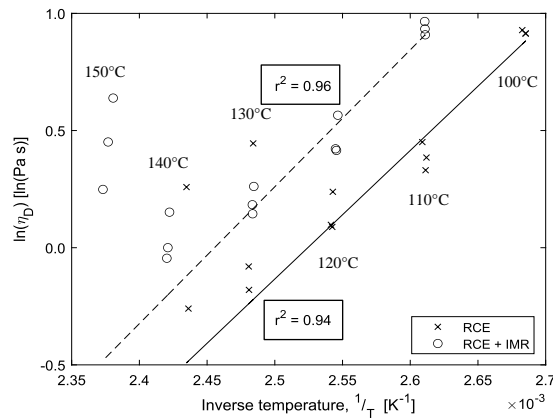


Figure 3.15: Arrhenius viscosity analysis for the rapid cure epoxy resin systems, where the best fit line only considers 100°C – 120°C RCE data and 110°C – 130°C RCE+IMR data.

In Figure 3.16, a representative viscosity data set for each temperature ranging from 100°C – 130°C for RCE and 110°C – 140°C for RCE+IMR was shown. The shift to cooler temperatures was warranted since the RCE and RCE+IMR resins could not reach the cure temperature before gelling at 140°C and 150°C, respectively. The immediate decrease in viscosity for each data set was associated with the sample reaching the isothermal temperature. The rapid cure epoxy resins compared favorably to the modified WLF model, Equation (12), capturing the dwell viscosity and gelation. The constants C_1 , C_2 , and C_3 were empirically determined and are different from the c_1 and c_2 used in the reaction kinetics model. The additional IMR appeared to increase the dwell time because of the delayed reaction but otherwise did not influence the resin's viscosity profile. The viscosity modeling parameters are shown in

Table 3.5 and the T_g from DMA was used in the WLF diffusion model. The dynamic mechanical analysis curves from 50°C – 200°C are shown in Figure 3.17. From the rheological model, the RCE resin maintained a viscosity below 5 Pa•s at 120°C for 4.1 minutes. Maintaining this low viscosity indicated a reasonable prepregging temperature can be up to 120°C for this rapid cure epoxy resin.

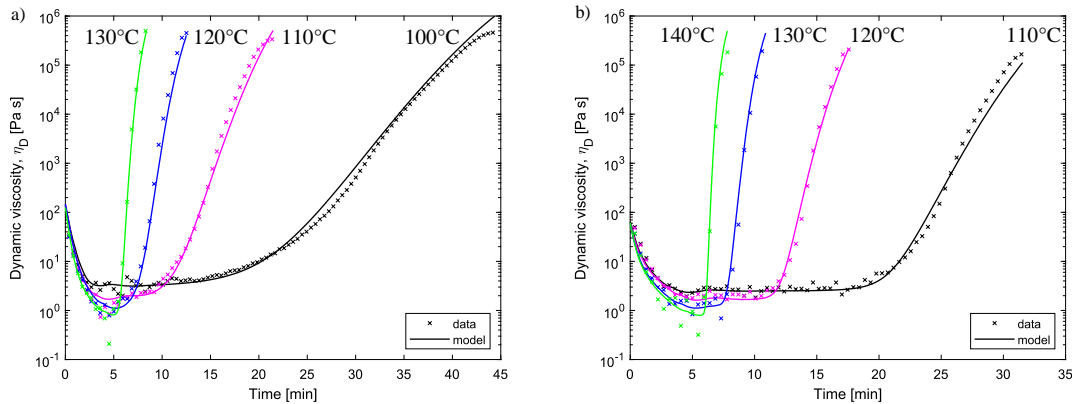


Figure 3.16: Isothermal viscosity behavior [X] compared with rheological model [-] for the RCE resin (a) and RCE+IMR (b).

Table 3.5: Rheological physical constants and modeling parameters for the rapid cure epoxy resin systems.

Rheological parameter	RCE	RCE+IMR
η_{∞} [Pa s]	$9.7 \times 10^{-7} \pm 2.6 \times 10^{-7}$	$5.9 \times 10^{-7} \pm 2 \times 10^{-7}$
E_{η} [kJ/mol]	46 ± 4	49 ± 4
c_1 [Pa s]	190	330
c_2 [K]	1170	1810
c_3 [Pa s]	3.5×10^5	1.5×10^5

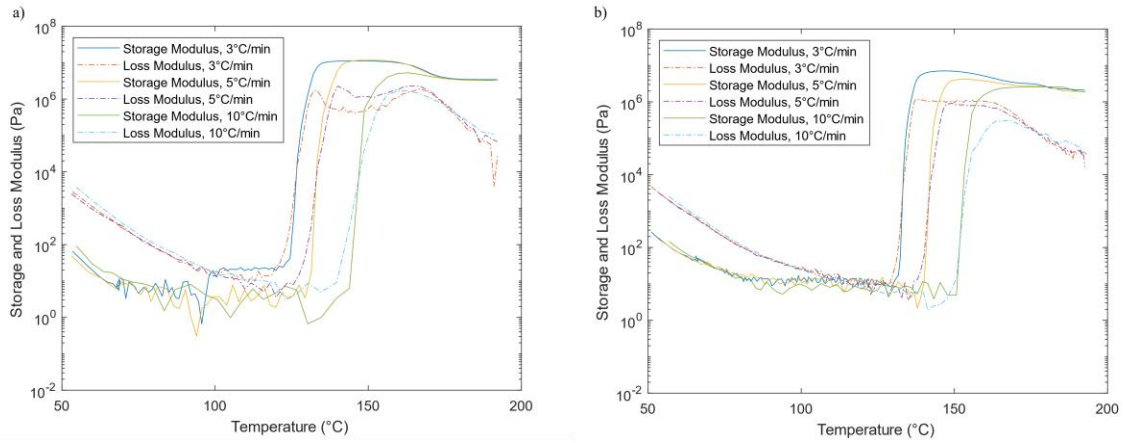


Figure 3.17: Dynamic mechanical analysis of the a) RCE and b) RCE+IMR resins at 3, 5, and 10°C/min from 50°C – 200°C.

3.4 Hot-Melt Prepregging Modeling

The characterized rapid cure epoxy resin properties were used to model the impregnation quality for a force-controlled and displacement-controlled impregnation process. The force-controlled impregnation process was the hot-melt S-wrap configuration and the displacement-controlled impregnation process was the hot-melt nip-roller configuration. The fiber bed compaction was estimated from Equation (3.27). A detailed description of Equation (3.27) was provided in Section 2.1.1. The fiber bed permeability for the irregularly shaped fibers was given by Equation (3.28). A detailed description of Equation (3.28) was given in Section 2.1.2.

$$P = A \frac{\left(\sqrt{\frac{V_f}{V_o}} - 1\right)}{\left(\sqrt{\frac{V_a}{V_f}} - 1\right)^4} \quad (3.27)$$

$$K = r^2 C \left(\sqrt{\frac{V_{f \max}}{V_f}} - 1 \right)^{\frac{5}{2}} \quad (3.28)$$

3.4.1 Hot-Melt Prepregging: S-Wrap Configuration

A simplification of the S-wrap process is shown in Figure 3.5, where the resin film on the top and bottom of the fiber bed created a sandwich structure. In this roller configuration, tensioned fibers were pulled over rollers. The S-wrap configuration can be considered a force-controlled impregnation process. The tension served two purposes 1) maintain fiber alignment and 2) generate pressure as the sandwich structure passed over the rollers. These rollers were idle or driven. Idle rollers generated greater tension and thus pressure for impregnation, which depended on the roller internal friction. Essentially, the resistance of the rollers to turn caused an increase in line tension. If not monitored, the tension could reach a critical value where fibers begin breaking resulting in fiber fraying or other defects forming along the prepreg. Accurate measurement of fiber tension was necessary to accurately model the prepreg process. Additionally, the friction within the system may become too great and exceed the pulling force of the prepreg line. While more expensive to implement, the driven rollers can match the line speed of the process which result in negligible pulling force increases and provided more control over the degree of fiber bed compaction. Therefore, it was generally preferred to drive the rollers or reduce the internal friction of the roller.

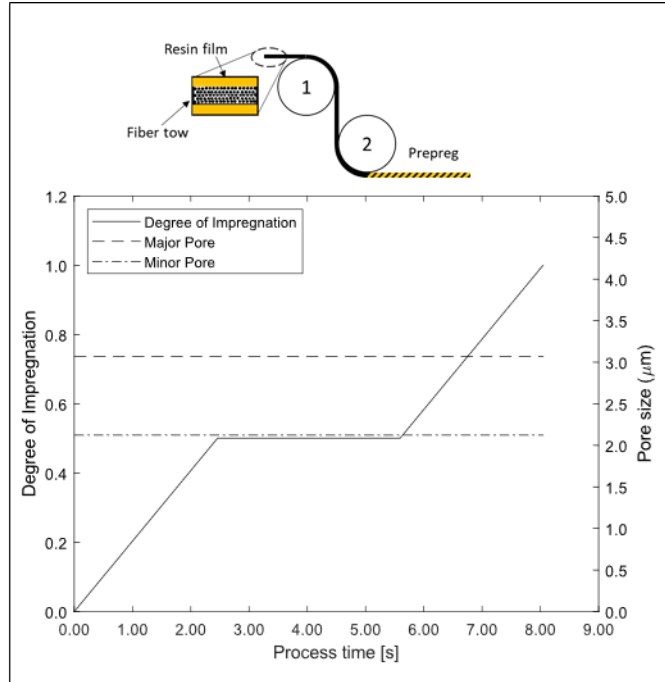


Figure 3.18: Impregnation and cure through an S-Wrap hot-melt process for a rapid cure epoxy resin.

In general, the S-wrap configuration applied lower pressures over the span of 8 seconds which allowed for less fiber bed compaction while saturating the fiber bed compared to the nip-roller configuration. The mechanism for resin infiltration was caused by the tension and roller layout, therefore the S-wrap configuration was considered a force-controlled process. The direct control over pressure allowed this process configuration to control the infiltration profile throughout the process. The lower pressure resulted in less fiber bed compaction and therefore larger average pore sizes, which was seen in Figure 3.18. The larger pore sizes throughout the process made this configuration suitable for multi-phase resins where infiltration of the solids into the fiber bed was preferred. Additionally, the irregular shape of the fibers created major and minor pore sites with varying pore sizes.

3.4.2 Hot-Melt Prepregging: Nip-Roller Configuration

The fiber bed compaction through the nip-roller configuration was dependent on roller gap, film thickness, roller diameter, line speed, and resin flow rate. The gap initially set by the rollers and film thickness dictated the maximum possible fiber bed compaction and therefore the

maximum driving pressure for flow in the process. The roller diameter influenced the contact duration with the rollers. Where larger rollers increased the contact time and required lower pressures to fully infiltrate the fiber bed. The applied pressure to drive the resin into the fiber bed was not constant. The curvature of the roller caused the compaction rate of the fiber bed to change through the nip-rollers. Additionally, the fiber volume fraction pressure relationship in Equation (3.27) was non-linear. The film thickness changed throughout the process as resin filled the fiber bed, which influenced the available space for the fiber bed to occupy. The film depletion rate was dependent on the residence time under pressure and therefore a function of the line speed.

As a consequence of the non-linear displacement rate and pressure relationship, the infiltration profile of the resin through the process was non-linear. An example of the non-linearity was shown in Figure 3.19. The displacement rate was non-linear since it was based on the curvature of the roller in contact with the sandwich structure. From 0.00 to 0.10 seconds, the fiber bed was rapidly compressed, and the displacement rate was faster than the resin flow rate. Between 0.10 to 0.20, the resin flow rate and displacement rate were balanced allowing the resin to flow without further compacting the fiber bed. Beyond 0.20 seconds, the resin flow rate exceeded the displacement rate allowing the fiber bed to relax, which resulted in increasing pore sizes. Where the fiber bed was initially and rapidly compacted, but the slight change in pressure was balanced by the film depletion, therefore the infiltration was approximately linear. Then the fiber bed achieved a critical degree of compaction and the pressure rapidly rose for the midpoint of the process, before the depletion rate of resin and reduced permeability overcame the compaction rate and the infiltration rate decreased. Throughout the process, the permeability changed based on the fiber volume fraction. The permeability changed depending on the fiber bed compaction and were estimated with any of Equation (3.28). The changing fiber volume fraction caused the major and minor pore sizes to change throughout the process and caused the pores to decrease to $0.5\mu\text{m}$, which would have filtered out significant amounts of the solid present.

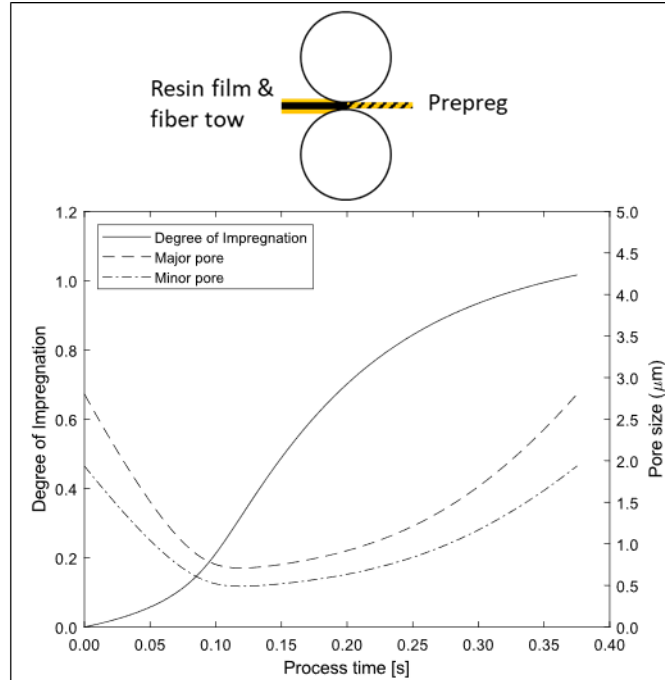


Figure 3.19: Simplified nip-roller impregnation progress between point I (initial contact with roller) and II (end of contact with roller) of the nip-rollers.

Since the displacement rate was a function of line speed, tuning line operations through trial and error became challenging as the non-linear pressure and permeability relationships were linked to line speed. The brief contact time of 0.35 seconds meant greater pressure was required for the same line speed. As line speeds were increased, the compression of the fiber bed increased accordingly. This was caused by the inability for the resin to appreciably flow as material passes through the rollers. Since the resin was not allowed sufficient time to flow as material passes between the rollers, the film thickness remained relatively thick. This caused either material to spill out the sides of the line or the fiber bed lock due to excessive force. Additionally, the higher pressures caused a reduction in inter-fiber spacing, which reduced permeability. Which made the process more appropriate for resins with low viscosity. The high fiber volume fraction during processing would also lead to particles in multi-phase resins to filter smaller particles. The fiber bed compaction became more severe at faster production speeds.

3.5 Conclusions

The rapid cure epoxy resins followed autocatalytic kinetics with WLF diffusion model and modified WLF viscosity model. However, adding an additional 2.5wt% internal mold-release to the epoxy resin hindered the 1st step of the reaction. The additional IMR was hypothesized to act as a diffusive barrier for the initial barrier to overcome. After the IMR migrated to the sample surface, the 2nd reaction step proceeded unhindered. While an additional 2.5wt% of internal mold-release retarded the 1st step of the reaction, the final degree of cure was unchanged. Additionally, at 150°C, the RCE resin was able to achieve 94% cure after 2 minutes, making this a suitable temperature and cure time for compression molding. Below 140°C, the reaction was diffusion limited and post curing would be needed. Furthermore, the viscosity model showed that at 120°C, the RCE resin viscosity could remain below 5 Pa•s for 4.1 minutes, before the cross-linking reaction significantly raised the viscosity. Therefore, the RCE resin can sustain viscosities suitable for prepregging up to 120°C. This resin is viable for high-volume composites manufacturing since it is able to infiltrate at temperatures up to 120°C and perform a cure cycle at 150°C in 2 minutes.

The rapid cure epoxy resin with particles was modeled in a hot-melt impregnation process with properties of the kidney-bean shaped carbon fibers described in Chapter 2. The S-wrap process demonstrated lower pressures were required for the same impregnation compared to the nip-roller process. As a result, particles of 3μm were able to infiltrate the fiber bed in the S-wrap configuration compared to the nip-roller layout with 0.9μm pores. The force-controlled process (S-wrap) allowed for appreciably more particles to penetrate the fiber bed and provided a scalable way to control the particle infiltration since pore size was not dependent on line speed. In contrast, the nip-roller process average pore size was dependent on the line speed. Therefore, the force-controlled process layout performed considerably better for resin with filler content to penetrate the fiber bed. The average pore size for kidney bean shaped carbon fiber and other fiber diameters were geometrically defined and decreased with fiber volume fraction. Based on the average pore sizes, a general rule to follow was that particle diameters should not exceed fiber radius when infiltrating fiber beds.

3.6 References

- [1] Reichenadter A, Bank D, Mansson JAE. A novel rapid cure epoxy resin with internal mold release. *Polym Eng Sci* 2021;61:1819–28. <https://doi.org/10.1002/pen.25703>.
- [2] Martensson P, Zenkert D, Akernno M. Effects of manufacturing constraints on the cost and weight efficiency of integral and differential automotive composite structures. *Compos Struct* 2015;134:572–8. <https://doi.org/10.1016/j.compstruct.2015.08.115>.
- [3] Tenney DR, Davis John G. J, Johnston NJ, Pipes RB, McGuire JF. Structural Framework for Flight II: NASA's Role in Development of Advanced Composite Materials for Aircraft and Space Structures. *Nasa/Cr-2019-220267* 2019;II:216–72.
- [4] Edwards T. Composite Materials Revolutionise Aerospace Engineering. *Ingenia* 2008:24–8.
- [5] Barbosa GF, Carvalho J. Analytical model for aircraft design based on Design for Excellence (DFX) concepts and use of composite material oriented to automated processes. *Int J Adv Manuf Technol* 2013;69:2333–42. <https://doi.org/10.1007/s00170-013-5211-7>.
- [6] Balijepalli B, Bank DH, Baumer RE, Lowe M, Ma L, James A. High quality carbon fiber epoxy prepregs for a wide range of reinforcement architectures, *SPE-ACCE Conference Proceedings*; 2018.
- [7] Liu D, Ding JP, Fan XY, Lin XY, Zhu YD. Non-isothermal forming of glass fiber/polypropylene commingled yarn fabric composites. *Mater Des* 2014;57:608–15. <https://doi.org/10.1016/j.matdes.2014.01.027>.
- [8] Li M, Gu YZ, Zhang ZG, Sun ZJ. A simple method for the measurement of compaction and corresponding transverse permeability of composite prepregs. *Polym Compos* 2007;28:61–70. <https://doi.org/10.1002/pc.20255>.
- [9] Schichtel JJ, Chattopadhyay A. Modeling thermoset polymers using an improved molecular dynamics crosslinking methodology. *Comput Mater Sci* 2020;174:109469. <https://doi.org/10.1016/j.commatsci.2019.109469>.
- [10] Molyneux M, Murray P, P. Murray B. Prepreg, tape and fabric technology for advanced composites. *Composites* 1983;14:87–91. [https://doi.org/10.1016/S0010-4361\(83\)80003-2](https://doi.org/10.1016/S0010-4361(83)80003-2).
- [11] Dave R, Kardos JL, Dudukovic MP. A Model For Resin Flow During Composite Processing .1. General Mathematical Development. *Polym Compos* 1987;8:29–38. <https://doi.org/10.1002/pc.750080106>.
- [12] Astrom BT, Pipes RB, Advani SG. On flow through aligned fiber beds and its application to composites processing. *J Compos Mater* 1992;26:1351–73. <https://doi.org/10.1177/002199839202600907>.

- [13] Lam RC, Kardos JL. The permeability and compressibility of aligned and cross-ply carbon-fiber beds during processing of composites. *Polym Eng Sci* 1991;31:1064–70. <https://doi.org/10.1002/pen.760311411>.
- [14] Lee C, Ho J, Wei K. Resin Transfer Molding (RTM) Process of a High Performance Epoxy Resin. I: Kinetic Studies on Cure Reaction. *Polym Eng Sci* 2000;40:929–34.
- [15] Simon SL, Gillham JK. Cure kinetics of a thermosetting liquid dicyanate ester monomer high-tg polycyanurate material. *J Appl Polym Sci* 1993;47:461–85. <https://doi.org/10.1002/app.1993.070470308>.
- [16] Enns JB, Gillham JK. Time Temperature Transformation (TTT) Cure Diagram - Modeling the Cure Behavior of Thermosets. *J Appl Polym Sci* 1983;28:2567–91. <https://doi.org/10.1002/app.1983.070280810>.
- [17] Shaw SJ. Rubber modified epoxy resins. *Polym Eng Sci* 1994;34:165–209. https://doi.org/10.1007/978-94-011-1260-4_6.
- [18] Kim DS, Macosko CW. Reaction injection molding process of glass fiber reinforced polyurethane composites. *Polym Eng Sci* 2000;40:2205–16. <https://doi.org/10.1002/pen.11352>.
- [19] Wakeman MD, Cain TA, Rudd CD, Brooks R, Long AC. Compression moulding of glass and polypropylene composites for optimised macro- and micro-mechanical properties II. Glass-mat-reinforced thermoplastics. *Compos Sci Technol* 1999;59:709–26. [https://doi.org/10.1016/S0266-3538\(98\)00124-9](https://doi.org/10.1016/S0266-3538(98)00124-9).
- [20] Dibenedetto AT. Prediction Of The Glass-Transition Temperature Of Polymers - A Model Based On The Principle Of Corresponding States. *J Polym Sci Part B-Polymer Phys* 1987;25:1949–69. <https://doi.org/10.1002/polb.1987.090250914>.
- [21] Mishra R, Behera BK, Rajpurohit AN, Behera P, Petru M, Muller M. Effect of internal mold release agent on flexural and inter laminar shear properties of carbon and glass fabric reinforced thermoset composites. *Polym Adv Technol* 2021;32:282–93. <https://doi.org/10.1002/pat.5084>.
- [22] Karbhari VM, Chhabra G. Effect of resin system parameters on resin transfer molding of vinyl ester based composites—a statistically designed study. *Polym Plast Technol Eng* 1995;34:599–620. <https://doi.org/10.1080/03602559508012207>.
- [23] Karbhari VM. Effect of internal mold release agent on the cure and property variation in resin transfer molding composites. *J Mater Sci Lett* 1998;17:2061–2. <https://doi.org/10.1023/A:1006663612780>.
- [24] Serré C, Vayer M, Erre R. Behavior of internal mold release agent during BMC thermosets composites cure and aging. *J Mater Sci Lett* 2001;20:1989–91. <https://doi.org/10.1023/A:1013107407505>.

- [25] Bjeković R, Piotrowicz K. Epoxy resin and release agents part I: Influence of external and internal release agents on the adhesive properties of epoxy resin. *J Appl Eng Sci* 2015;13:45–50. <https://doi.org/10.5937/jaes13-7210>.
- [26] Briscoe BJ, Khan MB, Richardson SM. Rotary injection reaction injection molding (RI-RIM). Part II: Interfacial segregation of release systems. *Polym Eng Sci* 1990;30:175–86. <https://doi.org/10.1002/pen.760300307>.
- [27] Briscoe BJ, Khan MB, Richardson SM. Rotary injection reaction injection molding (RI-RIM). Part I: Basic design features. *Polym Eng Sci* 1990;30:162–74. <https://doi.org/10.1002/pen.760300306>.
- [28] Reese J, Baumer R, Bank D, Chaudhary A. Patent Application Publication Pub . No . : US 2018 / 0104299 A1. US 2018/0355134A1, 2018.
- [29] E2070-13 Standard Test Methods for Kinetic Parameters by Differential Scanning Calorimetry Using Isothermal Methods. West Conshohocken: ASTM International; 2018. <https://doi.org/https://doi.org/10.1520/E2070-13R18>.
- [30] D3418-15 Standard Test Method for Transition Temperatures and Enthalpies of Fusion and Crystallization of Polymers by Differential Scanning Calorimetry. West Conshohocken: ASTM International; 2015. <https://doi.org/https://doi.org/10.1520/D3418-15>.
- [31] D4440-15 Standard Test Method for Plastics: Dynamic Mechanical Properties Melt Rheology. West Conshohocken: ASTM International; 2015. <https://doi.org/https://doi.org/10.1520/D4440-15>.
- [32] D7028-07 Standard Test Method for Glass Transition Temperature (DMA Tg) of Polymer Matrix Composites by Dynamic Mechanical Analysis (DMA). West Conshohocken: ASTM International; 2015. <https://doi.org/https://doi.org/10.1520/D7028-07R15>.
- [33] Reichanadter A, Dustin JS, Balijepalli B, Mansson JA. Process modeling and flexible manufacturing of multi- phase resin based thermoset and thermoplastic. SPE-ACCE, SPE-ACCE Conference Proceedings; 2018.
- [34] Reichanadter AM, Dustin JS, Mansson JAE. Process modeling and manufacturing of thermoplastic prepreg tape. *Int. SAMPE Tech. Conf.*, vol. 2019- May, 2019. <https://doi.org/10.33599/nasampe/s.19.1489>.
- [35] Tangential Circles 2019. www.ambrsoft.com/TrigoCalc/Circles2/Circles2Tangent_.htm.
- [36] Grunenfelder LK, Dills A, Centea T, Nutt S. Effect of prepreg format on defect control in out-of-autoclave processing. *Compos Part a-Applied Sci Manuf* 2017;93:88–99. <https://doi.org/10.1016/j.compositesa.2016.10.027>.
- [37] Nam JD, Seferis JC. Application of the kinetic composite methodology to autocatalytic-type thermoset prepreg cures. *J Appl Polym Sci* 1993;50:1555–64. <https://doi.org/10.1002/app.1993.070500909>.

- [38] Shiravand F, Hutchinson JM, Calventus Y. Influence of the isothermal cure temperature on the nanostructure and thermal properties of an epoxy layered silicate nanocomposite. *Polym Eng Sci* 2014;54:51–8. <https://doi.org/10.1002/pen.23540>.
- [39] Li W, Hou L, Zhou Q, Yan L, Loo LS. Curing behavior and rheology properties of alkyl-imidazolium-treated rectorite/epoxy nanocomposites. *Polym Eng Sci* 2013;53:2470–7. <https://doi.org/10.1002/pen.23500>.
- [40] Balasubramani PK, Iroh JO. Mechanism and kinetics of curing of diglycidyl ether of bisphenol a (DGEBA) resin by Chitosan. *Polym Eng Sci* 2017;57:865–74. <https://doi.org/10.1002/pen.24463>.
- [41] Kamal MR, Sourour S. Kinetics And Thermal Characterization Of Thermoset Cure. *Polym Eng Sci* 1973;13:59–64. <https://doi.org/10.1002/pen.760130110>.
- [42] Craig ID, Parker R, Rigby NM, Cairns P, Ring SG. Maillard reaction kinetics in model preservation systems in the vicinity of the glass transition: Experiment and theory. *J Agric Food Chem* 2001;49:4706–12. <https://doi.org/10.1021/jf0100752>.
- [43] Wisanrakkit G, Gillham JK. The Glass-Transition Temperature (T_g) As An Index Of Chemical Conversion For A High-T_g Amine Epoxy System - Chemical And Diffusion-Controlled Reaction-Kinetics. *J Appl Polym Sci* 1990;41:2885–929. <https://doi.org/10.1002/app.1990.070411129>.
- [44] Rabinowitch E. Collision, co-ordination, diffusion and reaction velocity in condensed systems. *Trans Faraday Soc* 1937;33:1225–32. <https://doi.org/10.1039/tf9373301225>.
- [45] Cadenato A, Salla JM, Ramis X, Morancho JM, Marroyo LM, Martin JL. Determination of gel and vitrification times of thermoset curing process by means of TMA, DMTA and DSC techniques - TTT diagram. *J Therm Anal* 1997;49:269–79. <https://doi.org/10.1007/bf01987448>.
- [46] Foreman J, Sauerbrunn SR, Marcozzi CL. Thermal Analysis & Rheology Exploring the Sensitivity of Thermal Analysis Techniques to the Glass Transition n.d.
- [47] Kasapis S, Al-Marhoobi IM, Mitchell JR. Testing the validity of comparisons between the rheological and the calorimetric glass transition temperatures. *Carbohydr Res* 2003;338:787–94. [https://doi.org/10.1016/S0008-6215\(03\)00012-0](https://doi.org/10.1016/S0008-6215(03)00012-0).
- [48] Gracia-Fernández CA, Gómez-Barreiro S, López-Beceiro J, Tarrío Saavedra J, Naya S, Artiaga R. Comparative study of the dynamic glass transition temperature by DMA and TMDSC. *Polym Test* 2010;29:1002–6. <https://doi.org/10.1016/j.polymertesting.2010.09.005>.
- [49] Bair S, Yamaguchi T, Brouwer L, Schwarze H, Vergne P, Poll G. Oscillatory and steady shear viscosity: The Cox-Merz rule, superposition, and application to EHL friction. *Tribol Int* 2014;79:126–31. <https://doi.org/10.1016/j.triboint.2014.06.001>.

- [50] Ramis X, Salla JM. Time-temperature transformation (TTT) cure diagram of an unsaturated polyester resin. *J Polym Sci Part B Polym Phys* 1997;35:371–88. [https://doi.org/10.1002/\(SICI\)1099-0488\(19970130\)35:2<371::AID-POLB13>3.3.CO;2-6](https://doi.org/10.1002/(SICI)1099-0488(19970130)35:2<371::AID-POLB13>3.3.CO;2-6).
- [51] Kenny JM, Apicella A, Nicolais L. A model for the thermal and chemorheological behavior of thermosets .1. Processing of epoxy-based composites. *Polym Eng Sci* 1989;29:973–83. <https://doi.org/10.1002/pen.760291502>.

4. MANUFACTURING AND CHARACTERIZING UNIDIRECTIONAL, THERMOPLASTIC PREPREG TAPE

I have presented portions of this chapter in a technical report exchange with E.I. du Pont de Nemours and the Institute for Advanced Composites Manufacturing Innovation (IACMI).

In this chapter, a thermoplastic prepreg line was used to produce polyamide/Kevlar[®] fiber prepreg tape. The guiding prepreg principles from the hot-melt prepregging in Chapter 3 were used to design and build a prepreg line capable of thermoset and thermoplastic tape production. The resulting polyamide/Kevlar[®] fiber prepreg tape was characterized for its mechanical and thermoelastic properties to validate the design and operation of the prepreg line.

4.1 Introduction and Background

Composites were appealing for their excellent specific strength/stiffness in aerospace and now the automotive industry for their weight savings [1]. The automotive industry has several constraints when selecting materials. The high production volume of automotive demanded cycle times near 1 minute to be economically feasible [2–4]. Advances have been made in rapid curing, thermosetting resins to achieve these cycle times [5]. Unfortunately, additional constraints have been leveraged and materials must be selected with the ability to be recycled/reused at end of life. Therefore, thermosetting resins were at a distinct disadvantage because of the barrier to reuse thermosets. Additionally, these materials must be capable of performing in a crash situation, thus energy absorption and failure mode were equally important as stiffness/strength [6,7]. Unlike carbon and glass fiber which fail brittlely, Kevlar[®] fibers exhibit ductile failure and impact tolerance [7]. Additionally, Kevlar[®] fibers possess tensile modulus of 70 – 120 GPa [8], but the compressive properties were lacking [7]. Thus, Kevlar[®] composites could supplement glass or carbon fiber composites to produce crash tolerant components, while retaining compressive properties.

Typically, glass or carbon fiber composites were considered for their cost savings or exceptional weight savings, however the failure modes for these composites were brittle and posed a serious health hazard during a crash. In contrast, Kevlar[®] composites exhibit ductile failure and have excellent impact performance. Additionally, the automotive industry is facing increased

pressure for vehicle components to be recycled or reused at end of life. Therefore, future composite components should be thermoplastic based rather than thermoset. As a result, polyamide/Kevlar[®] composites satisfy the need for crash resistant and recyclable composites. Thermoplastic prepreg manufacturing does pose a barrier for adoption, as manufacturing the prepreg tape can be challenging since thermoplastics have a much higher viscosity compared to thermosets. In response, DuPont has formulated a polyamide-6 resin uniquely tailored for prepregging with a low viscosity and excellent thermal stability.

To address the crash performance and end of life recycling, polyamide/Kevlar[®] composites should be considered as a supplemental material to improve crash performance of composite components. Additionally, polyamides have an existing recycling infrastructure in place. Furthermore, thermoplastic composites lend themselves to efficient manufacturing processes such as compression or hybrid overmolding suitable for the automotive industry [9–11]. While the part forming and end use of the polyamide/Kevlar[®] composites were appealing, there were still challenges when making the intermediate pre-impregnated composite tape (prepreg). The physics governing resin flowing through aligned fibers has been captured by Darcy's law (Equation (1.1)). This related the permeability (K), bed thickness (L), viscosity (η), fiber volume fraction (V_f), applied mechanical pressure (ΔP), and capillary pressure (P_c) to the superficial velocity ($\frac{dX}{dt}$) at which material flows through a porous medium. Thermoplastics were more challenging to prepreg compared to thermosets because thermoplastics generally have a high melt viscosity, on the order of 100 Pa•s, whereas thermosets have a viscosity around 1 Pa•s.

$$\frac{dX}{dt} = \frac{K(\Delta P + P_c)}{\eta L (1 - V_f)} \quad (4.1)$$

To investigate the potential polyamide/Kevlar[®] thermoplastic composites have in the automotive industry, polyamide/Kevlar[®] unidirectional prepreg tape was manufactured at the Manufacturing Design Laboratory (MDLab) at Purdue University and the resulting prepreg characterized. The hot-melt extrusion prepreg manufacturing conditions were reported for repeatable processing of this material system. The resin was a polyamide-6 which was specially formulated for a low melt viscosity and higher temperature stability during processing to avoid the issues with other thermoplastic prepregging. The manufactured prepreg was to be characterized for its mechanical properties (tensile, flexural, shear, and compressive – stiffnesses and strengths).

The experimentally measured mechanical, thermoelastic, and rheological properties are reported along with the manufacturing process conditions, sample preparation, analysis method, and discussion regarding the experimental results.

4.2 Materials, Manufacturing, and Methods

4.2.1 Materials

The thermoplastic resin used in this study was polyamide-6 based, trade named VZL-36D. The reinforcing fibers used for prepreg manufacturing and characterization were aramid fiber (Kevlar® 49). The fibers were a 2840 denier which corresponded to a filament count of 1333 per yarn. The polyamide-6 resin and Kevlar® fibers were provided by DuPont.

4.2.2 Prepreg Manufacturing

The thermoplastic prepreg tape line was developed as a hot-melt prepreg line at the Manufacturing Design Laboratory (MDLab) spanned 10m and was designed to study manufacturing conditions for unique resin and fiber combinations. The line typically operated at a speed of 0.5 – 2.5m/min (1.5 – 8FPM) and produced up to 75mm wide tape, with a thickness up to 1mm. The prepreg tape line was designed to process carbon, Kevlar®, and glass fibers with any thermoplastic or thermoset resin, including high performance thermoplastics, such as PEEK. Thermoset resins were restricted to 2-part resins with a sufficiently high uncured glass transition temperature for the resin to be a solid at room temperature. The resin extrusion system was designed to operate with a second melt pump to process two-part resin systems. Additionally, the impregnation die can be refitted to produce composite strands with a diameter up to 3mm for discontinuous fiber composites (long discontinuous unidirectional fiber thermoplastics, LFT).

The 48-position fiber creel was loaded with 26 bobbins of Kevlar® 49 and each yarn was pre-tensioned to 320g. An image of the fibers loaded on the creel is shown in Figure 4.1. The fibers were collimated using two combs on the spreader unit before entering the fixed bar to evenly distribute the individual yarns into a uniform web, as shown in Figure 4.1. Since Kevlar® fibers can hold up to 5wt% water, they were dried before processing. The spreader was equipped with an IR lamp which allowed the fibers to reach a temperature of 175°C to dry the Kevlar® fibers before entering the impregnation die. The fiber temperature was measured at the surface using a

handheld infrared thermometer. The dried fibers were necessary to eliminate negative influence on the properties.



Figure 4.1: Overview image of the prepreg tape line's 48 position creel (left) and fixed bar fiber spreading unit (right).

The polyamide-6 resin was pre-dried at 80°C for 14 hours at ambient pressure with no purge gases used before being extruded. A $\frac{3}{4}$ " single screw (non-vented, non-mixing) extruder (36 L/D) heated the resin to a temperature of 270°C and pressurized the polymer to 800psi for the melt pump. The extruder had 4 heating zones, with the following temperature profile used: Zone 1 – 250°C, Zone 2 – 260°C, Zone 3 – 265°C, and Zone 4 – 270°C. The melt pump (0.6cc/rev) was used as a metering device to control the flow of molten polymer into the impregnation die. The melt pump calibration curve was provided in Appendix 0. All die zones were operated at 310°C.

An overview of the extruder, melt pump, and impregnation die assembly can be seen in Figure 4.2. The resin was pumped into the fiber bed using by controlling the tension in the fibers and dragging the fibers across the ridges in the die, effectively pumping the resin into the fiber bed. The lips of the die were adjustable with three set screws to allow for production of prepreg up to 1mm thick. An example of the PA-6/Kevlar® prepreg exiting the die is shown in Figure 4.3. Then the tape went through a series of rollers to ensure the tape exited the die level. Tape that exited the die at an angle resulted in excess resin on one surface while the other surface was deficient of resin, which resulted in warped and unsatisfactory tape.



Figure 4.2: Overview image of the prepreg tape line's extruder, melt pump, and impregnation die.



Figure 4.3: PA-6/Kevlar[®] prepreg exiting the impregnation die.

The prepreg line operated across a range of operating speeds to determine optimal manufacturing conditions for the PA-6/Kevlar[®] prepreg. The melt pump was operated from 10 – 60 RPM while the line speed was 1.5 – 8 FPM. The impregnation die length is 1ft which corresponded to a fiber residence time inside the die from 8 to 40 seconds. While the line and pump speeds were varied over various manufactured preregs, the impregnation die was consistently heated to 310°C. An abbreviated summary of the prepreg line operating conditions is shown in Table 4.1, while a complete list is shown in Appendix 0.

Table 4.1: PA-6/Kevlar® prepreg manufacturing conditions

Prepreg ID	Pump Speed [RPM]	Line Speed [FPM]	Yarn Count	Die Temp [°C]	Expected V_f
18	14.5	2.0	26	310	0.51
19	14.5	2.0	26	310	0.51
20	13.5	2.0	26	310	0.52
21	14.5	2.0	26	290	0.51
22	19.0	2.0	26	310	0.43
23	30.0	2.0	26	310	0.33
24	30.0	2.0	26	310	0.33
25	30.0	2.0	26	310	0.33
26	60.0	4.0	26	310	0.33
27	42.0	3.0	26	310	0.34
28	40.0	3.0	26	310	0.35
29	15.0	1.5	26	310	0.42
30	45.0	4.5	26	310	0.42
31	12.0	2.0	26	310	0.55

The expected fiber volume fraction in Table 4.1 was based on a mass balance around the impregnation die, as shown in Equation (4.2). Where the pump displacement (V_{pump}), pump rotational speed (ω), puller speed (V_{puller}), yarn count (N_{yarn}), filament count ($N_{filament}$), and fiber radius (r) were used to define the expected fiber volume fraction. The expected prepreg fiber volume fraction was checked at three pump-to-puller ratios and found agreement with this estimate. The comparison of estimated to measured fiber volume fraction is shown in Figure 4.4.

$$V_f^{expected} = \frac{N_{yarn}N_{filament}\pi r^2}{\frac{V_{pump}\omega}{V_{puller}} + N_{yarn}N_{filament}\pi r^2} \quad (4.2)$$

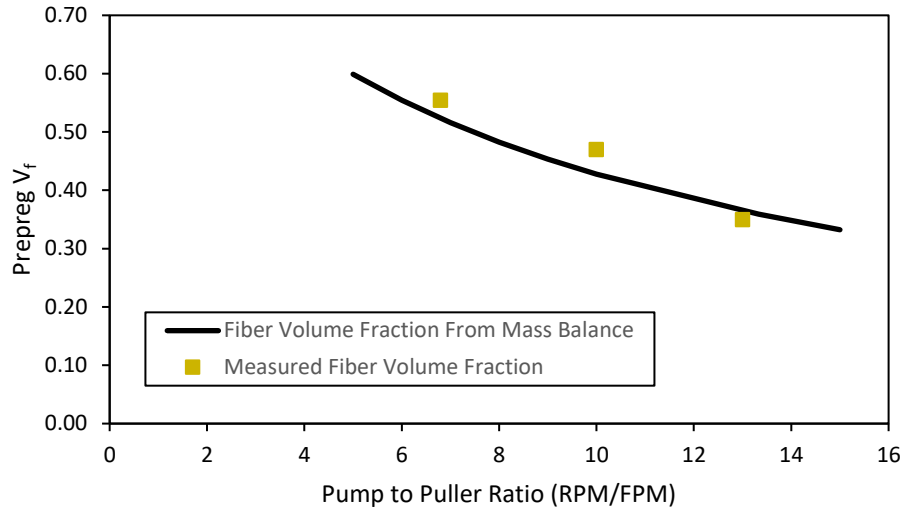


Figure 4.4: Estimated fiber volume fraction compared to measured fiber volume fraction for different pump to puller ratios. Assuming 26 yarns of Kevlar[®] were used.

A set of nip and guiding rollers were added at the exit of the die, which introduced a new variable and resulted in inconsistent fiber volume fractions along the width of the prepreg tape. Figure 4.5 labels the different regions of the prepreg tape, displayed a representative micrograph of the prepreg tape, and the resulting fiber volume fractions for the different prepreg sections along its width. This also showed the fiber volume fraction varied along the width by 0.2, which is very significant. The cause of this was misaligned rollers, resulting in the fibers in the tape to shift towards one side of the web. This was possible because the resin was still molten when exiting the die and had yet to develop any transverse modulus. Additionally, this prepreg had exceptionally high fiber content because the lip opening was too restricted, resulting in resin leaking out the die entrance. These were corrected in the batch of prepreg that was characterized.

The addition of the rollers after the die had to be adjusted to avoid inconsistent fiber volume fractions along the width of the prepreg tape. Figure 4.5 labels the different regions of the prepreg tape, displayed a representative micrograph of the prepreg tape, and the resulting fiber volume fractions for the different prepreg sections along its width. The microscopy images were analyzed in ImageJ and used image thresholding to determine the fiber volume fraction. ImageJ thresholding requires a non-color (8-bit) image and the threshold values to be specified by the user. Threshold values can range from 0 – 255 (for 8-bit) and can differ depending on the type of sample and

microscope settings. Typical threshold values used for the PA-6/Kevlar[®] prepreg ranged from 150 – 160 depending on microscope exposure and aperture settings.

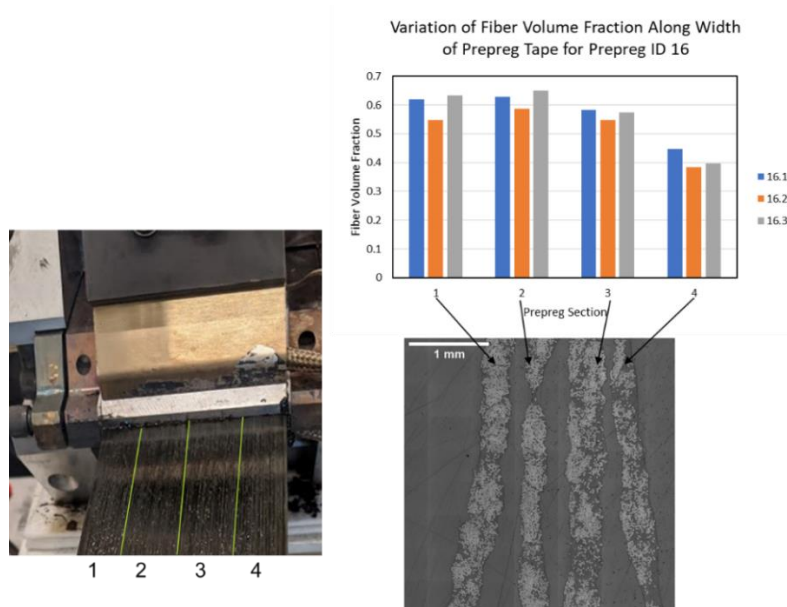


Figure 4.5: Example from prepreg ID 16 showing the fiber volume fraction varying at different locations along the prepreg width. The spacing between prepreg strips is a result of the mounting epoxy, not because there is a resin rich layer at the prepreg surface.

4.2.3 Specimen Preparation for Mechanical Testing

The manufactured PA-6/Kevlar[®] prepreg was consolidated into flat, 10” square plates for coupon preparation. The prepreg was dried before compression molding by holding the tape at 80°C for 14 hours. A total of 31 plates were produced from 15 different iterations of prepreg to identify ideal prepreg manufacturing and compression molding conditions. The prepreg that produced the best unidirectional plates without cracking were plates made from prepreg ID 28.2. This prepreg had a consistent fiber volume fraction of 0.35 along the width of the tape. While this was low, other attempts with prepreg at a higher fiber volume fractions resulted in cracked plates. The ideal compression molding conditions were to preheat the upper press platen to 275°C and the lower to 270°C. Furthermore, it was necessary to perform a hand layup on a preheated mold at 280°C, to ensure consistent consolidation. It was noted that attempting to use a cold tool would result in poor consolidation or prolonged exposure to high temperatures and degrade the material. After placing the mold between the platens, pressure was applied once the mold reached 240°C,

60psi was applied for 10 minutes. The final mold temperature before cooling was typically 250°C. Pressure was removed once the mold cooled to 210°C and the plate was demolded once the mold was below 45°C. A summary of compression molding conditions can be found in Table 4.2, compression molding conditions for untested plates can be found in Appendix A.

Table 4.2: Pressing conditions for PA-6/Kevlar® prepreg

Plate #	Prepreg ID	Layup	Press Force [ton]	Peak Press Temperature [°C]
23	28.2	[0] ₆	3	246
24	28.2	[0] ₆	3	250
25	28.2	[0] ₆	3	250
26	28.2	[0] ₆	3	248
31	28.2	[0,90] _{2s}	3	248

Five plate samples were compression molded using a 30-ton press for mechanical and thermoelastic characterization. Four plates (Plate # 23 – 26) had a unidirectional layup and were composed of 6 plies to determine the 0° and 90° properties. Approximately 3.5 strips of prepreg were used per ply, since the tapes were ~2.8” wide. The half strip location in the ply was alternated to stagger the prepreg and avoid any defects in the prepreg being concentrated in one area through the thickness of the laminate plate. The fifth sample (Plate #31) was a symmetric, cross-ply laminate composed of 8 plies to determine the $\pm 45^\circ$ shear properties. The layups used in this characterization are shown in Table 4.2.

Normally, test coupons would be cut using the surface grinder, however the IACMI 7.3.3 [12] project noted the Kevlar® material tended to fray with that method. Instead, the waterjet was used to cut test coupons from each plate, which made clean cuts. The cut profiles used, and sample naming convention are shown in Figure 4.6. Typically, tabbed samples were used for tensile testing, however, the 0° and 90° tensile coupons were cut into dog-bones with dimensions following ASTM D638-14 for Type I [13]. Dog-bone samples were used to determine accurate tensile stiffness values of the composite samples. We are well aware that the dog-bone samples are not optimal for strength characterization and should not at this stage be considered to be fully representative, even though no shearing or unexpected deformation was observed in the clamping area. Any samples with failure near to the clamping area were disregarded. The compression

samples were prepared following the Modified ASTM D 695 Compression Test [14], which called for samples approximately 100mm long and 12.5mm wide. The flexure samples were prepared following ASTM D7264 with dimensions approximately 200mm long and 12.5mm wide [15]. Shear samples were approximately 150mm long (50mm shorter than recommended by ASTM D3518-18) and 25.4 mm wide [16]. The shortened samples were necessary because of limited plate size and requirement to cut the samples at a 45° angle from the 10” plate. An example of the cut plate and naming convention are shown in Figure 4.7. Thickness and width measurements for all mechanical testing samples were measured in three locations along the gage length and were averaged and reported in the Appendix 0. The coefficient of thermal expansion (CTE) samples were cut to 37.5mm squares. All samples were dried at 80°C prior to testing for 14 hours.

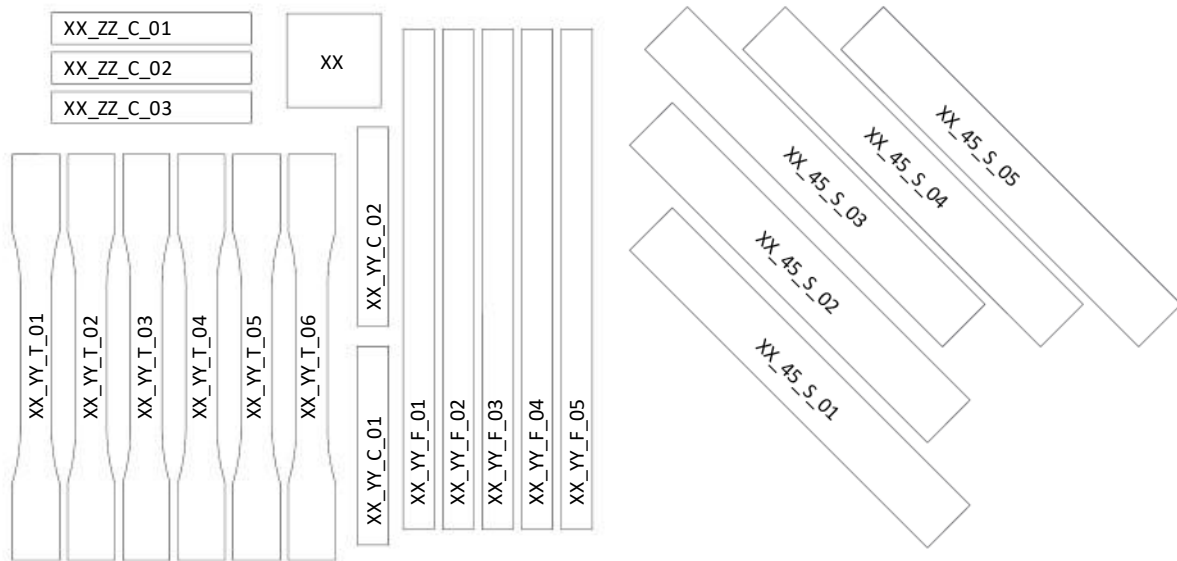


Figure 4.6: Waterjet cutting profile for unidirectional samples (left) and $\pm 45^\circ$ samples (right).

File naming convention: XX = plate number, YY = fiber orientation (0° or 90°), ZZ = fiber orientation (90° or 0°), T = tensile test, C = compression test, F = 3pt bending test, and S = shear test.

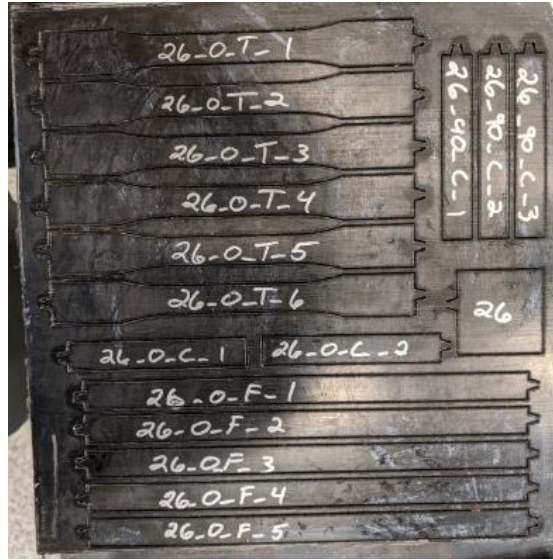


Figure 4.7: Plate 26 after being waterjetted, showing the naming convention used for unidirectional samples.

The unidirectional laminate plates 23 – 26 had their fiber volume fraction checked in five different regions. The resulting fiber measurements are shown in Table 4.3. The fiber volume fraction between each plate ranged from 0.325 – 0.352, which was an acceptable variation in the fiber content. Additionally, fiber volume fraction throughout the individual plates was observed to not vary significantly. The fiber volume fraction for the resulting plates was low, but plates with higher fiber volume fractions would crack. For this reason, the prepreg with a fiber volume fraction of 0.35 was characterized.

Table 4.3: Fiber volume fraction from manufactured plates from prepreg ID 28 showing consistent fiber content throughout the plate and across plates.

Plate ID	V_f	Plate ID	V_f	Plate ID	V_f	Plate ID	V_f
23.1	0.324	24.1	0.322	25.1	0.353	26.1	0.346
23.2	0.328	24.2	0.372	25.2	0.347	26.2	0.355
23.3	0.315	24.3	0.349	25.3	0.343	26.3	0.342
23.4	0.316	24.4	0.374	25.4	0.39	26.4	0.346
23.5	0.342	24.5	0.345	25.5	0.347	26.5	0.344
Average	0.325	Average	0.352	Average	0.356	Average	0.347

Mechanical testing sample gauge sections were spray painted white and speckled with black ink, while the CTE samples were speckled with a fine layer of white, temperature resistant paint. The speckle on the sample surface was used to determine the surface strains during testing. The CTE samples were speckled using the spray paint, because full coats of spray paint result in tests measuring the CTE of the paint, rather than the sample.

4.2.4 Digital Image Correlation (DIC) Strain Measurement

Digital image correlation (DIC) was used to measure the surface strains of the sample rather than strain gauges. The samples were sprayed with a light coat of white spray paint. The spray paint can nozzle was kept approximately 8 inches away from the sample surfaces. Multiple light coats of paint were applied to the sample surface using a sweeping pattern to make sure no streaks of paint occurred on the sample surface as described in the “VIC Speckle User Manual” from Correlated Solutions [17]. Coats were approximately every 10 minutes. The paint on the samples was allowed to dry for 1 hour before an ink speckle pattern was applied in a single stroke from the ink stamp roller.

Two 5MP camera were setup to acquire images of the sample during loading. The cameras were adjusted to make sure the gage section of the sample was in the field of view for both cameras. 30 – 40 calibration images were taken using the calibration pattern (patterns from Correlated Solutions) for the VIC 3D calibration, as described in “VIC-3D Easy Guide Setup Procedures for the VIC-3D 5MP Quasi Static System” [18]. The acquired images were post processed in VIC Snap 3D. A region of interest was selected in the gage section of the sample (approximately 25mm long and several millimeters away from the sample edges). The longitudinal, lateral, and shear strains in this region were averaged and reported as discrete values for each image.

4.2.5 Tensile Testing Methodology

The tensile testing was performed with a 22kip MTS loadframe on samples with a $[0]_6$ or $[90]_6$ layup to determine the directional dependent tensile stiffness and strength properties. A dog-bone coupon geometry was used in order to acquire accurate stiffness measurements. The crosshead displacement rate was set to 2mm/min, as described by ASTM D3039 with the load and displacement data being recorded at 10Hz [19]. Tensile strain (ϵ_t) measurements were recorded

using digital image correlation (DIC), where two cameras recorded images in sync with the load vs displacement data. The tensile stress (σ_t) of the sample was calculated from the tensile load (P) and cross section of the sample (width, w and thickness, t), shown in Equation (4.3). The DIC method was able to calculate the surface strain field from sequential images of the sample.

$$\sigma_t = \frac{P}{wt} \quad (4.3)$$

Samples were loaded into the hydraulic grips and secured with Emory cloth to ensure no slipping occurred in the grips. Samples were stressed until the sample could no longer carry significant load. The sample dimensions and load measurements were used to determine the sample stress. Sample stresses vs strain were plotted to determine the Young's modulus (E_t) and ultimate tensile strength in the fiber direction (0° or 1-direction) and transverse (90° or 2-direction), shown in Equation (4.4). The Young's modulus was defined as the slope of the stress-strain curve in the linear region of the curve.

$$E_t = \frac{\Delta\sigma_t}{\Delta\epsilon_t} \quad (4.4)$$

4.2.6 Shear Testing Methodology

The shear testing was performed with a 22kip MTS loadframe with a crosshead displacement of 2mm/min, as described by ASTM D3518 [16]. This test used samples with a $[\pm 45]_{2s}$ layup and loaded them in tension to determine the shear modulus (G_{12}) and strength. Load vs displacement data was recorded at 10Hz and was synced with the captured images with the DIC system. The DIC system was used in the same way as the tensile testing, to determine the surface strains. Samples were loaded in the same manner as the tensile samples. The shear stress (τ_{12}) for each sample was determined using the relation between load and cross-sectional area in Equation (4.5).

$$\tau_{12} = \frac{P}{2(wt)} \quad (4.5)$$

The shear strain was defined by the longitudinal strain (ϵ_x) and lateral strain (ϵ_y), shown in Equation (4.6). The shear strength was measured and reported as the maximum of the stress the sample was able to withstand. The shear modulus of elasticity was defined as the slope of the shear stress – shear strain (γ_{12}) curve in the linear region and was algebraically shown in Equation (4.7) .

$$\gamma_{12} = \epsilon_x - \epsilon_y \quad (4.6)$$

$$G_{12} = \frac{\Delta\tau_{12}}{\Delta\gamma_{12}} \quad (4.7)$$

4.2.7 Compression Testing Methodology

The compression testing was performed with a 22kip MTS loadframe on samples with a $[0]_6$ or $[90]_6$ layup to determine the directional dependent compressive stiffness and strength properties. The crosshead displacement rate was set to 1mm/min, as described by the Modified ASTM D 695 Compression Test. Load vs displacement data was recorded at 10Hz. The DIC system was not used to measure strain since the sample surface was mostly obscured by the fixture. A rectangular sample was placed into the modified Boeing test fixture. Four screws were tightened by hand to secure the sample vertically in place while allowing the sample to freely slide vertically. Vertical alignment of the sample was ensured by firmly pressing the sample against the two alignment pins on the test fixture. The compressive load was introduced through the top of sample with a flat platen. The exposed sample above the test fixture was approximately 3mm. An example of the experimental setup is shown in Figure 4.8. The test was concluded once the sample crushed, buckled, or did not fail, but the platen was too close to the test fixture.

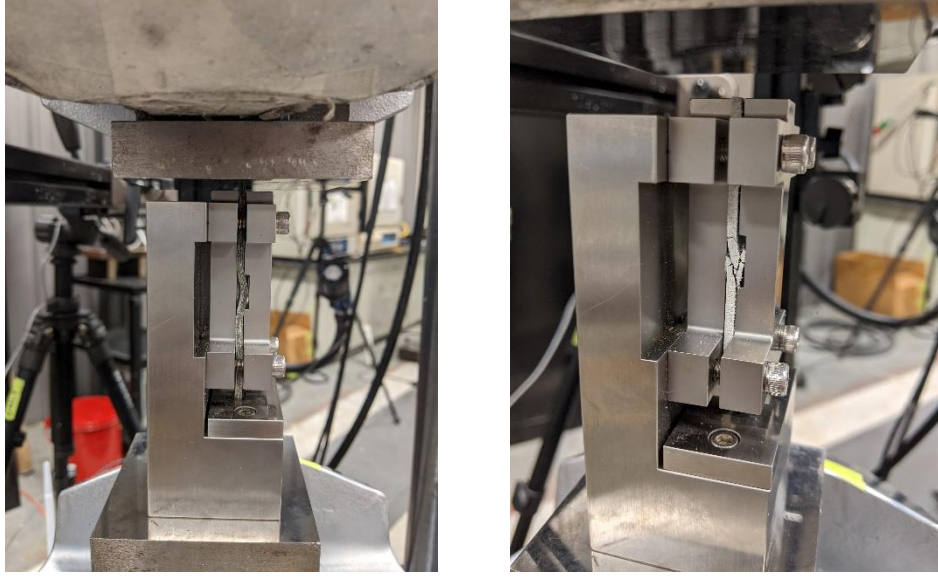


Figure 4.8: Compression test setup using the standard modified D695 test fixture. Samples are from a failed 0° sample (left) and 90° (right).

The compressive strain (ϵ_c) of the sample was calculated using the following approximation, where sample length is L .

$$\epsilon_c = \frac{\Delta L}{L} \quad (4.8)$$

The compressive stress (σ_c) of the sample was calculated using the same equation for tensile stress, force divided by the average cross-sectional area, Equation (4.9). The strength was defined as the maximum compressive stress experienced by the sample. The compressive modulus (E_c) was calculated as the slope of the linear portion of the stress-strain curve from the test, (4.10).

$$\sigma_c = \frac{P}{wt} \quad (4.9)$$

$$E_c = \frac{\Delta \sigma_c}{\Delta \epsilon_c} \quad (4.10)$$

4.2.8 Flexure Testing Methodology

The compression testing was performed with a 5kip MTS loadframe on samples with a $[0]_6$ or $[90]_6$ layup to determine the directional dependent flexural stiffness and strength properties. The

crosshead displacement rate was set to 1mm/min, as described by the ASTM D7264 [15]. Typically, a 32:1 span to thickness ratio is used, however the IACMI 7.3.3 project noted their woven Kevlar® samples were not failing at 32:1 and moved to a smaller ratio of 16 (which is allowed in the standard), where strength values could be measured. The smaller span to thickness ratio was chosen for this work since the composites characterized had a low fiber content and thermoplastic matrix, which were presumed to be quite flexible. The span to thickness ratio for this work was 14.8:1 because of a slight experimental error when initially measuring the span, hence the small deviation from ASTM D7264's optional span to thickness ratio of 16:1. A 3-pt bending fixture with a 33.9 mm span was used, as shown in Figure 4.9. The flexure sample lengths were approximately 203 mm, which are well above the recommended 20% longer than span suggested in the standard. The extra length was in anticipation of the sample having a large displacement to failure. The exact sample lengths were not recorded since these were not used in later calculations. The load and displacement measurements were recorded at 10Hz.



Figure 4.9: Flexure sample test setup using 3-point bending test fixture with a 33.9mm span.

Flexural stress (σ_f) was calculated using the load applied, the span (L), the average width (w), and thickness (t) of the sample, Equation (4.11). The flexural strength was defined as the maximum stress experienced by the sample during testing.

$$\sigma_f = \frac{3PL}{2wt^2} \quad (4.11)$$

The flexural stiffness (E_f) can be calculated from the slope of the load-displacement ($\frac{\Delta P}{\Delta \delta}$) curve along with the span, width, and thickness of the sample (Equation (4.12)).

$$E_f = \frac{L^3}{4wt^3} \frac{\Delta P}{\Delta \delta} \quad (4.12)$$

4.2.9 Rheological Testing Methodology

The temperature and strain rate dependence of the polyamide-6's resin's dynamic viscosity (η_D) was measured using a Discovery Hybrid Rheometer. 25mm parallel plate geometry with a sample gap between 800 – 1100 μm was used for each sample. Samples were weighed to be approximately 0.7g to achieve the desired gap range. The polyamide-6 resin was pre-dried at 80°C for 14 hours at ambient pressure with no purge gases used. The rheometer chamber was purged with a steady 8LPM of N_2 to help prevent the sample from degrading in air. Resin samples were loaded into a preheated rheology chamber and were melted in between the parallel plates. The samples were trimmed to prevent any excess material sticking out between the parallel plates and removed any material on the top plate (since this would influence the inertial calibration).

The samples would dwell at the test temperature for 30 seconds before experiencing a range of strain rates (ω , in radians/sec) ranging in frequencies from 1 to 50Hz with 5 points per decade at a constant strain of 0.03. The strain control mode used with the Trios software was “non-iterative sampling” with an initial stress of 10 $\mu\text{N}\cdot\text{m}$. The tested temperatures ranged from 250 – 290°C in 5°C increments. The dynamic viscosity was defined by the ratio of the loss modulus (G'') to the strain rate, Equation (4.13). The dynamic viscosity was defined by the Cross Model [20] which relates the zero ($\eta_{0,shear}$) and infinite ($\eta_{\infty,shear}$) shear rate viscosities (functions of temperature) with the shear rate (γ , in Hz) dependence of the polymer melt. The zero and infinite shear rate viscosities are defined using the Arrhenius model for viscosity where the activation energy for flow is E_η , R is the ideal gas constant, T is temperature in Kelvin, and η_∞ is the viscosity at a constant shear rate extrapolated to infinite temperature, Equation (4.14). The Cross Rate Constant

(m) and the Cross Time Constant (C) were empirically fitted to the rheological data. The Cross model is shown in Equation (4.15)

$$\eta_D = \frac{G''}{\omega} \quad (4.13)$$

$$\eta_i = \eta_\infty e^{\frac{E\eta}{RT}} \quad (4.14)$$

$$\eta_D(T) = \eta_{\infty, shear} + \frac{\eta_{0, shear} - \eta_{\infty, shear}}{1 + (C\gamma)^m} \quad (4.15)$$

4.2.10 Coefficient of Thermal Expansion Testing Methodology

The coefficient of thermal expansion (α_i) was determined using the DIC method with a hot stage. Three unidirectional samples were tested to determine the CTE values for the 0° and 90° directions. A 37.5 mm square sample was placed on release film inside a hot stage such that the sample surface could be viewed through the 25mm diameter window. The sample was ramped from room temperature to 140°C at 4°C/min with 8 minute isothermal dwells every 10°C. A single camera was used to record images at 0.2Hz, this data was synced with the temperature recordings of the sample surface. The strain (ϵ_i) measurements were recorded as the average strain during the isothermal dwell once the sample temperature (T) had reached equilibrium. This method was used as this has given more reliable measurements than the dynamic scans without isothermal dwell. The coefficient of thermal expansion was determined by comparing the linear slope of the principal strain vs temperature curve, Equation (4.16).

$$\alpha_i = \frac{\Delta\epsilon_i}{\Delta T} \quad (4.16)$$

4.3 Results & Discussion

4.3.1 Rheological Characterization

The neat polyamide-6 resin was subjected to oscillatory shear with frequencies ranging from 1 – 50 Hz. The resin exhibited shear thinning behavior across these frequencies. The temperature and frequency dependence of the resin is shown in Figure 4.10. In these tests, the resin

was able to achieve a low melt viscosity, 15 Pa•s, for polyamide-6, which makes this resin well suited for prepreg manufacturing. However, the resin surface was noted to become unstable above 300°C, as such tests above 290°C were not included. The sample surface would oxidize with the air in the chamber, despite the sample chamber receiving a steady Nitrogen flow. The chamber was not airtight which allowed the oxidation to occur. The sample would only show signs of degradation at the surface in the form of a “skin” layer forming. This skin layer would influence the viscosity measurements and cause a slightly elevated viscosity measurement for that temperature. This was not considered to be an issue during prepregging since the resin would not be in contact with air while in the die at elevated temperatures. Additionally, these effects were only noted when the sample would remain above 290°C for 10 minutes.

The viscosity data for the PA-6 resin was fitted to the Cross Model (Equation (4.15)) as this has been shown to describe shear thinning polymers. The Cross Rate Constant (m) was found to be 0.52 and the Cross Time Constant (C) was found to be 0.93 seconds. The zero and infinite shear Arrhenius fitting parameters are shown in Table 4.4. These fitting parameters provided a good fit for the data shown in Figure 4.10.

Table 4.4: Arrhenius parameters for the zero and infinite shear viscosities of the PA-6 resin.

	E_{η} [kJ/mol]	η_{∞} [Pa•s]
Zero shear ($\eta_{0,shear}$)	50.75	3.26E-04
Infinite shear ($\eta_{\infty,shear}$)	54.85	3.17E-04

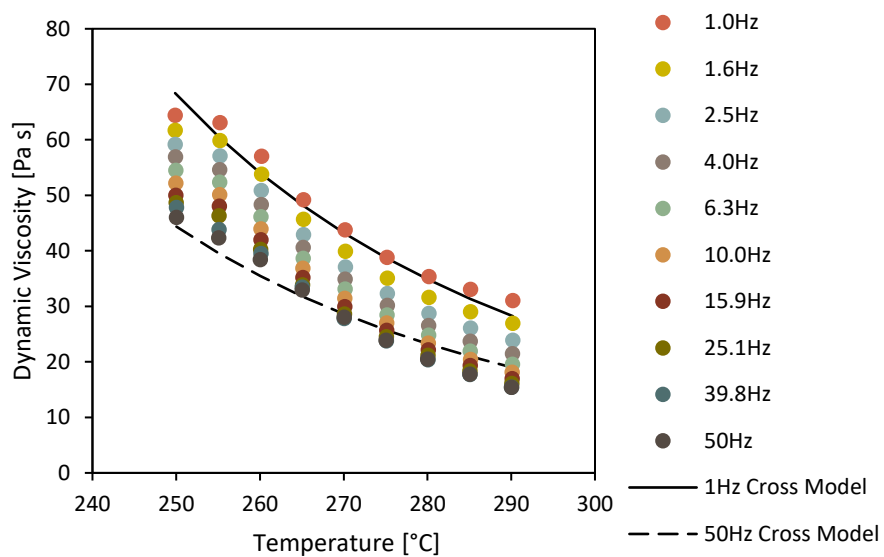


Figure 4.10: PA-6 resin dynamic viscosity vs frequency for temperatures 250 to 290°C. For clarity, the Cross Model (Equation (4.15)) fit is shown for 1Hz and 50Hz, demonstrating the model fit.

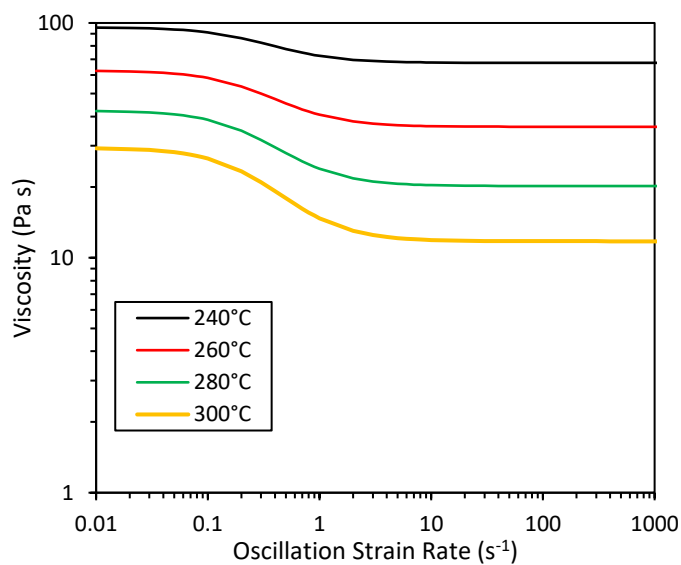


Figure 4.11: Viscosity vs shear rate as modeled with (4.15) for temperatures ranging from 240°C – 300°C.

4.3.2 Tensile Samples

Plates 23 and 26 were used to determine the stiffness and strength in the fiber direction of the PA-6/Kevlar[®] composites. Figure 4.12 shows the failed tensile samples from plates 23 and 26. All of the tensile samples from plate 26 failed in the gage section and had a clear fiber failure classified by a lateral failure in the gage section towards one end of the gage section with some long splitting observed in some samples. In plate 23, samples 23_0_T_03 and 23_0_T_04 failed in the grip section, otherwise the samples followed the failure pattern scene in plate 26. Samples 23_0_T_04, 23_0_T_05, and 23_0_T_06 from plate 23 were noted to have some fiber misalignment visible on at the sample surface. This was likely caused during the compression molding of the plate and these samples were not included in the strength or stiffness measurements.



Figure 4.12: Failed 0° tensile samples from plates 23 and 26. The sample nomenclature is described in Figure 4.6.

Twelve samples were tested from plates 23 and 26 for 0° mechanical properties. All samples exhibited a linear stress vs strain curve until failure, shown in Figure 4.13. The 0° samples failed consistently at a strain between 1.6 and 1.8%, with two samples from plate 23 failing before 1.6%. These were a part of the samples that had a disturbance in the fiber orientation during compression molding and can be disregarded. The Young's modulus (E_1) was found to be 27.40 ± 0.80 GPa and the ultimate tensile strength to be 463.8 ± 28.4 MPa. While, the strength values

were reported, the true strength value was likely higher since a dog-bone geometry was used. These values are reported in Figure 4.13.

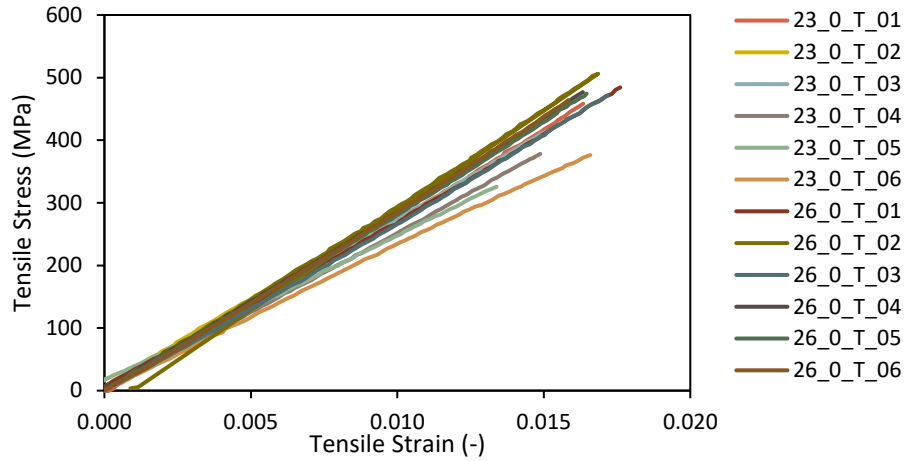


Figure 4.13: Stress vs strain curve for 0° samples from plates 23 and 26. The sample nomenclature is described in Figure 4.6.

The tensile stiffness values along the fiber direction were low for Kevlar®49 fiber composites at this fiber volume fraction (0.35). Rules of mixtures would predict the stiffness to be 43 GPa at this fiber volume fraction for Kevlar® 49 fibers, shown in Figure 4.14. The upper-bound modulus rule of mixtures was used to predict the composite's modulus in the fiber direction, Equation (4.17). A fiber modulus (E_{fiber}) value of 124 GPa was used to represent the composite with Kevlar® 49 fibers. Because of the large difference between experimental and predicted stiffness, the rules of mixtures was repeated with Kevlar® fibers with a modulus of 83 GPa to represent the composite with Kevlar® 29 fibers. Both curves used the stiffness of the resin (E_{resin}) as 3.55 GPa, because this was the experimentally determined E_2 value which should represent the resin's modulus. The Kevlar® fibers in the composite were confirmed to be Kevlar® 49 fibers, therefore the lower stiffness could be a result of the prepreg manufacturing conditions since the Kevlar® fibers were exposed to 310°C for about 30 seconds. This temperature exposure could have caused the Kevlar® fibers to degrade, therefore reducing the fiber's stiffness.

$$E_1 = E_{\text{fiber}} V_f + E_{\text{resin}}(1 - V_f) \quad (4.17)$$

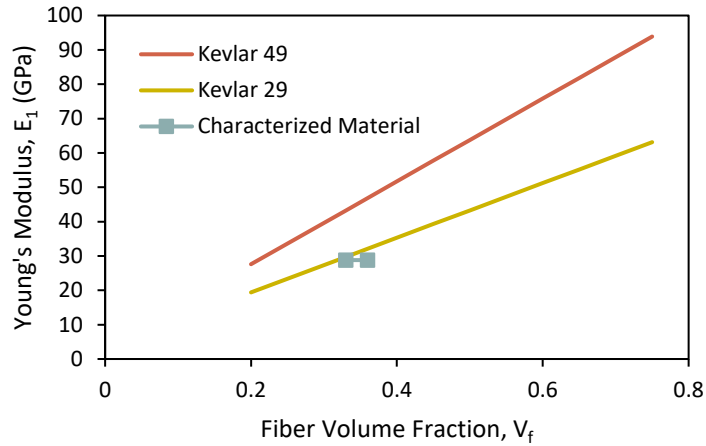


Figure 4.14: Rules of mixing for tensile Young's modulus in the fiber direction for Kevlar[®] 29 and 49 fibers compared to the experimentally measured values for PA-6/Kevlar[®] prepreg.

Table 4.5: Tensile modulus and strength results from plates 23 and 26 for the 0° samples. The sample nomenclature is described in Figure 4.6.

Sample Name	Tensile Modulus [GPa]	Tensile Strength [MPa]
23_0_T_01	27.46	459.9
23_0_T_02	28.03	417.1
23_0_T_03	27.34	414.3
23_0_T_04	25.22	377.6
23_0_T_05	22.65	325.8
23_0_T_06	22.90	375.7
26_0_T_01	26.25	484.8
26_0_T_02	28.34	505.6
26_0_T_03	25.90	475.7
26_0_T_04	27.72	476.9
26_0_T_05	27.36	475.1
26_0_T_06	28.29	464.9
Average	27.41 ± 0.80	463.8 ± 28.4

Twelve tensile samples from plates 24 and 25 were tested to determine the 90° mechanical properties. The samples had a linear stress vs strain curve until failure, although the data was

noisier since the 90° samples did not carry as much load as the 0° samples. The 90° samples all exhibited lateral failure parallel to the fibers and failed inside the gage length. Some samples exhibited failure in multiple locations, but the mode was the same at both locations. The failed samples are shown in Figure 4.15. The samples all failed at strains from 0.75 – 1.04%, except for sample 24_90_C_01 from plate 24. It was unclear why this sample failed at a lower stress vs strain than all other 90° samples. Since this sample was near the edge of the plate there was a possibility that a defect was introduced during compression molding, which effected this sample, but not the others. Additionally, the stress vs strain curve in Figure 4.16 show the samples carried a finite load at 0% strain. This was caused by some of the samples being loaded incorrectly and allowing the test to begin while the sample was pre-loaded. This occurred when the hydraulic grips closed on the sample and compressed the sample, then the crosshead was moved to return the sample to a neutral position. Unfortunately, the samples showed low strength values, which meant small changes in the initial loading conditions were evident in the stress vs strain curve. This difference in initial loading did not influence the Young's modulus or strength measurements. The Young's modulus (E_2) was found to be 3.55 ± 0.52 GPa and the ultimate tensile strength to be 30.8 ± 2.2 MPa. These values are reported in Table 4.6. Additionally, polyamide-6 resin was reported to have modulus in the range of 1.4 – 4.2 GPa [21], which indicated the resin was not degraded from the prepregging process.



Figure 4.15: Failed 90° tensile samples from plates 24 and 25. The sample nomenclature is described in Figure 4.6.

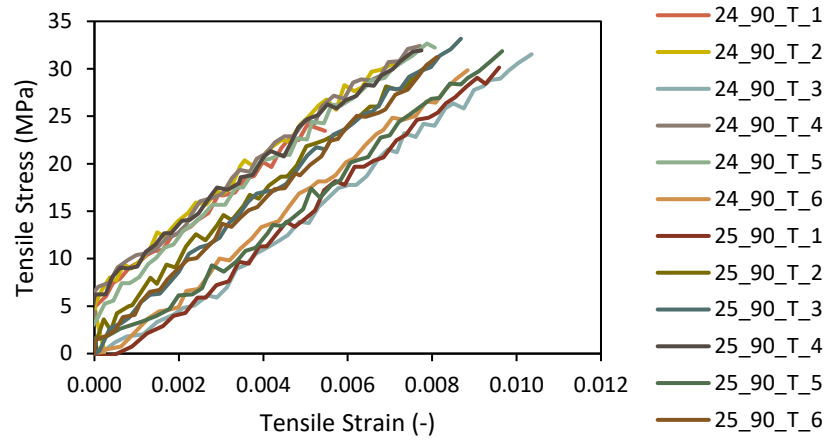


Figure 4.16: Tensile stress vs strain curve for 90° samples from plates 24 and 25. The sample nomenclature is described in Figure 4.6.

Table 4.6: Tensile modulus and strength results from plates 24 and 25 for the 90° samples. The sample nomenclature is described in Figure 4.6.

Sample Name	Tensile Modulus [GPa]	Tensile Strength [MPa]
24_90_T_1	3.53	24.1
24_90_T_2	3.57	30.7
24_90_T_3	2.26	31.5
24_90_T_4	3.60	32.4
24_90_T_5	3.80	32.0
24_90_T_6	3.52	29.8
25_90_T_1	3.08	30.1
25_90_T_2	4.12	30.8
25_90_T_3	4.00	33.1
25_90_T_4	3.96	31.9
25_90_T_5	3.04	31.8
25_90_T_6	4.09	31.3
Average	3.55 ± 0.52	30.8 ± 2.2

4.3.3 Shear Samples

Five shear samples were tested from plate 31. In Figure 4.17, the stress vs strain curves for the shear samples remained linear until ~2% strain where the samples became nonlinear. The samples failed at strains ranging from 8% to 25% with an average ultimate shear stress of 50.1 ± 4.8 MPa. The shear modulus was calculated from the linear region of the stress vs strain curve,

below 2% strain. The shear modulus was found to be 1.12 ± 0.06 GPa. Shear modulus and strength values for each sample are reported in Table 4.7.

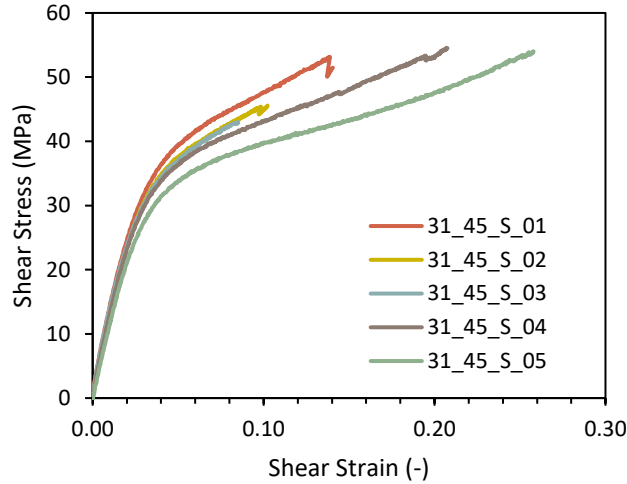


Figure 4.17: Shear stress vs strain for samples from plate 31 with layup $[(\pm 45)]_{2S}$. The sample nomenclature is described in Figure 4.6.

Table 4.7: Shear modulus and strength results from plate 31. The sample nomenclature is described in Figure 4.6.

Sample Name	Shear Modulus [GPa]	Shear Strength [MPa]
31_45_S_1	1.19	53.2
31_45_S_2	1.14	45.6
31_45_S_3	1.13	43.0
31_45_S_4	1.11	54.6
31_45_S_5	1.01	54.0
Average	1.12 ± 0.06	50.1 ± 4.8

4.3.4 Compression Samples

Ten 0° and ten 90° compression samples were tested to failure or to the strain limit of the test fixture. The 0° exhibited buckling in the gage section of the test fixture and the 90° samples experienced a shear failure. Figure 4.19 shows typical examples of the compression samples failing. The samples did not fail at the end, instead, the failure occurred in the gage section. Some samples did not fail by the time the crosshead platen reached the test fixture; in those cases, the ultimate

stress was recorded at the maximum stress the samples carried before the crosshead reached the test fixture.

The 0° compression samples stress vs strain curves in Figure 4.18 showed a linear stress vs strain region with strains ranging from 0.2% to 0.8%. The Young's modulus was calculated from this linear region. The stress vs strain curve below 0.2% was nonlinear, which was caused by the sample settling slightly in the test fixture. All 0° samples exhibited non-linearity beyond 1% strain. The 0° samples exhibited consistent stress vs strain curves, except for sample 23_0_C_01. This was the first sample tested and the screws holding the sample in place may have been too loose. This did not impact the modulus or strength values significantly. The 0° compressive Young's modulus was 10.47 ± 1.39 GPa and the compressive strength was 131.5 ± 6.5 MPa with results for each sample reported in Table 4.8. The compressive properties in the fiber direction are significantly worse than in tension. This result was expected as Kevlar® has poor compressive stiffness and strength [8].

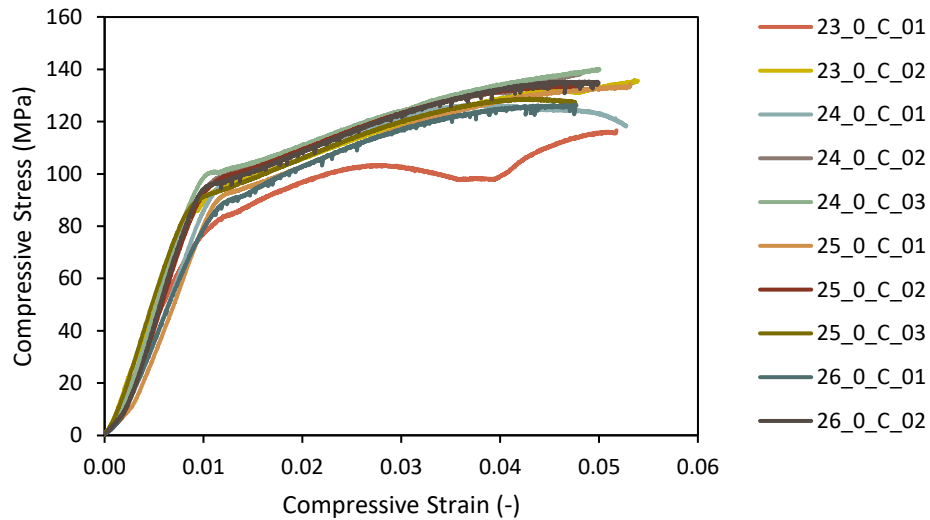


Figure 4.18: Compressive stress vs strain curves for unidirectional 0° samples. The sample nomenclature is described in Figure 4.6.

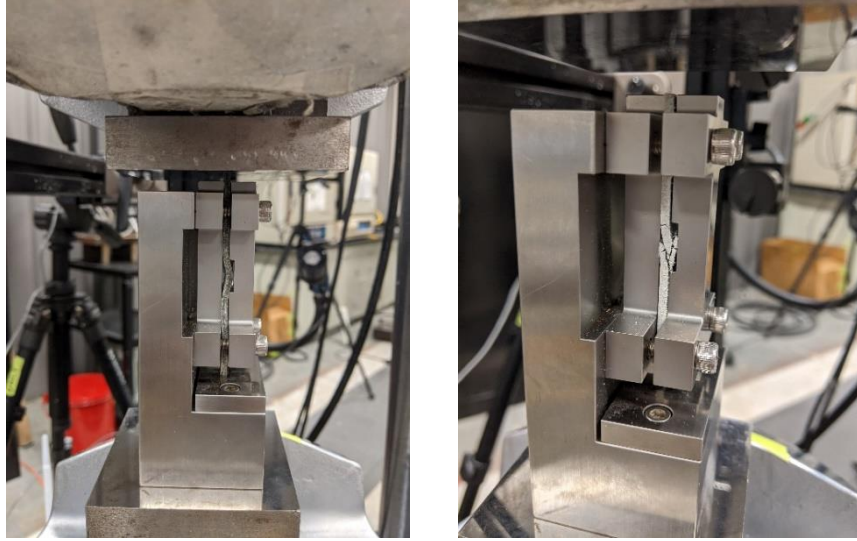


Figure 4.19: Typical failure examples for compression 0° samples (left) in buckling and 90° samples (right) in shear.

Table 4.8: Compression modulus and strength results from plates 23, 24, 25, and 26 for the 0° samples.

Sample Name	Compressive Modulus [GPa]	Compressive Strength [MPa]
23_0_C_1	9.48	116.7
23_0_C_2	9.90	136.0
24_0_C_1	8.83	126.5
24_0_C_2	10.65	138.4
24_0_C_3	12.19	138.3
25_0_C_1	8.39	134.4
25_0_C_2	11.40	134.0
25_0_C_3	11.72	128.8
26_0_C_1	9.47	126.5
26_0_C_2	12.62	135.4
Average	10.47 ± 1.39	131.5 ± 6.5

The 90° compression samples stress vs strain curves in Figure 4.20 shows a linear stress vs strain region with strains ranging from 0.8% to 2%. The Young's modulus was calculated from this linear region. The stress vs strain curve below 0.8% was nonlinear, which was caused by the sample settling slightly in the test fixture. All 90° samples exhibited non-linearity beyond 2.2% strain. The 90° samples exhibited slightly less consistent stress vs strain curves compared to the 0° samples. This was probably caused by the lower loads and sample settling into the fixture. The 90°

compressive Young's modulus was 13.13 ± 0.30 GPa and the compressive strength was 89.7 ± 8.0 MPa with results for each sample reported in Table 4.9. The compressive Young's modulus in the transverse fiber direction are very similar to the tensile modulus which was expected. The ultimate compressive strength was significantly larger than the tensile strength which indicated the resin did not form a strong bond with the fibers. This poor resin/fiber interaction meant the tensile coupons failed prematurely.

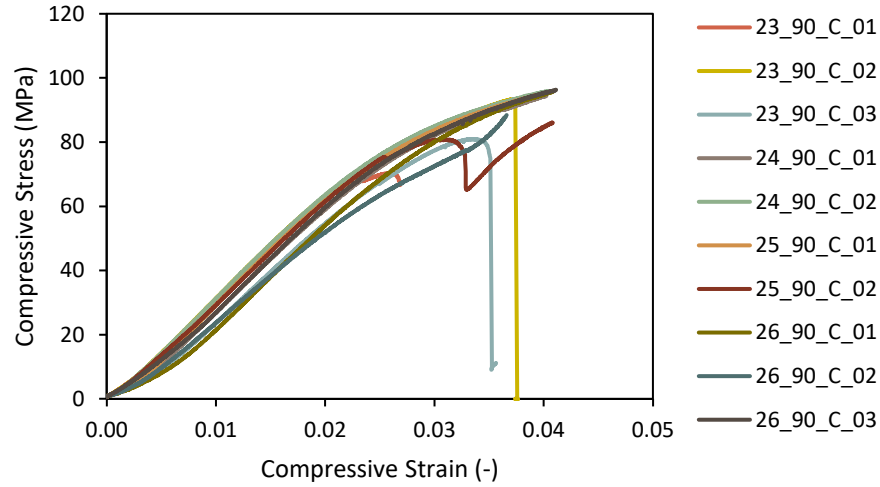


Figure 4.20: Compressive stress vs strain curves for unidirectional 90° samples. The sample nomenclature is described in Figure 4.6.

Table 4.9: Compression modulus and strength results from plates 23, 24, 25, and 26 for the 90° samples. The sample nomenclature is described in Figure 4.6.

Sample Name	Compressive Modulus [GPa]	Compressive Strength [MPa]
23_90_C_1	3.32	70.7
23_90_C_2	3.38	93.3
23_90_C_3	3.14	80.9
24_90_C_1	3.30	94.5
24_90_C_2	3.39	95.9
25_90_C_1	3.35	95.0
25_90_C_2	3.26	86.1
26_90_C_1	2.50	95.8
26_90_C_2	2.68	88.4
26_90_C_3	3.02	96.3
Average	3.13 ± 0.30	89.7 ± 8.0

4.3.5 Flexure Samples

Nine 0° flexure samples from plates 23 and 26 were tested in 3-point bending with the resulting load vs displacement curves shown in Figure 4.21. Sample 23_0_F_01 was tested with an incorrect span and was not reported. The span used for the remaining nine samples was 33.9mm to give a span to thickness ratio of 14.7. The narrower span was chosen because of the flexibility noted by the IACMI 7.3.3 project. The load vs displacement curve was linear until a displacement of 0.4mm. The Young's modulus was calculated from this linear region. All 0° flexure samples exhibited nonlinearity above 0.6mm. The 0° flexural Young's modulus was 21.34 ± 0.69 GPa and the flexural strength was 345.5 ± 39.2 MPa with results for each sample reported in Table 4.10.

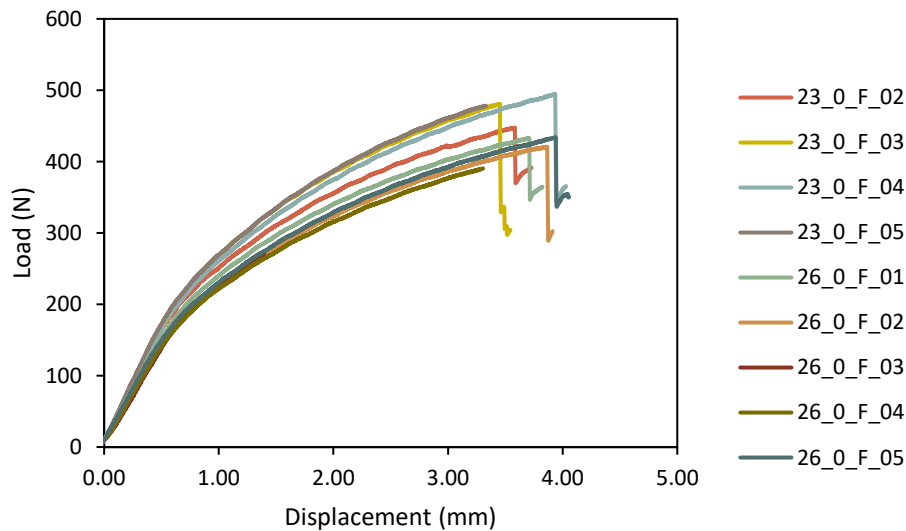


Figure 4.21: 3-point bending load vs displacement curve for 0° samples from plates 23 and 26. The sample nomenclature is described in Figure 4.6.

Table 4.10: Flexural modulus and strength results from plates 23 and 26 for the 0° samples. The sample nomenclature is described in Figure 4.6.

Sample Name	Flexural Modulus [GPa]	Flexural Strength [MPa]
23_0_F_02	21.80	356.3
23_0_F_03	22.90	362.0
23_0_F_04	21.44	380.7
23_0_F_05	20.44	351.7
26_0_F_01	21.35	365.8
26_0_F_02	20.86	354.8
26_0_F_03	21.08	239.1
26_0_F_04	20.67	337.2
26_0_F_05	21.56	361.7
Average	21.34 ± 0.69	345.5 ± 39.2

Ten 90° flexure samples from plates 24 and 25 were tested in 3-point bending with the resulting load vs displacement curves shown in Figure 4.22. Sample 23_0_F_01 was tested with an incorrect span and was not reported. The span used was 33.9mm to give a span to thickness ratio of 14.7. The narrower span was chosen because of the flexibility noted by the IACMI 7.3.3 project. The load vs displacement curve was linear until 0.6mm of displacement. The Young's modulus was calculated from this linear region. The 90° flexural Young's modulus was 3.58 ± 0.42 GPa and the flexural strength was 45.8 ± 4.0 MPa with results for each sample reported in Table 4.11.

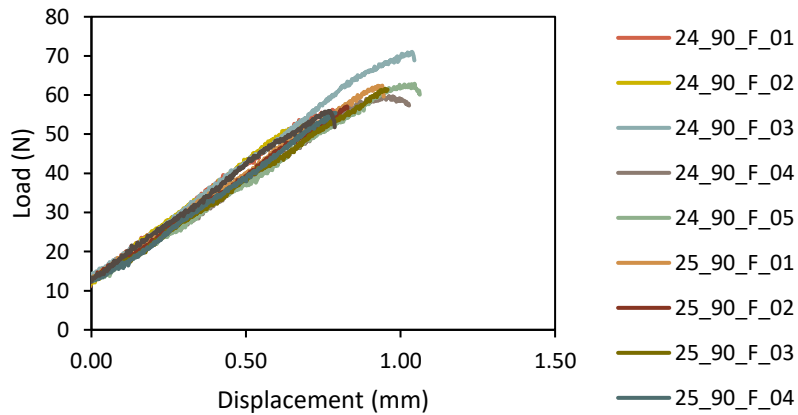


Figure 4.22: 3-point bending load vs displacement curve for 90° samples from plates 24 and 25. The sample nomenclature is described in Figure 4.6.

Table 4.11: Flexural modulus and strength results from plates 24 and 25 for the 90° samples. The sample nomenclature is described in Figure 4.6.

Sample Name	Flexural Modulus [GPa]	Flexural Strength [MPa]
24_90_F_01	3.75	43.2
24_90_F_02	3.78	39.8
24_90_F_03	3.51	51.9
24_90_F_04	2.96	42.6
24_90_F_05	2.67	41.6
25_90_F_01	3.51	49.0
25_90_F_02	3.83	47.1
25_90_F_03	3.80	51.7
25_90_F_04	4.07	46.6
25_90_F_05	3.88	44.1
Average	3.58 ± 0.42	45.8 ± 4.0

4.3.6 Thermoelastic Characterization

Three coefficient of thermal expansion samples were tested from plates 24, 25, and 26. The same sample and test was able to measure the thermal strains in the 0° and 90° directions. Plate 23's sample was broken when cutting out the sample and was not tested. The thermal strain vs temperature curves are shown in Figure 4.23. The thermal strains in the fiber direction (0°) were nearly zero with a CTE₁ of $-2.0 \pm 1.9 \mu/\text{°C}$, which was expected for Kevlar® fiber composites. The thermal strains transverse to the fiber direction (90°) were significantly larger. The CTE₂ below the T_g (80°C) was $171.2 \pm 3.2 \mu/\text{°C}$ and above the T_g (100°C) was $189.3 \pm 6.2 \mu/\text{°C}$. These CTE₁ and CTE₂ values for each sample were reported in Table 4.12 and

Table 4.13, respectively. The sample from plate 24 exhibited strange behavior above the T_g. An error likely occurred during testing, however the precise reason for this discrepancy was unclear, as a result this sample was omitted when reporting the CTE values.

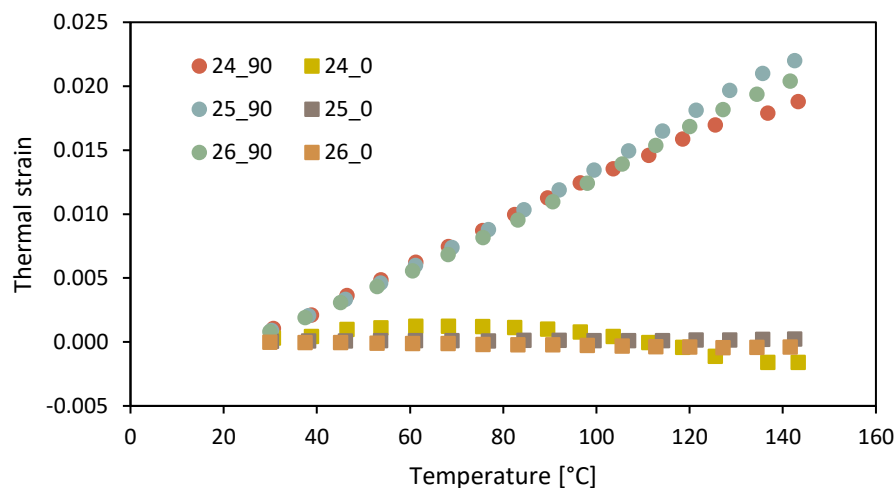


Figure 4.23: Thermal strain vs temperature curves from plates 24, 25, and 26 for strains in the 0° and 90° directions. The sample nomenclature is described in Figure 4.6.

Table 4.12: Coefficient of thermal expansion along the fiber direction for samples from plates 24, 25, and 26. The sample nomenclature is described in Figure 4.6.

Sample Name	CTE ₁ below T _g [$\mu/\text{°C}$]	CTE ₁ above T _g [$\mu/\text{°C}$]
24_0	1.4	-46.1
25_0	-0.1	3.8
26_0	-3.9	-0.8
Average	-2.0 ± 1.9	1.5 ± 2.3

Table 4.13: Coefficient of thermal expansion transverse to the fiber direction for samples from plates 24, 25, and 26. The sample nomenclature is described in Figure 4.6.

Sample Name	CTE ₂ below T _g [$\mu/\text{°C}$]	CTE ₂ above T _g [$\mu/\text{°C}$]
24_90	175.1	125.0
25_90	174.4	195.5
26_90	168.0	183.1
Average	171.2 ± 3.2	189.3 ± 6.2

4.4 Conclusions

This study covered the hot melt manufacturing process used at the Manufacturing Design Laboratory to produce polyamide-6/Kevlar® prepreg tape. A variety of prepreg manufacturing conditions were considered, but the ideal tape was manufactured with a die temperature of 310°C,

melt pump 40RPM, and a line speed of 3FPM to produce prepreg with a fiber volume fraction of 0.35. Higher fiber volume fractions led to cracking during compression molding. The PA-6 (polyamide-6) resin was specially formulated at DuPont for high temperature processing (310°C), thermal stability, and low viscosity. The polyamide-6 was characterized for its rheological properties and was found to exhibit shear thinning. At 300°C, the resin exhibited a viscosity of 15 – 40 Pa•s, which was reasonably low for a polyamide-6 resin. The Cross Model (Equation (4.15)) provided an excellent fit of the rheological data.

Additionally, the prepreg tape was studied to experimentally determine the directionally dependent: tensile, compression, flexure, shearing, and thermoelastic properties of PA-6/Kevlar® 49 prepreg. The mechanical properties for the prepreg tape with a fiber volume fraction of 0.35 are summarized in Table 4.14. The 0° tensile stiffness was lower than expected for Kevlar® 49 fibers. The prepregging process was not cause for the poor mechanical properties as the time the Kevlar® fibers were exposed to 310°C in the die was brief (less than 30 seconds) and the 90° modulus was in the typical range expected for PA-6. The 90° tensile strength was very low compared to the compressive strength in the same direction. This indicated the resin/fiber interface was poorly bonded. The poor bonding was not caused by the prepregging operation as the fibers were dried before entering the impregnation die and the prepreg was re-melted during compression molding. Therefore, the polyamide did not bond well to the Kevlar® fibers and sizing may need to be added for better properties. The compressive properties in the 0° direction were significantly worse compared to the tensile properties, however this result was expected as Kevlar® was known for poor compressive properties as a result of the fiber architecture.

Table 4.14: Summary of material properties from characterization tests for PA-6/Kevlar® prepreg.

Sample Type	Modulus (GPa)	Strength (MPa)	ν_{12}
Tension [0°]	27.41 ± 0.80	463.8 ± 28.4	0.45 ± 0.05
Tension [90°]	3.55 ± 0.52	30.8 ± 2.2	
Compression [0°]	10.47 ± 1.39	131.5 ± 6.5	
Compression [90°]	3.13 ± 0.30	89.7 ± 8.0	
Flexure [0°]	21.3 ± 0.7	345.5 ± 39.2	
Flexure [90°]	3.58 ± 0.42	45.8 ± 4.0	
Shear	1.12 ± 0.06	50.1 ± 4.8	

4.5 References

- [1] Jones RM. *Mechanics of Composite Materials*. 2nd ed. CRC Press; 1999. <https://doi.org/10.1201/9781498711067>.
- [2] Bernet N, Wakeman MD, Bourban PE, Månson JA. An integrated cost and consolidation model for commingled yarn based composites. *Compos - Part A Appl Sci Manuf* 2002;33:495–506. [https://doi.org/10.1016/S1359-835X\(01\)00140-3](https://doi.org/10.1016/S1359-835X(01)00140-3).
- [3] Glebes R, Dustin J, Mansson J-A. Technical Cost Modeling Methodology for Novel Manufacturing. *SAMPE 2019 - Charlotte, NC*, vol. 2019- May, SAMPE; 2019. <https://doi.org/10.33599/nasampe/s.19.1490>.
- [4] Verrey J, Wakeman MD, Michaud V, Månson J-AE. Manufacturing cost comparison of thermoplastic and thermoset RTM for an automotive floor pan. *Compos Part A Appl Sci Manuf* 2006;37:9–22. <https://doi.org/10.1016/j.compositesa.2005.05.048>.
- [5] Reichenadter A, Bank D, Mansson JAE. A novel rapid cure epoxy resin with internal mold release. *Polym Eng Sci* 2021;61:1819–28. <https://doi.org/10.1002/pen.25703>.
- [6] Park SJ, Seo MK, Ma TJ, Lee DR. Effect of chemical treatment of Kevlar fibers on mechanical interfacial properties of composites. *J Colloid Interface Sci* 2002;252:249–55. <https://doi.org/10.1006/jcis.2002.8479>.
- [7] Clifton S, Thimmappa BHS, Selvam R, Shivamurthy B. Polymer nanocomposites for high-velocity impact applications-A review. *Compos Commun* 2020. <https://doi.org/10.1016/j.coco.2019.11.013>.
- [8] Kulkarni S V., Rice JS, Rosen BW. An investigation of the compressive strength of Kevlar 49/epoxy composites. *Composites* 1975;6:217–25. [https://doi.org/10.1016/0010-4361\(75\)90417-6](https://doi.org/10.1016/0010-4361(75)90417-6).
- [9] Witik RA, Gaille F, Teuscher R, Ringwald H, Michaud V, Manson JAE. Economic and environmental assessment of alternative production methods for composite aircraft components. *J Clean Prod* 2012;29–30:91–102. <https://doi.org/10.1016/j.jclepro.2012.02.028>.
- [10] Manson J-AE, Wakeman MD, Bernet N. Composite Processing and Manufacturing—An Overview. *Compr Compos Mater* 2000;577–607. <https://doi.org/10.1016/b0-08-042993-9/00167-4>.
- [11] Jansson N, Wakeman WD, Månson JAE. Optimization of hybrid thermoplastic composite structures using surrogate models and genetic algorithms. *Compos Struct* 2007;80:21–31. <https://doi.org/10.1016/j.compstruct.2006.02.036>.
- [12] Galvin J, Cutting R, Reichenadter A, Mansson J, Goodsell J. Project 7.3 Characterization of Kevlar®-Reinforced Composites for Predictive Simulation. 2021.

- [13] ASTM D638-14 Standard Test Method for Tensile Properties of Plastics 2006:1–15. <https://doi.org/10.1520/D0638-14.1>.
- [14] Modified ASTM D695 Compression Test Fixture (Boeing BSS 7260) – Wyoming Test Fixtures n.d.
- [15] ASTM D7264/D7264M-07. Standard Test Method for Flexural Properties of Polymer Matrix Composite Materials. Annu B ASTM Stand 2007;i:1–11. <https://doi.org/10.1520/D7264>.
- [16] D 3518. Standard Test Method for In-Plane Shear Response of Polymer Matrix Composite Materials by Tensile Test of a 645 ° Laminate 1. Annu B ASTM Stand 2007;94:1–7. <https://doi.org/10.1520/D3518>.
- [17] VIC Speckle Kit User Manual. Correlated Solutions; n.d.
- [18] Easy Guide Setup Procedures for the VIC-3D 5MP Quasi-Static System. 2013.
- [19] ASTM D3039/D3039M-17. Standard Test Method for Tensile Properties of Polymer Matrix Composite Materials. Annu B ASTM Stand 2014:1–13. <https://doi.org/10.1520/D3039>.
- [20] Xie J, Jin YC. Parameter determination for the cross rheology equation and its application to modeling non-Newtonian flows using the WC-MPS method. Eng Appl Comput Fluid Mech 2016;10:111–29. <https://doi.org/10.1080/19942060.2015.1104267>.
- [21] Overview of materials for Nylon 6. vol. 12. 2021.

APPENDIX A: PREPREG AND LAMINATE PROCESS CONDITIONS

Table A-1: Compression molding conditions for PA-6/Kevlar® prepreg

Plate #	Prepreg ID	Layup	Press Force [ton]	Peak Press Temperature [C]
1	0	[0] ₄	5	254
2	0	[0] ₈	5	276
3	0	[(0/90) ₂] _s	5	277
4	12041	[0] ₈	5	273
5	12051	[0] ₈	5	271
6	6	[0] ₈	5	267
7	10	[0] ₈	5	266
8	12	[0] ₈	5	269
9	12041	[0] ₈	5	259
10	14	[0] ₈	5	269
11	15	[0] ₈	3	270
12	16	[0] ₃	3	265
13	18	[0] ₈	3	265
14	17	[(0/90) ₄]	3	267
15	17	[90/0 ₃] _s	3	268
16	20	[90/0 ₃] _s	3	265
17	15	[90/0 ₃] _s	3	262
18	15	[90/0 ₃] _s	3	282
19	24	[0] ₈	3	264
20	28.2	[0] ₆	3	253
21	28.2	[0] ₆	3	245
22	28.2	[0] ₆	3	253
23	28.2	[0] ₆	3	246
24	28.2	[0] ₆	3	250
25	28.2	[0] ₆	3	250
26	28.2	[0] ₆	3	248
27	29.1	[0] ₆	3	248
28	30.1	[0] ₆	3	250
29	30.1	[0] ₆	3	251
30	28.2	[0,90] _{2s}	3	250
31	28.2	[0,90] _{2s}	3	248

Table A-2: Prepreg manufacturing conditions for PA-6/Kevlar[®] thermoplastic unidirectional tape

Name	Pump Speed [RPM]	Line Speed [FPM]	Yarn Count	Die Temp [°C]	Expected V _f
1	42.0	5.0	36	310	
2	36.0	5.0	36	310	
3	30.0	5.0	36	310	
4	36.0	5.0	36	310	
5	36.0	5.0	36	310	
6	34.0	5.0	36	310	
7	58.0	8.0	36	310	
8	58.0	7.8	36	310	
9	58.0	7.5	36	310	
10	34.0	5.0	35	310	
11	14.4	2.0	32	310	
12	16.5	2.0	32	310	
13	15.5	2.0	32	310	
14	14.8	2.0	32	310	
15	14.5	2.0	32	310	
16	14.4	2.0	28	310	
17	14.4	2.0	24	310	
18	14.5	2.0	26	310	0.51
19	14.5	2.0	26	310	0.51
20	13.5	2.0	26	310	0.52
21	14.5	2.0	26	290	0.51
22	19.0	2.0	26	310	0.43
23	30.0	2.0	26	310	0.33
24	30.0	2.0	26	310	0.33
25	30.0	2.0	26	310	0.33
26	60.0	4.0	26	310	0.33
27	42.0	3.0	26	310	0.34
28	40.0	3.0	26	310	0.35
29	15.0	1.5	26	310	0.42
30	45.0	4.5	26	310	0.42
31	12.0	2.0	26	310	0.55

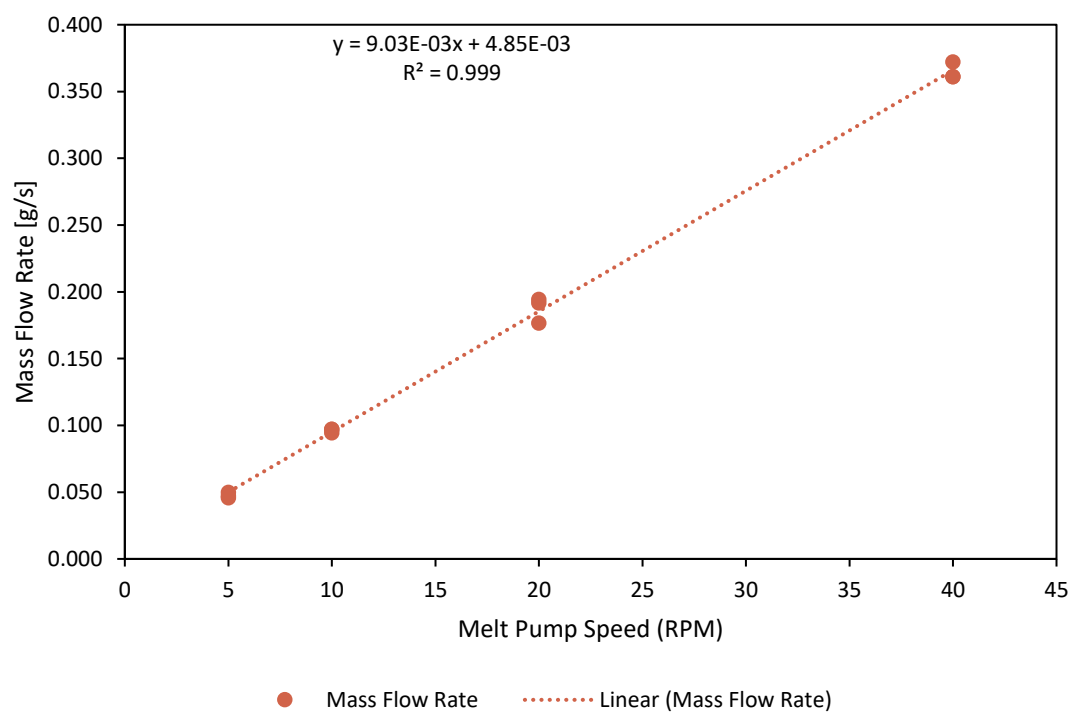


Figure A-1: Prepreg line melt pump calibration curve with PA-6 resin at 260°C.

APPENDIX B: MECHANICAL TESTING SAMPLE DIMENSIONS

Table B-1: 0° tensile sample dimensions from the PA-6/Kevlar® prepreg

Sample Name	Width [mm]	Average [mm]	Thickness [mm]	Average [mm]
23_0_T_1	12.65	12.62	2.41	2.40
23_0_T_2	12.61		2.45	
23_0_T_3	12.65		2.39	
23_0_T_4	12.64		2.39	
23_0_T_5	12.65		2.39	
23_0_T_6	12.49		2.39	
26_0_T_1	12.53	12.52	2.44	2.36
26_0_T_2	12.55		2.41	
26_0_T_3	12.53		2.36	
26_0_T_4	12.54		2.35	
26_0_T_5	12.51		2.31	
26_0_T_6	12.46		2.31	

Table B-2: 90° tensile sample dimensions from the PA-6/Kevlar® prepreg

Sample Name	Width [mm]	Average [mm]	Thickness [mm]	Average [mm]
24_90_T_1	12.89	12.86	2.22	2.25
24_90_T_2	12.86		2.22	
24_90_T_3	12.89		2.23	
24_90_T_4	12.91		2.24	
24_90_T_5	12.85		2.29	
24_90_T_6	12.78		2.27	
25_90_T_1	12.66	12.61	2.27	2.25
25_90_T_2	12.56		2.31	
25_90_T_3	12.56		2.22	
25_90_T_4	12.57		2.25	
25_90_T_5	12.67		2.23	
25_90_T_6	12.62		2.22	

Table B-3: $\pm 45^\circ$ shear sample dimensions from the PA-6/Kevlar[®] prepreg

Sample Name	Width [mm]	Average [mm]	Thickness [mm]	Average [mm]
31_45_S_1	25.33	25.38	3.19	3.16
31_45_S_2	25.39		3.25	
31_45_S_3	25.39		3.29	
31_45_S_4	25.36		3.10	
31_45_S_5	25.41		2.99	

Table B-4: 0° compression sample dimensions from the PA-6/Kevlar[®] prepreg

Sample Name	Width [mm]	Average [mm]	Thickness [mm]	Average [mm]
23_0_C_1	12.64	12.64	2.47	2.36
23_0_C_2	12.64		2.26	
24_0_C_1	12.67	12.68	2.21	2.21
24_0_C_2	12.69		2.21	
24_0_C_3	12.68		2.20	
25_0_C_1	12.52	12.49	2.58	2.55
25_0_C_2	12.48		2.56	
25_0_C_3	12.47		2.51	
26_0_C_1	12.55	12.54	2.34	2.26
26_0_C_2	12.53		2.18	

Table B-5: 90° compression sample dimensions from the PA-6/Kevlar® prepreg

Sample Name	Width [mm]	Average [mm]	Thickness [mm]	Average [mm]
23_90_C_1	12.90	12.90	2.14	2.17
23_90_C_2	12.89		2.16	
23_90_C_3	12.89		2.20	
24_90_C_1	12.87	12.87	2.34	2.33
24_90_C_2	12.88		2.32	
25_90_C_1	12.67	12.67	2.14	2.23
25_90_C_2	12.66		2.33	
26_90_C_1	12.70	12.72	2.19	2.17
26_90_C_2	12.74		2.18	
26_90_C_3	12.71		2.14	

Table B-6: 0° 3-point bending sample dimensions from the PA-6/Kevlar® prepreg

Sample Name	Width [mm]	Average [mm]	Thickness [mm]	Average [mm]
23_0_F_1	12.10	12.19	2.30	2.30
23_0_F_2	12.08		2.30	
23_0_F_3	12.05		2.27	
23_0_F_4	12.08		2.31	
23_0_F_5	12.63		2.34	
26_0_F_1	11.95	12.05	2.24	2.21
26_0_F_2	11.93		2.22	
26_0_F_3	11.99		2.19	
26_0_F_4	11.95		2.22	
26_0_F_5	12.44		2.19	

Table B-7: 90° 3-point bending sample dimensions from the PA-6/Kevlar® prepreg

Sample Name	Width [mm]	Average [mm]	Thickness [mm]	Average [mm]
24_90_F_1	12.31	12.39	2.32	2.38
24_90_F_2	12.28		2.34	
24_90_F_3	12.28		2.38	
24_90_F_4	12.27		2.41	
24_90_F_5	12.82		2.45	
25_90_F_1	12.04	12.17	2.32	2.26
25_90_F_2	12.07		2.26	
25_90_F_3	12.07		2.24	
25_90_F_4	12.07		2.24	
25_90_F_5	12.63		2.26	

5. EXPERIMENTAL OBSERVATIONS OF MULTI-PHASE THERMOPLASTIC RESINS IN PREPREG MANUFACTURING

In this Chapter, the prepreg line developed in Chapter 4 was used to study multi-phase thermoplastic resins in a hot-melt prepregging process. The investigation into multi-phase resins was an extension of the filtration issues reported in Chapter 3 with the rapid cure epoxy resin when prepregging [1]. In that work, it was concluded that a change in manufacturing process from nip-roller to S-wrap to alleviate the filtration issue because lower pressures were required. The lower pressures resulted in less fiber bed compaction which allowed for more particles to infiltrate the fiber bed. Now this study will consider the effect line tension has in a hot-melt S-wrap configuration for multi-phase thermoplastic resins on the resin and particle infiltration of the fiber bed.

5.1 Introduction and Background

As noted in Chapter 4, polyamide/Kevlar[®] was selected as a material system because of its applicability to the automotive industry for potential weight savings and crash performance. These polyamide resins can have their mechanical properties enhanced through the addition of solid fillers, such as rubber particles or glass beads. For instance, rubber particles were commonly added to improve impact performance of polyamide [2,3]. The improved toughness has important implications for energy absorption during a high-speed impact (eg. automobile crash, sports equipment). The addition of glass beads can improve the stiffness and dimensional stability of a molded part. Which was important for meeting stiffness design requirements and meet consistent part tolerances.

In composite laminates, adding a rubber particle at the ply interfaces improved interlaminar fracture properties [4–7]. A rubber particle rich interlayer between lamina plies has been demonstrated to prevent transverse cracking from spreading through the laminate [7]. The most common way these particles were introduced into the laminate were by preparing a separate resin film layer with the rubber particles and applying this between layers of prepreg [4,6,8,9]. This process of preparing a film between the plies was known as interleaving [10–12]. Typically, the rubber toughened layer was 15 – 30 μ m thick with particle diameters from 50nm – 3 μ m [2,13].

Placement of the layer ensured the rubber particles remained in the inter-ply regions, to improve the interlaminar fracture properties. While other work by Liu et al. blended the rubber particles into the resin before infiltrating the fiber bed and noted that the rubber particles were filtered by the fiber bed [5]. The filtration of the rubber particles at the fiber surface was viewed as an in-situ method for creating a particle rich layer in the inter-ply region. Since the resin was rubber toughened prior to impregnation, the particles have the opportunity to penetrate the fiber bed, rather than remain at the prepreg surface. Additionally, the study did not vary pressure nor quantify the particles that penetrated the fiber bed. Instead, the particles were assumed to reside in the inter-ply region.

While many studies have been conducted on the benefits of polymer filled composites on mechanical properties [4–9], they have not investigated the manufacturing conditions on solid particles infiltrating the fiber bed. Since impregnation pressure has been known to change the fiber volume fraction and thus the inter-fiber spacing, the processing conditions during resin impregnation should be investigated for particle penetration into the fiber bed. Furthermore, there may be prepregging conditions paired with suitable particle sizes where particles infiltrate the fiber bed rather than deposit on the fiber surface. Therefore, three polyamide-66 resins will be considered in this study. A neat, rubber toughened, and glass bead filled resin will be used to establish hot-melt tension settings with fiber bed saturation and particle infiltration.

5.2 Materials, Manufacturing Conditions, and Methods

5.2.1 Materials

The three prepreg resins used in this study were polyamide-6,6 (PA66) based to evaluate manufacturing conditions on particle infiltration and fiber bed saturation. One PA66 resin contained 33wt% glass bead (GB PA-66) to represent “hard” particles. This resin was compounded by Premier Plastics. Another PA66 resin was rubber toughened to represent “soft” particles. The resin’s tradename was Zytel® ST801, which will be referred to as RT PA-66. An unfilled PA66 resin was used as the control to compare resin infiltration and will be referred to as neat PA-66. Neither resin supplier provided information on the particle size nor distribution, however SEM showed the rubber particles to be approximately 250nm in diameter and optical microscopy showed the glass particles were approximately 10μm in diameter. The neat PA-66 resin’s

tradename was Zytel® 101. All resins were purchased from Premier Plastics. The fiber reinforcement was 2840 denier Kevlar® 49 which had a filament count of 1,333 per yarn. The fiber reinforcement was provided by DuPont with an average filament diameter of 12 μ m.

5.2.2 Viscosity Measurements

For rheological characterization, all PA66 resins were consolidated into 0.75" diameter samples and dried for 14 hours at 80°C. The samples each weighed approximately 0.7g. This was to ensure consistent gap sizes. The rheological behavior of the PA66 resins were determined using a TA Instruments Discovery HR-2. 25mm disposable parallel plates were used with an approximate gap of 1mm. The gap between the plates was zeroed before each sample was placed between the plates. To determine the strain rate and temperature dependent properties, tests were performed in 5°C increments from 270 – 300°C. At each temperature, a 5-point per decade logarithmic frequency sweep from 1 – 40Hz was performed at 10% strain.

The chamber was preheated to 280°C, then the pre-weighed samples were placed on the plate. The heat from the chamber was used to melt the sample and bring the plates in contact with the sample. Any excess material was trimmed away. From this process, the chamber temperature would have fallen to 260°C, before the test had started. A 15LPM flow rate of N₂ was sent through the sample chamber to maintain consist temperatures throughout the chamber and prevent the sample from degrading. Samples that displayed signs of degradation were omitted from the data sets when determining model parameters for the viscosity profile. Each resin temperature and frequency sweep were repeated in triplicate. The resulting rheological data was fitted to the Carreau-Yasuda model (Equation (1.19)) [14]. With the zero and infinite shear viscosities temperature dependence described by the Arrhenius relationship shown in Equation (5.2). The terms $\eta_{i,shear}$, λ , a , and n were fitted using the log normal error assumption, shown in Equation (5.3). From this method, the A_i and $E_{\eta,i}$ terms were fitted by plotting the natural log of $\eta_{i,shear}$ vs the inverse temperature.

$$\eta_D(T, \dot{\gamma}) = (\eta_{0,shear}(T) - \eta_{\infty,shear}(T))(1 + (\lambda\dot{\gamma})^a)^{\frac{n-1}{a}} + \eta_{\infty,shear} \quad (5.1)$$

$$\eta_{i,shear}(T) = A_i e^{\frac{E_{\eta,i}}{RT}} \quad (5.2)$$

$$Error^2 = \sum \left(\ln \left(\eta_{D,data}(\dot{\gamma}, T) \right) - \ln \left(\eta_{D,model}(\dot{\gamma}, T) \right) \right)^2 \quad (5.3)$$

5.2.3 Manufacturing Conditions

A thermoplastic hot-melt extrusion prepreg process was used to manufacture PA-66/Kevlar® at four tension levels with a diagram of the process shown in Figure 5.1. The 48-position fiber creel was loaded with 25 Kevlar® bobbins. The line tension was controlled on the creel for each bobbin. The total line tension for each manufacturing trial are reported in Table 5.1. The fibers were spread via a fixed bar spreader. The spreader was fitted with an IR lamp to dry the fibers before entering the impregnation die. The polyamide-66 resins were dried at 80°C for 8 hours at ambient pressure with no purge gases used before being used in the prepregging process.

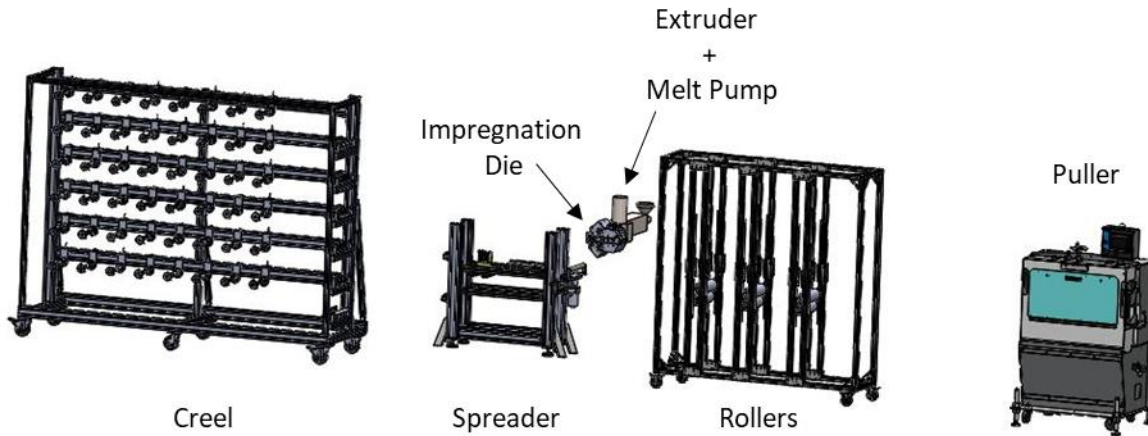


Figure 5.1: Thermoplastic extrusion hot-melt impregnation line layout, where the process moved from left to right.

A ¾" single screw (non-vented, non-mixing) extruder (36 L/D) heated the resin to a temperature of 270°C and pressurized the polymer to 800psi for the melt pump. The extruder had 4 heating zones, with the following temperature profile used: Zone 1 – 270°C, Zone 2 – 280°C, Zone 3 – 285°C, and Zone 4 – 290°C. The melt pump (0.6cc/rev) was used as a metering device to control the flow of molten polymer into the impregnation die. All die zones were operated at 310°C. A single screw extruder fed molten PA66 to a melt pump which metered the flow of molten material into the die. The melt pump delivered 0.6cc/rev and was set to 20RPM for the neat and

rubber toughened resins, but was increased to 24RPM for the glass filled resin because dry spots were noted in the resulting prepreg tape. The die utilized a wave plate design to pump the resin into the fiber bed. The tape was pulled through the die with a caterpillar puller at 2FPM. Approximately 50ft of prepreg tape was produced for each material tension setting. A set of nip-rollers at the exit of the die was used to cool the tape and ensured the tape was level when exiting the die.

Table 5.1: Total web tensions as measured at the creel.

Resin Material	Tension 1 (g)	Tension 2 (g)	Tension 3 (g)	Tension 4 (g)
Neat PA-66	2975	4700	6200	7825
RT PA-66	3100	4600	6200	7675
GB PA-66	3200	4625	6325	7950

5.2.4 Prepreg Line Modeling Methods

The flow front velocity of the resin during fiber bed impregnation was captured by Darcy's Law, Equation (1.1). This related the permeability (K), bed thickness (L), viscosity (η), fiber volume fraction (V_f), and applied pressure (P) to the superficial velocity ($\frac{dX}{dt}$) of the flow front at which material moves through a porous medium. The differential form of Darcy's law is shown in Equation (1.1) [15]. This model was used to describe the flow of resin into the fiber bed.

$$\frac{dX}{dt} = \frac{K P}{\eta X(1 - V_f)} \quad (5.4)$$

The applied pressure (P) for Darcy flow was calculated from the force balance (F) over the die's ridge, Equation (5.5). The horizontal ($F_{x,i}$) and vertical ($F_{y,i}$) components of the force were calculated from the wrap angle ($\theta_{1,i}$ and $\theta_{2,i}$) described in Figure 3.6 and tow tension (T) with Equations (5.6) and (5.7), respectively. The pressure (P_i) generated over each ridge was calculated from the force balance (Equations (5.5) - (5.8)) around the ridge was dependent on the wrap angle. Where F_i was force on the resin and $F_{x,i}$ and $F_{y,i}$ were the horizontal and vertical forces, respectively [16,17]. The contact area (A_i) over the ridge radius (R) was given in Equation (5.9).

$$F_i = \sqrt{F_{x,i}^2 + F_{y,i}^2} \quad (5.5)$$

$$F_{x,i} = T \cos(\theta_{1,i}) + T \cos(\theta_{2,i}) \quad (5.6)$$

$$F_{y,i} = T \sin(\theta_{1,i}) + T \sin(\theta_{2,i}) \quad (5.7)$$

$$P_i = \frac{F_i}{A_i} \quad (5.8)$$

$$A_i = \pi R_i w \frac{\theta_{1,i} + \theta_{2,i}}{360^\circ} \quad (5.9)$$

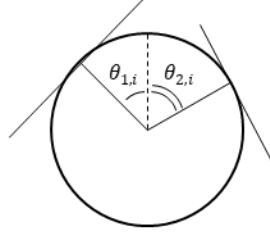


Figure 5.2: Representation of wrap angle of fibers around the die ridge.

The process tension was measured at the fiber creel and was reported in Table 5.1. To account for the rise in tension caused by the fiber drag from the spreader unit, the Capstan equation was used (Equation (5.10)), which related the coefficient of friction (μ) between the spreader and the Kevlar[®] fiber and the total wrap angle (ϕ) across all spreader bars. Where $\mu = 0.2$ [18] and $\phi = 640^\circ$. While the rise in tension caused by moving the fibers over ridges of the die through a viscous fluid was estimated by the viscous drag force from Stokes flow (Reynolds number $\ll 1$), shown in Equation (5.11). Where η was the resin viscosity, θ was the wrap angle (in radians) around the ridge, V was the fiber speed, R was the radius of the ridge, w was the width of the ridge, and h_0 was the initial resin film thickness [19–21]. The film thickness was assumed to be $60\mu\text{m}$.

$$T = T_o e^{\mu\phi} \quad (5.10)$$

$$T(\theta) = T_o + \frac{\eta\theta VRw}{h_0} \quad (5.11)$$

To model the prepreg infiltration process, the permeability was estimated from the final, fiber-bed fiber volume fraction. This was the local fiber volume fraction, not the overall fiber volume fraction of the prepreg tape. The permeability relationship used was Gebart's model [22] for hexagonally packed fibers. Where the $V_{f \max}$ was 0.901 and the fiber radius was $6\mu\text{m}$.

$$K_{hex\ pack} = \frac{16 r^2}{9\pi \sqrt{6}} \left(\sqrt{\frac{V_{f\ max}}{V_f}} - 1 \right)^{\frac{5}{2}} \quad (5.12)$$

5.2.5 Microscopy Methods

Three samples were cut perpendicular to the fibers from each manufacturing trial for optical microscopy to evaluate fiber bed saturation and particle infiltration. Each sample of 75mm wide prepreg was separated into 4 sections by cutting along the fibers to fit each sample into the sample polisher holder. The samples were mounted into epoxy pucks with a 1" diameter and were polished with a Leco SS-1000 Automated Polisher. The samples were first ground with a 220-grit wheel at 300RPM until all samples were exposed. Then a series of 550 and 1200 grit wheels were used at 150RPM, each for approximately 10 minutes. Then the samples were polished with a series of MD-Largo, MD-Dac, and MD-Nap wheels with a polishing compound consisting of 9μm, 3μm, and 0.25μm particle diameter suspensions, respectively. All The polished samples were imaged with a Leica DMI 5000 M. Mosaic images of the samples were created with Surveyor.

The samples were post processed in ImageJ to evaluate local fiber-bed fiber volume fraction, resin saturation, and glass bead infiltration. The microscopy images were analyzed in ImageJ and used image thresholding to determine the fiber volume fraction. ImageJ thresholding required a non-color (8-bit) image and the threshold values to be specified by the user. Threshold values can range from 0 – 255 (for 8-bit) and can differ depending on the sample material and microscope settings. Typical threshold values used for the neat PA-66/Kevlar® prepreg ranged from 185 – 187, for the rubber-PA-66 prepreg was 169 – 177, and for the GB PA-66 prepreg was 158 – 176. The threshold values were dependent on the microscope exposure and aperture settings used for the respective resins.

5.3 Results and Discussion

5.3.1 Viscosity Measurements

The viscosity of each PA-66 resin was measured and fitted to the Carreau-Yasuda model shown in Equation (1.19). The neat PA-66 resin had a zero-shear viscosity near 200 Pa•s. The addition of the rubber particles did not have a significant effect on the viscosity profile. The

addition of the glass beads to the PA-66 resin had a significant effect on the zero-shear viscosity, which was nearly 1,000 Pa•s. A comparison on the viscosity profiles modeled by Equation (1.19) are shown in Figure 5.3 with the rheological parameters reported in Table 5.2. The rheological data are reported in Appendix C.

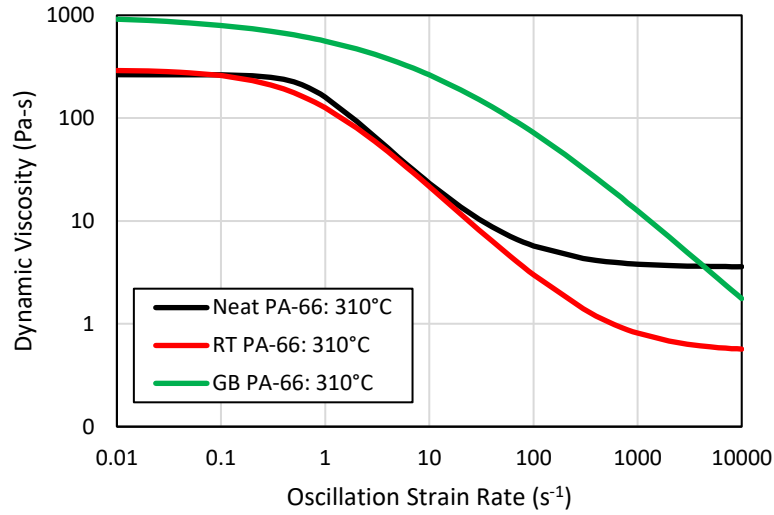


Figure 5.3: Carreau model description of the viscosity for PA-66 resins. Model parameters were reported in Table 5.2.

Table 5.2: Rheological parameters to Carreau-Yasuda model for neat PA-66, RT PA-66, and GB PA-66 resins.

Rheological Parameter	Neat PA-66	RT PA-66	GB PA-66
A_o (Pa•s)	1.45×10^{-1}	7.31×10^{-2}	7.32×10^{-2}
$E_{\eta,o}$ (J/mol)	35200	38900	44600
A_{∞} (Pa•s)	5.43×10^{-7}	7.74×10^{-11}	1.02×10^{-5}
$E_{\eta,\infty}$ (J/mol)	73500	106100	42600
λ (s ⁻¹)	1.46	1.48	0.074
n (-)	0.0378	0.0446	0.0488
a (-)	2.30	1.03	0.450

5.3.2 Experimental Observations on Prepreg Quality

The neat PA-66 based prepreg was a natural color resin which allowed to visually observe any degradation caused by the prepregging process. As is seen in Figure 5.4, the neat PA-66

prepreg did not have noticeable areas of color change, indicating the material was not degraded at these processing conditions. The rubber toughened and glass bead filled resins were colored black and visual inspection of the prepreg for degradation was not possible. However, since the base resins and the manufacturing conditions were the same, the rubber toughened and glass bead filled resins can be reasonably assumed that neither experienced degradation. Each prepreg had a noticeably different surface finish. The neat PA-66 prepreg had a smooth surface feel. The smooth surface was expected as no additives were present. The rubber toughened prepreg had a smooth surface, but the surface also had small bumpy features. This was assumed to be caused by the presence of the rubber particles. Finally, the glass bead filled prepreg had a noticeably rough, abrasive surface finish. The surface roughness was assumed to be caused by the glass particles. All PA-66 resin pellets were noted to have a smooth surface prior to prepregging.

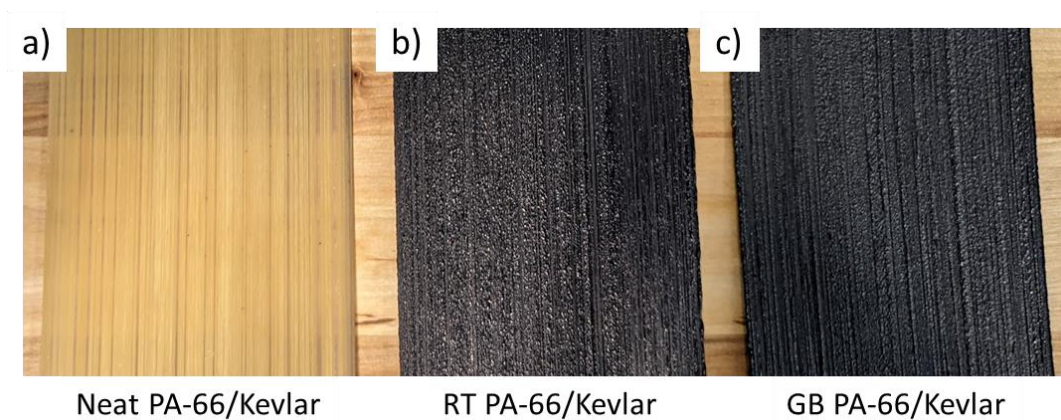


Figure 5.4: Examples of the a) neat PA-66, b) RT PA-66, and c) GB PA-66 prepreps.

Both the neat PA-66 and RT PA-66 prepreg tapes were flexible when bent transverse to the fibers. This was an indication that the fiber bed was well impregnated and the resins possessed similar modulus. In contrast, the GB PA-66 resin was rather stiff when flexing and cracked along the fibers. This was an early indication that the GB PA-66 resin was not saturating the fiber bed. Also, the increased stiffness indicated that the addition of glass beads stiffened the transverse direction, which was expected. The increased surface roughness may ease the layup process as the roughness provides a small amount of mechanical interlocking, which would help ensure the prepreg remains stationary when placed for a laminate layup.

All of the prepregs manufactured had a nominal thickness of 0.5 – 0.6mm thick. While the neat PA-66 prepreg felt smooth and had a nominal thickness between 0.5 – 0.6mm, microscopy showed the prepreg thickness actually had variability in the prepreg thickness. As can be seen in Figure 5.5, the low fiber tension resulted in non-uniform prepreg thickness in the neat PA-66/Kevlar[®]. The local fiber bundles were thicker and regions between bundles had fewer fibers at the lower line tensions. The sparsely distributed fibers resulted in thin sections of the prepreg, which could create splits in the prepreg. As the tension increased, the fibers appeared to distribute more evenly along the prepreg width and produced a more uniform prepreg thickness. This indicated that the spreading was improved with increased tension and perhaps the higher tension prevented the resin from shifting the fibers while in the impregnation die. Increasing the prepreg thickness also increased the fiber-bed fiber volume fraction. The overall prepreg fiber volume fraction did not change because the resin flow rate was held constant for all tensions.

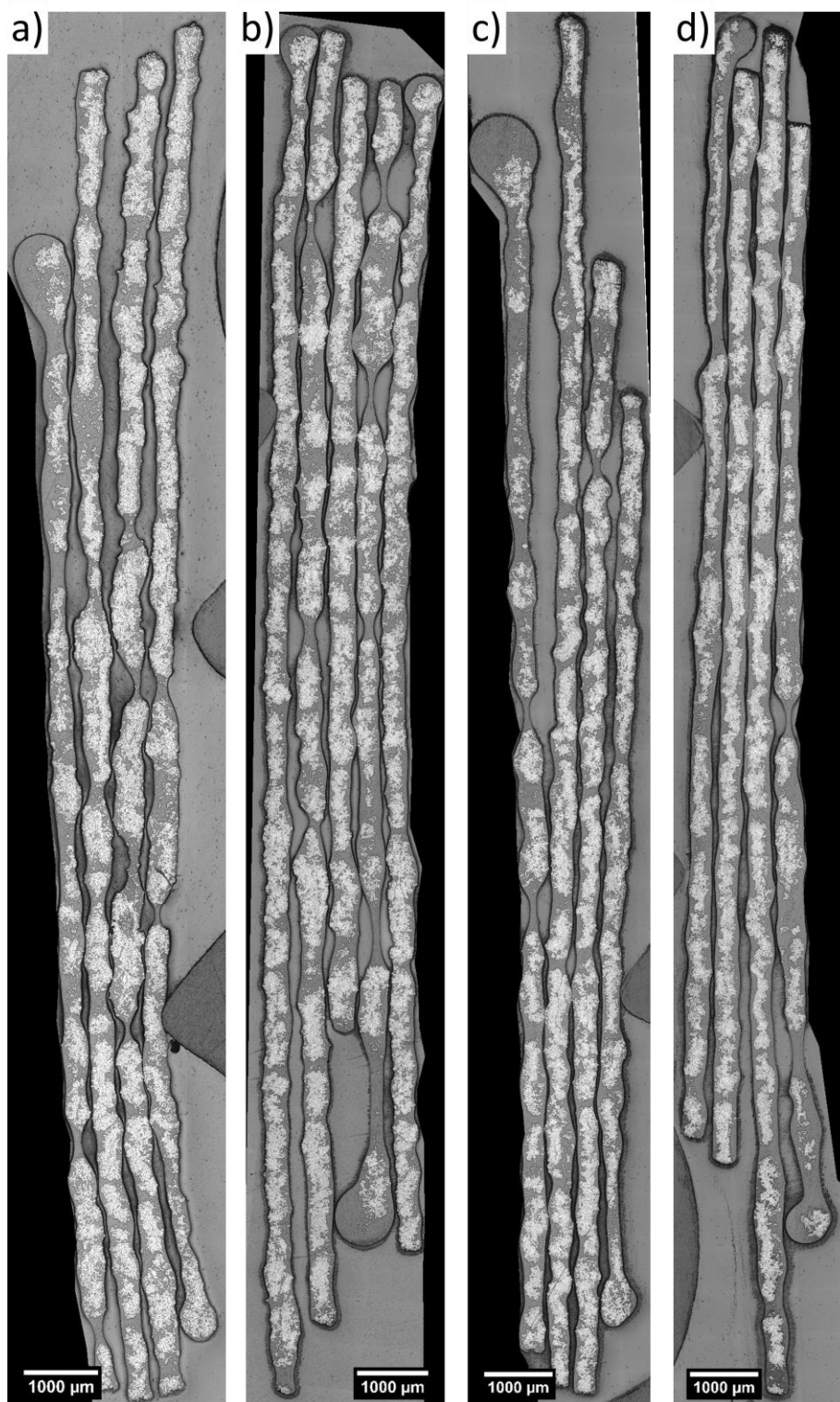


Figure 5.5: Optical microscopy of neat PA-66 prepreg showing the variability in prepreg thickness and local fiber volume fraction for tension a) level 1 (min), b) level 2, c) level 3, and d) level 4 (max) as described in Table 5.1. Each piece of prepreg was cut into 4 sections.

Unlike the neat PA-66, the RT PA-66 prepreg did not polish well. Figure 5.6 shows the black streaking was localized to the prepreg material and did not significantly extend into the potting epoxy material and was not present in the neat resin. Thus, the black streaking was likely caused by the rubber particles plastically smeared from the polishing process. Cryogenic polishing may be required to attain images from optical microscopy with the rubber toughened resin. The RT PA-66 prepreg maintained a much more uniform prepreg thickness regardless of fiber tension, as is shown in Figure 5.6. The fiber distribution along the width of the prepreg remained relatively constant regardless of the fiber tension. The local fiber-bed fiber volume fraction increased with tension similarly as was observed in the neat PA-66 prepreg. The local fiber volume fraction was expected to increase with tensions as the degree of fiber bed compaction was known to increase with fiber tension because of the increased pressure pumping the resin into the fiber bed.

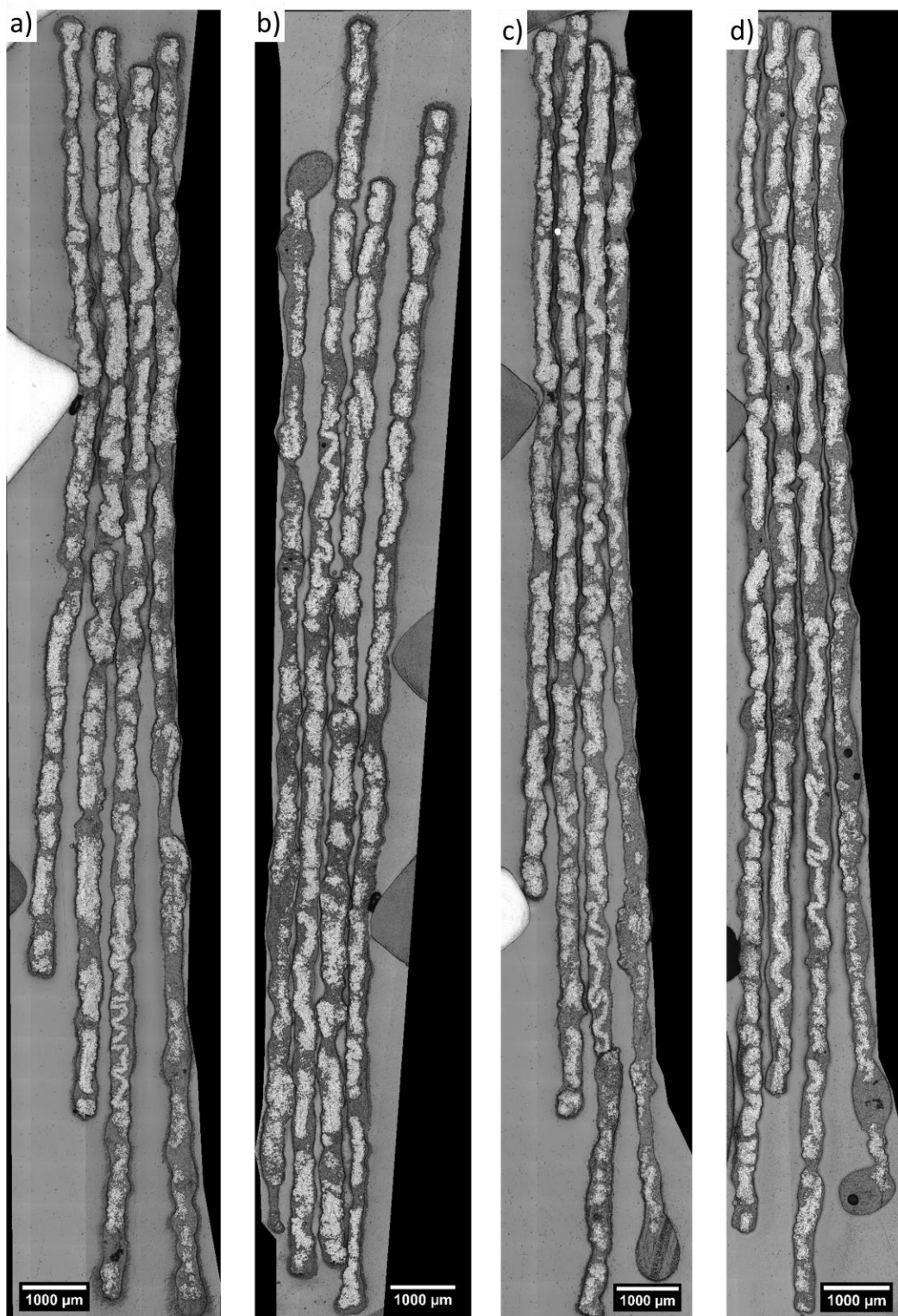


Figure 5.6: Optical microscopy of RT PA-66 prepreg showing the variability in prepreg thickness and local fiber volume fraction for tension a) level 1 (min), b) level 2, c) level 3, and d) level 4 (max) as described in Table 5.1. Each piece of prepreg was cut into 4 sections.

Like the RT PA-66, the GB PA-66 polished poorly relative to the neat PA-66 prepreg, as was shown in Figure 5.7. Even though the glass particle diameters were on the same order as the Kevlar[®] fibers, the particles separated from the PA-66 resin because depending on the particle position along the cutting plane dictated how much of the particle remained embedded in the resin. As the glass particles were removed from the resin, they left behind a void and was able to scratch the polished surface. Like the RT PA-66 prepreg, the GB PA-66 prepreg had a much more uniform prepreg thickness which was independent of tension. From Figure 5.7, the fibers can be seen forming individual fiber bundles despite forming a uniform web when entering the impregnation die. The high melt viscosity of the GB PA-66 resin ($\sim 500 \text{ Pa}\cdot\text{s}$) compared to the $\sim 50 \text{ Pa}\cdot\text{s}$ of the neat and RT PA-66 likely caused the fibers to shift while in the impregnation die. The higher tension slightly improved the fiber distribution, but overall the fibers remained in discrete bundles. Like the neat and RT PA-66 prepreg, the local fiber-bed fiber volume fraction increased with tension. The fiber-bed fiber volume fraction was expected to increase with tensions as the degree of fiber bed compaction was known to increase with fiber tension because of the increased pressure pumping the resin into the fiber bed.

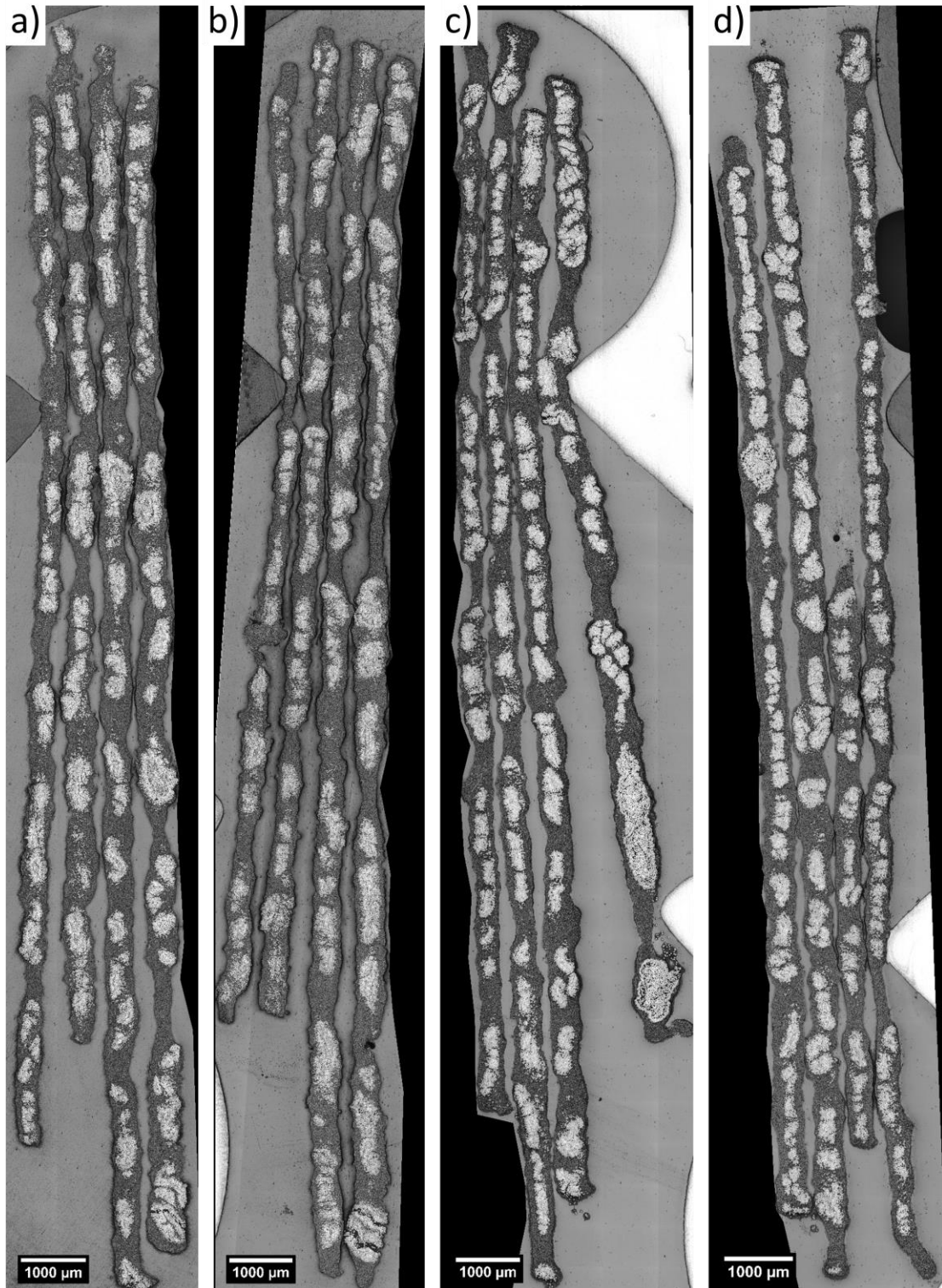


Figure 5.7: Optical microscopy of GB PA-66 prepreg showing the variability in prepreg thickness and local fiber volume fraction for tension a) level 1 (min), b) level 2, c) level 3, and d) level 4 (max) as described in Table 5.1. Each piece of prepreg was cut into 4 sections.

Overall, the neat PA-66 at each tension setting consistently saturated the fiber beds up to 400 μm thick with very few unsaturated regions. The RT PA-66 typically saturated fiber beds with a thickness up to 300 μm across the tension levels 1 – 3. Even in the thicker fiber beds at these tension levels, the regions were primarily saturated. At the highest tension, the typical fiber bed thickness for saturation decreased to 250 μm , which was likely because of the increased fiber-bed fiber volume fraction at the higher tensions. The resin infiltration at this tension level was highly sporadic, potentially indicating the particles formed a cake layer at this tension, however, this could not be confirmed with optical microscopy. The GB PA-66 resin exhibited poor fiber bed saturation and did not exhibit a consistent fiber bed thickness for saturation. The typical fiber bed thicknesses capable of resin saturation for each resin and manufacturing condition are summarized in Table 5.3.

Table 5.3: Typical fiber bundle thicknesses that were able to be saturated with the PA-66 resins. Bolded values indicated samples that had poor overall fiber bed saturation.

Tension	Fiber Bed Thickness (μm)		
	Neat PA-66	RT PA-66	GB PA-66
1	400	300	220
2	400	250	150
3	400	340	230
4	400	250	170

The GB PA-66 prepreg did show some signs of particle accumulation at the fiber-bed surface, however the resin flow into the fiber bed was small, so the accumulation was minimal. There was no evidence of a cake layer forming in the RT or GB PA-66 prepreg. Even though there was the possibility of glass particles being removed from the sample during polishing, the GB PA-66 prepreg did not show signs of particles significantly infiltrating the fiber beds. The cake layer did not form because there was not significant flow into the fiber bed. There were some localized areas where a glass particle was present up to 3 fibers into the fiber bed. The particles that did infiltrate likely became entrapped at constriction sites. These fiber-beds had a local fiber volume fraction of 0.5 – 0.7, where increasing the tension increased the fiber volume fraction. At these fiber volume fractions, the expected pore size would range from 1.5 – 3 μm for Kevlar[®] fibers. Therefore the lack of particles infiltrating the fiber bed agreed with the sieving prediction in Figure 3.4 when

considering a hexagonal packing arrangement of the fiber bed. For the glass particles to infiltrate the fiber-bed, the local fiber volume fraction would have needed to be near 0.3.

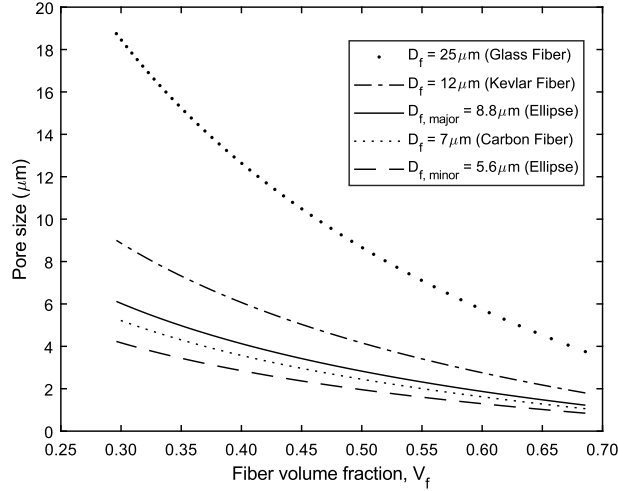


Figure 5.8: Average pore size for hexagonally packed fibers as a function of fiber volume fraction for various fiber diameters.

From the prepreg manufacturing trials with the neat, RT, and GB PA-66 resins, the effect of particles helped produce a prepreg with uniform thickness. The neat resin had narrow spots form along the prepreg tape width because of a lack of fibers in certain sections. In those regions, a molten resin bridge formed between the neighboring fiber bed. The bridge was held together because of the surface tension until the resin surface cooled and a skin layer formed. These thin sections along the prepreg width were not present in the particle filled resins because the particles improved the melt strength. The particles stabilized the formation of the bridge. Additionally, the frequency of the thin sections in the neat PA-66 resin were reduced as tension increased; because the fibers resisted shifting while in the impregnation die. Therefore, the fiber distribution along the tape width was more uniform and less areas were lacking fibers. While the increased tension tended to improve the distribution of the fibers along the width for the neat PA-66, the significantly higher viscosity of the GB PA-66 resin caused a significant shift of the fibers in the die and the fibers formed discrete fiber bundles regardless of fiber tension.

5.3.3 Modeling Prepreg Infiltration

Select fiber beds for each manufacturing trial were modeled using permeability, viscosity, and pressure models to describe the prepregging process. The models are discussed in Section 5.2.4. Example fiber beds for the neat PA-66 resin based prepreg are shown in Figure 5.9 for each tension setting. These were chosen as representative fiber beds for each of the manufacturing conditions. The fiber-bed V_f ranged from 0.56 – 0.65 for the representative fiber beds with a tendency to increase with fiber tension. The fiber bed thicknesses varied from 210 – 290 μm . The fiber-bed fiber volume fraction and thicknesses are reported in Table 5.4 and 5.5, respectively.

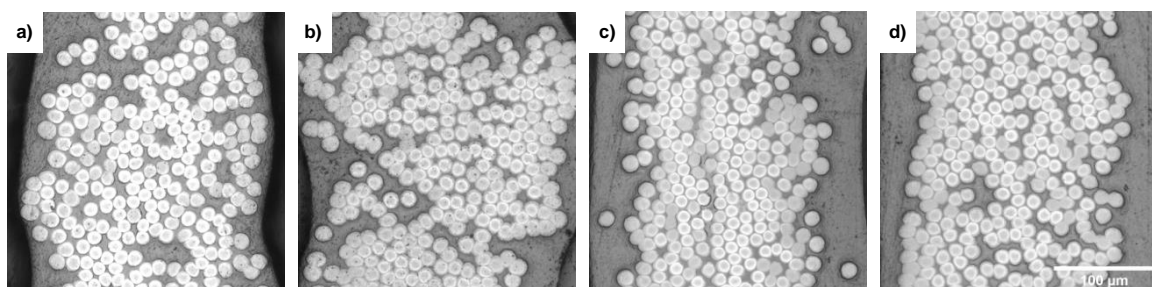


Figure 5.9: Optical microscopy of neat PA-66/Kevlar[®] prepreg for tension settings of: a) 2975g, b) 4700g, c) 6200g, and d) 7825g showing the resin was able to consistently saturate the fiber bed at each fiber tension.

The resin infiltration modeling of neat PA-66 resin into the representative fiber beds shown in Figure 5.9 were plotted in Figure 5.10. The modeled infiltration profile showed good agreement with the experimental findings reported in Table 5.3, where the neat PA-66 was able to consistently saturate the fibers beds across all tension levels. These fiber beds were observed to be up to 400 μm thick and the infiltration profiles that were modeled show similar predictions. The increase in tension did not necessarily result in further infiltration flow fronts because the increased pressure caused the fiber-bed fiber volume fraction to increase, as well, which decreased the permeability.

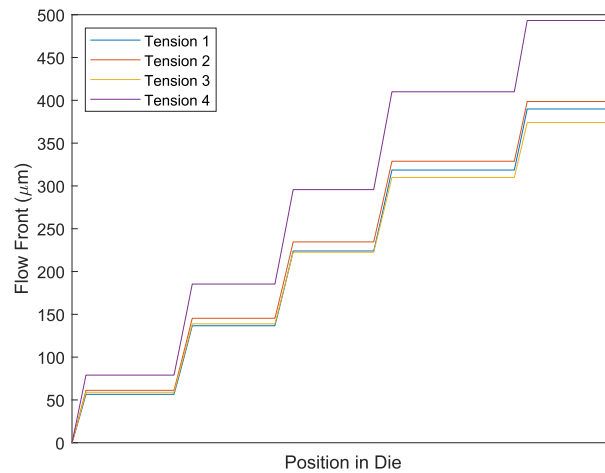


Figure 5.10: Modeled infiltration profiles with neat PA-66 resin for the fiber beds shown in Figure 5.9. Fiber bed values used in modeling are reported in Table 5.4 and Table 5.5. Tension levels were reported in Table 5.1.

The RT PA-66 was shown to infiltrate fiber beds of approximately 300 μ m for tension levels 1 – 3, but had less consistency with fiber bed infiltration at tension level 4. Representative fiber beds for the RT PA-66 resin based prepreg at each tension level are shown in Figure 5.11. The representative fiber beds had local V_f that ranged from 0.55 – 0.70 with a tendency to increase with fiber tension. Compared to the prepreg produced from neat PA-66, RT PA-66 prepreg fiber bed thicknesses had more variability from 170 – 390 μ m. The fiber-bed fiber volume fraction and thicknesses are reported in Table 5.4 and Table 5.5, respectively.

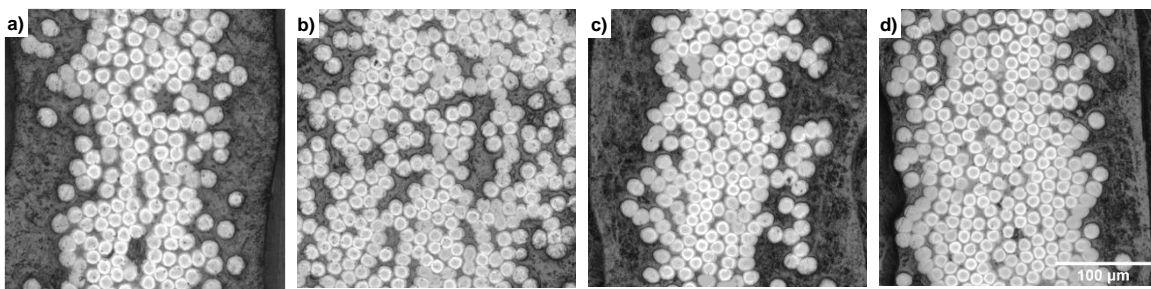


Figure 5.11: Optical microscopy of rubber toughened PA-66/Kevlar® prepreg for tension settings of: a) 3100g, b) 4600g, c) 6200g, and d) 7675g showing the resin was able to saturate the fiber bed when the fiber bed was suitably thin at each fiber tension.

The infiltration modeling of RT PA-66 resin into the representative fiber beds shown in Figure 5.11 were plotted in Figure 5.12. The modeled infiltration profile showed good agreement with the experimental findings reported in Table 5.3, where the RT PA-66 was able to consistently saturate fiber beds with a thickness of 300 μm for tension levels 1 – 3, which was captured by the infiltration modeling. The experimental observations for tension level 4 showed less saturation and more variability in saturation, which was reflected in the model with a predicted infiltration depth of 150 μm for tension 4.

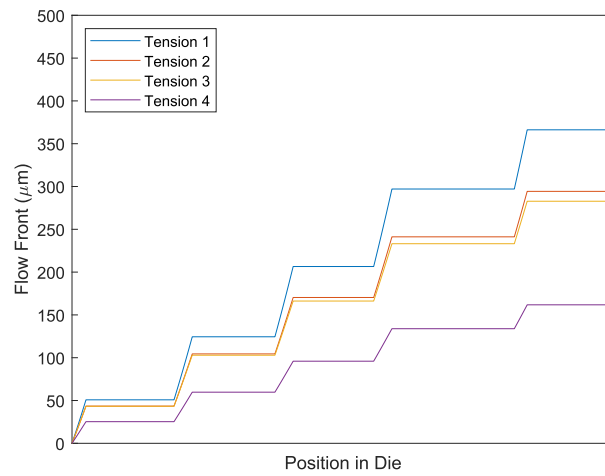


Figure 5.12: Modeled infiltration profiles with RT PA-66 resin for the fiber beds shown in Figure 5.11. Fiber bed values used in modeling are reported in Table 5.4 and Table 5.5. Tension levels were reported in Table 5.1.

From the experimental observations, the GB PA-66 resin was inconsistent with its ability to infiltrate the fiber bed, regardless of tension level, as reported in Table 5.3. Representative fiber beds for the GB PA-66 resin based prepreg at each tension level are shown in Figure 5.13. The representative fiber beds had fiber-bed V_f that ranged from 0.55 – 0.73 with a tendency to increase with fiber tension. The selected fiber bed thicknesses varied from 150 – 250 μm . The fiber-bed fiber volume fraction and thicknesses are reported in Table 5.4 and Table 5.5, respectively.

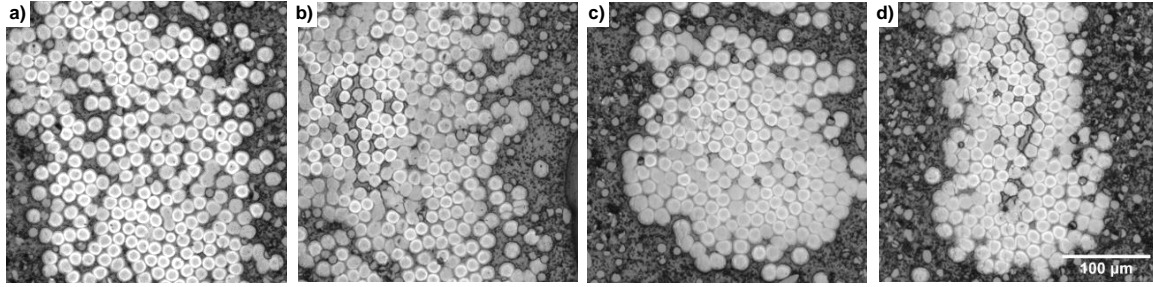


Figure 5.13: Optical microscopy of GB PA-66/Kevlar® prepreg for tension settings of: a) 3200g, b) 4625g, c) 6235g, and d) 7950g showing the resin was only able to saturate the lowest tension while the other tensions were partially saturated.

The infiltration modeling of the GB PA-66 resin into the representative fiber beds shown in Figure 5.13 were plotted in Figure 5.14. The model predicted resin infiltration distances ranging from 20 – 60 μm , which was low compared to the experimental observations of $\sim 150\mu\text{m}$. A possible explanation for this was the hard glass particles created a scenario where shear rates were higher than the 10s^{-1} that were used when modeling the infiltration process, which would have meant the viscosity in the model was being over-estimated. The high viscosity would have caused an under prediction in the resin infiltration. Additionally, the capillary pressure was neglected in the model, which could have accounted for the under-predicted resin infiltration. Regardless of the reason, the GB PA-66 resin poorly infiltrated the fiber beds, which was reflected in the model.

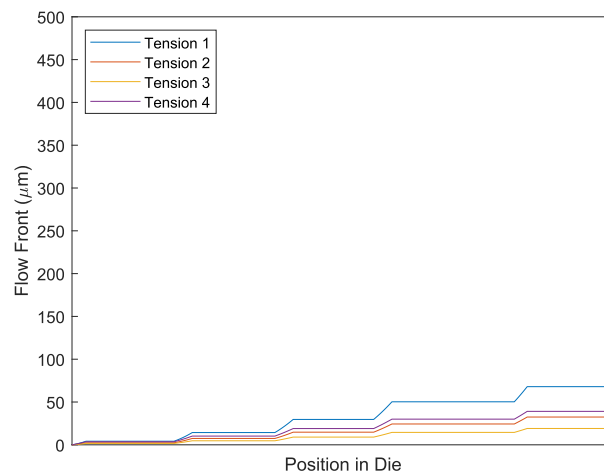


Figure 5.14: Modeled infiltration profiles with GB PA-66 resin for the fiber beds shown in Figure 5.13. Fiber bed values used in modeling are reported in Table 5.4 and Table 5.5. Tension levels were reported in Table 5.1.

Table 5.4: Fiber-bed fiber volume fractions for the fiber beds shown in Figure 5.9, Figure 5.11, and Figure 5.13.

Tension Setting	Fiber-bed Fiber Volume Fraction		
	Neat PA-66	RT PA-66	GB PA-66
1 (min)	0.56	0.58	0.55
2	0.58	0.55	0.61
3	0.65	0.66	0.72
4 (max)	0.62	0.70	0.73

Table 5.5: Fiber bed thicknesses for the fiber beds shown in Figure 5.9, Figure 5.11, and Figure 5.13 and were model inputs for Darcy's law.

Tension Setting	Fiber Bed Thickness		
	Neat PA-66	RT PA-66	GB PA-66
1 (min)	247	173	216
2	286	385	250
3	216	194	245
4 (max)	252	248	150

The GB PA-66 poorly infiltrated the fiber bed compared to the neat and RT PA-66 resins. Which was a result of the high viscosity and larger particle diameters compared to the RT PA-66. A model comparison at tension level 1 for the three resins is provided in Figure 5.15. Where the neat PA-66 resin and RT PA-66 resin were expected to infiltrate fiber beds to nearly 400 μ m and 350 μ m, respectively. Unlike the GB PA-66, which was approximately 70 μ m.

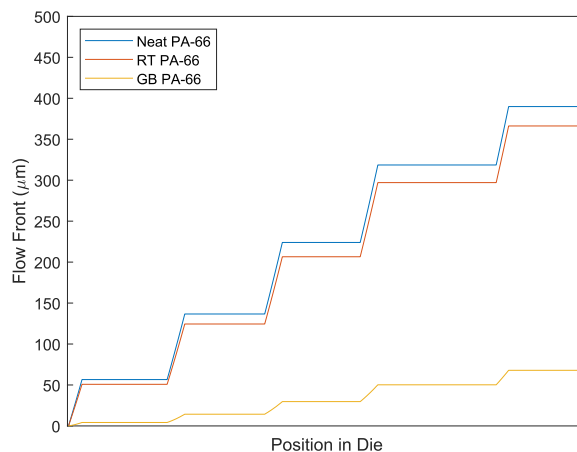


Figure 5.15: Modeled infiltration profiles for neat, rubber toughened, and glass bead filled PA-66 prepreps at tension level 1.

5.4 Conclusions

Three polyamide-66 resins were used in a hot-melt extrusion prepregging process to produce prepreg tape at 4 different tension levels. The resins were a neat, rubber toughened (RT), and glass bead (GB) filled PA-66 resin and were chosen to study the manufacturing effects on multi-phase resins. The neat PA-66 was observed to consistently infiltrate the fiber beds up to 400 μ m thick regardless of line tensions considered and was used as a baseline for comparison. While line tension did not change the fiber bed saturation for the neat PA-66, the fiber distribution along the width was improved, resulting in a more consistent prepreg thickness. The variations in prepreg thickness were caused by small sections of prepreg not having fibers and the resin surface tension forming a thin resin bridge between adjacent fiber bundles. The addition of rubber or glass particles in the resin immediately eliminated the fiber bed thickness issue because the particles stabilized the resin bridge.

The addition of rubber particles did reduce the fiber beds that the RT PA-66 resin could infiltrate to 300 μ m for tension levels 1 – 3. The higher tension reduced the fiber saturation to fiber beds with a thickness of 250 μ m and the saturation was less consistent. The addition of rubber particles did reduce the infiltration distances from the base resin by 20% with significant a significant 50% reduction when the fiber volume fraction reached 0.70. This indicated the particles may have started filtering in the fiber bed, forming a cake layer. Which was possible, since the fiber bed pores were on average 1.5 μ m wide. The addition of glass particles significantly decreased the ability for the resin to saturate the fiber bed by up to 70% compared to the neat PA-66. This corresponded to fiber bed saturations of 150 – 230 μ m and the fiber bed saturation was inconsistent at each manufacturing condition. The glass particles also caused a substantial increase in resin viscosity compared to the neat and RT PA-66 resins, which resulted in poor fiber bed saturation and the fibers to shift in the impregnation die. Despite the fibers entering the die in a uniform web, the fibers formed discrete fiber bundles, which was believed to be caused by the high melt viscosity.

Select fiber-beds were selected for each manufacturing condition and used as a representative fiber bed. The thickness and fiber volume fraction of these representative beds were used to model the infiltration profile. Overall, the models provided reasonable predictions for the resin infiltration. Additionally, the increase in tension did not necessarily correspond to improved resin infiltration of the fiber bed because of the increased fiber bed compaction reducing the

permeability, which was captured in the infiltration model. When inconsistent resin infiltration was observed for the manufacturing trial, the infiltration model was able to predict the poor saturation.

5.5 References

- [1] Reichanadter A, Bank D, Mansson JAE. A novel rapid cure epoxy resin with internal mold release. *Polym Eng Sci* 2021;61:1819–28. <https://doi.org/10.1002/pen.25703>.
- [2] Wu H, Krifa M, Koo JH. Rubber (SEBS-g-MA) Toughened Flame-Retardant Polyamide 6: Microstructure, Combustion, Extension, and Izod Impact Behavior. *Polym - Plast Technol Eng* 2018;57:727–39. <https://doi.org/10.1080/03602559.2017.1344856>.
- [3] Wu G, Zhang K, Takagi K, Sano H, Yui H. Rubber-toughened polyamide-6 with a low thermal expansion coefficient: Effect of preferential distribution of rubber and inorganic filler. *Polym Int* 2016;65:102–8. <https://doi.org/10.1002/pi.5036>.
- [4] Naffakh M, Dumon M, Gérard JF. Study of a reactive epoxy-amine resin enabling in situ dissolution of thermoplastic films during resin transfer moulding for toughening composites. *Compos Sci Technol* 2006;66:1376–84. <https://doi.org/10.1016/j.compscitech.2005.09.007>.
- [5] Liu D, Li G, Li B, Luan Y, Ling H, Yang X. In-situ toughened CFRP composites by shear-calender orientation and fiber-bundle filtration of PA microparticles at prepreg interlayer. *Compos Part A Appl Sci Manuf* 2016. <https://doi.org/10.1016/j.compositesa.2016.01.015>.
- [6] Groleau MR, Shi YB, Yee AF, Bertram JL, Sue HJ, Yang PC. Mode II fracture of composites interlayered with nylon particles. *Compos Sci Technol* 1996;56:1223–40. [https://doi.org/10.1016/S0266-3538\(96\)00080-2](https://doi.org/10.1016/S0266-3538(96)00080-2).
- [7] Takeda N, Ogihara S. Micromechanical characterization of local deformation in interlaminar-toughened CFRP laminates. *Compos Part A Appl Sci Manuf* 1998;29:1545–52. [https://doi.org/10.1016/S1359-835X\(98\)00067-0](https://doi.org/10.1016/S1359-835X(98)00067-0).
- [8] Caprino G, Iaccarino P, Lamboglia A. The effect of shear on the rigidity in three-point bending of unidirectional CFRP laminates made of T800H/3900-2. *Compos Struct* 2009;88:360–6. <https://doi.org/10.1016/j.compstruct.2008.04.014>.
- [9] Hojo M, Matsuda S, Tanaka M, Ochiai S, Murakami A. Mode I delamination fatigue properties of interlayer-toughened CF/epoxy laminates. *Compos Sci Technol* 2006;66:665–75. <https://doi.org/10.1016/j.compscitech.2005.07.038>.
- [10] Khan SU, Kim JK. Improved interlaminar shear properties of multiscale carbon fiber composites with bucky paper interleaves made from carbon nanofibers. *Carbon N Y* 2012. <https://doi.org/10.1016/j.carbon.2012.07.011>.

- [11] Ma L, Wu L, Cheng X, Zhuo D, Weng Z, Wang R. Improving the interlaminar properties of polymer composites using a situ accumulation method to construct the multi-scale reinforcement of carbon nanofibers/carbon fibers. *Compos Part A Appl Sci Manuf* 2015. <https://doi.org/10.1016/j.compositesa.2015.01.023>.
- [12] Jackson A, Dutton S, Gunnion AJ, Kelly D. Effect of manufacture and laminate design on energy absorption of open carbonfibre/ epoxy sections. *ICCM Int Conf Compos Mater* 2009.
- [13] Young RJ, Maxwell DL, Kinloch AJ. The deformation of hybrid-particulate composites. *J Mater Sci* 1986;21:380–8. <https://doi.org/10.1007/BF01145498>.
- [14] Gallagher MT, Wain RAJ, Dari S, Whitty JP, Smith DJ. Non-identifiability of parameters for a class of shear-thinning rheological models, with implications for haematological fluid dynamics. *J Biomech* 2019;85:230–8. <https://doi.org/10.1016/j.jbiomech.2019.01.036>.
- [15] Lam RC, Kardos JL. The permeability and compressibility of aligned and cross-ply carbon-fiber beds during processing of composites. *Polym Eng Sci* 1991;31:1064–70. <https://doi.org/10.1002/pen.760311411>.
- [16] Reichanadter A, Dustin JS, Balijepalli B, Mansson JA. Process modeling and flexible manufacturing of multi- phase resin based thermoset and thermoplastic. *SPE-ACCE, SPE-ACCE Conference Proceedings*; 2018.
- [17] Reichanadter AM, Dustin JS, Mansson JAE. Process modeling and manufacturing of thermoplastic prepreg tape. *Int. SAMPE Tech. Conf.*, vol. 2019- May, 2019. <https://doi.org/10.33599/nasampe/s.19.1489>.
- [18] Jackson KE. Friction and Wear Behavior of Aluminum and Composite Airplane Skins. *NASA Tech Pap* 1984.
- [19] Stokes GG. On the Effect of the Internal Friction of Fluids on the Motion of Pendulums. *Math Phys Pap* 2010:1–10. <https://doi.org/10.1017/cbo9780511702266.002>.
- [20] Connor M, Toll S, Manson J-AE. On surface energy effects in composite and impregnation consolidation 1995;6:289–95.
- [21] Connor M, Toll S, Manson JAE, Gibson AG. A Model For The Consolidation Of Aligned Thermoplastic Powder Impregnated Composites. *J Thermoplast Compos Mater* 1995;8:138–62.
- [22] Gebart BR. Permeability of unidirectional reinforcements for RTM. *J Compos Mater* 1992;26:1100–33. <https://doi.org/10.1177/002199839202600802>.

APPENDIX C: RHEOLOGICAL DATA

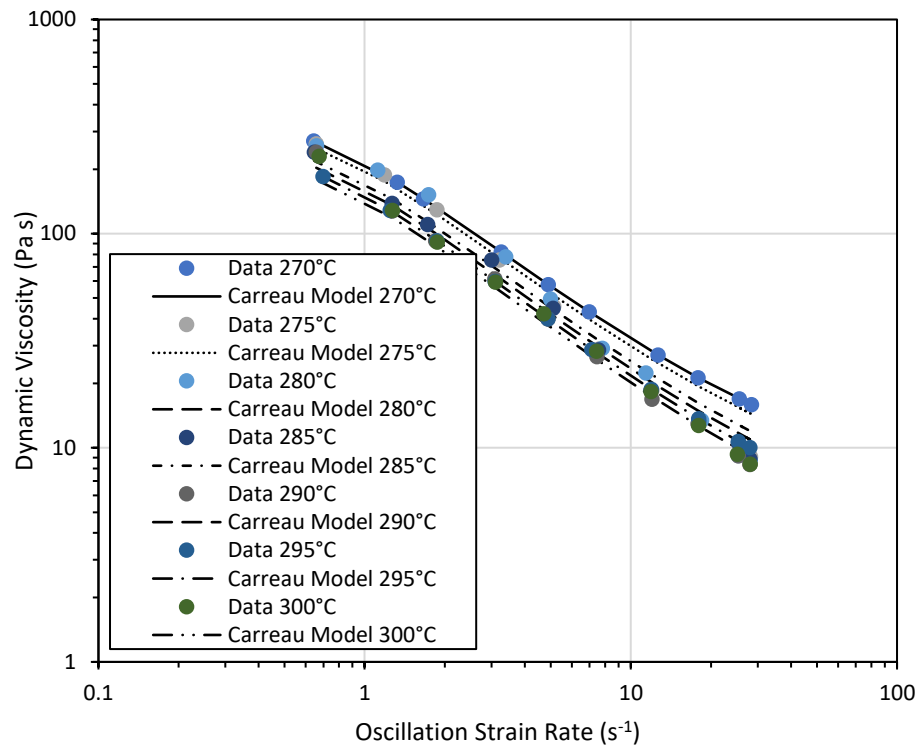


Figure C-1: Neat PA-66 experimental viscosity profile compared to Equation (1.19).

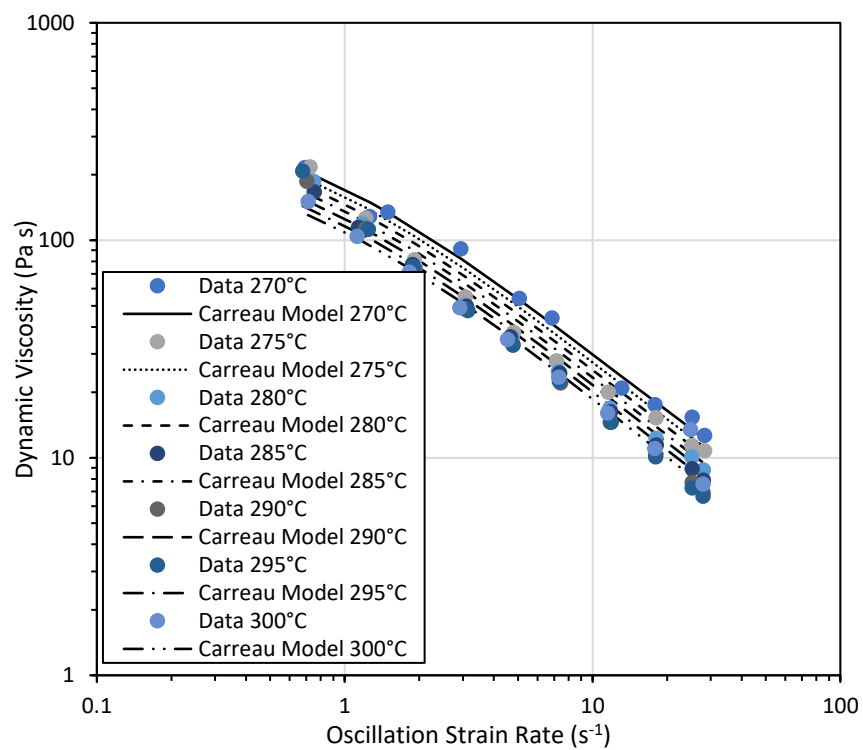


Figure C-2: RT PA-66 experimental viscosity profile compared to Equation (1.19).

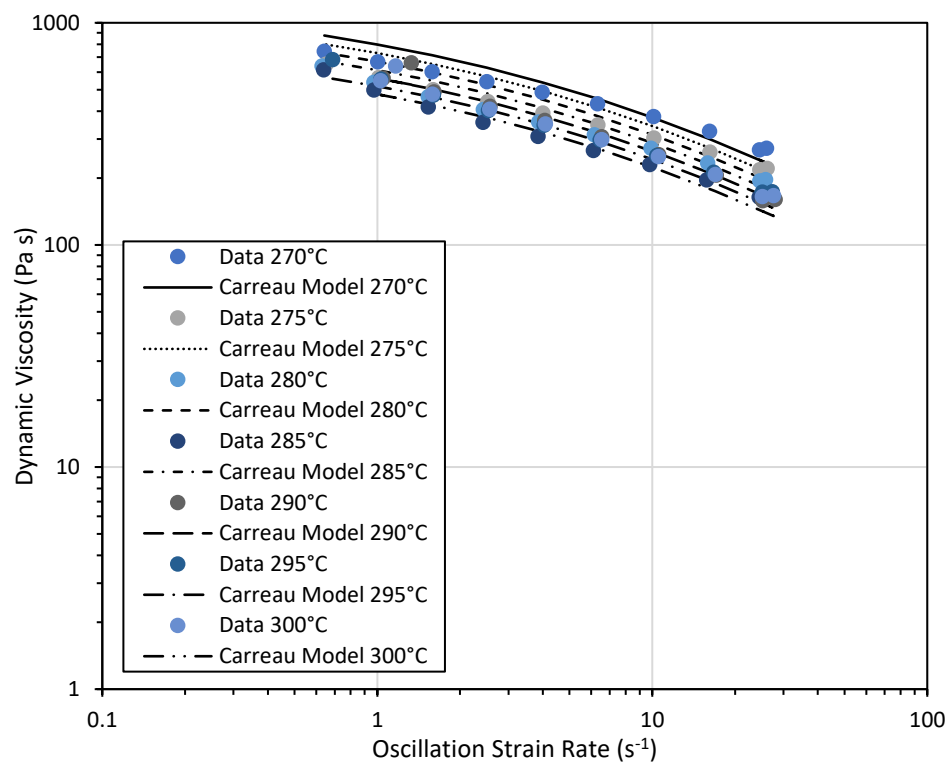


Figure C-3: GB PA-66 experimental viscosity profile compared to Equation (5.1).

6. CONCLUSIONS

In the pursuit of reducing the costs of polymer-composite based parts, epoxy resin formulations have been altered for 2-minute cure times and introduced internal mold-release to reduce mold preparation times. Additionally, carbon fiber manufacturers are working with low-cost process for PAN fibers, resulting in kidney-bean shaped carbon fiber. Fillers have been added to resins to improve cure times, resin stiffness, thermal stability, or resin toughness. These changes to material properties solved certain manufacturing or performance deficiencies, but these improvements may have unforeseen consequences.

In this doctoral thesis work, aspects of the fiber and matrix were characterized to model thermoset and thermoplastic hot-melt impregnation processes. An experimental study of the compaction behavior of kidney-bean shaped carbon fiber and simulation of the fiber's permeability was conducted. The results of those studies were presented in Chapter 2. A rapid cure epoxy resin with internal mold-release was characterized for its cure kinetic and chemorheological behavior. The characterized material was modeled through a hot-melt impregnation process. The results of this work were presented in Chapter 3. The principles learned from the thermoset hot-melt process were used to develop a thermoplastic hot-melt prepreg line to produce 75mm wide prepreg tape. A validation study of the line and resulting prepreg characterization was presented in Chapter 4. Then the hot-melt prepreg line was used to study manufacturing effects on particle infiltration. The resin and particle infiltration study of rubber and glass bead filled resins was presented in Chapter 5.

By studying these systems, I have addressed the following research questions:

1. What is the compaction behavior of kidney-bean shaped carbon fiber?
2. What effect does the packing arrangement and unit cell orientation of kidney-bean shaped fibers have on fiber bed permeability?
3. How does the presence of polar protic and aprotic internal mold-releases impact the cure kinetics of epoxy resins?
4. During hot-melt prepregging, what effect does fiber tension have on resin and particle infiltration into the fiber bed for hard and ductile particles?

6.1 Compaction Behavior of Kidney-Bean Shaped Carbon Fiber

Product cost sensitive industries, such as automotive, struggle to justify using carbon fiber over a lower cost glass fiber alternative. These higher costs of carbon fiber were often inculcated on the carbonization process with long dwell times at high temperatures, but the majority of cost comes from the polyacrylonitrile (PAN) precursor fabrication. Changing the PAN fiber processing conditions to make inexpensive PAN fiber caused the fiber cross-section to appear kidney-bean shaped. This cross-sectional shape persisted through the carbonization step and expressed itself in the final carbon fiber shape. The push for low cost carbon fiber with comparable mechanical properties to traditional carbon fiber has incentivized manufacturers to produce carbon fiber from lower grade PAN resulting in kidney-bean shaped fiber. Existing relationships for fiber bed compaction considered circular fibers.

The compaction data showed the irregular shape of carbon fiber required more pressure to compact, which has implications during infiltration and consolidation efficiency compared to circular carbon fiber. This work demonstrated that the difference in compaction trends was not solely caused by the fiber stiffness, but also a change in the non-linear elastic response of the fiber bed. Furthermore, the compaction data for kidney-bean shaped carbon fiber was not modeled by Equation (2.1) with physically valid V_a values. Therefore, a shape correction factor was proposed for the Gutowski model, shown in Equation (2.22), which provided an excellent fit with the compaction data. The shape correction factor was based on $\frac{1}{\text{Aspect ratio}}$ and applied to the non-linear elastic response. The shape correction factor accounted for the fiber bed's resistance to compaction with a physical constant describing the fiber's irregular shape. The modified Gutowski model accurately predicted the compaction for the kidney-bean shaped fibers with a cross-sectional aspect ratio of 1.57. Additionally, the proposed extension to the Gutowski model recovered the original solution for circular fibers. Finally, the extension of the Gutowski model to irregularly shaped fibers was important as inexpensive carbon fibers become commonly available.

$$P = A \left(\frac{\left(\frac{\sqrt{V_f} - 1}{\sqrt{V_o}} \right)^4}{\left(\frac{\sqrt{V_a} - 1}{\sqrt{V_f}} \right)^4} \right)^{\frac{1}{\phi}} \quad (2.22)$$

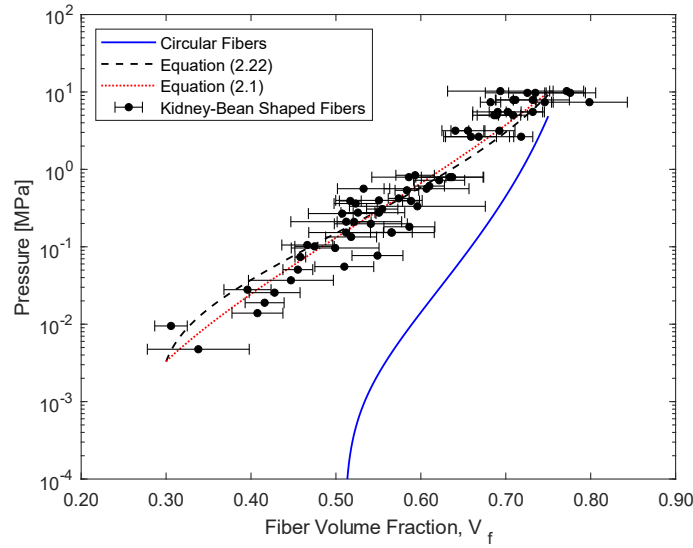


Figure 6.1: Kidney-bean shaped fiber compaction data compared to circular fibers. The kidney-bean shaped fibers were fitted to Equations (2.1) and (2.22) with the model parameters shown in Table 2.1. Error bars represented replicate error of the compacted tows.

6.2 Simulated Permeability of Kidney-Bean Shaped Carbon Fiber

Importantly, all polymer composites must at one stage undergo a resin infiltration process. With the commercial availability of kidney-bean shaped carbon fibers, implications of the fiber shape on permeability needed to be explored for its impact on subsequent composites manufacturing processes. Previous fiber permeability studies expanded permeability trends to various packing arrangements, orientations, and shapes, they had not considered a kidney-bean shaped fiber's effect on permeability.

A representative kidney-bean shaped fiber (KB-fiber) was used to establish different unit cell configurations for this novel carbon fiber shape. Since the KB-fiber had some degree of asymmetry, there were two valid hexagonal packing arrangements and the packing arrangements considered are shown in Figure 6.2. The unit cells were placed in fiber arrays and flow simulations were performed to determine the fiber's transverse permeability. The simulations demonstrated that unit cell orientation affected the permeability. Thus, an upper and lower bound for KB-fiber permeability was established based on unit cell arrangement and orientation, shown in Figure 2.19. At a minimum, the hexagonal packed unit cell orientation caused a 17% reduction in permeability for the same unit cell and fiber volume fraction between the $\pm 90^\circ$ and 0° orientations. In the most extreme case, a 47% reduction in the permeability was observed between the $\pm 90^\circ$ and 0°

orientations. Additionally, the permeability's dependence on unit cell orientation increased with fiber volume fraction. The true permeability of KB-fibers will lie somewhere between these bounds, since fiber packing in polymer composites has a variety of local packing arrangements, fiber orientations, and fiber volume fractions.

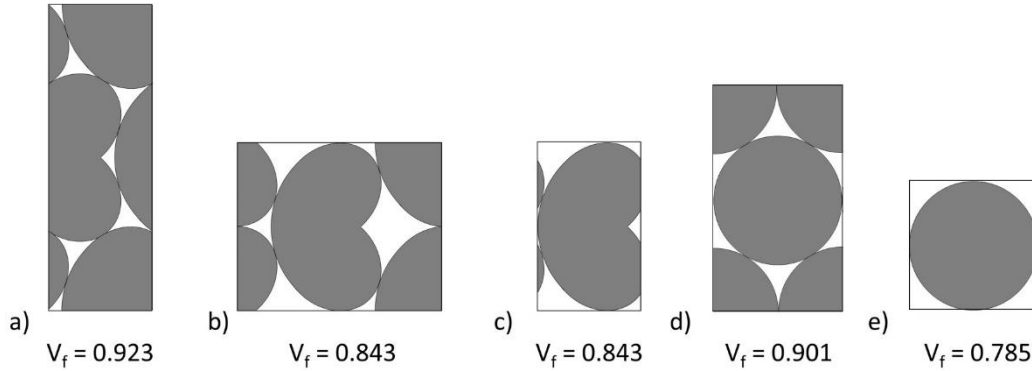


Figure 6.2: Examples of fiber packing unit cells with their maximum packing fraction for a) hexagonal pack – 1 KB-fiber, b) hexagonal pack – 2 KB-fiber, c) square pack KB-fiber, d) hexagonal pack circular fiber, e) square pack circular fiber.

The permeability for the KB-fiber was consistently lower across all unit cell arrangements and orientations when compared to circular fibers with hexagonal packing. At maximum, a 74% reduction in permeability was observed for the KB-fiber which corresponded to a 3.86 time increase in infiltration compared to traditional carbon fiber. The permeability was also modeled using the Carman-Kozeny equation (Equation (2.4)) and Gebart's model (Equation (2.23)). Equation (2.4) was able to fit the KB-fiber permeability when unique shape factors were fitted for each unit cell arrangement, orientation, and fiber volume fraction. The fitting resulted in the Kozeny constant having a parabolic relationship with fiber volume fraction. In contrast, Equation (2.23) provided an appropriate fit to the KB-fiber permeability vs fiber volume fraction with a unique constant for each unit cell arrangement and orientation. Thus, Equation (2.23) was found to be better suited to describe the transverse permeability for the KB-fiber.

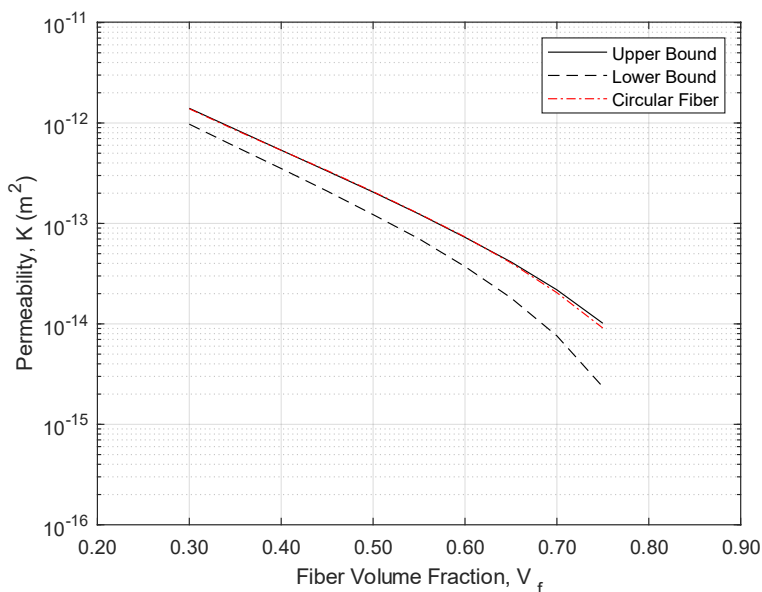


Figure 6.3: Upper and lower bound permeability across all KB-fiber unit cells compared to circular fibers with hexagonal packing.

6.3 Characterization of a Rapid Cure Epoxy Resin with Internal Mold-Release

The rapid cure epoxy resin was a propane, 2,2-bis[p-(2,3-epoxypropoxy)phenyl] epoxy with dicyandiamide curative, internal mold-release, and a urea based accelerant. The base epoxy formulation contained a non-polar wax type internal mold-release and achieved 90% cure in 80 seconds compared to the 100 seconds when a polar wax type internal mold-release was added. The addition of 2.5wt% polar internal mold-release to the epoxy resin hindered the 1st step of the reaction. The additional IMR was hypothesized to act as a diffusive barrier for the initial barrier to overcome. After the IMR migrated to the sample surface, the 2nd reaction step proceeded unhindered. While an additional 2.5wt% of internal mold-release retarded the 1st step of the reaction, the final degree of cure was unchanged. While the 20 second delay in reaction when the polar internal mold-release was present did not appear significant, this represented a 17% increase in the cure time. This increased cure time would substantially influence the viability of this resin in the automotive industry.

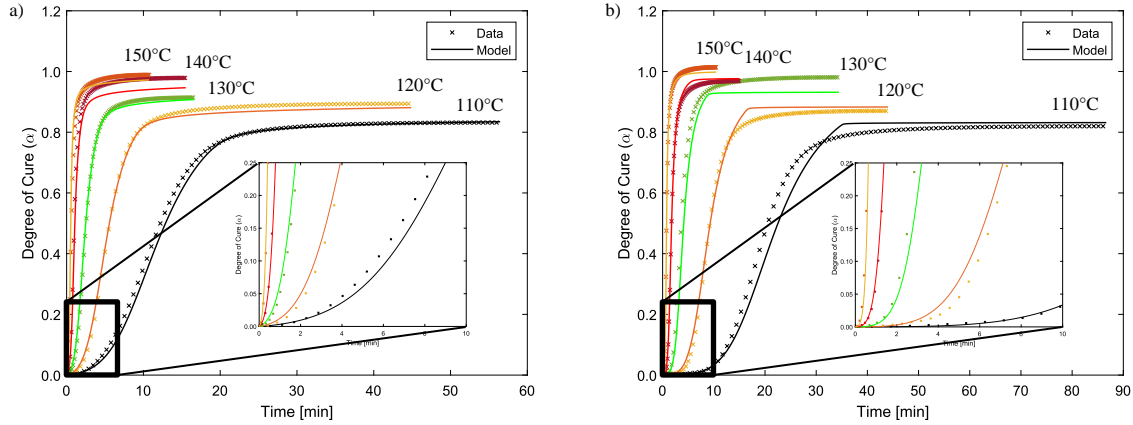


Figure 6.4: a) RCE and RCE+IMR b) resins isothermal cure [X] comparison to autocatalytic kinetics with WLF diffusion model [-].

Both of the rapid cure epoxy resins followed autocatalytic kinetics with WLF diffusion model and modified WLF viscosity model. Additionally, at 150°C, the RCE resin was able to achieve 94% cure after 2 minutes, making this a suitable temperature and cure time for compression molding. Below 140°C, the reaction was diffusion limited and post curing would be needed. Furthermore, the viscosity model showed that at 120°C, the RCE resin viscosity could remain below 5 Pa·s for 4.1 minutes, before the cross-linking reaction significantly raised the viscosity. Therefore, the RCE resin can sustain viscosities suitable for prepregging up to 120°C. This base rapid cure epoxy resin was viable for high-volume composites manufacturing since it was able to infiltrate at temperatures up to 120°C and perform a cure cycle at 150°C in 2 minutes.

The rapid cure epoxy resin with particles was modeled in a hot-melt impregnation process with properties of the kidney-bean shaped carbon fibers described in Chapter 2. The S-wrap process demonstrated lower pressures were required for the same impregnation compared to the nip-roller process. As a result, particles of 3μm were able to infiltrate the fiber bed in the S-wrap configuration compared to the nip-roller layout with 0.9μm pores. The force-controlled process (S-wrap) allowed for appreciably more particles to penetrate the fiber bed and provided a scalable way to control the particle infiltration since pore size was not dependent on line speed. In contrast, the nip-roller process average pore size was dependent on the line speed. Therefore, the force-controlled process layout performed considerably better for resin with filler content to penetrate the fiber bed. The average pore size for kidney bean shaped carbon fiber and other fiber diameters were geometrically defined and decreased with fiber volume fraction. Based on the average pore

sizes, a general rule to follow was that particle diameters should not exceed fiber radius when infiltrating fiber beds.

6.4 Manufacturing Effects on Resin and Particle Infiltration in Multi-Phase Thermoplastic Prepreg Tape

A thermoplastic hot-melt extrusion prepreg line was developed in Chapter 4 to study thermoplastic prepreg tape production. The line layout is shown in Figure 6.5. In Chapter 5, three polyamide-66 resins were used in a hot-melt extrusion prepegging process to produce prepreg tape at 4 different tension levels. The resins were a neat, rubber toughened (RT), and glass bead (GB) filled PA-66 resin and were chosen to study the manufacturing effects on multi-phase resins. The neat PA-66 was observed to consistently infiltrate the fiber beds up to 400 μ m thick regardless of line tensions considered and was used as a baseline for comparison. While line tension did not change the fiber bed saturation for the neat PA-66, the fiber distribution along the width was improved, resulting in a more consistent prepreg thickness. The variations in prepreg thickness were caused by small sections of prepreg not having fibers and the resin surface tension forming a thin resin bridge between adjacent fiber bundles. The addition of rubber or glass particles in the resin immediately eliminated the fiber bed thickness issue because the particles stabilized the resin bridge.

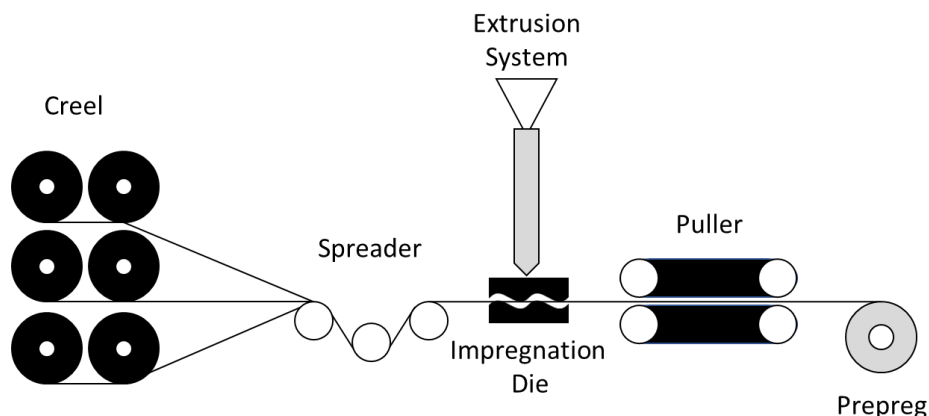


Figure 6.5: Thermoplastic extrusion hot-melt impregnation line layout, where the process moved from left to right.

The addition of rubber particles did reduce the fiber beds that the RT PA-66 resin could infiltrate to 300 μm for tension levels 1 – 3. The higher tension reduced the fiber saturation to fiber beds with a thickness of 250 μm and the saturation was less consistent. The addition of rubber particles did reduce the infiltration distances from the base resin by 20% with significant a significant 50% reduction when the fiber volume fraction reached 0.70. This indicated the particles may have started filtering in the fiber bed, forming a cake layer. Which was possible, since the fiber bed pores were on average 1.5 μm wide, as described in Figure 6.6. The addition of glass particles significantly decreased the ability for the resin to saturate the fiber bed by up to 70% compared to the neat PA-66. This corresponded to fiber bed saturations of 150 – 230 μm and the fiber bed saturation was inconsistent at each manufacturing condition. The glass particles also caused a substantial increase in resin viscosity compared to the neat and RT PA-66 resins, which resulted in poor fiber bed saturation and the fibers to shift in the impregnation die. Despite the fibers entering the die in a uniform web, the fibers formed discrete fiber bundles, which was believed to be caused by the high melt viscosity.

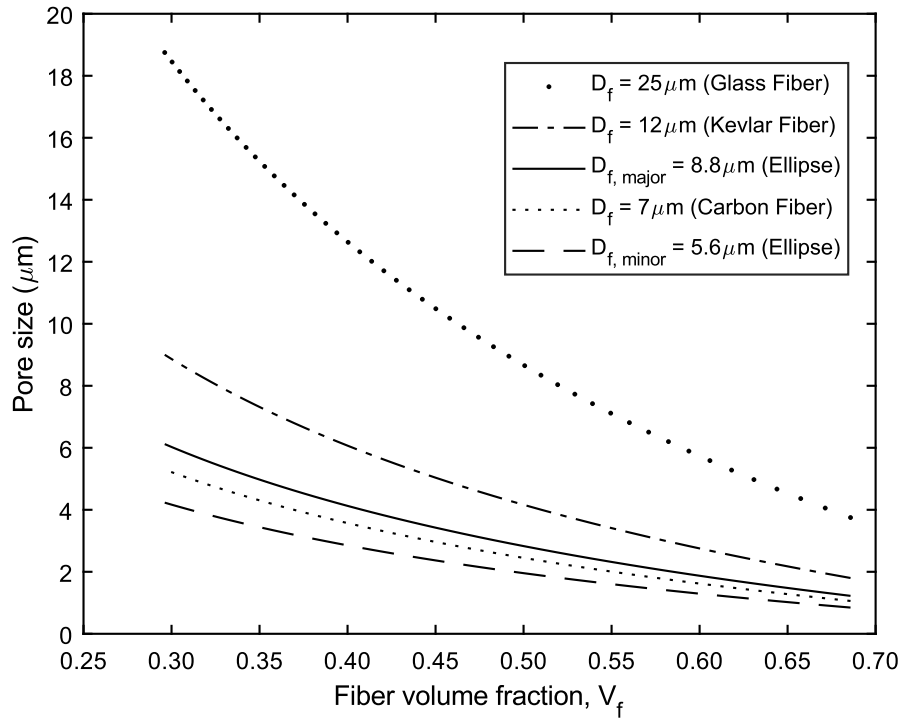


Figure 6.6: Average pore size for hexagonally packed fibers as a function of fiber volume fraction for various fiber diameters.

Select fiber-beds were selected for each manufacturing condition and used as a representative fiber bed. The thickness and fiber volume fraction of these representative beds were used to model the infiltration profile. Overall, the models provided reasonable predictions for the resin infiltration. Additionally, the increase in tension did not necessarily correspond to improved resin infiltration of the fiber bed because of the increased fiber bed compaction reducing the permeability, which was captured in the infiltration model. When inconsistent resin infiltration was observed for the manufacturing trial, the infiltration model was able to predict the poor saturation. The GB PA-66 poorly infiltrated the fiber bed compared to the neat and RT PA-66 resins. Which was a result of the high viscosity and larger particle diameters compared to the RT PA-66. A model comparison at tension level 1 for the three resins is provided in Figure 6.7. Where the neat PA-66 resin and RT PA-66 resin were expected to infiltrate fiber beds to nearly 400 μ m and 350 μ m, respectively. Unlike the GB PA-66, which was approximately 70 μ m.

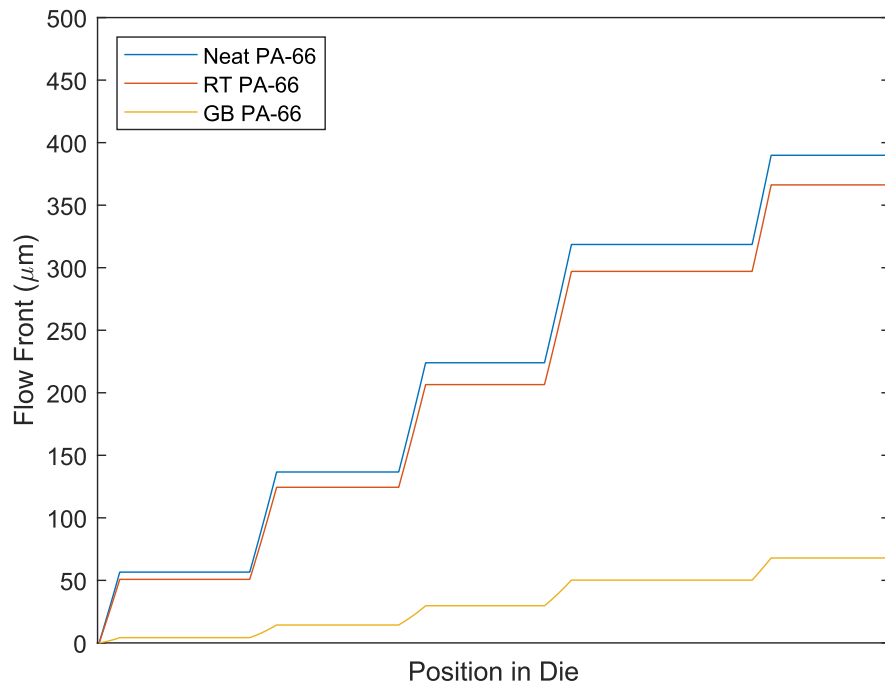


Figure 6.7: Modeled infiltration profiles for neat, rubber toughened, and glass bead filled PA-66 prepreps at tension level 1.

6.5 Summary

In summary, I have been able to highlight aspects of low-cost materials for prepreg manufacturing and the issues that may arise when selecting different fiber types, geometries, as well as resin modifications. The change in carbon fiber cross-sectional geometry effected the compaction behavior and caused additional force to be applied for comparable compaction. Thus, higher compression molding pressures may be required for similar part consolidation when compared to traditional carbon fiber. Additionally, the permeability of these low-cost carbon fiber was highly dependent on unit cell packing arrangement and flow direction. This implies the resin infiltration processes into these fiber beds may vary depending on the in-plane fiber orientation. Additionally, these permeabilities were generally lower than traditional carbon fiber, resulting in lengthier infiltration times.

A rapid cure epoxy resin with internal mold-release, targeted for 3-minute part cycle times was characterized with polar and non-polar internal mold-release. The addition of mold-release reduces mold preparation times, but also influenced the cure rate. The polar mold-release was found to increase cure times by 20 seconds, which significantly effected the 3-minute part cycle time. The rapid cure epoxy resin system was paired with the kidney-bean shaped carbon fiber through a thermoset hot-melt impregnation process. Because of quality control issues related to solids selectively filtering at the fiber bed during prepregging, the process was modeled to identify processing guidelines. An S-wrap process was deemed well suited for this material system because of the lower pressures reduced the degree of fiber bed compaction and allowed more particles to infiltrate the fiber bed.

The operational design principles established with the thermoset prepreg were used to develop a thermoplastic prepreg tape line. The line was used to study the manufacturing effects on resin and particle infiltration into fiber beds. A neat, rubber toughened, and glass bead filled PA-66 were used to correlate line tension with infiltration quality. The rubber toughened PA-66 was able to infiltrate the fiber bed comparably to the neat PA-66 up until the highest tension setting, where there was a significant reduction in the rubber toughened PA-66 resin infiltration. While, the larger glass bead particles had poor resin infiltration, regardless of tension levels. This indicated particle filled resins were much more sensitive to line tension compared to unfilled resins because of particle filtration issues caused by the fiber bed sieving the particles.